AUBURN

SAMUEL GINN
COLLEGE OF ENGINEERING

Research Report

EXPERIMENTAL DETERMINATION OF BRAKING FORCE DISTRIBUTION IN STEEL PILE BENT BRIDGES

Submitted to

The Alabama Department of Transportation

Prepared by

Justin D. Marshall, Ph.D., P.E.
J. Brian Anderson, Ph.D., P.E.
Robert W. Barnes, Ph.D., P.E.
Matthew D. Barr
Anna J. Quinn
Hongyang Wu

APRIL 2020

Highway Research Center
Harbert Engineering Center
Auburn, Alabama 36849

www.eng.auburn.edu/research/centers/hrc.html

1. Report No. ALDOT 930-928	**2. Government Accession No.**	**3. Recipient Catalog No.**
4 Title and Subtitle Experimental Determination of Braking Force Distribution in Steel Pile Bent Bridges		**5 Report Date** April 2020 **6 Performing Organization Code**
7. Author(s) Justin D. Marshall, J. Brian Anderson, Robert W. Barnes, Matthew D. Barr, Anna J. Quinn, Hongyang Wu		**8 Performing** ALDOT 930-928
9 Performing Organization Name and Address Highway Research Center Department of Civil Engineering 238 Harbert Engineering Center Auburn, AL 36849		**10 Work Unit No. (TRAIS)** **11 Contract or Grant No.**
12 Sponsoring Agency Name and Address Alabama Department of Transportation 1409 Coliseum Boulevard Montgomery, Alabama 36130-3050		**13 Type of Report and Period Covered** Technical Report **14 Sponsoring Agency Code**
15 Supplementary Notes		

16 Abstract

The research conducted in this project was undertaken to gain insight into to the load path and intensity of the longitudinal braking force in highway bridge substructures, specifically shorter span, simply-supported bridges. To evaluate braking force magnitude and distribution, two types of field tests were conducted static tests and dynamic braking tests. From these field tests, the data was processed and an analytical model was created and calibrated. The last component of the research project was a limited parametric study which further studied the distribution of the longitudinal braking force in substructure elements for simply supported spans typical in Alabama. The research demonstrated that the abutments will experience a maximum of approximately 75 percent and an individual column bent will experience a maximum of about 35 percent of the braking force. The demand in an individual component is related primarily to the position of the braking vehicle component and the relative stiffness of that component.

17 Key Words		**18 Distribution Statement** No restrictions. This document is available to the public through the National Technical Information Service, Springfield, Virginia 22161	
19 Security Classification (of this report) Unclassified	**20 Security Classification (of this page)** Unclassified	**21 No. of pages** 253	**22 Price**

FORM DOT F 1700.7 (8-72)

Research Report

ALDOT Research Project #930-928

EXPERIMENTAL DETERMINATION OF BRAKING FORCE DISTRIBUTION IN STEEL PILE BENT BRIDGES

Submitted to

The Alabama Department of Transportation

Prepared by

Justin D. Marshall
J. Brian Anderson
Robert W. Barnes
Matthew D. Barr
Anna J. Quinn
Hongyang Wu

Highway Research Center

and

Department of Civil Engineering

at Auburn University

APRIL 2020

DISCLAIMERS

The contents of this report reflect the views of the authors, who are responsible for the facts and the accuracy of the data presented herein. The contents do not necessarily reflect the official views or policies of Auburn University or the Federal Highway Administration. This report does not constitute a standard, specification, or regulation.

NOT INTENDED FOR CONSTRUCTION, BIDDING, OR PERMIT PURPOSES

Justin D. Marshall, Ph.D., P.E.
Research Supervisor

ACKNOWLEDGEMENTS

The authors would like to acknowledge all those who have participated in this project either as part of the team or the ALDOT Bridge and Maintenance Bureaus personnel who provided input throughout the process. Special thanks to the Maintenance Bureau for providing the Load Truck, the snooper truck, and traffic control during the field testing portion of the research effort.

Abstract

The research conducted in this project was undertaken to gain insight into to the load path and intensity of the longitudinal braking force in highway bridge substructures, specifically shorter span, simply-supported bridges. With the LRFD Specifications requiring a larger magnitude of force than the Standard Specifications, it became necessary to better understand the implications of braking and what magnitude of forces are going to be generated. To evaluate braking force magnitude and distribution, two types of field tests were conducted. First, static pull tests were conducted on each span with using an ALDOT Load Truck and a heavy tow-truck. Second, dynamic braking tests were conducted on the center and right side of spans 2, 3 and 5 using an ALDOT Load Truck stopping entirely with a single span of the bridge. From these field tests, the data was processed and an analytical model was created and calibrated to the field data. Calibrating the displacements and accelerations of the bridge between the field data and model results was crucial to be able to validate the accuracy of the model results. Bent shear forces from the static and dynamic tests were recorded and analyzed to determine how they compared to code provisions. The last component of the research project was a limited parametric study which further studied the distribution of the longitudinal braking force based on the position of the loading and the stiffness of the substructure element for simply supported spans typically constructed in Alabama. The research demonstrated that the abutments will experience a maximum of approximately 75 percent of the braking force and an individual column bent will experience a maximum of about 35 percent of the braking force. The demand in an individual component is related primarily to the position of the braking vehicle with respect to the substructure component and the relative stiffness of that component with respect to other substructure elements.

Table of Contents

List of Tables

List of Figures

Chapter 1 Introduction

1.1 Background and Problem Statement

One of the most common bridge types in Alabama is the multi-span bridge with prestressed concrete girders, a cast-in-place concrete bent cap and driven steel HP pile bents. In cases when the bent is in the flow channel, the steel piles are encased with non-structural concrete for 3 feet above the mudline which serves to prevent section loss. If there is more than 14 feet between the top of the encasement and the bent cap, welded sway bracing is used in either a one or two-story condition to provide lateral stiffness and strength. Recent work at Auburn University has looked at the lateral behavior of unbraced pile bents from the perspective of modeling, analysis and design for lateral forces (i.e. wind). This work focused on this same bridge type but investigated the primary horizontal force in the longitudinal direction, the braking force. Figure 1-1 and Figure 1-2 are from a typical multi-span bridge located on County Road 9 Macon County, Alabama.

Figure 1-1 Side View of a Typical ALDOT Multi-Span Steel Bent Bridge

Figure 1-2 Galvanized HP Pile Bents Typical of Alabama Steel Pile Bent Bridges

For these bridges the primary lateral force along the length of the bridge is due to the braking force of vehicles on the bridge. In the transition from the Standard Specification (AASHTO, 2002) to the LRFD Specification (AASHTO, 2017) the braking force has significantly increased for short and medium span bridges. The Standard Specification required a longitudinal force of 5 percent of the live load. The LRFD Specification has increased that to 25 percent of the live load. This results in an increase of 400 percent for this type of short to moderate span bridge.

The prestressed girders in these bridges are designed as simple-span with an expansion joint at each bent. For each girder, the typical detail has a fixed bearing on one end and a free bearing at the other end to allow for thermal expansion and contraction. According to this reasoning, all the longitudinal force would go into the fixed bearing. This load would then have to be resisted by the pile bent or abutment at the fixed bearing. In the longitudinal direction pile bents are assumed to resist loads as a cantilever element. Large longitudinal shears can cause significant increases in the pile size due to large unbraced lengths and p-delta effects coupled with the gravity loads. The challenge for this newly increased braking force is to now design the piles with a substantial increase in shear.

In reality, even expansion bearings have the capacity to resist significant shear forces through friction between the girder and elastomeric bearing pad. Recent testing at the University of Illinois (Steelman, et al., 2013) observed a frictional coefficient between the prestressed concrete girder and the bearing pad to range from 0.2 to 0.5. This indicates that it is very likely that even a free bearing has the capacity to transfer a significant amount of braking force. This alone would allow more than one bent to share the braking load for a single span. As this deformation would transfer force to adjacent bents, it would also transfer force to the abutment. In addition to the elastic load path, the dynamic nature of the force will also engage the bridge inertia. This creates a very complex load path and distribution. Based on information from bridge engineers, these longitudinal braking forces can play an important role in sizing of the steel piles.

Recent work at Auburn University has looked at the lateral behavior of unbraced pile bents from the perspective of modeling, analysis, and design for lateral forces (i.e. wind) in the transverse direction (Skinner 2016 and Campbell 2016). These projects involved full scale load tests of sacrificial test bents and load testing a newly constructed short span bridge. The focus of this project is to research the lateral behavior of unbraced pile bents in the longitudinal direction. The primary cause of force in this direction is a result of vehicle braking.

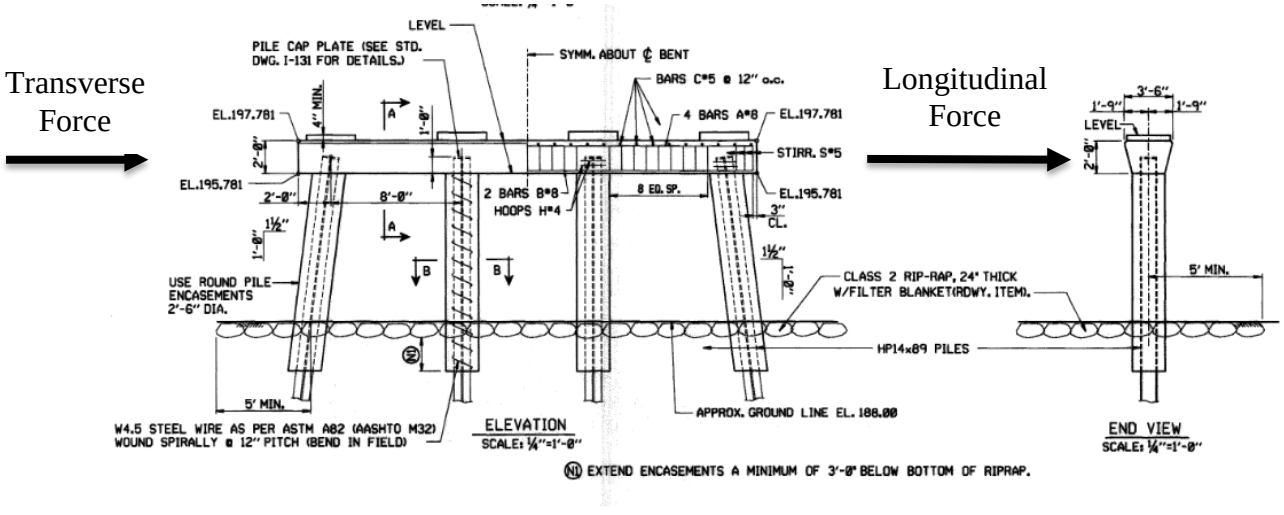

Figure 1-3 Elevation and End View of Bridge Bent (ALDOT 2013)

The focus of this project will be static and dynamic experimental testing coupled with analytical modeling to determine the load path and load distribution for longitudinal braking forces in steel pile bent bridges. This information will guide designers in determining longitudinal braking force load transfer in structural design.

1.2 Bridge Description

The bridge that was tested for this project spans over Old Town Creek located on County Road 9 in Macon County Alabama. This location was chosen for this project because of previous research projects that have been conducted on this bridge. The bridge consists of six 40 ft spans supported by HP pile bents with a cast-in-place reinforced concrete bent cap (Figure 1-4). Each bent consists of four HP 14X89 piles that vary in length and are embedded into the cap a minimum of 12 inches. The exterior piles are typically battered at a slope of 1.5:12. Bents 3 & 4 lie in the main channel and are galvanized steel without concrete encasement. Bents 2, 5, and 6 are encased in non-structural concrete to a minimum depth of 3 ft below the mudline.

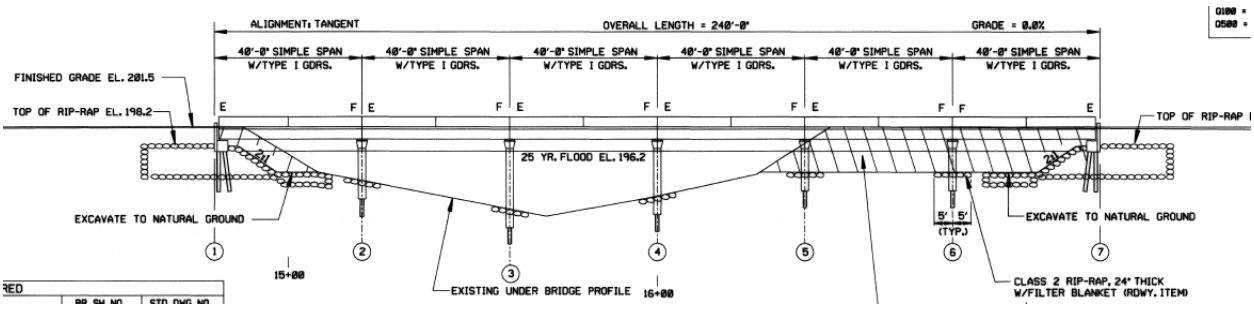

Figure 1-4 Elevation of Bridge over Old Town Creek (ALDOT 2013)

1.3 Research Objectives

One existing steel pile bent bridge was tested as part of this project. The results of the testing were coupled with analytical models to meet the following research objectives:

1) Experimentally determine the load path and force distribution for longitudinal braking force in multi-span, simple-span steel pile bent bridges using static and dynamic loading.
2) Construct and calibrate a numerical model of the tested bridge using the experimental results including the effect of the shear stiffness of the bearing connection and pile data.
3) Conduct a parametric study using the calibrated numerical bridge model. This study investigated the variation of multiple parameters which impact the braking force distribution to the pile bents and abutments.
4) Develop recommendations for designers on how the longitudinal braking forces should be applied to pile bents and abutments in a bridge structure.

1.4 Research Scope

The scope of this study is limited to determination of the braking force distribution in short and moderate span, simple-span, prestressed concrete girder bridges with steel pile bents. One existing bridge was instrumented and tested statically and dynamically to identify the load path and force distribution in the bridge under the effects of the heavily loaded truck stopping on an individual span. An analytical model was constructed using the structural and geotechnical information of the constructed bridge and validated using the measured results from the experimental testing. Following the development of a calibrated analytical model, a parametric study was completed using numerical models of steel pile bent bridges. Specific parameters of the bridges were modified in order to determine the effect of those parameters on the distribution of braking force within the bridge.

1.5 Organization of Report

Chapter 2 of this report provides a literature review of important topics related to longitudinal braking force and analytical modeling of bridge superstructure and substructure. Chapter 3 describes the instrumentation types and placement on the bridge in addition to the data acquisition used to capture data during the static and dynamic tests. Chapter 4 describes the preliminary analytical model and the different tests that were carried out of the bridge. Chapter 5 provides the results and the discussion of results from all the experimental tests. Chapter 6 describes the process of generating a validated analytical model of the Old Town Creek bridge using the results from the static and dynamic testing. Using the process developed in Chapter 6, Chapter 7 reports the process and results of a parametric study looking at several variables important to the distribution of braking force among column bents and abutments. Chapter 8 provides the conclusions and recommendations for the research project.

Chapter 2 Literature Review

2.1 Introduction

This chapter covers background information related to bridge design codes, truck braking, and modeling considerations. A review of literature on the following topics was conducted: design codes and philosophies, longitudinal braking, road-tire friction, bearing pads, and different analysis methods for modeling of the bridge. Overall, previous work related to this project is limited, which lead to a wide-ranging review of topics to achieve a thorough understanding of how to complete this research project.

2.2 Transition for Standard Specification to Load-and-Resistance Factor Design Specification

Prior to 2007, the AASHTO Standard Specification was the most widely used code for bridge design in the United States. With the first edition published in 1931, it was updated periodically, and by 1949, was regularly updated every 4 years until the publication of the 17th edition. As design capabilities progressed and alternative design philosophies were adopted, the Federal Highway Administration and the States established that Load-and-Resistance Factor Design (LRFD) shall be the standard used in all bridge design by 2007 (AASHTO, 2002). This transition came about due to a request by the Subcommittee on Bridges and Structures for the review of foreign design specifications and codes to understand their philosophies compared to the underlying design philosophies of the Standard Specification. It was discerned that the Standard Specification had inconsistences, conflicts, and gaps in its methodology as well as no incorporation of the newly developed LRFD philosophy that was quickly becoming popular among structural engineers in Canada and Europe (AASHTO, 2017).

The underlying design philosophy on which the Standard Specification is built is working stress design (WSD). Within WSD, an allowable stress is determined as a fraction of the material's load carrying capacity, this capacity shall not be exceeded by the design stresses. It was not until the early 1970's that WSD incorporated the variability of certain loads such as wind or vehicular. To account for this variable predictability, design factors were computed and a shift to the design philosophy known as load factor design (LFD) was created. LFD still failed to consider the variability of properties of the structural elements, themselves, though. For these reasons, LRFD became the predominant design method because it incorporates the variability of

structural elements explicitly (AASHTO, 2017). Additionally, LRFD relies on factors derived from statistical methods and presents them in an easy to use manner.

2.3 Longitudinal Braking Force

Upon the switch between design methodologies, the design amount of longitudinal braking force increased significantly. This is especially true for common short- to medium-span bridges. In the Standard Specification, the equation for braking force is

$$BR_{Standard\ Spec} = 0.05 \times (LL + Concentrated\ Load) \times N_{Lanes} \qquad \text{Equation 2-1}$$

Where

$$LL = lane\ load$$

$$N_{Lanes} = Number\ of\ Lanes\ Carrying\ Traffic\ in\ the\ Same\ Direction$$

The lane load plus the concentrated load for moment is specified in Article 3.7 of the Standard Specification. The lane load is 0.64 klf and the concentrated load is 72 kips, as prescribed in the HS20-44 loading. Application of the reduction for multiple-loaded lanes as directed in Article 3.12 (2002) must also be included. The reduction in live load intensity shall be applied prior to computing the breaking force using $\mathrm{BR_{LRFD}} = \text{maximum}\begin{Bmatrix} 0.25 \times \text{axle weight} \\ 0.05 \times (\text{axle weight} + \text{LL}) \end{Bmatrix} \times \mathrm{N_{Lanes}} \times \mathrm{MPF}$. Reducing the live load incorporates the "improbability of the coincident maximum loading" as stated in the Standard Specification (2002).

In the LRFD Specification, braking force is computed as follows

$$BR_{LRFD} = maximum\begin{Bmatrix} 0.25 \times axle\ weight \\ 0.05 \times (axle\ weight + LL) \end{Bmatrix} \times N_{Lanes} \times MPF \qquad \text{Equation 2-2}$$

Where,

$$axle\ weight = 72\ kips$$

$$LL = 0.64\ k/ft$$

$$N_{Lanes} = Number\ of\ Lanes\ Carrying\ Traffic\ in\ the\ Same\ Direction$$

$$MPF = Multiple\ Presence\ Factor$$

Additionally, in the Commentary to the LRFD Specifications it explicitly states that for short- and medium-span bridges, the braking force used in design can be significantly greater than the Standard Specification braking force. This is due to the data being used to determine the braking force having not been modified since at least the early 1940's, and it does not account for the improved baking capacity of trucks in today's era (AASHTO, 2017). Published in the Commentary to the LRFD Specifications are Figure 2-1 through Figure 2-4 that illustrate how insufficient the Standard Specification has become in accounting for braking force and how it trailed Canada in their respective design codes.

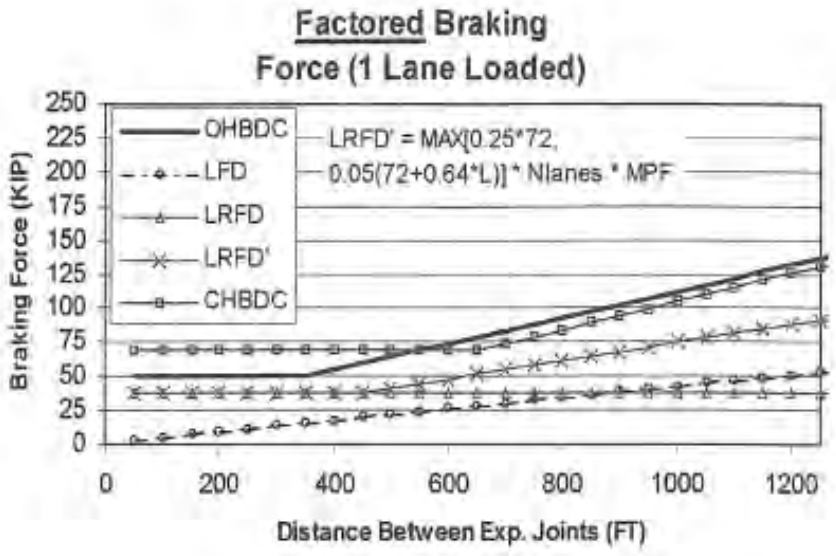

Figure 2-1 – Factored Braking Force Comparisons for 1 Lane Loaded (AASHTO, 2017)

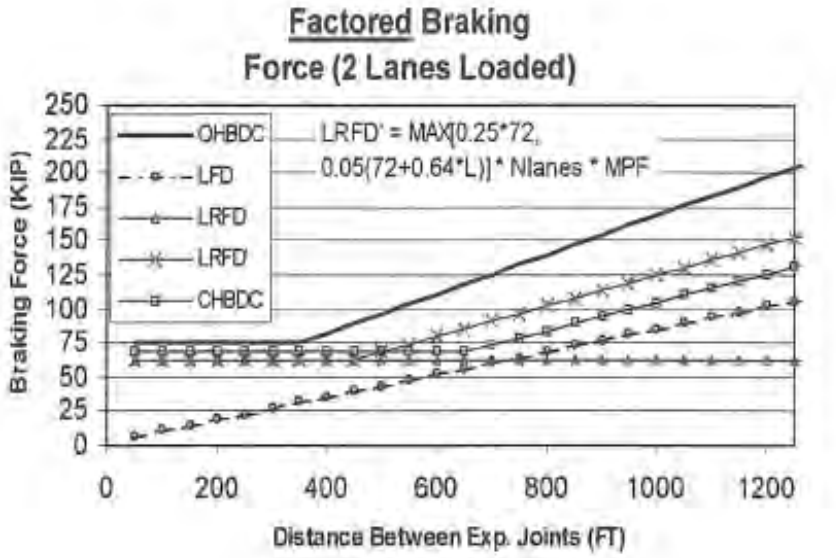

Figure 2-2 – Factored Braking Force Comparisons for 2 Lanes Loaded (AASHTO, 2017)

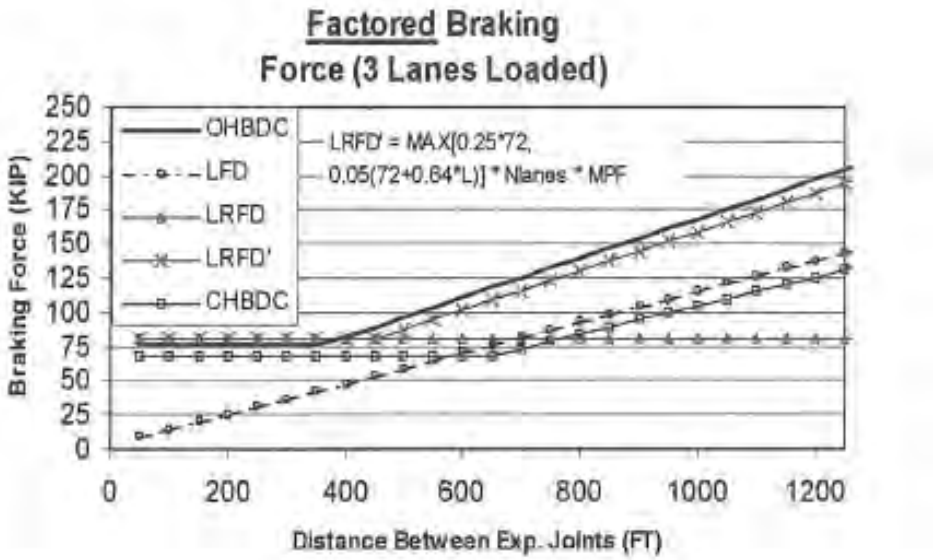

Figure 2-3 – Factored Braking Force Comparisons for 3 Lanes Loaded (AASHTO, 2017)

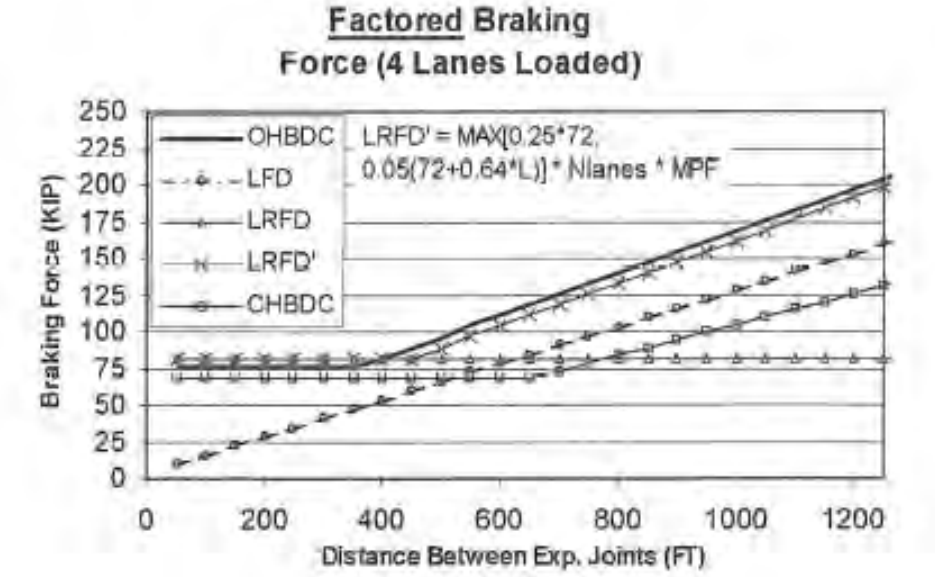

Figure 2-4 – Factored Braking Force Comparisons for 4 Lanes Loaded (AASHTO, 2017)

In all of the figures, Ontario Highway Bridge Design Code (OHDBC), LFD is the factored braking force as specified in the Standard Specification. LRFD is the originally specified braking force (up to the 2001 Interim edition) and LRFD' is the current specified braking force. CHBDC is the braking force specified by the Canadian Highway Bridge Design Code. It is not known where the data used to create these graphs originated, but it illustrates how the increase in braking force could pose issues with rehabilitation projects where the bridge was

designed according to the Standard Specification but is now governed by LRFD Specifications. Furthermore, it shows how design of new structures could require larger structural components and foundations to satisfy braking force design requirements.

With the lane load appearing in both equations, its significance cannot be neglected. For both codes, the lane load is 0.64 kips per linear foot. Its purpose is to "emulate a caravan of vehicles" and was introduced in 1944 (Chen and Duan 1999).

2.4 Friction

The amount of longitudinal force transmitted into the superstructure from the braking vehicle is dependent upon the friction between the tire and road interface. The 25 percent as specified in the LRFD Specification could be interpreted as the estimated maximum coefficient of friction expected between the tires and roadway. For a non-skewed bridge without elevation change, the friction force is directly related to the coefficient of friction for the bridge deck surface and the normal force of the vehicle undergoing the braking maneuver. The friction coefficient is also dependent on many factors such as: amount of moisture on the pavement, temperature, whether the vehicle has locked its brakes during the maneuver and the type of surface.

Locked-wheel braking occurs when the brakes grip too tightly to the wheel, causing the vehicle to slide. During this type of braking, sliding friction is used, and is less than the peak achievable friction value (Torbic, et al. 2003). For all of the tests conducted in this research, the goal was to complete the braking maneuver within the span of interest without inducing locking of the brakes. Since it is extremely difficult to know precisely the coefficient of friction for a bridge deck, data from the Federal Motor Vehicle Safety Standard (FMVSS) 121 was used to compute approximate values for the coefficient of friction for various truck configurations, vehicle speeds, and braking distances over those speeds. These values aided in the formulation of expected deceleration rates and coefficients of friction during testing. In order to calculate these values from the FMVSS 121 (2008), the standard constant-acceleration kinematic equation presented in $v_f^2 = v_o^2 + 2a(\Delta x) v_f^2 = v_o^2 + 2a(\Delta x)$ was rearranged and used to obtain a deceleration rate.

$$v_f^2 = v_o^2 + 2a(\Delta x) \qquad \text{Equation 2-3}$$

Where,

$$v_f = final\ velocity$$

$$v_o = initial\ velocity$$

$$a = deceleration$$

$$\Delta x = change\ in\ displacement$$

The deceleration rate was divided by gravity (32.2 ft/s^2) to arrive at an acceleration value in terms of gravity. These values ranged between 0.34g to 0.39g for trucks that were loaded, unloaded, and loaded with an unbraked trailer. The following table is the maximum likely deceleration rates resulting from the calculations using the FMVSS 121 data (2008).

Table 2-1 – Vehicle Speed and Braking Distance and the Resulting Deceleration Rates

		Truck Braking Distance (ft)			**Truck Deceleration Rate (g)**		
Vehicle Speed (mph)	Vehicle Speed (ft/s)	Loaded single-unit truck (1)	Unloaded truck tractors and single-unit trucks (2)	Loaded truck tractors with an unbraked control trailer (3)	(1)	(2)	(3)
20	29.33	35	38	40	0.382	0.352	0.334
25	36.67	54	59	62	0.387	0.354	0.337
30	44.00	78	84	89	0.385	0.358	0.338
35	51.33	106	114	121	0.386	0.359	0.338
40	58.67	138	149	158	0.387	0.359	0.338
45	66.00	175	189	200	0.387	0.358	0.338
50	73.33	216	233	247	0.387	0.358	0.338
55	80.67	261	281	299	0.387	0.360	0.338
60	88.00	310	335	355	0.388	0.359	0.339

In order to accurately model the dynamic tests, using a reasonable value for the achievable braking deceleration is vital to ensuring the proper amount of force is being transmitted longitudinally.

2.5 Truck Braking Capacity

Trucks in today's modern era use compressed air to deliver air to each individual wheel's brake. Due to this, there is a slight delay in response as a result of the compressibility of the air. As the pedal is released, air is released from the system into the atmosphere and replaced by air from the compressor. For this reason, pumping of the brakes must be avoided so as not to deplete the compressed air too quickly (Torbic, et al. 2003). Additionally, when the air becomes depleted, the compressibility of the brakes decreases, and they are less capable of providing braking ability to the vehicle. If there is no air, the brakes cannot effectively engage.

2.6 Bearing Pads

Within the bridge design specifications for the state of Alabama, there are numerous types of bearing pads that could be used in design. Bearing pads play an integral role in transferring the forces in the superstructure to the substructure. From shape to thickness, material, reinforcement, and composition of the bearing pad, all of these factors have an effect. In this bridge, Type 2, Mark B1 elastomeric bearing pads were used. The pads were 14.5 in long by 9 in wide by 0.75 in thick. The thickness was composed of two layers of elastomer with one 12-gauge steel shim in between. Figure 2-5 is the standard detail for these bearing pads.

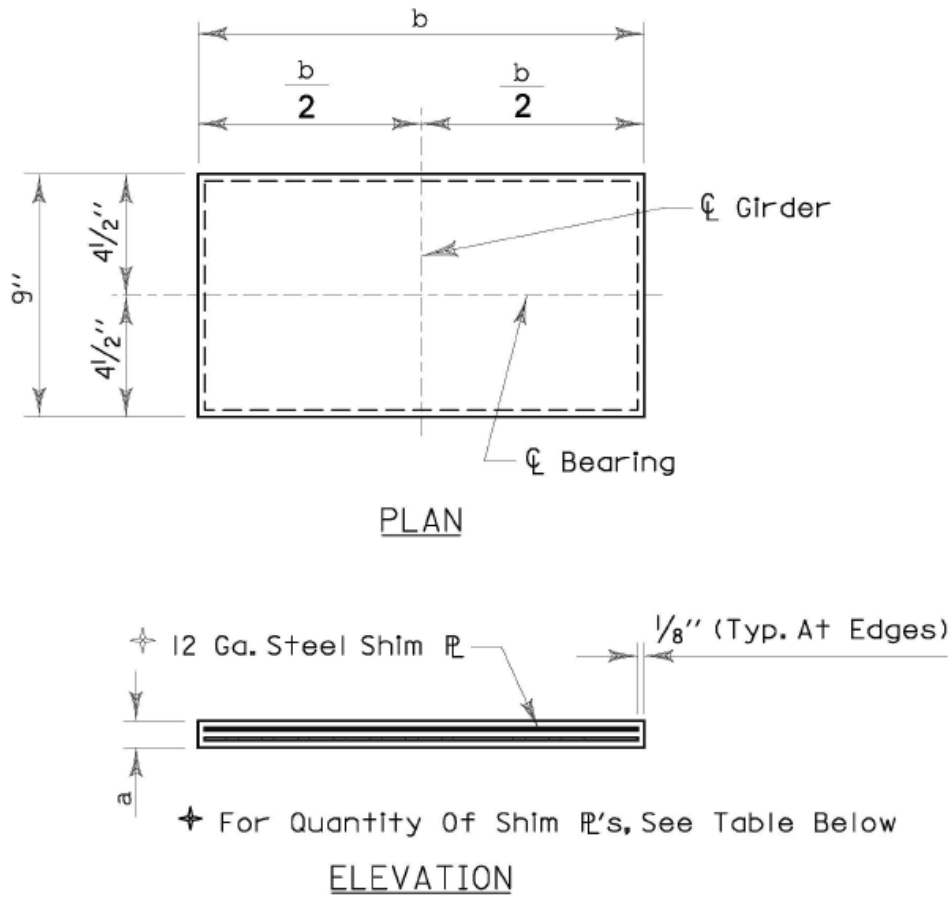

ELASTOMERIC BEARING PAD DETAIL
(FOR BEARING MARK "B" & "VB")

Figure 2-5 – Standard Detail for ALDOT Elastomeric Bearing Pad Detail (ALDOT 2013)

Elastomeric bearing pads are designed to be able to support and transfer the vertical forces from the girders of the bridge to the bents. They allow for horizontal movements and rotations of the girders as a result of thermal expansion or contraction, beam end rotations, traffic loads, elastic shortening, and time-dependent changes in the concrete such as creep and shrinkage.

When designing the bearing pad, the most important material property is the shear modulus, according to AASHTO section C14.7.5.2. The elastomer must have a specified shear modulus between 0.080 ksi and 0.175 ksi. Going beyond the upper limit for the shear modulus is

not allowed due to the elastomer having more creep at this stiffness then a softer bearing and because these bearings generally break at a smaller elongation then its softer counterparts. These undesirable qualities can be a result of more filler being present in the elastomer in order to reach the higher shear modulus value (AASHTO, 2017).

Typically, under service loads the bearing pads deflect horizontally and vertically as well as providing some damping of vibration to the superstructure. In order to compute the stiffnesses of a bearing pad, six equations can be derived from beam theory principles and are presented in "The Effect of Bearing Pads on Precast Prestressed Concrete Bridges" presented by Cai, Eddy, and Yazdani (2000) as follows:

$$k_x = \frac{EA_x}{H} \qquad \text{Equation 2-4}$$

$$k_y = \frac{GA_y}{H} \qquad \text{Equation 2-5}$$

$$k_z = \frac{GA_z}{H} \qquad \text{Equation 2-6}$$

$$k_{Rx} = \frac{GI_x}{H} \qquad \text{Equation 2-7}$$

$$k_{Ry} = \frac{EI_y}{H} \qquad \text{Equation 2-8}$$

$$k_{Rz} = \frac{EI_z}{H} \qquad \text{Equation 2-9}$$

Where:

$$E = Modulus\ of\ Elasticity$$

$$A = Cross - Sectional\ Area\ Corresponding\ to\ each\ Axis$$

$$H = total\ thickness\ of\ the\ bearing\ pad\ excluding\ rigid\ plates$$

$$I = Moment\ of\ Inertia\ Corresponding\ to\ each\ Axis$$

$$G = Shear\ Modulus$$

The value for the modulus of elasticity is assumed to be 30 ksi since there is no pad-specific test data as per 14.7.6.3.3 in the LRFD Specification (2017), and the shear modulus was assumed to be 0.135 ksi based off values presented in the Caltrans design memo (1994). The

cross-sectional properties, area and moment of inertia, can be calculated with the geometry of the bearing pad as detailed in the ALDOT Standard Details Drawing No. I-131 (2013).

2.7 Bridge Foundation and Soil Structure Interaction

Bridge substructures are often supported by one or more deep foundation systems. The most common deep foundation system for the bridges discussed in this thesis are driven pile foundations. These foundations typically include a single row of piles that are embedded into a bent cap. Previous work has been conducted to determine the behavior of these bridge substructures when loaded in the transverse direction. Loads in this direction are produced from wind, current, or impact. In this loading case, the pile spacing, and soil structure interaction is important to analyze and design for this loading condition.

Skinner's project focused on lateral load testing of driven steel pile bridge bents in the transverse direction, orthogonal to the direction considered here. The previous project was completed to better understand the behavior of these types of bridge substructures under lateral loads. Before the project began, a model of the bridge bents was created in the modeling software FB-Multipier. The initial model was designed using the soil profile from the geotechnical site investigation and the design plans for the bridge structure. A full-scale bridge test was conducted on the Old Town Creek Main Channel Bridge on County Road 9 in Macon County. The results of this test were used to adjust the model to better predict the behavior of this bridge structure.

Results from the full-scale lateral load test showed that the concrete encasements provide a large amount of additional lateral stiffness, even though they are not considered as a structural element. Results from this test also showed the encased pile sections did not appear to behave purely composite during loading, with the measured steel strains exceeding the measured concrete strains at instrumented cross-sections where steel and concrete strains were measured (Campbell 2016).

2.7.1 Pile Lateral Capacity

Piles are designed such that they meet strength and serviceability criteria. They are designed to have adequate strength under extreme loads and minimum deflections under service loads. In majority of cases, the maximum tolerable deflection will control the design of piles (Poulos and Davis 1980). Predicting the lateral behavior of a structural member can be difficult

given the high variability in soil stratigraphy and strength. Because of this it is important to understand the relationships between pile deflection, slope, shear, and bending moment. Figure 2-6 presents the relationship between these as a function of pile depth.

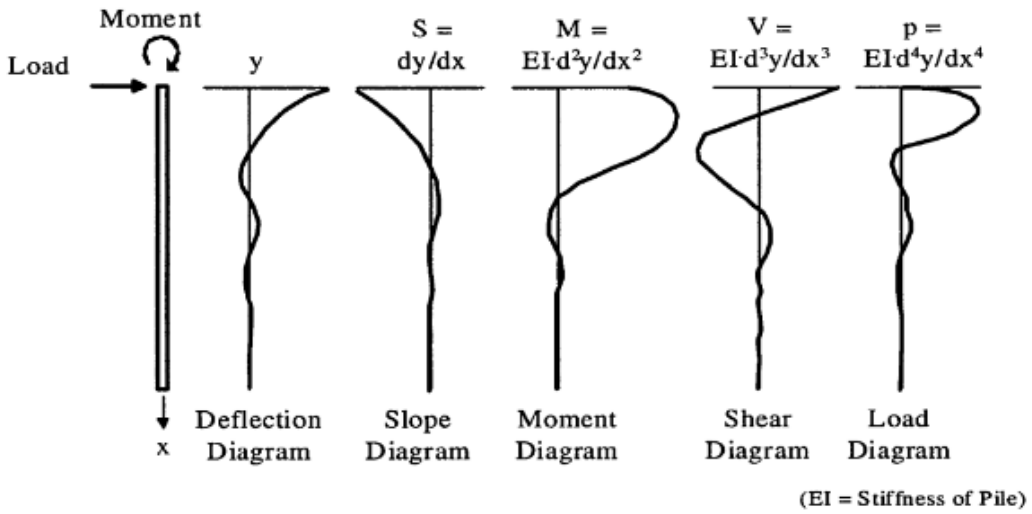

Figure 2-6 Pile deflections and forces as a function of depth (Reese and Wang 2006)

As the structural member applies force to the soil the soil pushes back until the local shear strength of the soil is overcome. This behavior is graphically represented by constructing a P-Y curve. P-Y curves define the lateral behavior of the soil by detailing the lateral deflection a pile experiences under certain loads. An example P-Y curve can be seen in Figure 2-7 and a graphical representation of the coordinate system and resisting mechanisms is in Figure 2-8..

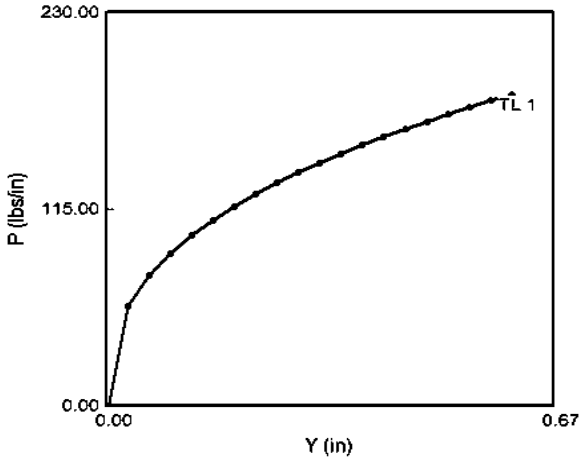

Figure 2-7 O'Neill p-y Curve for Lateral Soil Behavior (Skinner,2016)

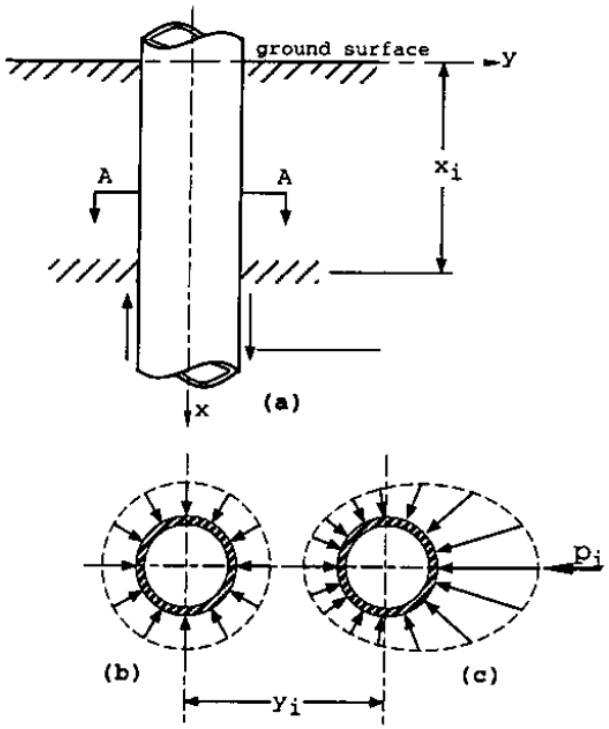

Figure 2-8 Definition of p and y related to lateral loading (Reese and Wang, 2006)

P-Y curves can be constructed for any soil condition along the length of the pile. Multiple P-Y curves are developed to analyze the soil structure interaction of a driven pile. The soil behavior along the length of a pile is often represented as a series of independent nonlinear springs, whose behavior is defined by the P-Y curves. This method is illustrated in Figure 2-9.

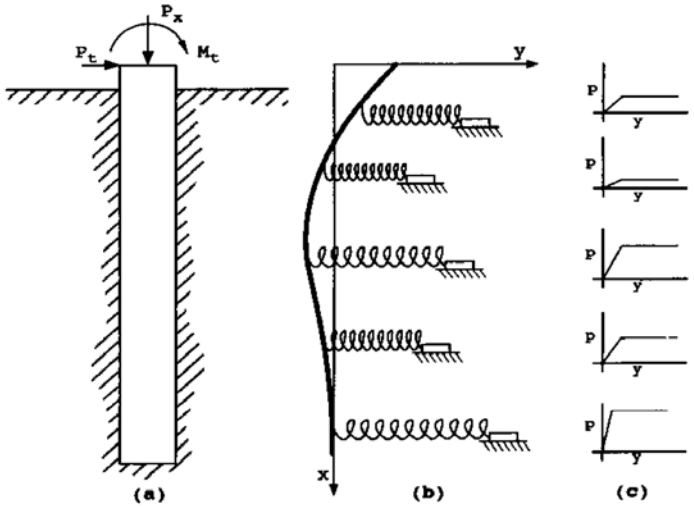

Figure 2-9 Non-linear Springs Acting on a Pile (Reese & Wang, 2006)

2.7.2 Development of p-y Curves

One way to construct P-Y curves is to analytically solve the differential equation for pile deflections at discrete points along the shaft. This method assumes the pile acts as a thin strip, whose behavior is governed by differential equation for bending used by (Hetenyi 1946) from classical beam theory presented in Equation 2-10 (Poulos and Davis 1980)

$$M = E_p I_p \frac{d^2y}{dz^2} \qquad \text{Equation 2-10}$$

Where: E_p= the modulus of elasticity of the pile

I_p= moment of inertia of the pile

y= the lateral displacement of the pile

z= pile depth

The above equation describes the behavior of the driven pile alone and does not consider the lateral resistance of the soil. The relationship between the lateral soil resistance (p), and the pile deflection (y) are given in.

$$p = ky \qquad \text{Equation 2-11}$$

Where: k= the modulus of subgrade reaction

Because of the nonlinearity of observed horizontal load-deflection curves for laterally loaded piles, resulting from local yielding of the soil long before ultimate failure occurs, the overall modulus of subgrade reaction depends largely on the deflection of the pile (Poulos and Davis 1980). It is a common assumption that the modulus of subgrade reaction varies linearly with depth for normally consolidated clay and remains constant for sands and overly consolidated clay (Hsiung and Chen 1997). Manipulating Equations 2-10 and 2-11 will yield the following governing differential equation that defines the relationship between soil resistance and pile deflection.

$$E_p I_p \frac{d^4y}{dz^4} + ky = 0 \qquad \text{Equation 2-12}$$

The solution to the differential equation is used to create curves of horizontal soil reaction versus horizontal displacement (p-y curves). This theory ignores the effects of axial load but is easily implemented and widely accepted for analyzing pile foundations under lateral loads.

2.8 Modeling Software

Throughout the duration of this project, three modeling software applications were used. Two were structural analysis and design software, CSiBridge v15.2.0 and SAP2000 v20.2.0, referred to as CSI and SAP, respectively, throughout the remainder of this thesis. Both of these are finite element programs capable of linear and nonlinear analyses and were used due to their ability to accurately model the bridge and the capability to perform static and dynamic analyses efficiently and accurately.

The third software utilized was FB-MultiPier, referred to as FBMP. This finite element geotechnical software is capable of modeling various structural elements as well as an entire bridge through linear or nonlinear analysis. The user inputs soil profiles and element geometry, then FBMP generates results for soil and structure behavior.

The ability to generate p-y curves was utilized for this project to transfer the lateral pile resistance capabilities into SAP by creating soil springs that replicate the effect of the below grade conditions on the pile bents. A p-y curve represents the soil resistance at a given depth, defined in terms of the soil's resistance per unit length versus deflection (Reese and Wang 1993). With the software automatically dividing the pier into numerous elements for analysis, the results output for each node in terms of p (lbs/in) versus y (in). By taking the slope of the linear portion of the curve, resulting in lbs/in/in units, and multiplying this value by the tributary length of that node, a stiffness in terms of lbs per inch was obtained and this was used as the stiffness of a spring added to the corresponding joint in SAP. A more thorough explanation of this procedure is outlined in Chapter 6.3.1.

2.9 Bridge Model Excitation – Dynamic Analysis Procedures

Two methods of excitation for the model of the bridge were researched. The goal was to investigate which method would impart the dynamic force on the bridge in the most similar method as in the field. In SAP2000 there is an option for a time history analysis or a response spectrum analysis.

2.9.1 Time-History Analysis

A time-history analysis provides for linear or nonlinear evaluation of a dynamic structures' response under loading. This loading may vary according to the function that is specified over the given time duration. In this method, the dynamic equilibrium equation given in

Equation 2-13 is solved by either direct integration or modal response history analysis (Chopra 2017).

$$m\ddot{u} + c\dot{u} + ku = \rho(t) \qquad \text{Equation 2-13}$$

Where,

$$m = mass$$
$$\ddot{u} = acceleration$$
$$c = damping$$
$$\dot{u} = velocity$$
$$k = stiffness$$
$$u = displacement$$
$$\rho(t) = forcing\ function$$

A time-history analysis was used in this instance.

2.9.2 Analysis Procedure

A linear analysis using a modal integration solution type was selected. Modal analysis superimposes the various mode shapes of a structure to characterize the displacements of each element in each individual mode shape. Then, all of the mode contributions are combined to determine the total response (Chopra 2017).

Mode shapes are representations of how the structure will naturally want to displace. Typically, the lower mode shapes provide the largest contribution to the overall structural response and are easier to accurately predict their behavior. When deciding how many modes is enough to consider, the modal mass participation ratio is the driving factor. To determine a sufficient number of modes, a minimum of 90 percent of the total mass should be involved in the analysis. This can benefit computational time, because once a sufficient number of modes is achieved, then the overall number of modes can be truncated if there is no benefit to including higher order modes (Computers and Structures, Inc. 2018).

Modal integration is also desirable when compared to direct integration because it does not have to integrate the fully coupled equations of motion for each time step under which the structure is loaded. Whereas in modal integration, each mode shape is integrated independently of one another and is normalized so that it can be superimposed with the other modes to obtain

the overall response. This significantly reduces computational effort and time (Computers and Structures, Inc. 2018).

2.10 Ramp Functions for Vehicle Deceleration Profiles

An important aspect of the dynamic analysis is to load the model similarly to how the bridge was loaded during braking in the field. In order to replicate the loading of the bridge during dynamic testing in the model, representing the vehicle deceleration profiles had potential to capture this time-dependent event. To do this, defining a ramp function based on vehicular longitudinal deceleration data is a way to incorporate the truck braking characteristics and apply a load to the model over time. Information from the National Highway Traffic Safety Administration's (NHTSA) report on Experimental Measurement of the Stopping Performance of a Tractor-Semitrailer from Multiple Speeds (Garrott, Heitz and Bean 2011) provided foundational information to support this method of modeling the braking of the truck.

In this report, creating a ramp function based on the deceleration rise time, the time it takes for the vehicle to reach constant deceleration; steady-state deceleration time, and the decrease of steady state deceleration to final stopping of the vehicle was evaluated. The aim of this paper was to investigate the stopping distance of a vehicle from varying initial speeds in order to create a single governing equation for maximum permitted stopping distance that could incorporate the various decelerations and initial speeds.

During the stopping tests in the NHTSA report, the longitudinal deceleration was recorded. From that data, a time history trace of the deceleration versus time was created as shown in Figure 2-10.

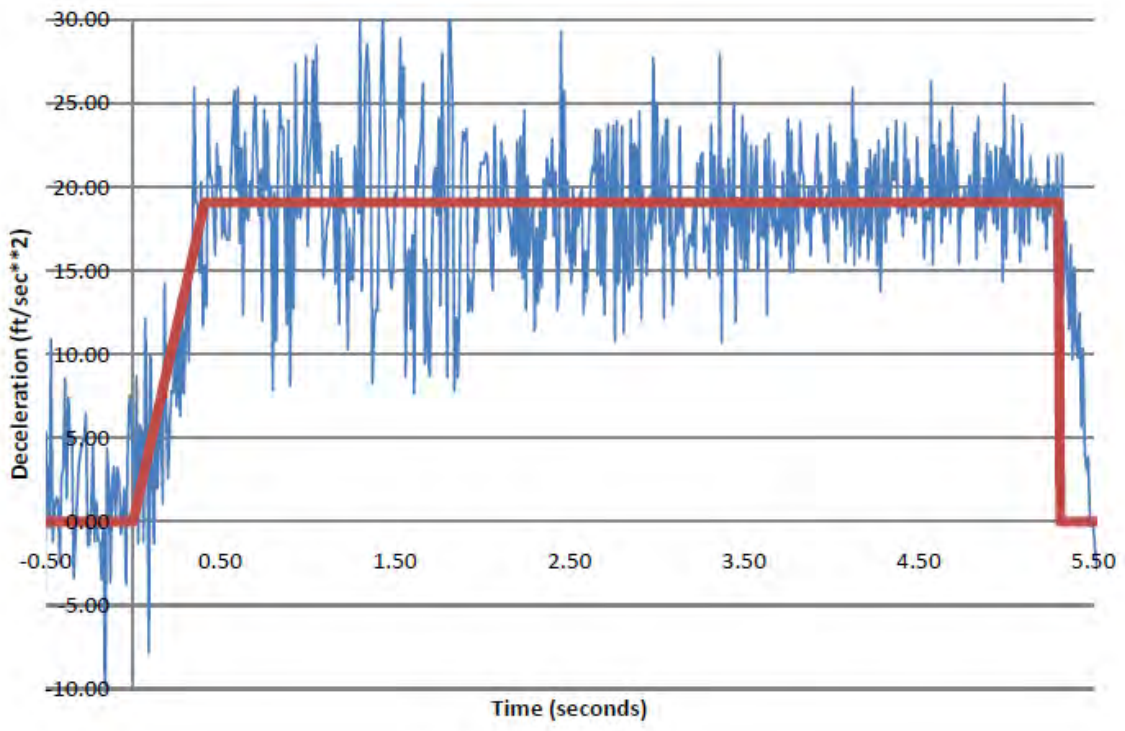

Figure 2-10 – Measured and Idealized Deceleration for a Typical 60 mph Stop (Garrott, Heitz and Bean 2011)

In each test, the deceleration rise time and the magnitude of the steady state deceleration were the most important values affecting the braking distance. For each test, the analyst determined the rise time in seconds based on their clearest indication of how long it took to reach the steady state deceleration. Doing this for each test provided results that where within the margin of compliance for the data set and indicated that this method of analyzing the deceleration profiles could produce accurate results when used determine other unmeasured values.

Chapter 3 Instrumentation and Data Acquisition

3.1 Introduction

To monitor the bridge during the static and dynamic load tests, instrumentation was selected and installed along the bridge. A Data Acquisition System (DAQ) was selected to record and collect data during the full-scale test. Sensors were selected to measure acceleration, displacement, and force. These sensors were chosen based on cost, functionality, and ease of attachment to the bridge. The data acquisition system was chosen based on the required sampling rate, accuracy, and compatibility with the sensors chosen.

3.2 Accelerometer

The acceleration of the bridge was monitored using a Seismic, Ceramic Shear Integrated Circuit Piezoelectric (ICP®) Accelerometer, Model 393A03 from PCB Piezotronics, shown in Figure 3-1. The accelerometer works by generating an electrical output proportional to the applied acceleration (PCB). This is accomplished by a seismic mass that under acceleration causes a stress on a sensing crystal. A detailed illustration is presented in Figure 3-1.

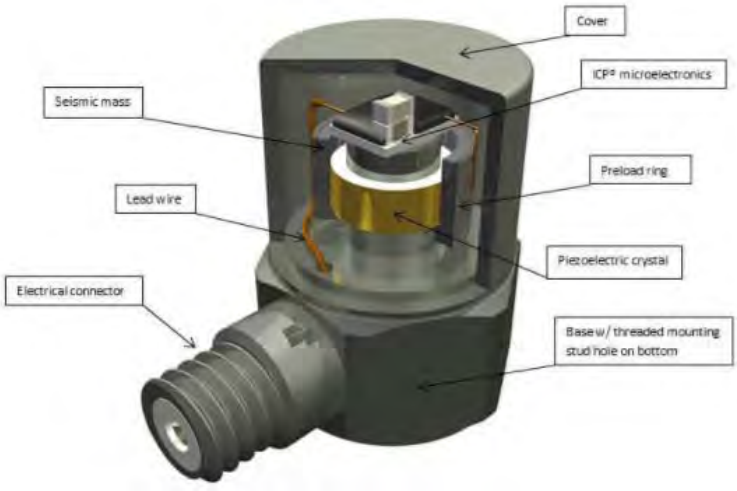

Figure 3-1 Typical ICP® Accelerometer (PCB)

The microelectronics in the device convert a high-impedance charge signal generated by a piezoelectric sensing element into a usable low-impedance voltage signal that can be readily transmitted, over ordinary two-wire or coaxial cables to any data acquisition or readout device (PCB).

Figure 3-2 Model 393A03 Shear ICP Accelerometer (PCB)

This accelerometer was chosen based on the sensitivity, measuring range, and frequency range available. The sensor has a sensitivity rating of 1000 millivolt per g acceleration and a measuring range of ± 5g. The sensor is capable of accurately reading frequencies between 0.5 and 2000 Hz, which encompasses the expected frequencies from the dynamic test.

To save money on a limited project budget, a cheaper Micro-Electro-Mechanical Systems (MEMS) accelerometer was explored. The accelerometer works by measuring the movement of a small mass in the sensor as acceleration is being applied (PCB). The small mass in the MEMS accelerometer is suspended between two parallel plates. This configuration forms two air gap capacitors between the proof mass and upper and lower plates. As acceleration is applied the mass moves causing one air gap to increase while the other decreases creating a change in capacitance proportional to acceleration (PCB). A detailed illustration of this presented in Figure 3-3.

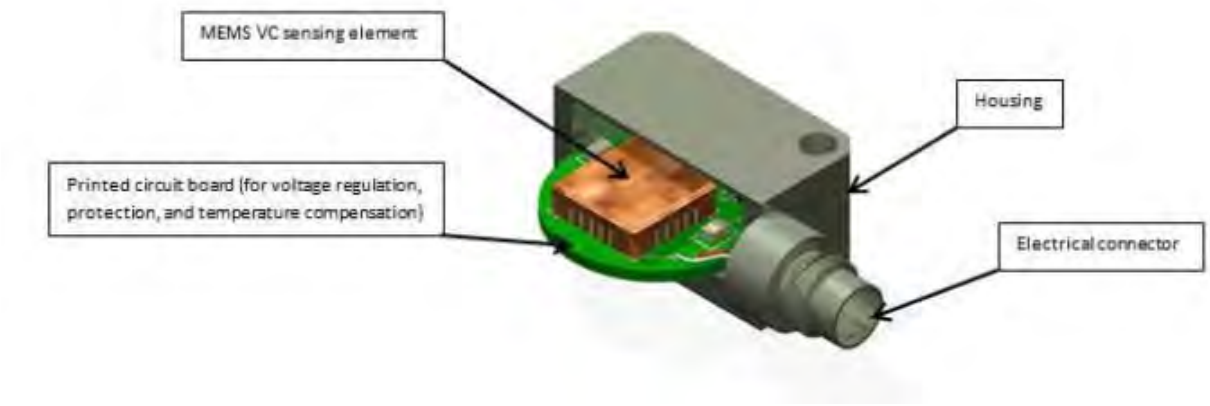

Figure 3-3 MEMS accelerometer construction (PCB)

This The benefit of this type of sensor is the relatively low cost and the ability to measure a static acceleration, such as gravity (PCB). The sensor chosen was an ADXL337 3-axis accelerometer from Analog Devices (Figure 3-4).

Figure 3-4 ADXL337 MEMS Accelerometer (Sparkfun)

The sensor has a sensitivity of 300 millivolt per g acceleration and a measuring range of ±3g. The sensor is capable of measuring frequencies between 0 and 1600 Hz.

3.3 Draw Wire Potentiometer

The sensor chosen to measure displacement for this project is the WDS-1000-P60-P Draw-Wire Potentiometer from Micro-Epsilon (Figure 3-5). This sensor was chosen based on successful use in previous projects at Auburn University (Skinner 2016). The sensor operates by transforming a linear motion into a change in resistance of the potentiometer (Micro-Epsilon). This process is accomplished by placing tightly wound measuring wire around a drum connected to a spring motor (Micro-Epsilon).

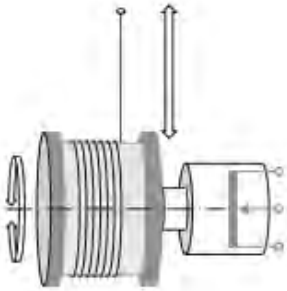

Figure 3-5 Function of Draw-Wire Potentiometer (Micro-Epsilon).

The sensor has a measuring range of 1000 millimeter and a resistance value of 1kOhm. The sensor can be connected to read the voltage differential between the wiper and the ground connection, illustrated in Figure 3-6.

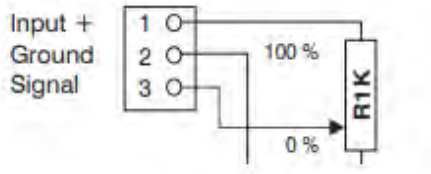

Figure 3-6 Operation Output (Micro-Epsilon)

As the draw-wire is pulled, the voltage differential between the signal and ground increase proportionally to the increased resistance.

3.4 Tension Link Load Cell

A tension link load cell was chosen to measure the force applied by pulling on the bridge during the static load test. This type of load cell consists of a metal frame that is subjected to either tension or compression, and a set of strain gauges. As the metal element is subjected to tension or compression the strain gauges measure the deflection. Foil strain gauges are typically used with this type of load cell. Each strain gauge consists of a foil element that has a specific resistance that is directly proportional to its length and width (DCL). A group of four strain gauges, known as a Wheatstone Bridge, is used to measure the deflection of the metal frame. This deflection is then calibrated to the force required to cause the deflection. The load cell chosen for this project is the DCL10 Tension Link Load cell depicted in Figure 3-7.

Figure 3-7 Tension Link Load Cell (DCL)

3.5 Inertial Measurement Unit (IMU)

The movement and acceleration of the truck was measured using a VN 300 Rugged IMU sensor (Figure 3-8).

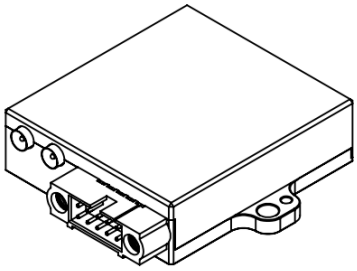

Figure 3-8 IMU Sensor (IMU)

The device uses an assortment of inertial sensors to record position, velocity, and acceleration. MEMS accelerometers are used to measure 3-axis acceleration (IMU). All IMU work, including preparation, recording, and processing was performed by Matt Wiest of the Mechanical Engineering Department at Auburn University.

3.6 Data Acquisition

To effectively collect data from the sensors, an appropriate Data Acquisition System (DAQ) is needed. The DAQ system needed must be compatible with the sensors being used and able to record data at the rate necessary for the dynamic test. It was decided to use National Instruments (NI) DAQ equipment due to the number of devices available with variable sampling parameters. NI DAQ systems are available in several options but the one chosen for this project was to use a NI Chassis that allowed for multiple types of modules.

3.6.1 Chassis

The chassis chosen for this project was the NI cDAQ – 9179 (Figure 3-9). This chassis was chosen for the number of slots and the ability to collect the amount of data needed for the dynamic tests. This chassis contains 14 slots for different modules to be placed.

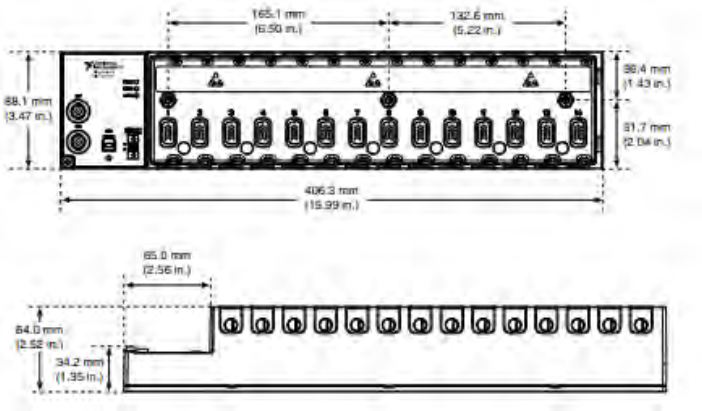

Figure 3-9 National Instruments cDAQ 9179 chassis

Each module connected to the DAQ system can be monitored and controlled independently. The chassis is mountable and can easily be configured to record and collect data as needed for the project. A USB 3.0 cable is used to connect the chassis to the computer, where NI software LabView can be used to program each module.

3.6.2 Acceleration

The NI 9234 module was chosen for this project to collect data from the accelerometer sensors. The NI 9234, shown in Figure 3-10, is a four-channel dynamic signal acquisition module for making high-accuracy measurements from Integrated Electronics Piezoelectric

sensors (NI 9234). This module was chosen because of the high sampling rate and resolution capabilities.

Figure 3-10 NI 9234 Module

This module allows for 4 accelerometers to be measured simultaneously at a sampling rate of 51.2 kS/s/ch with a 24-bit resolution. The NI 9234 is equipped with built in circuitry that is capable of filtering signals above the Nyquist Frequency. This reduces the frequencies in the analog signal that may cause aliasing.

3.6.3 Displacement

The NI 9202 module was selected to collect data from the draw-wire potentiometers. The 9202 module, shown in Figure 3-11, is a 16-channel voltage differential card cable of reading ±10 volt measuring range with 24-bit resolution.

Figure 3-11 NI 9202 Module

The module has a maximum sampling rate of 10 kS/s/ch and features programmable hardware filters (NI 9202). The draw-wire potentiometers will be connected as a single ended connection. NI supplied the connection diagram in Figure 3-12 for this type of wiring.

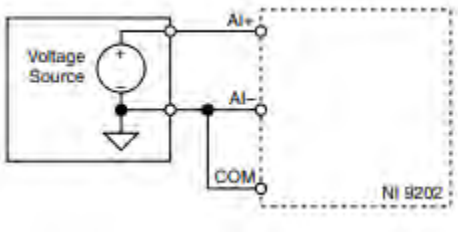

Figure 3-12 NI 9202 Connection Diagram

3.6.4 Force

The NI 9237 module was selected to collect the data from the dynamometer. The NI 9237 (Figure 3-13) is a simultaneous bridge module that contains all the signal conditioning required to power and measure up to four bridge-based sensors simultaneously (NI 9237).

Figure 3-13 NI 9237 Module

This module has a maximum sampling rate of 50 kS/s/ch at a 24-bit resolution. The module can be programmed to supply up to 10V internal excitation and has an input range of ±25 mV/V. The NI 9237 is equipped with a lowpass filter to block frequencies above the Nyquist Frequency.

3.6.5 Programming

National Instruments uses a graphical design program called LabVIEW. This program allows the user to write a program for hardware configuration, data measurement, and data processing using visual tools, called VIs. LabVIEW is preloaded with standard VIs for performing basic program commands. Some of the advanced VIs can be used in signal processing, which are vital tools for processing data. LabVIEW is also used to set parameters for the DAQ device so that data can be collected and stored appropriately.

3.7 Bench Testing and Sensor Verification

After selecting the sensors, some initial testing was performed to ensure the sensors would be capable of accurately reading the small magnitude displacements and accelerations expected for the full-scale test. To accomplish this, two tests were conducted, one using a

highway bridge and another using a shake table. The bridge test was performed to compare the performance of the ADXL and ICP ® accelerometers. The shake table test was performed using only the ICP® accelerometer to measure the performance using a known frequency input.

3.7.1 Highway 14 Bridge Test

The overpass bridge on Shug Jordan Parkway crossing Alabama Highway 14 in Auburn, AL was chosen due to its easy access and proximity to Auburn University. It was assumed for this test that the bridge structure would be as stiff or stiffer than the test bridge and would yield measurements in the same magnitude that will be recorded for the field test. The purpose of this test was to determine if the cheaper ADXL337 accelerometers can measure small accelerations from traffic riding over the bridge. To perform this initial test, one ADXL337 and one ICP® accelerometer were placed on the bridge bent pile such that both sensors were measuring in the same direction. Both accelerometers were programed at a sampling rate of 10,000 samples a second. Measurements were taken until it was determined there was enough data to compare the performance of the sensors.

Results from this initial test concluded that the ADXL 337 accelerometer did not have the capability to measure the small magnitude accelerations required for this project. Sample acceleration records are presented in Figures 3-14 and 3-15.

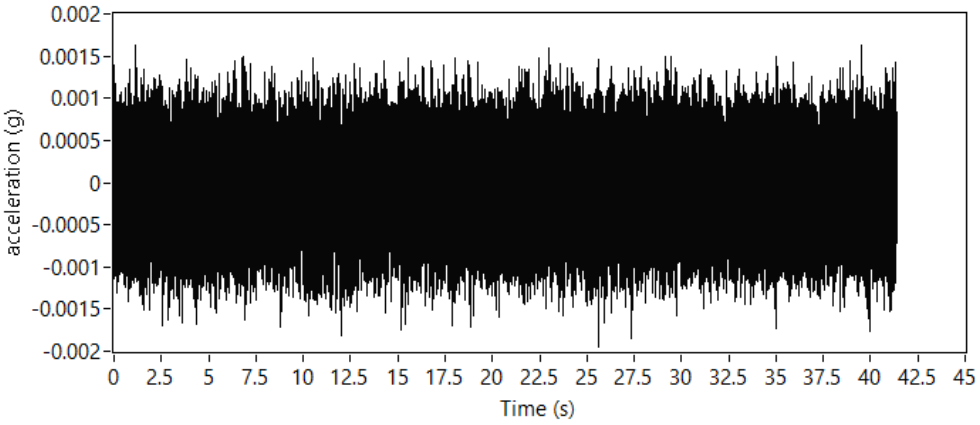

Figure 3-14 Raw Acceleration Data from ADXL 337

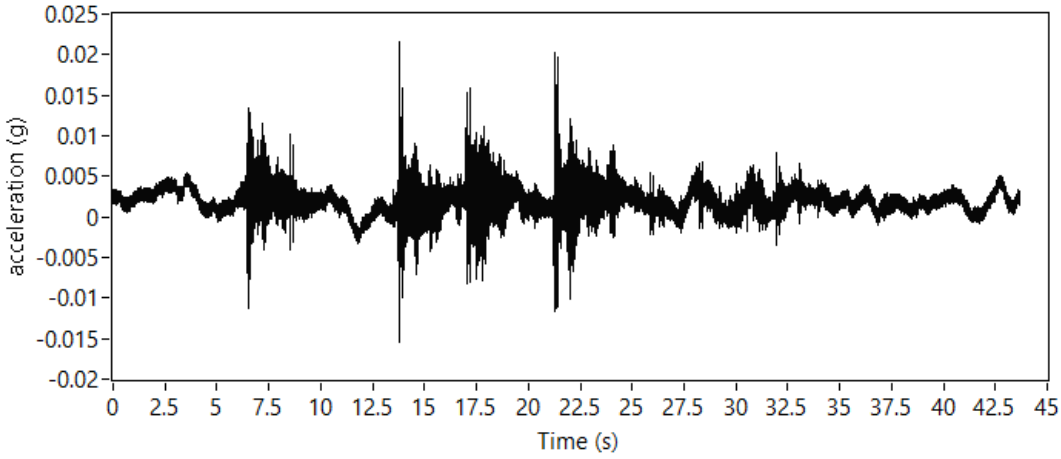

Figure 3-15 Raw Acceleration Data from ICP®

The raw accelerometer records were processed using filtering tools available in LabVIEW and Matlab. The filtering process involved performing a frequency analysis of the record to determine what frequency cutoff values would yield the best results. The data was first analyzed using a Fast Fourier Transform to determine the frequency spectra of the record. Results from the spectral analysis are presented in Figures 3-16 and 3-17.

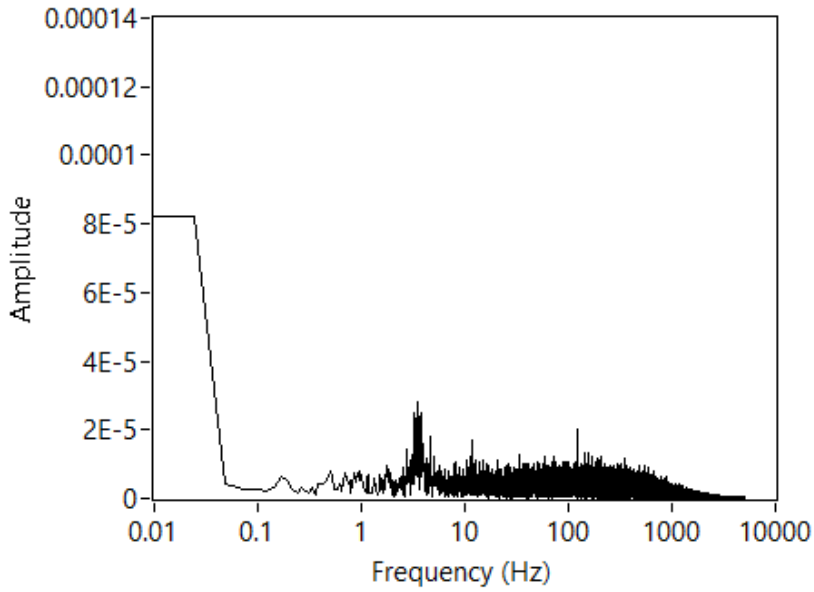

Figure 3-16 FFT of ADXL 337 Acceleration Data

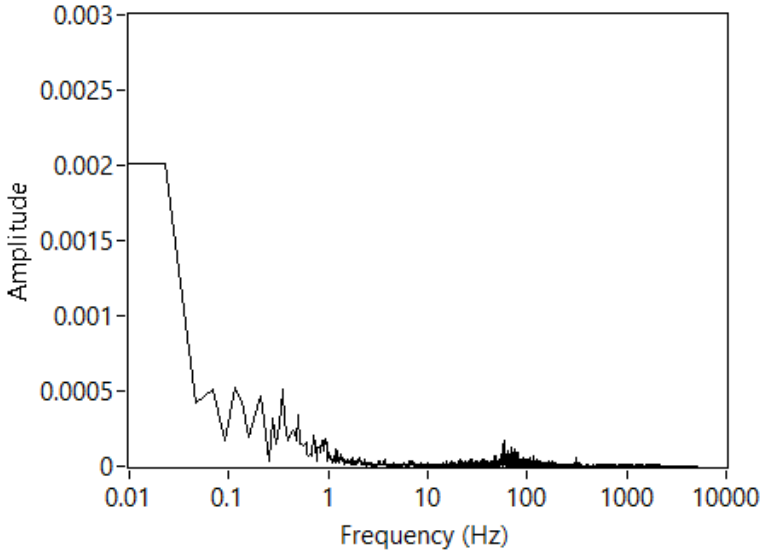

Figure 3-17 FFT of ICP® Acceleration Data

Additional frequency analysis was performed using a continuous wavelet transform (CWT). The CWT was performed to determine what frequencies were present during duration of the recording. These frequencies may be a noise electromagnetic interference that can be filtered from the signal. The results of the CWT for both accelerometers are presented in Figures 3-18 and 3-19.

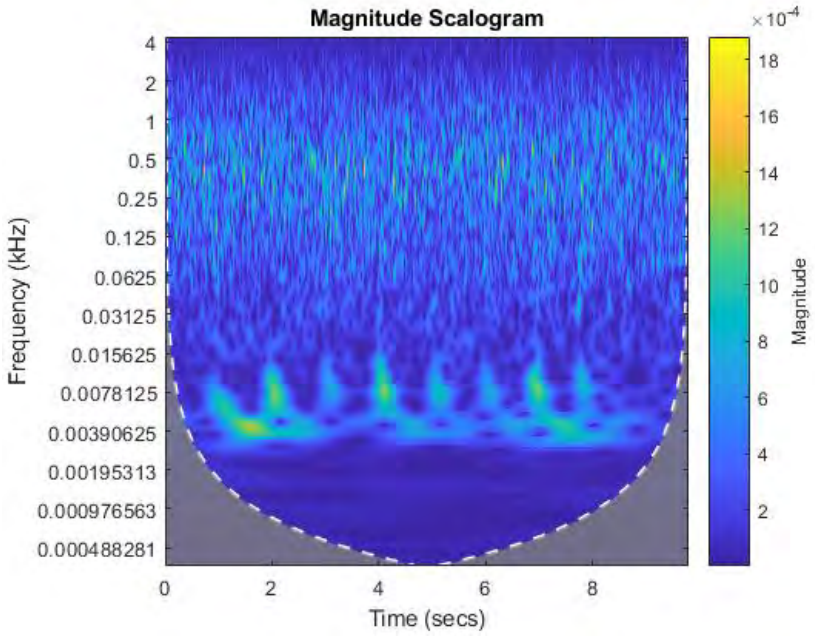

Figure 3-18 CWT of ADXL 337 Data

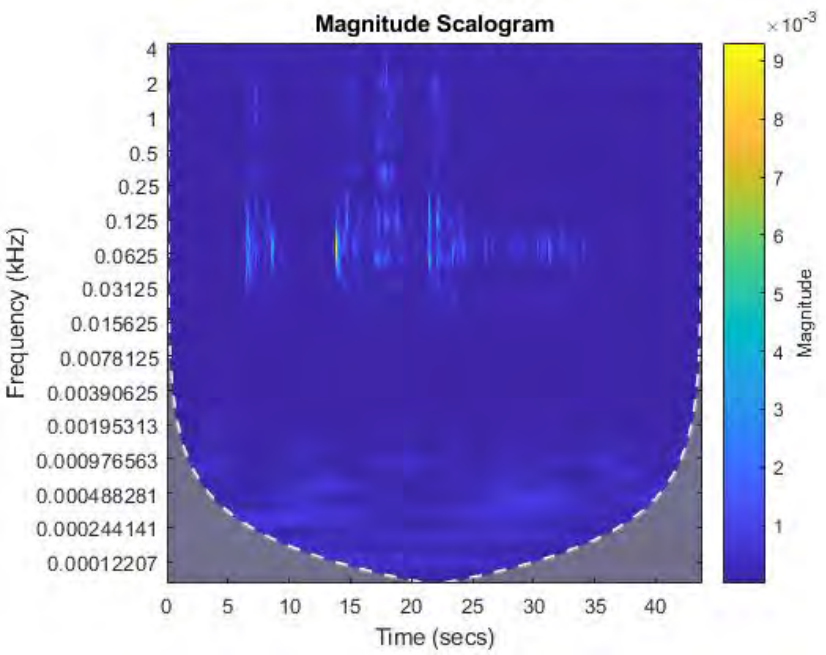

Figure 3-19 CWT of ICP ® Data

The CWT scalograms show a distinct frequency pattern in the ICP® recording but a random assortment of noise in the ADXL recording. This is also shown in the FFT frequency spectrum, indicating the electromagnetic noise is located in the frequency range of the event and therefore cannot be easily filtered. For this reason, the ICP® accelerometer was chosen for this project.

The raw data from the ICP® recording was filtered using a Butterworth bandpass filter. A 4^{th} order Butterworth filter was used because it is maximally flat in the passband and contains a relatively fast roll-off. The frequency cutoffs were chosen based on the results of the CWT. It was clear from the results that the frequencies that occurred during the event lie between 8 Hz and 500 Hz. The filtered ICP® data is presented in Figure 3-20.

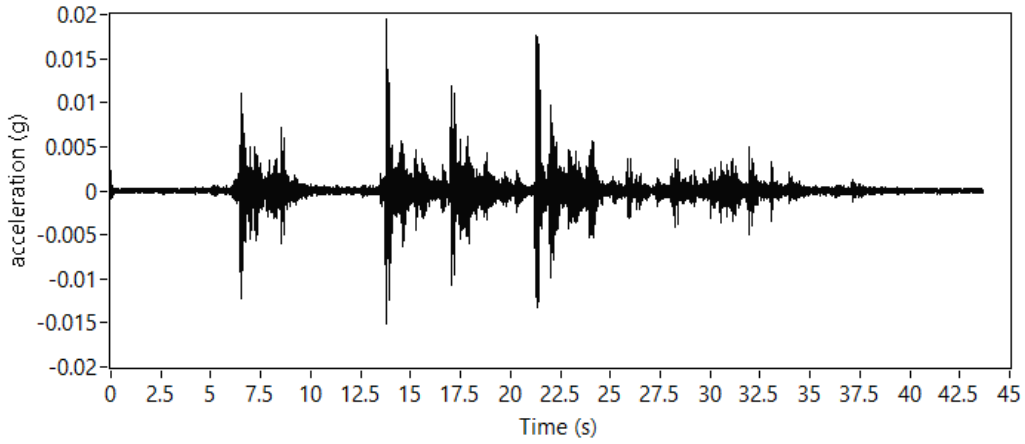

Figure 3-20 Filtered ICP® Acceleration Record.

The new acceleration record shows clearly the accelerations felt by the bridge when traffic was driving overhead. Each spike in the record represents a car driving over the joints in the bridge deck. Larger spikes were caused by heavier truck traffic, while smaller spikes represent smaller vehicles.

3.8 Instrumentation and DAQ System Assembly

The DAQ system for this experiment is made of several components discussed in Chapter 3. The test experiments performed in the previous sections were accomplished by using a signal sensor connected to one channel of the DAQ system. The field test will be conducted with 12 accelerometers and 12 draw wire potentiometers recording simultaneously. To accommodate this large number of sensors and to help with the ease of connecting sensors, the DAQ system was assembled in a housing box with numbered ports for each sensor.

3.8.1 Accelerometers

Accelerometers and cables were ordered from PCB electronics to be used for this experiment. Each accelerometer came with a serial number (SN) and a calibration card. Twelve military grade cables were ordered with the accelerometers. There were six 100ft cables and six 200ft cables. The cables had a 2-pin military connection on one end (Figure 3-21), to connect to the accelerometer, and a BNC connector (Figure 3-22) on the other to connect to the DAQ module.

Figure 3-21 2-Pin Military Connector

Figure 3-22 BNC Connector

Each cable was cataloged, numbered and assigned a specific accelerometer. Cables were organized using electrical cord wheels to make in-field installation easier.

Three NI 9234 modules were used to connect the cables to the DAQ system. The cards were fitted to the first three ports in the NI cDAQ 9179 chassis. Each card could connect four accelerometers, with channels numbered a0 through a3.

3.8.2 Draw Wire Potentiometers

The draw wire potentiometer sensor has a three-wire lead. Each wire is a specific color to help with wiring capabilities. The white wire is positive excitation, the black wire is negative excitation and the green wire is the wiper. Cables used from a previous project were used to connect sensors to the DAQ cards. These wires were a 4-wire braided 14 AWG with lengths of approximately 200 ft. The three wire leads from the sensor were connected using a screw pin connector. The other end of the wire had a female Amphenol connection (Figure 3-23).

Figure 3-23 Amphenol Connector

The amphenal connector was plugged into a male end that was then wired to the appropriate channel of the NI modules. This connection allowed for an easy plug and play function which helped with field installation.

The positive and negative excitation wire were connected to the NI 9237 module, which was used to provide an excitation of 5 mV. The NI 9202 was used to measure the voltage differential between the wiper and the negative excitation. To measure this voltage differential a jumper wire was used to connect the negative excitation terminal on the NI 9237 module to the negative signal port on the NI 9202 module. Four NI 9237 modules were used to power the 12 draw wire potentiometers. Each module was used to power three of the sensors. The fourth channel on the excitation card was used to connect a jumper wire to the ground terminal in the NI 9202 module.

3.8.3 DAQ Housing

The DAQ system (Figure 3-24) was housed in an all-weather container that contained a mounting board and a 12V rechargeable battery. The DAQ system chassis was connected to the mounting board along with a table frame that was built to house all the amphenol connecting ports for the draw wire potentiometers. The DAQ system was powered with a rechargeable 12V battery that was also attached to the mounting board.

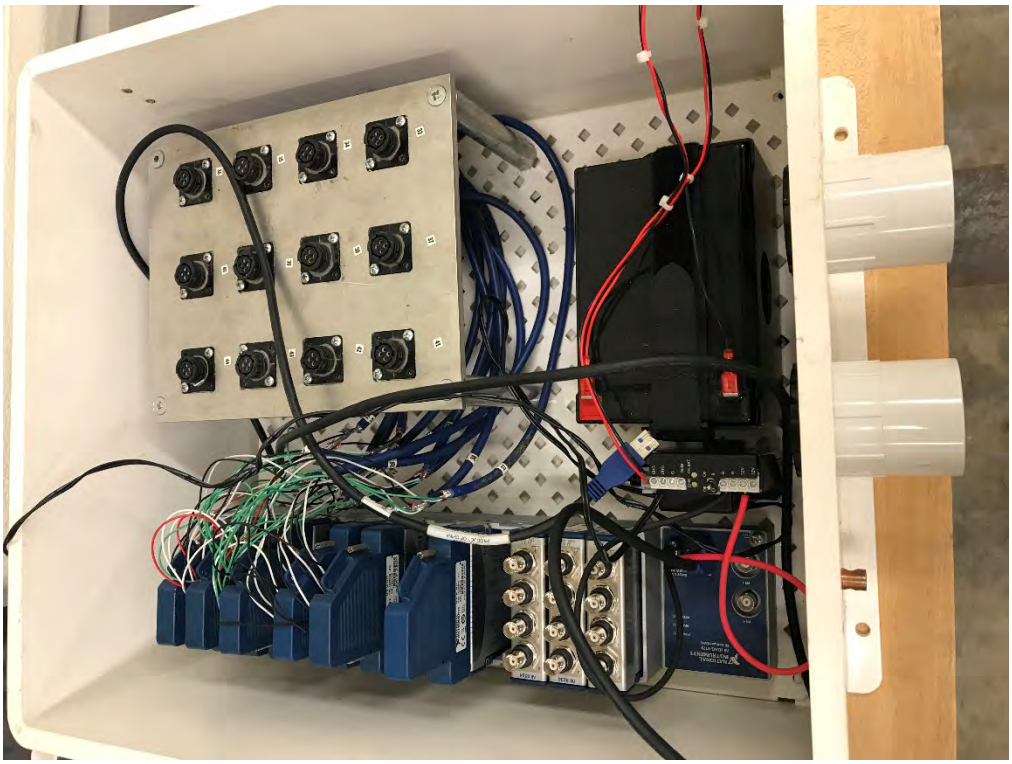

Figure 3-24 DAQ System Box

3.9 Summary

In this chapter the instrumentation used and the process used to validate that instrumentation was described. The National Instruments DAQ system and how all the instrumentation that will be used in the static and dynamic bridge tests will be attached to the DAQ system were presented.

Chapter 4 Field Testing and Analytical Modeling

4.1 Introduction

This chapter provides information on the bridge that was used for field testing, reviews the procedures for the static and dynamic tests, outlines the steps in the data analysis, and reviews the modeling procedures used.

4.2 Macon County Route 9 Bridge Description

The Macon County Route 9 bridge was constructed in 2014 and crosses over Old Town Creek in Shorter, Alabama. Figure 4-1 and Figure 4-2 are the plan and elevation views of the final design. The bridge has no horizontal curve or slope, features six 40 ft spans, four prestressed concrete girders per span, cast-in-place concrete bent caps, and five bents each with four piles. The exterior piles are battered at a 1.5/12 slope. The piles of Bents 2, 5, and 6 are steel HP 14x89 piles encased in non-structural concrete and the piles of Bents 3 and 4 are bare galvanized piles. The piles of Bents 3 and 4 are in the main channel of Old Town Creek. Additionally, the spans in this bridge are discontinuous and there are expansion joints between the girders and bridge deck at each bent.

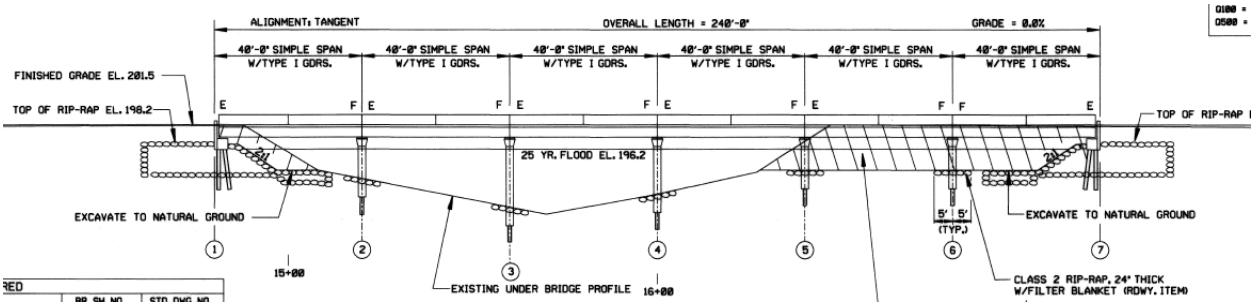

Figure 4-1 – Bridge over Old Town Creek Elevation View (ALDOT 2013)

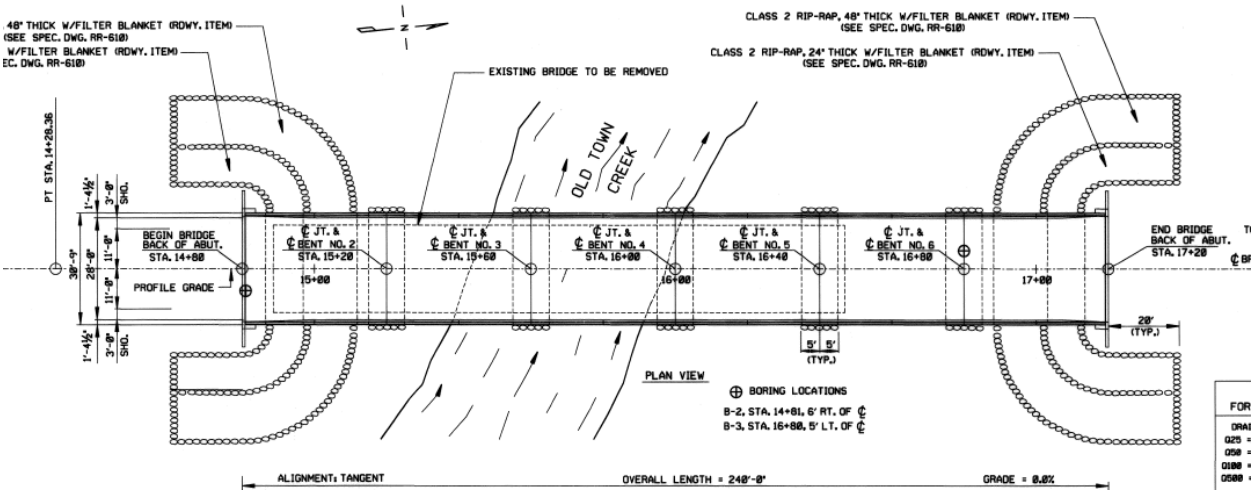

Figure 4-2 – Bridge over Old Town Creek Plan View (ALDOT 2013)

On the elevation view of the bridge plans, there is an “F” or an “E” at the end of each span. This is a designation for fixed or expansion, referring to the fixity of the girder ends. It is important to note that the designation “fixed” is ALDOT terminology meaning the longitudinal translation is restrained but rotation is not, acting more like a pinned connection rather than truly fixed. Figure 4-3 is an expansion connection at Abutment 1 where the clip has a slot, allowing for translation of the girder end. Figure 4-4 is a typical fixed connection where translation is not permitted.

Figure 4-3 – Expansion Joint Bearing Connection

Figure 4-4 – Fixed Bearing Connection

4.3 Instrumentation Setup

The bridge response during the field tests was measured using accelerometers and draw-wire potentiometers discussed in Chapter 3. Before the test began, cables and sensors were cataloged, and tested in a laboratory setting. The hardware for the Data Acquisition System (DAQ) was assembled and the code for recording and viewing the data was written. The DAQ systems was secured to a bracket board along with the battery pack and was housed in an all-weather box. A battery was used to power the system to reduce the amount of electrical noise that can be experienced when using a generator. The channels for the draw-wire were labeled for easy plug and play access for the system (Figure 4-5). The DAQ system was used to read and record measurements from the accelerometers, draw wire potentiometers and the load cell.

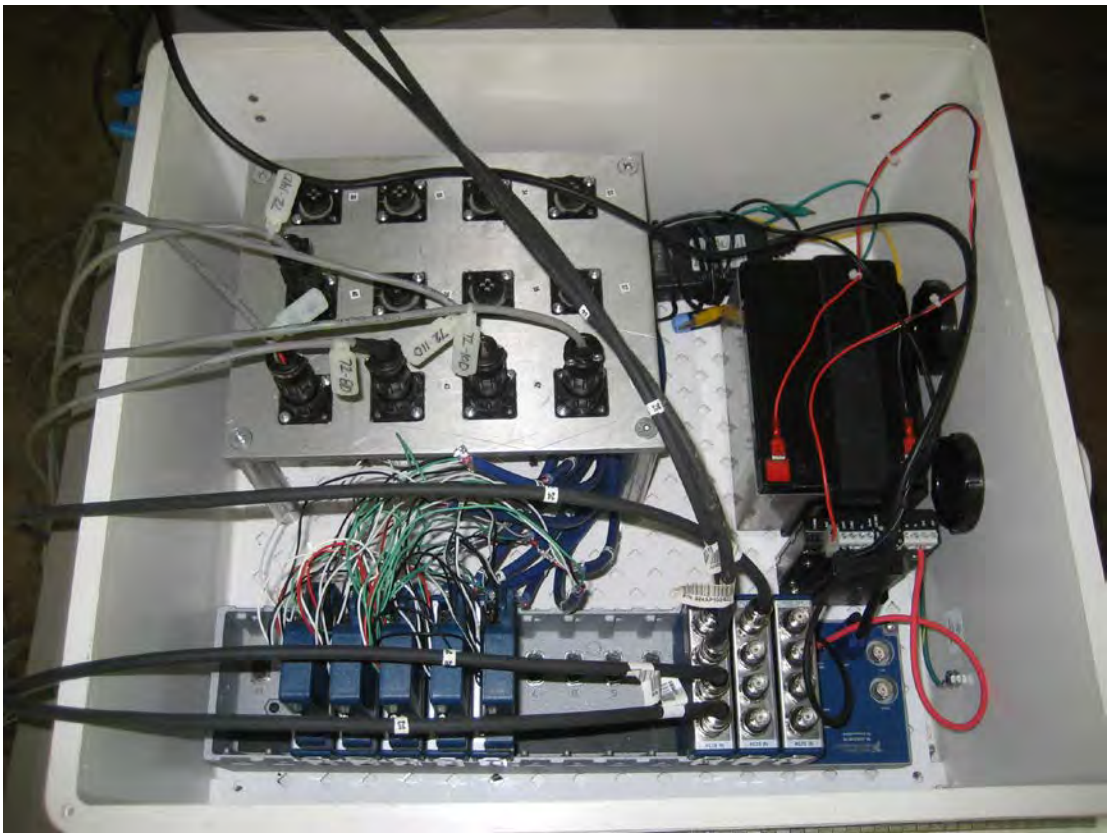

Figure 4-5 DAQ System

Accelerometers were placed at the centerline of each bent cap and on the inside girder of the southbound lane. An additional accelerometer was placed on the outside edge of Bent 3 to measure the torsional response of the bridge at this location. Draw wire potentiometers were used to measure the movements of the bridge bents relative to the bridge spans. Draw wire potentiometers were placed on Span 1 and Span 6 to measure the span movement relative to the stationary abutments. Tables 4-1 and 4-2 and Figures 4-6 through 4-8 detail the cataloged sensor locations, cables and DAQ channels.

Table 4-1 Accelerometer Placement and Numbering

Location	Serial No.	Sensitivity (mV/g)	Bias	Cable No.	Length (ft)	Module No.	Channel
Acc. SP-1	48021	1009	11.3	17	200	1	a0
Acc. B-2	50589	1034	11.1	18	200	1	a1
Acc. SP-2	50587	1043	11	19	200	1	a2
Acc. B-3	50586	1013	11	20	200	1	a3
Acc. SP-3	50588	1025	10.9	21	200	2	a0
Acc. B-3a	48027	981	11.2	22	200	2	a1
Acc. B-4	48028	994	11.3	23	100	2	a2
Acc. SP-4	51105	1014	11.2	24	100	2	a3
Acc. B-5	51109	1017	10.9	25	100	3	a0
Acc. SP-5	51106	1008	11.2	26	100	3	a1
Acc. B-6	51107	1005	11.2	27	100	3	a2
Acc. SP-6	51108	1009	11	28	100	3	a3

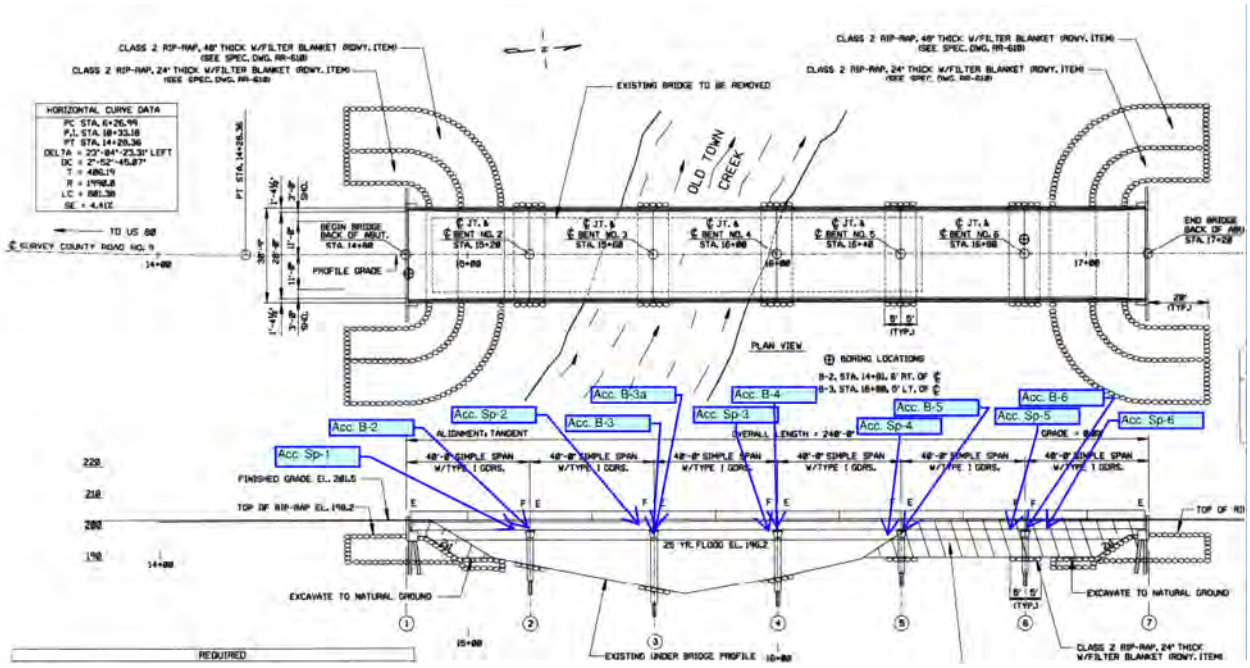

Figure 4-6 Accelerometer Locations

Table 4-2 Draw Wire Potentiometer Layout

Location	Serial No.	Sensitivity (mV/V/mm)	Cable No.	Length (ft)	Plug No.	Excitation (V)	Excitation Mod.	Excitation Ch.	Signal Channel
AB-1	55496	0.967	72-08	200	33	5	8	a0	a0
B-2SB	55495	0.967	72-14	225	34	5	8	a1	a1
B-2NB	56747	0.969	72-10	200	35	5	8	a2	a2
B-3SB	56746	0.969	72-11	200	36	5	9	a0	a3
B-3NB	22314	0.968	72-09	200	37	5	9	a1	a4
B-4SB	22312	0.968	72-12	200	38	5	9	a2	a5
B-4NB	21072	0.969	72-13	225	39	5	11	a0	a6
B-5SB	22313	0.969	72-140	200	40	5	11	a1	a7
B-5NB	19872	0.969	72-100	200	41	5	11	a2	a8
B-6SB	17720	0.968	72-110	200	42	5	12	a0	a9
B-6NB	22315	0.969	72-80	200	43	5	12	a1	a10
AB-7	24075	0.968	72-90	200	44	5	12	a2	a11

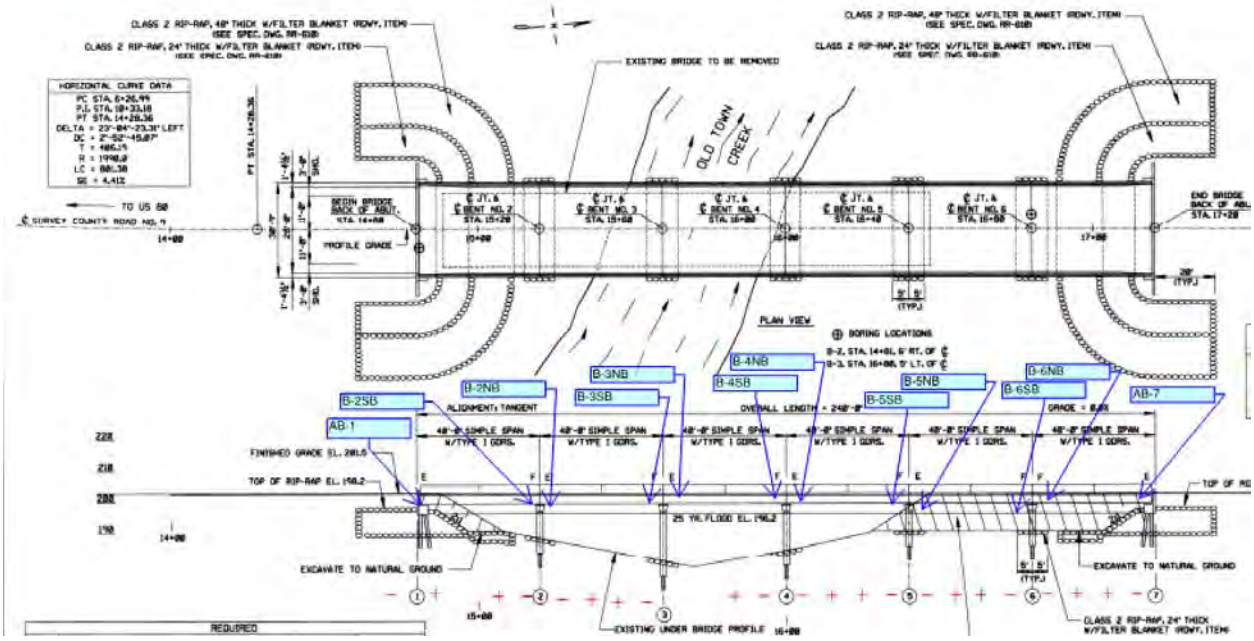

Figure 4-7 Draw Wire Potentiometer Locations

Aluminum angle iron was used to make lightweight brackets to attach sensors to the bridge. Accelerometer brackets were attached at the centerline of each bridge bent and on the inside girder of the southbound lane. Draw wire potentiometers required two brackets to be placed per sensor. One bracket was placed on the bottom of the inside girder of the southbound lane and the other bracket was attached to the face of the pedestal attached to the bridge bent cap. A photo of this attachment of wire-pots is shown in Figure 4-9.

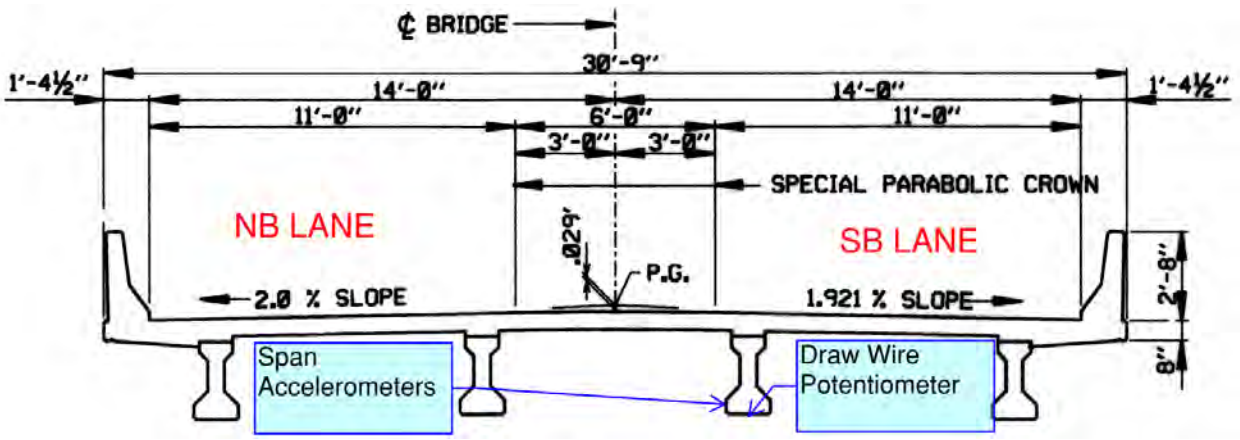

Figure 4-8 Sensor Placement

The brackets were attached to the bridge using a Devcon 5 Minute Epoxy resin. To place the sensor, the area was cleaned with a hand brush and then scrubbed with a wire brush. The epoxy resin was mixed together on a medium sized putty knife and applied to the aluminum surface. The bracket was placed in position and held for approximately 5 minutes or until the epoxy began to set.

Figure 4-9 Bracket Installation

A snooper truck provided by ALDOT was used to place the brackets located on Bents 3 and 4, which are in the Old Town Creek channel. Figure 4-10 shows the brackets being placed on Span 3 located over the creek channel.

Figure 4-10 Instrumentation Installation Bent 3

Once the brackets were in place, the sensors were attached, and the instrumentation cables were run along the underside of the bridge. Accelerometers were threaded into the bracket and hand tightened. Draw wire potentiometers were attached to a bracket using a threaded bolt. The wire and hook were drawn out and attached to an eye-hook that screwed into a bracket that was attached to the bridge bent. The cables were taped to the bottom of the inside girder to provide strain relief. Cables were wrapped around the bolts that secure the girder to the bent to provide additional strain relief and cable support (See Figure 4-11).

Figure 4-11 Instrumentation and Cabling

The IMU sensor used to measure the acceleration of the ALDOT load truck was attached to the truck using an aluminum bracket and the Devcon 5-minute epoxy. The cables for the sensor was taped to the truck and wired into a computer that was in the cab of the Load Truck.

4.4 Testing Procedure

4.4.1 Static Test Procedure

The static load test was performed using the ALDOT load truck in Load Configuration 2 (Figure 4-12) and a tow truck provided by Bill & Sons Wrecking Services. The load truck was parked on the span of interest facing north in the southbound lane. The tow truck was parked off the bridge to not interfere with the bridge movements (Figure 4-13). The rigging of the tension load cell between the tow truck and the load truck is shown in Figure 4-14.

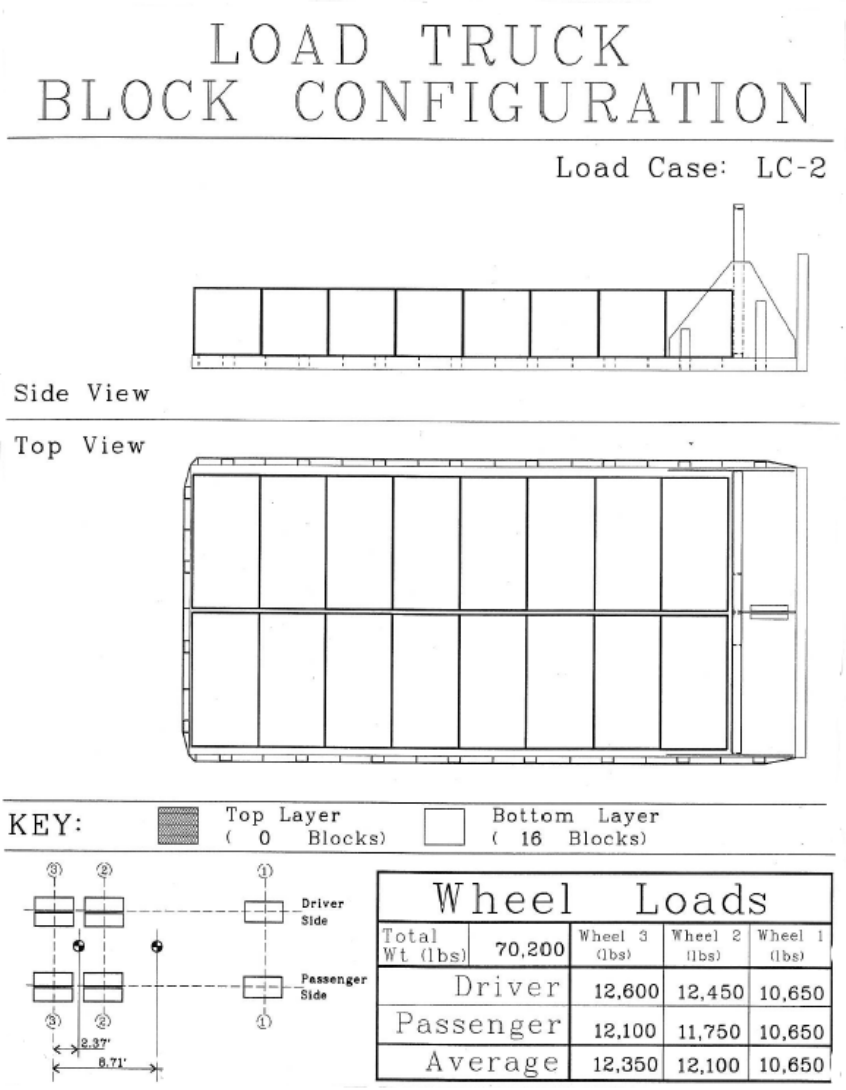

Figure 4-12 – ALDOT Load Truck Load Configuration 2

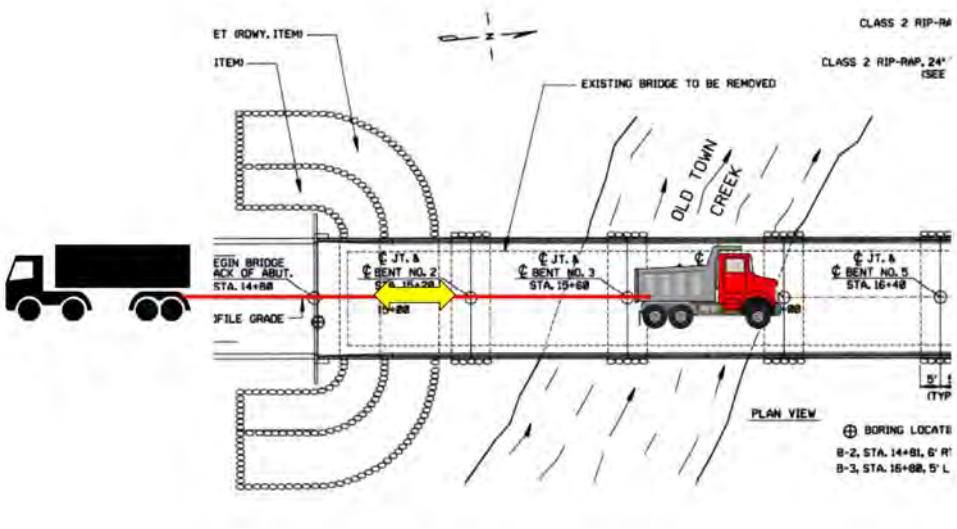

Figure 4-13 Static Load Test Diagram

The tow truck was rigged to pull on the parked load truck until the pull force on the cables was approximately 20 kips or the truck began to slide. This tension load was used because the frictional force between the concrete and tires of the load truck was approximated at half of the total weight of the truck. The load on the tow cables was measured using the DCL 10 Tension Link Load Cell.

Figure 4-14 Tension Link Load Cell

The bridge response was measured using 12 draw wire potentiometers. The DAQ system was reading and recording at approximately 2000 samples per second, the slowest sampling rate available using the NI 9202 Module. This sampling rate was thought to be high, but the amount of data could be reduced during data processing. All data collected from the DAQ system was stored in a LVM file, which could be read and analyzed using LabView.

4.4.2 Dynamic Test Procedure

The bridge was dynamically loaded by the applied braking force of the load truck in the longitudinal direction. Before testing began, the southbound lane was closed to thru traffic and traffic control provided by ALDOT was put in place. The dynamic tests were performed on Spans 2, 3, and 5 in the centerline of the road and in the middle of the southbound travel lane. The tests performed in the centerline were titled C-Span No. (Ex. Centerline Test on Span 5 was labeled C5) and tests in the southbound lane were titled R-Span Number. For each test, the load truck started approximately 100 ft off the bridge facing south in the southbound lane. The truck accelerated to a speed that would allow the truck to apply the brakes and completely stop on the 40 ft span of

interest. Through trial and error this speed was determined to be approximately 10 mph. After the back axle crossed the test span, the driver was signaled to apply the brakes and attempt to stop on the span being tested. A flagman located in the travel lane was used to signal the driver. Stopping locations were marked using spray paint and traffic cones on the bridge. Figure 4-15 presents a schematic of how the dynamic tests were performed.

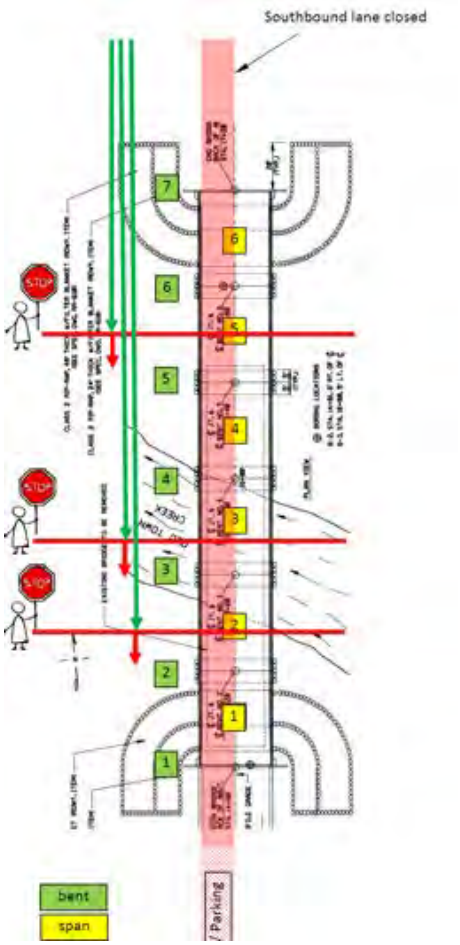

Figure 4-15 Dynamic Load Test Schematic

The dynamic response of the bridge was measured using 12 accelerometers and 12 draw-wire potentiometers. The DAQ system, which was located on the ground under Span 5, was set to record at a rate of 5000 samples per second. This sampling rate was used so that frequencies up to 2500 Hz could be recorded. This recording rate was thought to be conservative and would need to be reduced during the processing stage. The acceleration of the truck was measured using the VN 300 IMU sensor recording at a rate of 2000 samples per second. Hand-held radios were used to

communicate when to start and stop recording for each test. Time stamps were recorded at the beginning of each test to ensure the acceleration records were aligned properly.

4.5 Load Testing

4.5.1 June 06, 2018

After three days of instrumentation set-up, ALDOT brought the snooper truck to the test site to install the bridge sensors located over the Old Town Creek waterway. The instrumentation installation over the water took approximately 4 hours. The ALDOT load truck arrived on-site around noon and load testing began. Due to the low volume of traffic, several tests could be performed in consecutive runs. Only dynamic tests were performed on this day. Five tests were performed at the C5 location. Three tests were performed at the C3, C2, R2, R3, and R5 positions. While reviewing the data collected throughout the day, it was discovered that draw wire potentiometers' B-3SB, B-3NB, and B-4SB did not record data properly. The wiring inside the datalogger box was inspected for loose or broken connections but all connections were found to be secured. The sensors were unplugged and connected to different channels of the DAQ system and performed as expected. The ALDOT snooper truck was scheduled to return the following day to allow access to these sensors to check the connections at each of the bad sensors. The ALDOT ST – 6400 load truck that was used for the test caught fire and burned in route to the ALDOT yard in Montgomery, AL. Another load truck was scheduled to arrive at the test site from another region the following day.

4.5.2 June 07, 2018

The ALDOT snooper truck arrived and the connections at the sensors were checked and found to be secure. It was determined that there was a short in the cable connecting to the N-3NB sensor. The short occurred because the cables at the amphenol connector were stripped too far and were touching. The wires were fixed, and the sensors performed as expected.

The tow truck provided by Bill & Sons Wrecking Services and the new ALDOT load truck arrived mid-morning. The tow truck was rigged up to the ALDOT load truck to begin the static load tests (Figure 4-16).

Figure 4-16 Static Load Test Connection

Static load tests were performed on each span starting with Span 6. One test was performed on each span except Span 5, where two tests were performed.

Dynamic load tests were performed with the remaining time to collect proper data since the draw wire potentiometers were fixed and working properly. Two dynamic tests were performed at locations C2, C5, and R2. One dynamic test was performed at locations C3 and R5. The remainder of the day was used to disconnect all sensors that required the use of the snooper truck. The data from all tests was collected and processed using LabView. The results from these tests will be discussed in the following sections.

4.6 Data Reduction

Once the data from the tests had been collected, a program was written to view the data collectively. For the dynamic test, this involved analyzing the twelve accelerometers and twelve draw wire potentiometers. The static tests involved analyzing the tension link load cell and the twelve potentiometers. Part of analyzing the draw wire potentiometer data involved zeroing out each of the sensors at the start of each test. The data collected from the accelerometers was analyzed to determine the frequency makeup of the acceleration of the bridge. This information was used to determine if any filtering or signal manipulation was required. The IMU data was

processed to ensure the acceleration recorded were properly aligned with the data recorded from the DAQ system.

4.6.1 Zeroing Draw Wire Potentiometers

For each of the load tests performed, data from the draw wire potentiometers was collected at a rate of 5,000 Hz for the dynamic tests and 2,000 Hz for the static tests. The data that was collected was the voltage differential between the negative excitation and the positive signal. The voltage differential was collected in units of volts. In the initial setup of the draw wire potentiometers, the wire was drawn out and connected to the eye hook that was attached to the pedestal on top of the bent cap. During each of the tests, as the bridge components moved, the wire either drew in or pulled out, causing a change in the voltage reading.

In order to zero out draw wire potentiometer sensors, an average voltage reading was taken for the first second of each sensor record and was subtracted from the value of that record, resulting in making the data relative to the initial reading. The data was then converted from the voltage reading to a measurement reading using the calibration coefficient found in Table 5.2.

4.6.2 Sample Data Reduction

The acceleration data was analyzed in order to determine the frequency makeup of the acceleration records. A Fourier Transform was taken of several acceleration records (Figure 4-17).

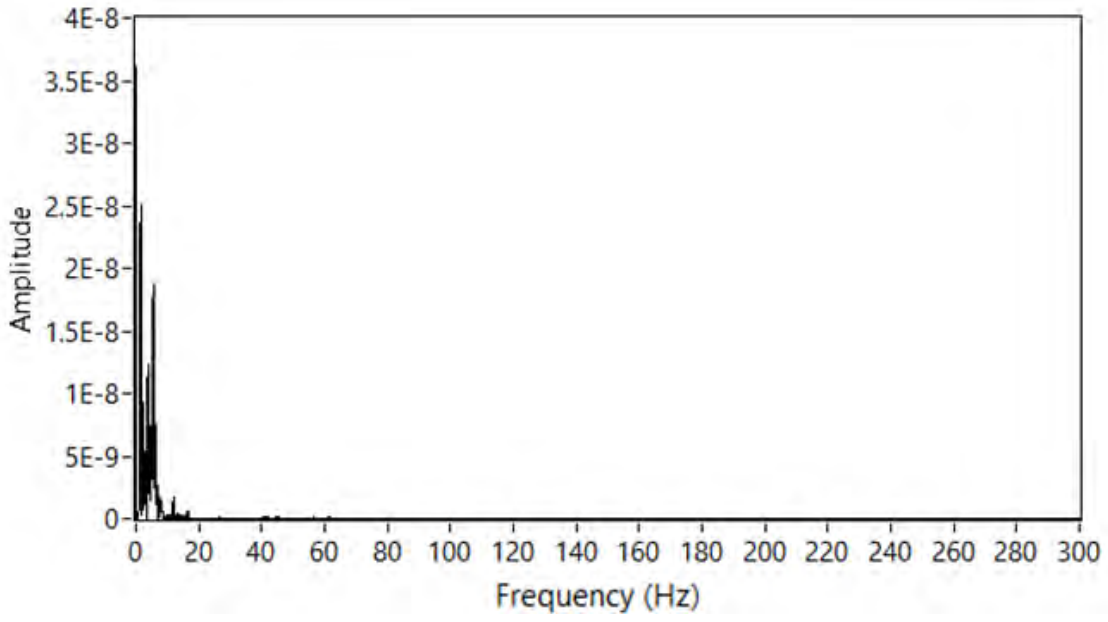

Figure 4-17 Fourier Spectrum of Acceleration Data

After reviewing the data, most of the frequencies did not exceed 250 Hz. Based on the results of the Fourier Transform, the number of samples could be reduced by a factor of ten.

To decrease the sample size, a prewritten sample compression function was added to the signal processing code in LabView. The function works by taking an average of a user defined set of data points and creates a single data point. For example, to reduce a data set by a factor of ten, the function reads every ten samples, takes an average, and creates a new data set. This process was performed on all data sets to make the vast data sets more manageable. After the data sets were compressed, a Fourier Transform was taken for the acceleration data sets to ensure no pertinent data was omitted (Figure 4-18).

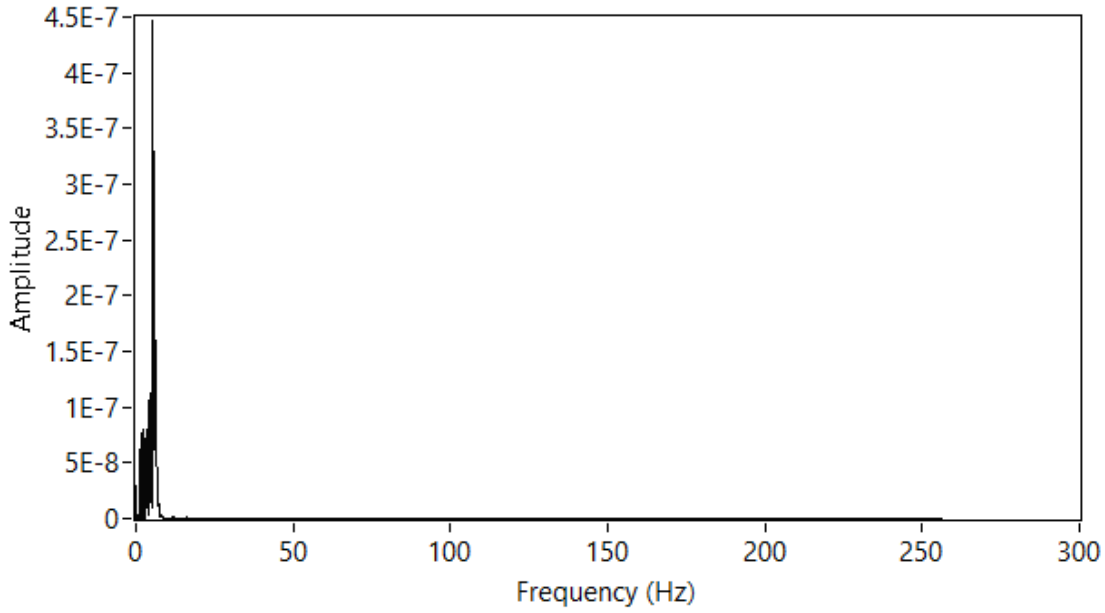

Figure 4-18 Fourier Spectrum of Acceleration Data after Sample Compression

4.6.3 Calculation of Bent Displacements

Data collected from draw wire potentiometers was used to calculate bent movements of the bridge. The potentiometers were set to measure bent movements relative to the connected span movements. Additional potentiometers were placed at each abutment to use as a stationary reference frame. The potentiometer readings relative to the stationary abutment readings were used to calculate the absolute bent movements. The following assumptions were made for this method to be applicable.

Assumption I. Bridge abutments are stationary and are not affected by other bridge components moving.

Assumption II. The spans act as a rigid body.

Assumption III. The spans do not come into direct contact with each other.

Assumption IV. The reference frame for the bent movements is positive in the direction of travel of the load truck (Figure 4-19).

Given these three assumptions, the bent movements can be calculated. The process for calculating the bent movements is presented in Figure 4-20.

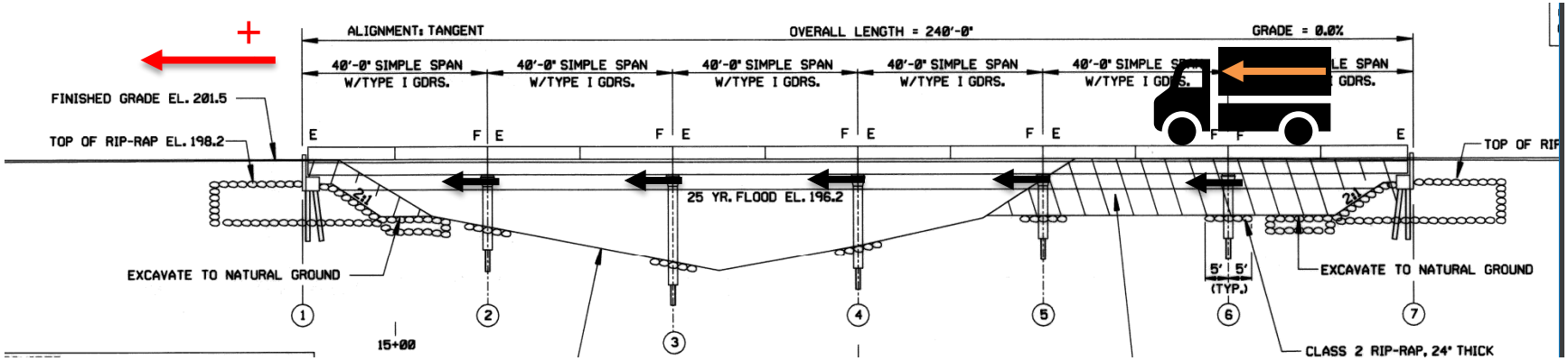

Figure 4-19 Bent Movement Reference Frame

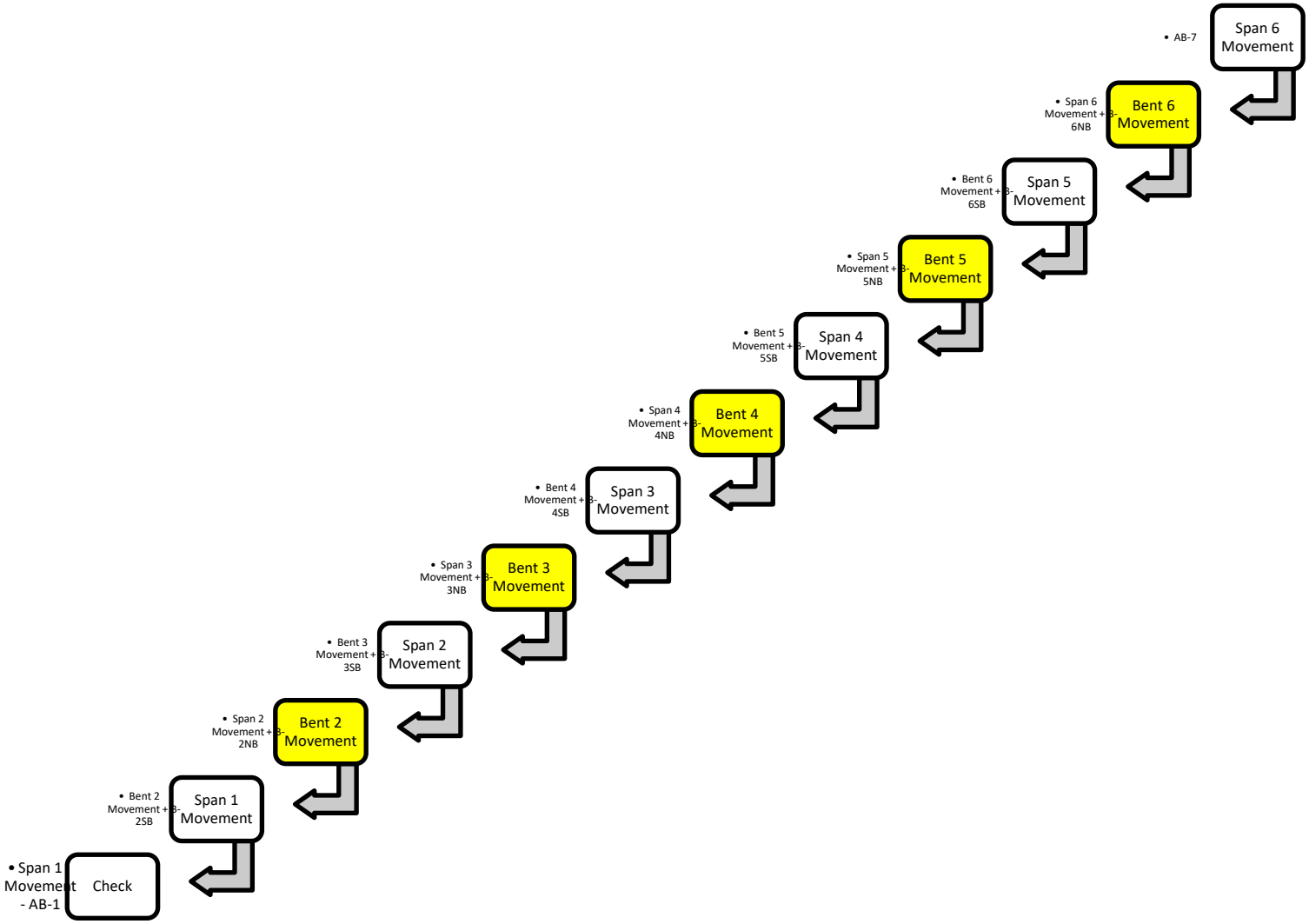

Figure 4-20 Bent Movement Calculation Algorithm (AB-7 Reference)

Similarly, the bent cap movements can be calculated starting with the measurements from the AB-1 draw wire potentiometer. Figure 4-21 illustrates this method.

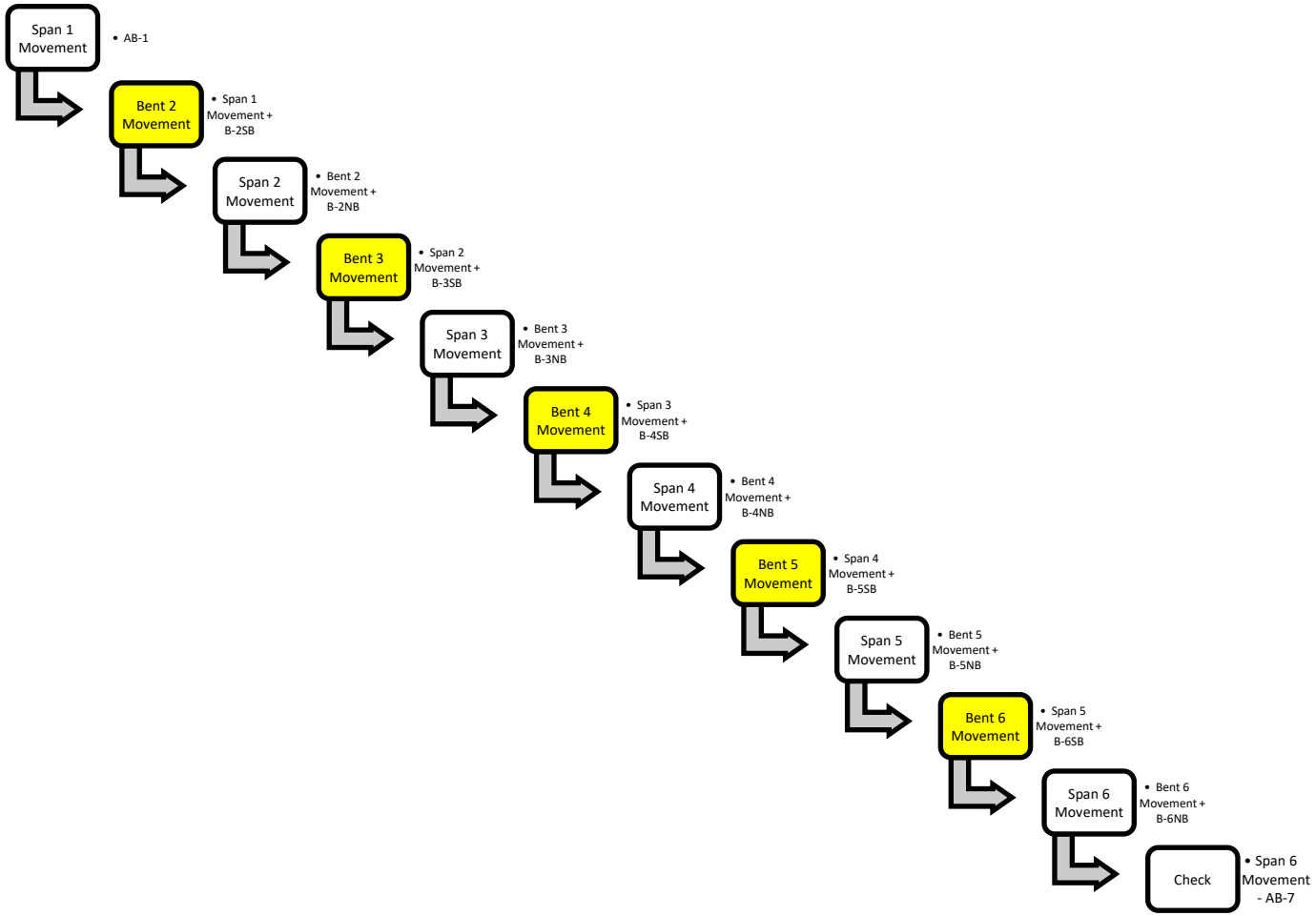

Figure 4-21 Bent Movement Calculation Algorithm (Starting at AB-1)

The bent movement calculations were performed in excel after the data sets were compressed enough that the Excel program could handle the calculations. Due to the malfunction of draw wire potentiometers B-3SB, B-3NB and B-4SB, bent movements from tests performed on 6-6-18 required a combination of the algorithms presented in Figure 4-20 and Figure 4-21. Because of this malfunction, Bent 3 movements for these experiments was not able to be calculated. Bent 2 movements were calculated using the algorithm presented in Figure 4-21 and Bent 4, Bent 5, and Bent 6 were calculated using the algorithm presented in Figure 4-20. All data that was collected was compared to determine trends in the data set.

4.6.4 Inertial Measurement Unit Data

IMU data was collected at a sampling rate of approximately 50 Hz. The IMU recorded the acceleration in the X, Y, and Z directions. Only the X direction accelerations were used during the analysis of the data. During the initial testing, it was noted that the internal clock on the computer used to collect, record, and read the data from the IMU was approximately 9.5 seconds slower than the clock on the computer used for the DAQ system communication. A time stamp for each test was recorded by the IMU sensor and the DAQ system. To align the records, 9.5 seconds were added to the IMU timestamp to match the timestamp from the DAQ computer. The data collected from the IMU was then adjusted to match the initial time of the DAQ data. An example of this adjustment is presented below in Figure 4-22.

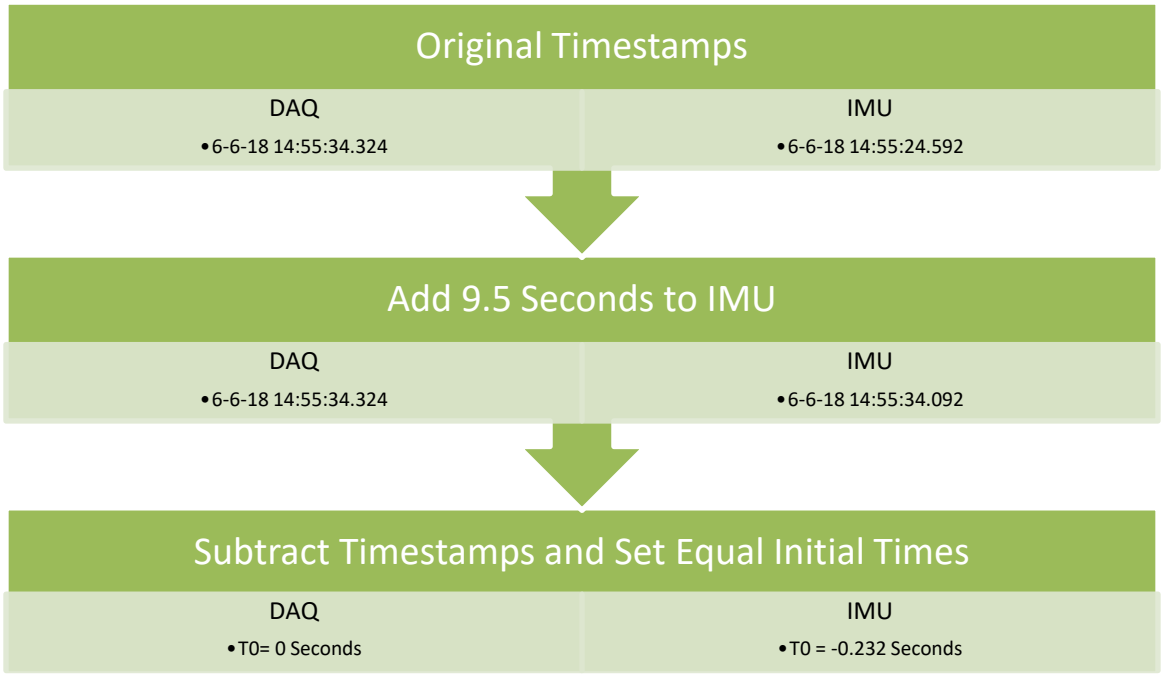

Figure 4-22 IMU Timestamp Adjustment Process

Chapter 5 Experimental Results and Discussion

5.1 Introduction

After the data was reduced, Microsoft Excel was used to plot and evaluate the data for trends and abnormal findings. To accomplish this, the acceleration records for each test, including the IMU acceleration data, was plotted on the same graph for comparison. These individual test graphs are presented in Appendix C.

5.2 IMU Truck Acceleration Data

The data collected from the IMU sensor was analyzed to identify the specific components of the truck deceleration. An example of this is presented in Figure 5-1.

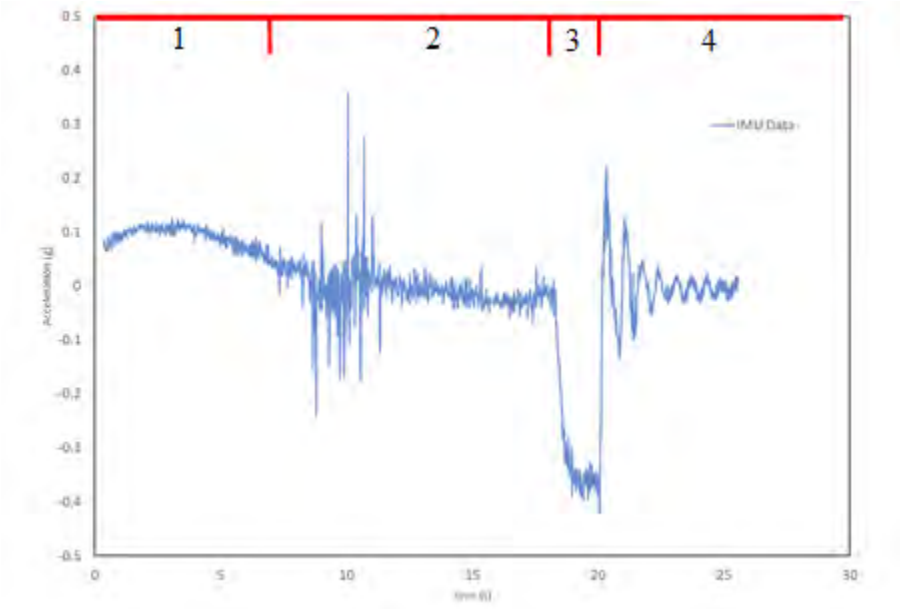

Figure 5-1 Sample Truck Acceleration Data

Each load truck acceleration recording contained four main components. The first component is the initial acceleration of the vehicle. This portion of the record is represented by a parabolic shape indicating the vehicle is increasing velocity until the target speed is obtained. The second portion of the record indicates an approximately constant acceleration as the truck maintains the target velocity. The third portion of the record indicated that the truck began braking at a near constant deceleration of 0.364g on average. The braking period for each test lasted on average 2.3 seconds. The fourth portion of the record indicated the truck rocking after coming to an initial stop. This rocking effect initially began with a high peak and decreased in amplitude with

time. The average peak acceleration of the initial snap back of the truck was approximately 0.293 g, which was 67 percent lower than the deceleration rate.

5.3 Static Tests

5.3.1 Span 6

The first Static Test performed was on Span 6. The load truck was moved to the centerline of Span 6 and rigged to the tow truck cable. The tension link load cell was connected to measure the tension on the tow rigging during the test. The tow truck began applying tension until the truck began to move. During this test, the truck began rolling before the test load reached the desired value of approximately 15 kips. The results of this test are presented in Figure 5-2.

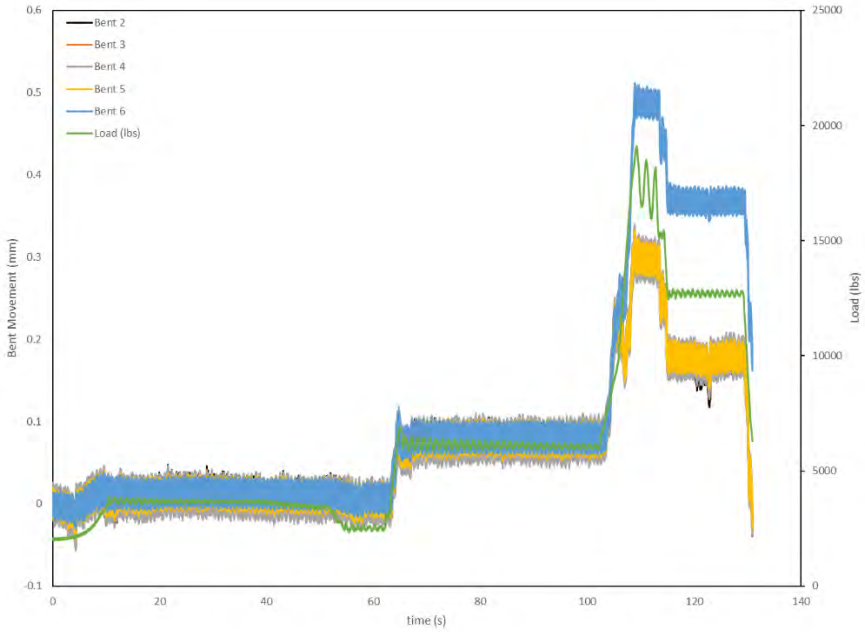

Figure 5-2 Bent Movements for Static Load Test Performed on Span 6

The results confirmed that the truck did begin to roll before the full load was applied. This is indicated by the step increments in the load cell reading and the bent movements. The maximum bent movement during this test was Bent 6. This was expected because the test was performed on the trailing span. The maximum bent movement was measured to be approximately 0.52 mm (0.020 in) at a load of 20,000 lbs. The movement of Bent 5 was measured to be approximately 0.31 mm (0.012 in) at the same loading.

5.3.2 Span 5

Two static tests were performed on Span 5 because the load truck began to move during the test. The tension applied to the load truck began at a reading of approximately 200 lbs and was quickly increased to a reading of 12,000 lbs before the truck began to move. The results from the first test are presented in Figure 5-3.

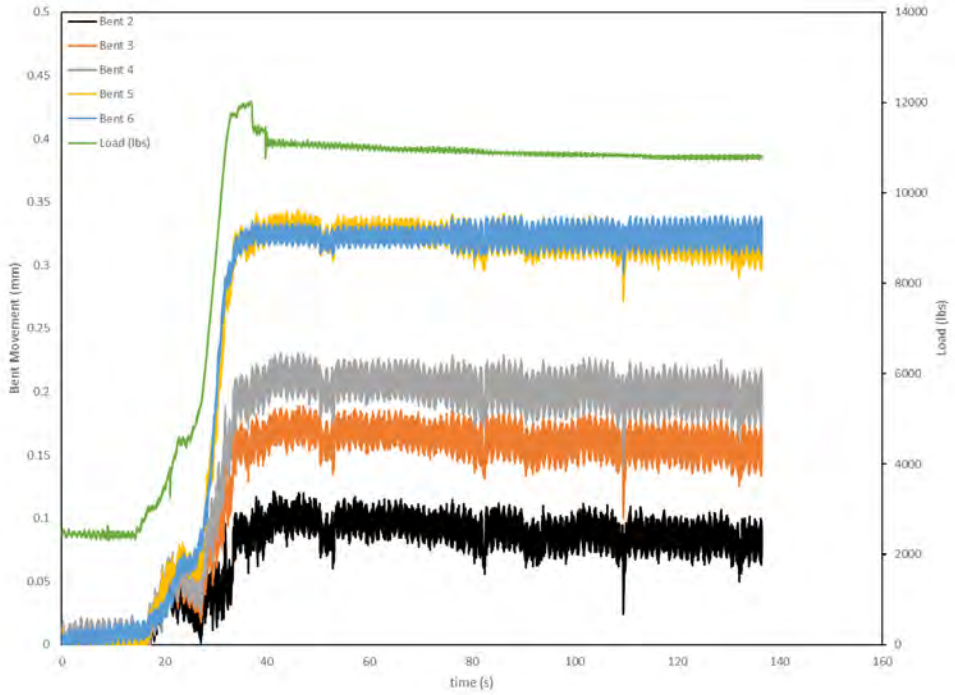

Figure 5-3 Bent Movements for First Static Load Test Performed on Span 5

The bent deflections for this test indicate that bent 5 and Bent 6 moved the most, approximately 0.33 mm (0.013 in) when the tension on the load truck was 12,000 lbs. Bent 4 deflections measured approximately 0.21 mm (0.0083 in), while Bent 3 deflected approximately 0.18 mm (0.0071 in). Bent 2 deflected the least amount with a maximum deflection of approximately 0.1 mm (0.0039 in) at the maximum loading.

The second test performed on Span 5 resulted in a more unique data set than the first test. During the test, the load on the truck was gradual increased until the desired load 18,000 lbs was obtained. After the test load was obtained, the load was released quickly causing the truck to rock back and forth. This caused the bridge to respond in a similar manner, indicated in the bent deflection data presented in Figure 5-4.

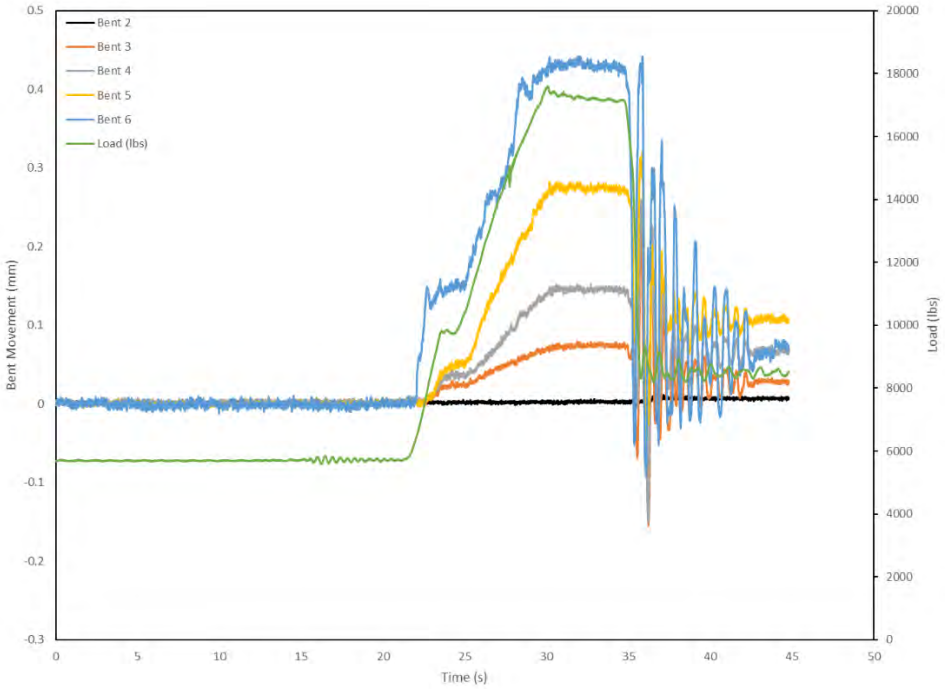

Figure 5-4 Bent Movements for Second Static Load Test Performed on Span 5

The initial load on the towing cable was measured to be approximately 6,000 lbs. This was not ideal but still yielded usable data. The load was increased until desired value of 18,000 lbs was obtained. The largest bent deflection was measured at Bent 6, with a maximum bent deflection of approximately 0.44 mm (0.017 in)). The maximum bent deflections decreased with each bent starting with Bent 5, which deflected approximately 0.30 mm (0.012 in)) at the highest test load.

5.3.3 Span 4

The static test performed on Span 4 yielded uniform bent deflections. The initial applied load measured approximately 40 lbs and was gradually increased to a load of approximately 18,000 lbs. The load was slowly released and allowed the bridge response to be clearly measured during the unloading process, presented in Figure 5-5.

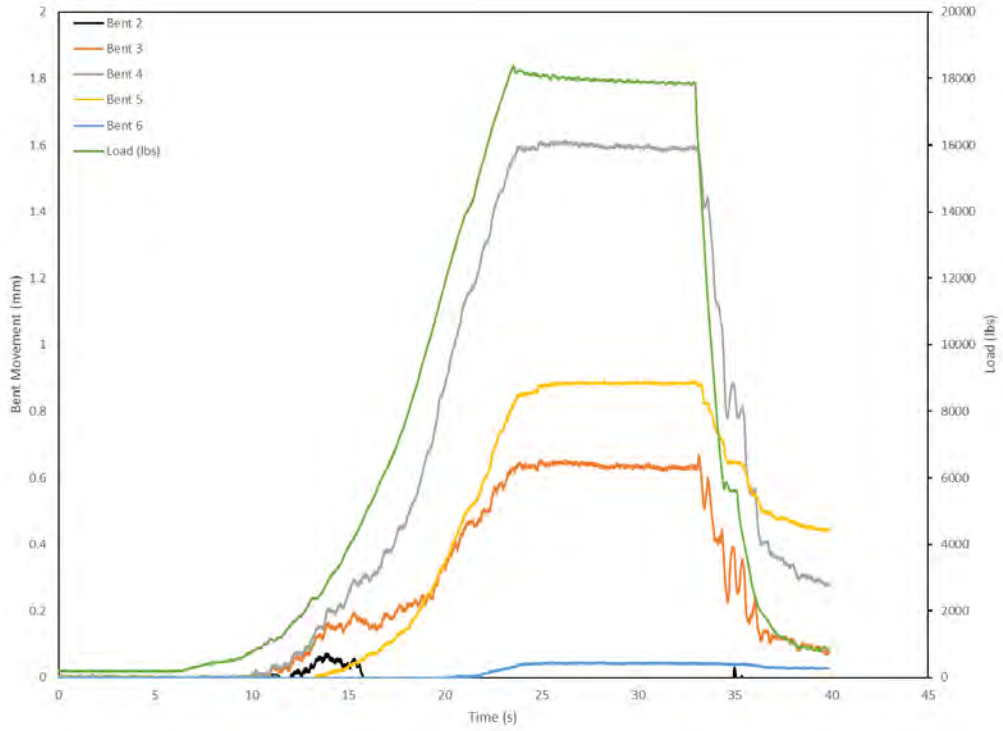

Figure 5-5 Bent Movements for Static Load Test Performed on Span 4

Bent 4 deflected the most with the maximum bent movement of approximately 1.6 mm (0.063 in) at the highest loading level of 18,000 lbs. The second highest bent deflections were measured at Bent 5, with a maximum deflection of approximately 0.8 mm (0.032 in). The third highest bent deflections occurred at Bent 3, with a maximum deflection of approximately 0.65 mm (0.026 in). Deflections measured at Bent 2 and Bent 6 were minimal.

5.3.4 Span 3

The static test performed on Span 3 yielded similar results to the test performed on Span 4. The data from this test illustrated the bridge response due to loading and unloading during the testing process, presented in Figure 5-6.

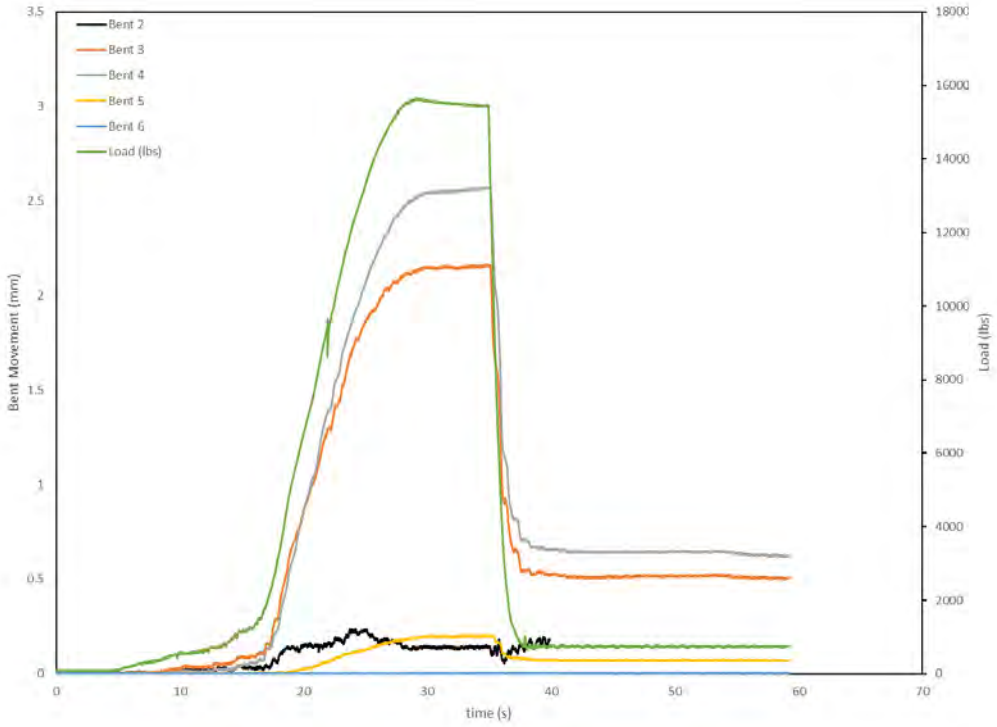

Figure 5-6 Bent Movements for Static Load test Performed on Span 3

The initial load on applied to the bridge was measured to be approximately 20 lbs. The load was gradually increased until approximately 16,000 lbs were applied. The maximum bridge response was measured at Bent 4, with a maximum deflection of approximately 2.5 mm (0.098 in) at the maximum loading. Bent 3 deflected the second highest amount, with a maximum measured deflection of 2.1 mm (0.083 in). Bent 2, Bent 5, and Bent 6 did not have a prominent response during this test.

5.3.5 Span 2

The static test performed on Span 2 resulted in some incomplete data. The measurements obtained during this test were slightly skewed due to possible movement of the draw wire potentiometers during the test (Figure 5-7). This was a problem encountered in many of the dynamic tests.

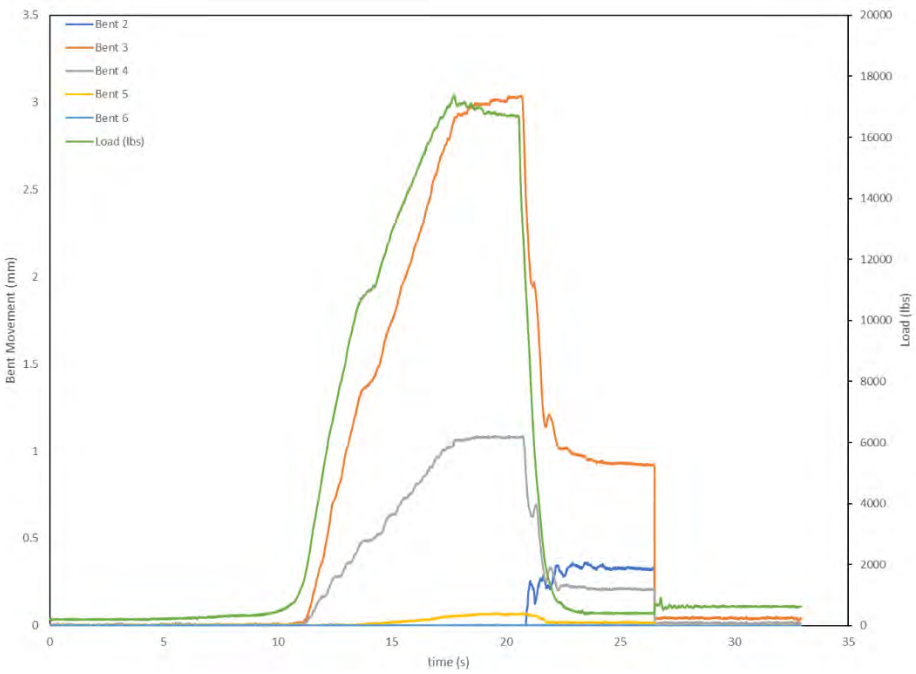

Figure 5-7 Bent Movements for Static Load Test Performed on Span 2

The initial load for this test was approximately 40 lbs. The applied load was gradually increased to a maximum load of approximately 18,000 lbs. The largest bridge response was measured at Bent 3, which had a maximum deflection of approximately 3 mm (0.12 in). This was the largest deflection measured during any of the static tests. This was expected because Bent 3 is the tallest and least stiff bent on the bridge. The data collected showed a sharp drop in the readings in all the draw wire potentiometer data. This is indicated by the sharp drop in the bent deflections for this test.

5.3.6 Span 1

The static test performed on Span 1 shown in Figure 5-8 indicated a maximum bent deflection measured at Bent 2, which was the only bent adjacent to the test. The bent deflection measured approximately 0.24 mm (0.0094 in) at the maximum loading of 16,000 lbs. Bent 3 and Bent 4 had minimal bent deflections with measured movements of 0.05 mm (0.0020) and 0.02 mm (0.00079), respectively. Bent 5 and Bent 6 did not experience any movement according to the collected data.

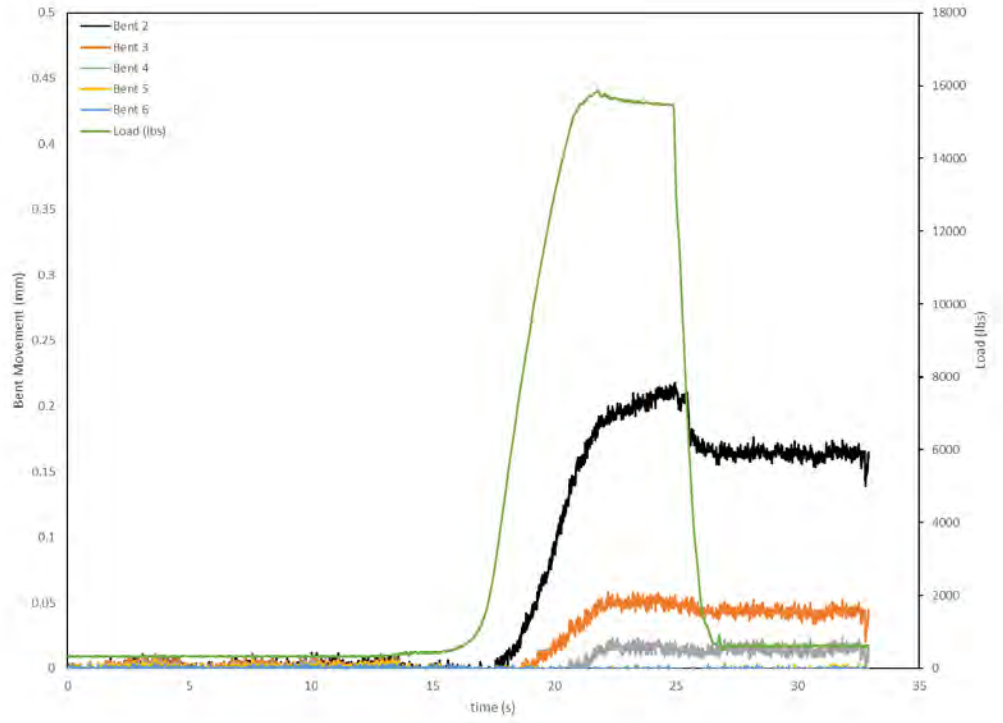

Figure 5-8 Bent Movements from Static Load Test Performed on Span 1

5.4 Dynamic Tests

Dynamic tests were performed on both days of testing. The data collected for these tests included the IMU truck data presented in the previous section, acceleration data from each bridge bent and span, and bent movements calculated from the draw wire potentiometer readings. Using this data, the bent movements were plotted together for comparison. The accelerations for each test were also plotted together for comparison. Samples of these graphs are presented in Figure 5-9 and Figure 5-10.

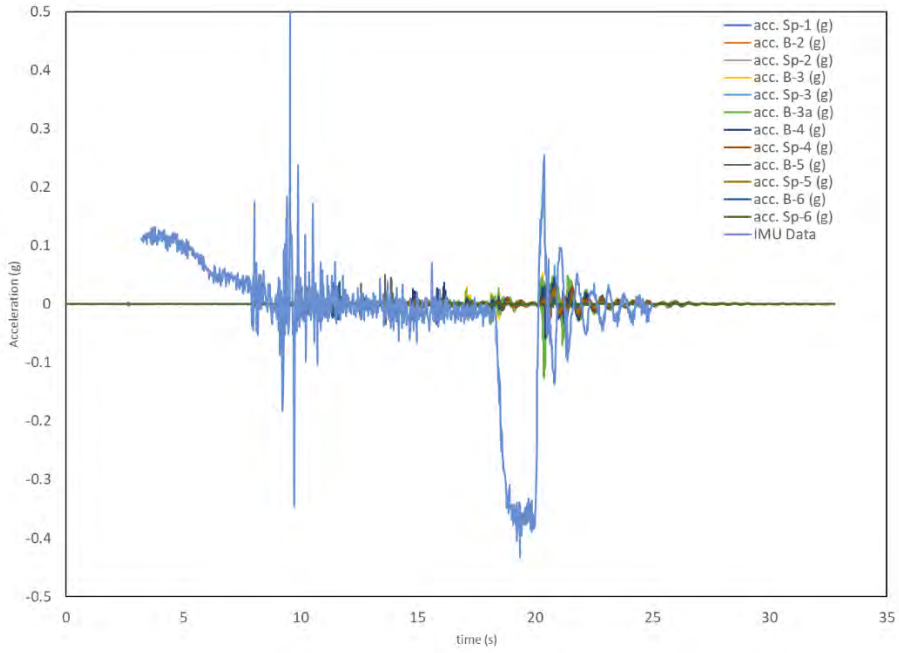

Figure 5-9 Combined Acceleration Records for Dynamic Test at C2

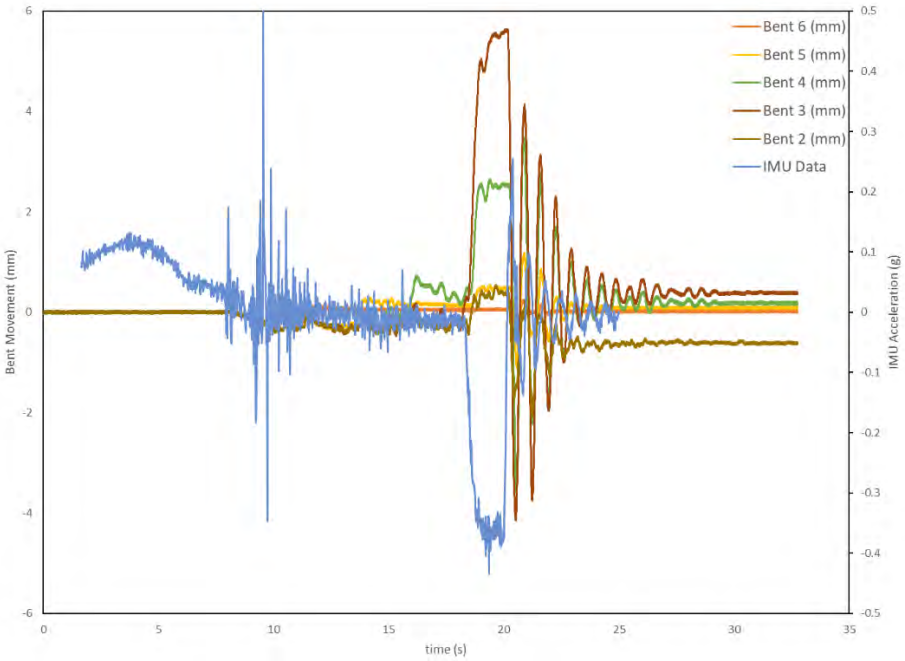

Figure 5-10 Combined Bent Movements for Dynamic Test at C2

The bridge bent movements and the acceleration records for the bridge closely follow the same pattern as the braking truck acceleration. It was evident in the data that the rocking of the truck after the initial braking has occurred had a similar effect on the bridge. After the braking had occurred there was a spike in bridge movement and acceleration followed by a decrease in

amplitude of the bridge response. In most of the tests, the bridge bent movements do not return to zero after the movement has stopped. This was determined to be result of the hooks that connect the wire to the eye hook for the potentiometers slightly shifting during bridge movement.

The acceleration data indicated that the acceleration experienced by the bridge was significantly lower than the acceleration measured on the load truck. On average the maximum acceleration measured on the bridge was 0.054g. This indicated that the maximum acceleration measured on the bridge was approximately 23 percent, on average, of the acceleration of the measured at the truck.

Each of these data sets was used to compare the results from the various tests at the same location (i.e. C5 or R3). The results were also used to compare the data between tests performed at the centerline or the edge of each span. The results in the following section will be grouped by individual location and then a comparison between the centerline and edge.

5.4.1 Location C5

This was the first location to be tested and resulted in 7 tests being performed. There were five tests performed on 6-6-18, when B-3SB, B-3NB, and B-4SB potentiometers were not working properly. Two additional tests were performed on 6-7-18, which had all sensors working properly. The maximum bent movements were used as a comparison for the bridge response. The maximum bent movements for each test at this location are presented in Figure 5-11.

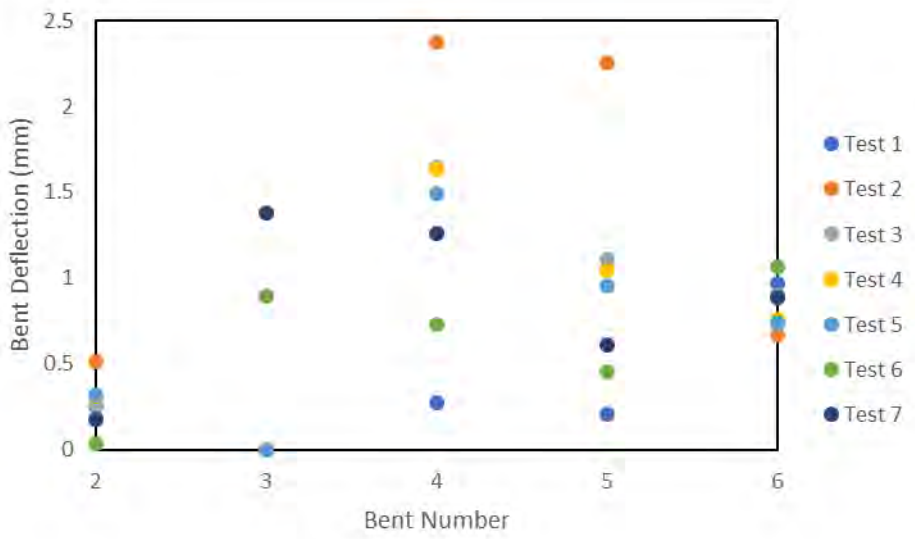

Figure 5-11 Maximum Bent Movements for C5 Dynamic Tests

The average braking deceleration for tests performed at this location was 0.272 g. This was the first span to be tested, which required several adjustments to be made from test to test. During Test 1 the truck stopped before fully crossing onto Span 5. On Test 2 the truck stopped past Span 5 and onto Span 4. The data initially appears to have a random scatter. This is because on some of the tests the truck did not stop completely on the span of interest. This is evident in the data from the high span movements during this test. The remainder of the tests were performed in a more uniform manner. Removing the data from Test 1 and Test 2, there appears to be a pattern that is depicted. A plot with data from Test 1 and Test 2 removed is presented in Figure 5-12.

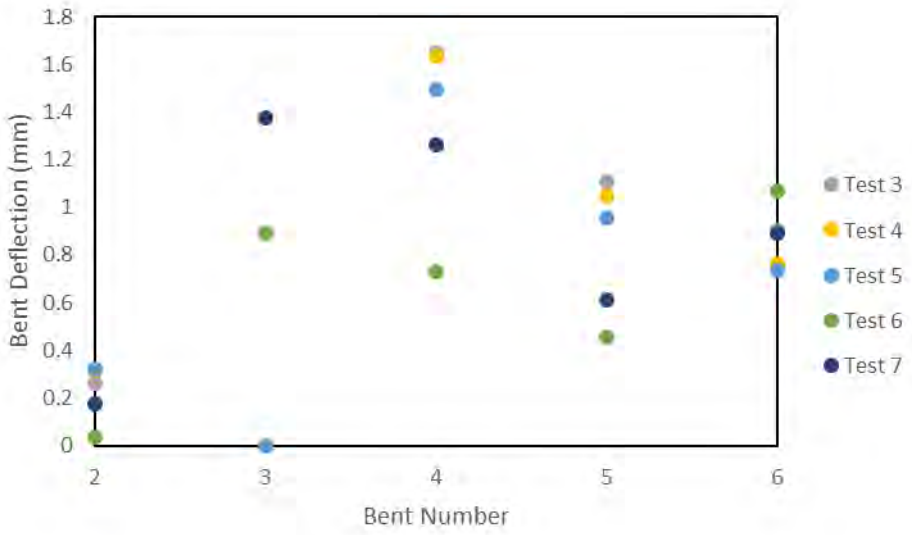

Figure 5-12 Maximum Bent Movements for C5 Dynamic Tests with Test 1 and 2 Removed

The data appeared to show that stopping at this location resulted in higher deflections at Bent 3 and Bent 4. This was expected due to these bents being taller and less stiff than the other bents in the substructure of the bridge.

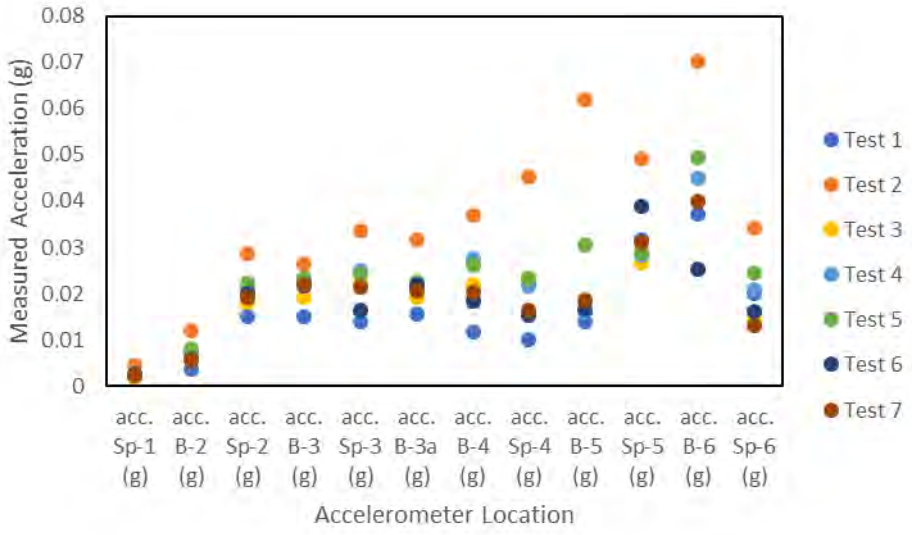

Figure 5-13 Maximum Measured Bridge Accelerations for Dynamic Tests at Location C5

The measured accelerations of the bridge (Figure 5-13) indicate the maximum accelerations occurred at Bent 6 and on Span 5. The average maximum measured acceleration in

these locations was 0.035 g, which was approximately 12 percent of the acceleration measured at the load truck.

5.4.2 Location R5

The next location of interest was located on the same span but in the shoulder of the southbound travel lane. This location was chosen to compare the results with the test performed at the centerline of this span. The maximum bent movements for the tests performed on this span are presented in Figure 5-14.

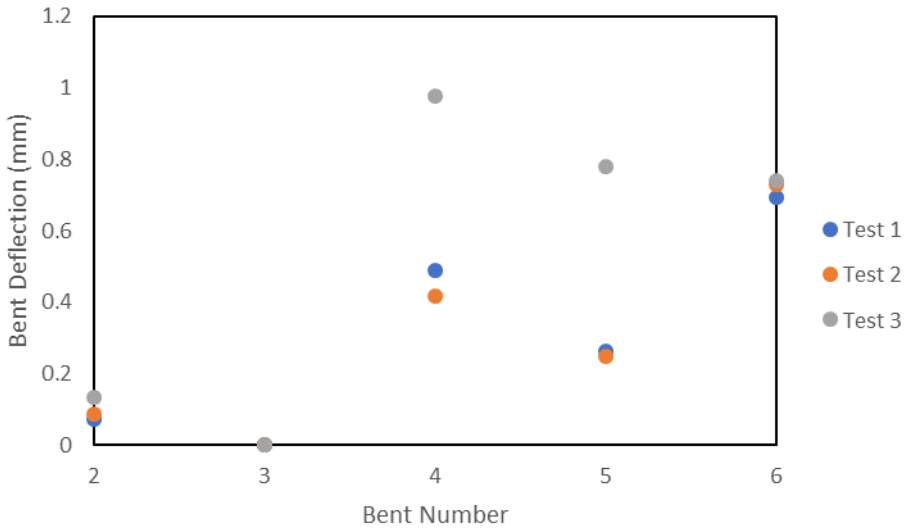

Figure 5-14 Maximum Bent Deflections for Dynamic Tests at Location R5

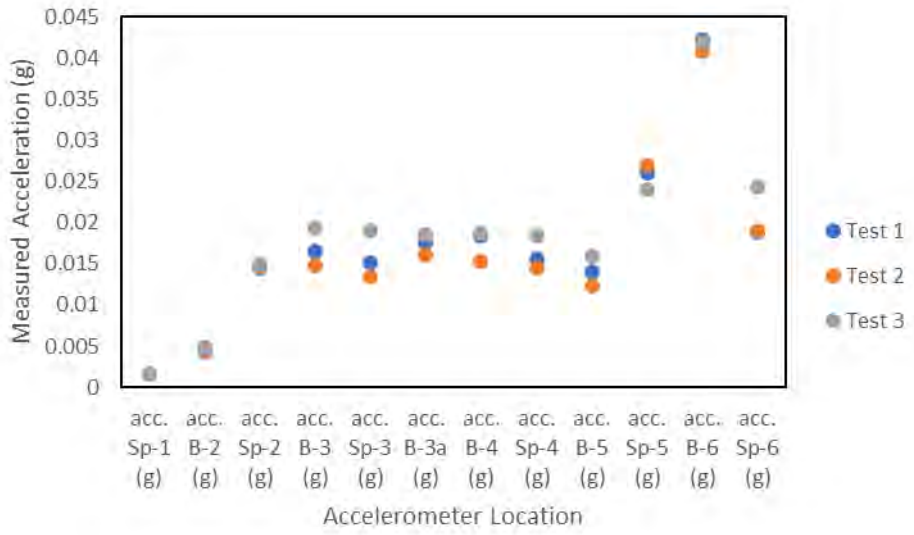

Figure 5-15 Maximum Measured Bridge Accelerations for Dynamic Tests at Location R5

The average measured deceleration of the load truck, shown in Figure 5-15, was approximately 0.189 g. The measured acceleration data shows that the highest measured accelerations of the bridge for the test performed at this location occurred at Bent 6 and on Span 5. The average maximum acceleration measured at these locations was approximately 0.042 g, which was 22 percent of the acceleration measured on the load truck. The average maximum acceleration measured for these tests was approximately 16 percent higher than the average from the tests performed at the centerline of this span.

5.4.3 Location C3

Four dynamic load tests were performed at location C3. There were three tests that were performed on 6-6-18, when draw wire potentiometers B-3SB, B-3NB, and B-4SB were not working properly, and one test performed on 6-7-18. The data from the tests performed at this location are presented in Figure 5-16 and Figure 5-17.

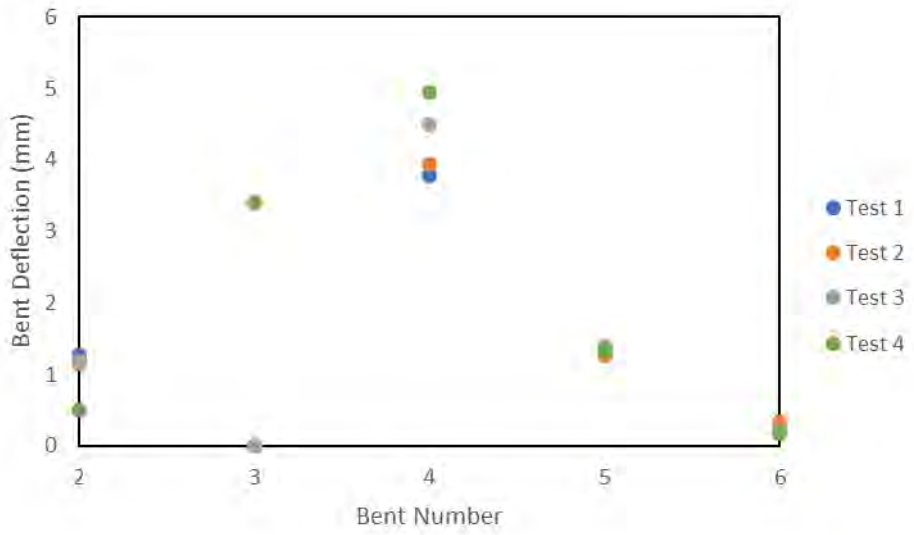

Figure 5-16 Maximum Bent Deflections for Dynamic Tests Performed at Location C3

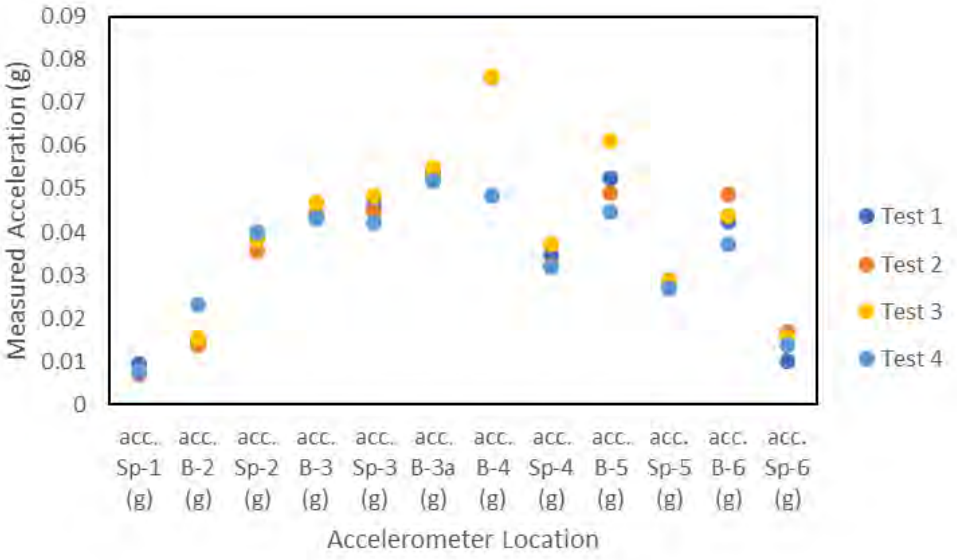

Figure 5-17 Maximum Measured Accelerations for Dynamic Tests Performed at Location C3

The maximum bent deflections for tests at this location were measured at Bent 4. The average maximum bent movement at this location was measured to be approximately 4.29 mm. The highest acceleration for dynamic tests performed at this location were also measured at Bent 4, where the maximum acceleration was measured to be approximately 0.076 g. The average acceleration measured at the load truck was approximately 0.254 g. The maximum measured acceleration on the bridge was approximately 29 percent of the acceleration measured on the load truck.

5.4.4 Location R3

Three tests were performed at location R3, which were all done on 6-6-18. The average maximum acceleration measured at the load truck was approximately 0.167 g. The results of the tests performed at this location are presented in Figure 5-18 and Figure 5-19.

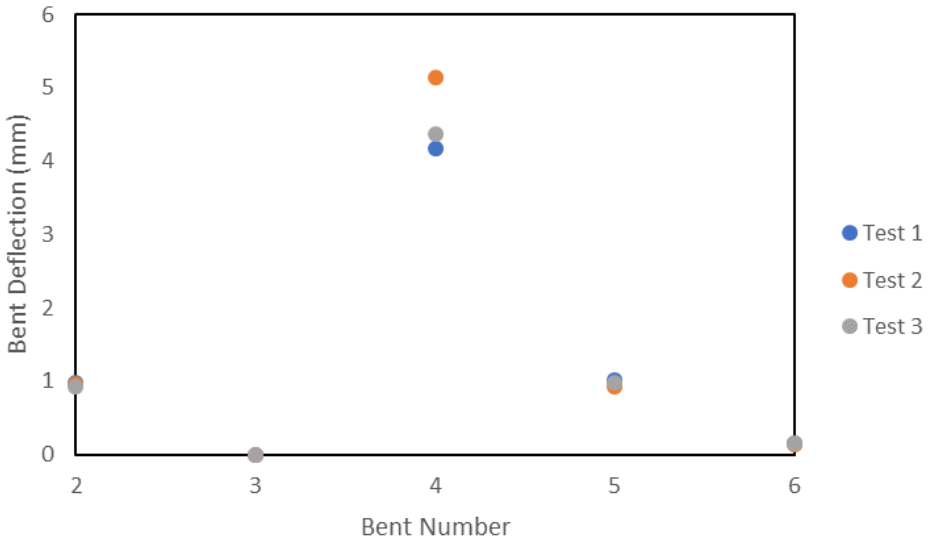

Figure 5-18 Maximum Bent Movements for Dynamic Tests Performed at Location R3

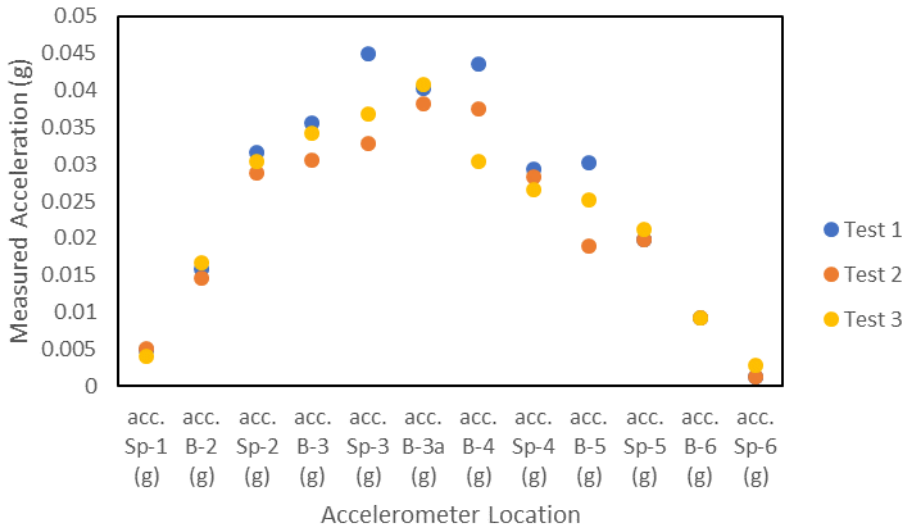

Figure 5-19 Maximum Measured Accelerations for Dynamic Tests Performed at Location R3

The highest bent deflections were measured at Bent 4, which was consistent with the tests performed at the centerline of this span. The average measured deflection at this bent was

approximately 4.55 mm compared to the 4.29 mm measured during the tests at location C3. The highest measured acceleration was located on Bent 4 and Span 3. This average measured acceleration of the bridge at these locations was 0.040 g, which was 24 percent of the maximum acceleration measured at the load truck.

5.4.5 Location C2

Five dynamic tests were performed at this location, three on 6-6-18 and two on 6-7-18. The average maximum acceleration of the load vehicle during these tests was measured to be approximately 0.442 g. The results of the dynamic tests performed at this location are presented in Figure 5-20 and Figure 5-21.

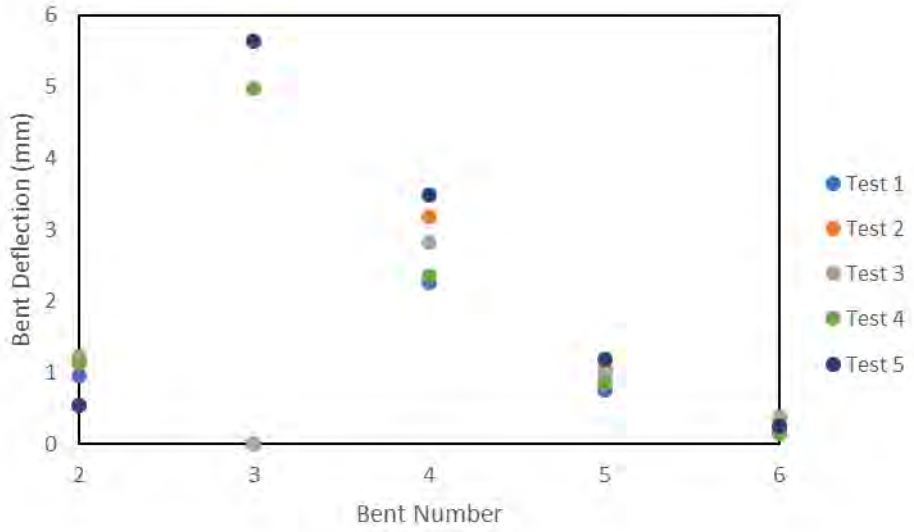

Figure 5-20 Maximum Bent Movements for Dynamic Tests Performed at Location C2

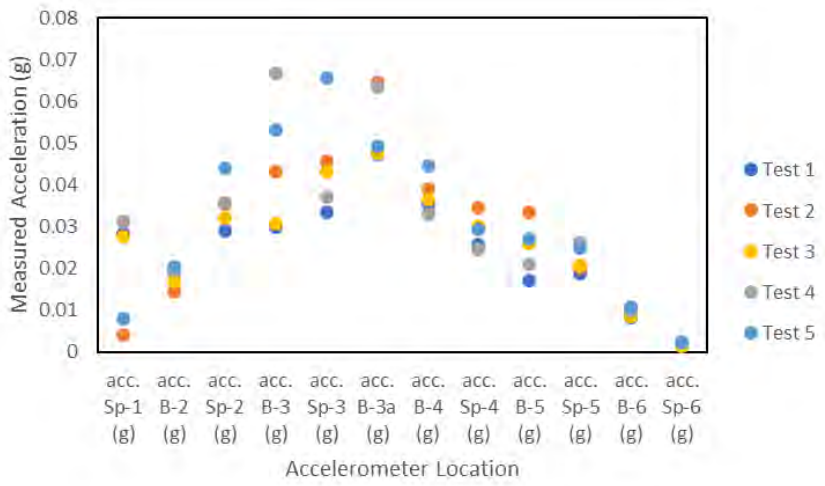

Figure 5-21 Maximum Measured Accelerations for Dynamic Tests Performed at Location C2

The largest bent deflections were measured at Bent 3. The average maximum bent deflections at this location were measured to be approximately 5.3 mm. The largest accelerations were measured on Bent 3 or Span 3. The average maximum acceleration at this location were measured to be approximately 0.059 g, which was 13 percent of the average acceleration measured at the load truck.

5.4.6 Location R2

Five dynamic tests were performed at location R2, three tests on 6-6-18 and two tests 6-7-18. The average maximum acceleration measured on the load truck during these tests was approximately 0.237 g. The results from the dynamic tests performed at this location are presented in Figure 5-22 and Figure 5-23.

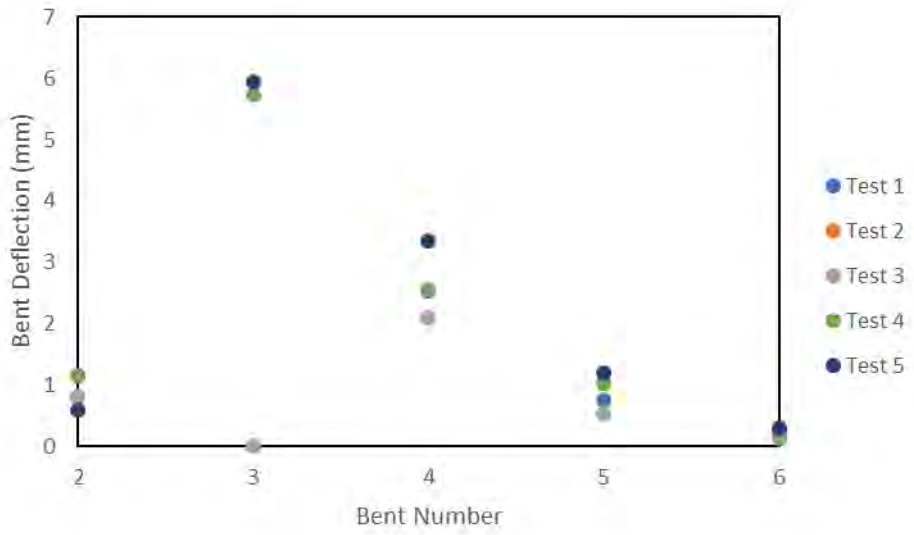

Figure 5-22 Maximum Bent Movements for Dynamic Tests Performed at Location R2

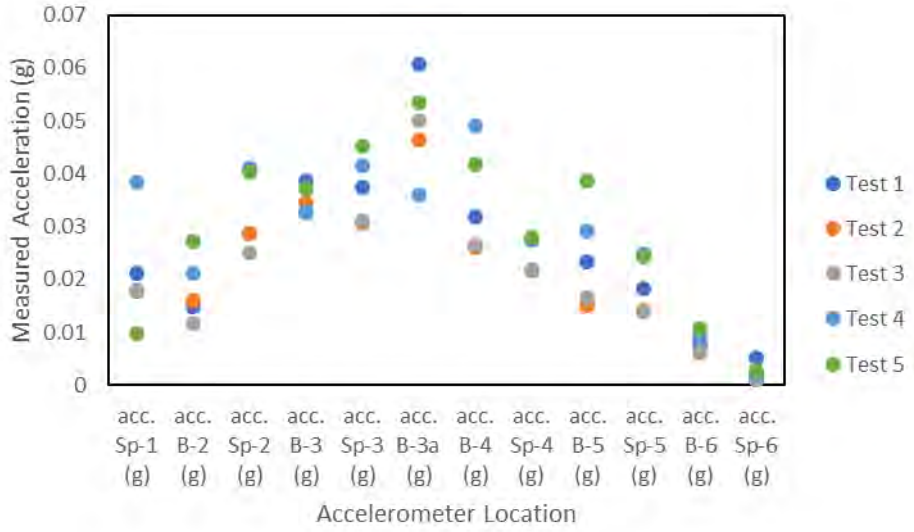

Figure 5-23 Maximum Measured Accelerations for Dynamic Tests Performed at Location R2

The maximum bent deflections were measured on Bent 3, which was consistent with the bent deflections measured for the test performed at the centerline of the span. The average bent deflection at this location was determined to be approximately 5.84 mm compared to 5.3 mm of bent deflection for the tests performed at the centerline. The maximum accelerations of the bridge were measured at Bent 3a. The average acceleration measured at this location was 0.049 g, which was approximately 21 percent of the maximum acceleration measured at the load truck.

Chapter 6 Analytical Modeling of Load Testing

6.1 Introduction

In order to supplement the information that can be generated by an experimental test, analytical modeling has been completed in order to further study the response of bridges to longitudinal braking forces. The first section of the chapter discusses the procedures utilized to develop the analysis models. Following this section, the analytical model results for the static and dynamic analyses are presented in this chapter. Results are presented beginning with the static model, followed by results of the dynamic testing. The main goal for the static tests was to provide a foundation for calibrating the model behavior before adding the dynamic aspects. The correlations between the model results and the field results are then evaluated. After the correlation between results are evaluated, the amount of shear force present in the bents is presented. With the ultimate goal of this project being determining the load path and intensity of the force going into the bents, observations on how the braking force is distributed are discussed.

6.2 Analytical Modeling Procedure

The steps in creating the model can be generalized into two phases: the CSiBridge phase and the SAP2000 phase. Construction of the bridge model began in CSiBridge v. 15.2.0. This program, produced by Computers and Structures, Inc., is a structural analysis software specifically for bridges and had advantages for building the initial, unrefined version of the model before transferring to SAP2000 for calibration and analysis. The advantage was the predefined bridge elements that made construction of the model significantly quicker and more realistic to the geometry of the real bridge. CSI provided a step-by-step process to build the superstructure and substructure and connected them appropriately.

6.2.1 Constructing the Analytical Model in CSIBridge

To begin, a layout line of 240 ft with a 0.0 percent grade was inserted with a 12 ft wide lane on either side of the layout line. From the components tab, the appropriate materials and section properties were defined to correspond to this bridge. The modeled elements included were

- Bridge deck
- Precast prestressed Type I AASHTO concrete girders
- Bearing pads

- Bent caps
- Galvanized HP14x89 piles
- Encased HP14x89 piles
- Abutments

With these elements properly defined, the deck cross section was created. The software creates the deck as shell elements and the girders as frame elements. For the deck, CSI subdivides the end spans into thirty-two shell elements and interior spans into forty-eight shell elements. Figure 6-1 is a wire-frame view illustrating how the interior spans have more shell elements then end spans. This is due to the girder lines being discontinuous from the superstructure. This definition results in two connections, one on either side of the centerline of the bent cap to the two girder ends, requiring more joints for element connections.

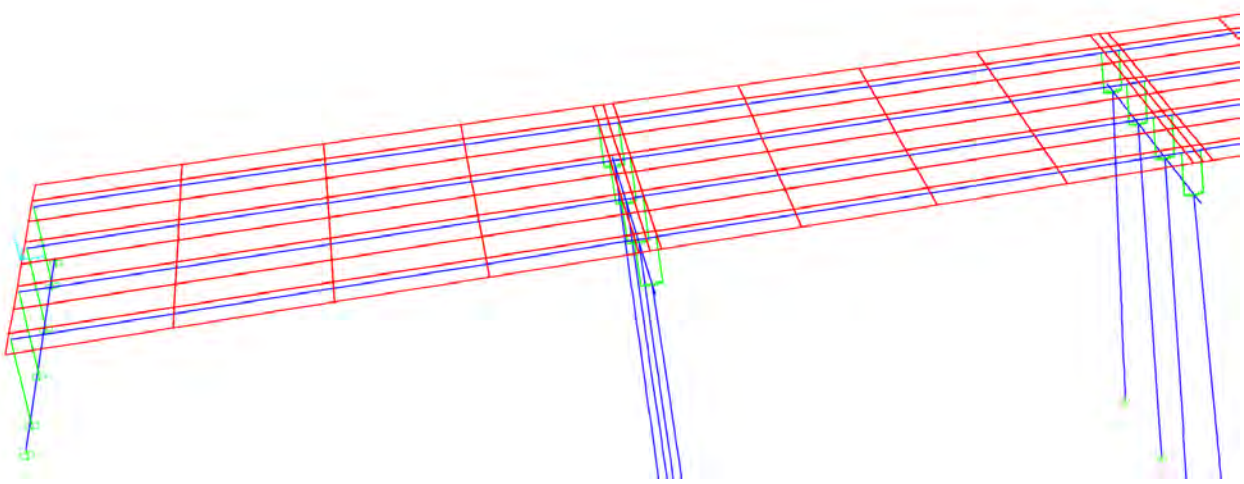

Figure 6-1 – Bridge Modeler Shell Element Discretization for Interior and Exterior Spans

The girder frame elements are automatically discretized into lengths that are the same as the shell elements above them. This results in four 117.75 in long elements and one 9 in long element for end spans and four 115.5 in long elements and two 9 in long elements for interior spans. The girders are connected to the deck via rigid links automatically defined by CSI. Figure 6-2 displays the input used in CSI to generate the superstructure. The remaining inputs not shown in this figure are: Right Overhang Data, Live Load Curb Locations, and Insertion Point Location.

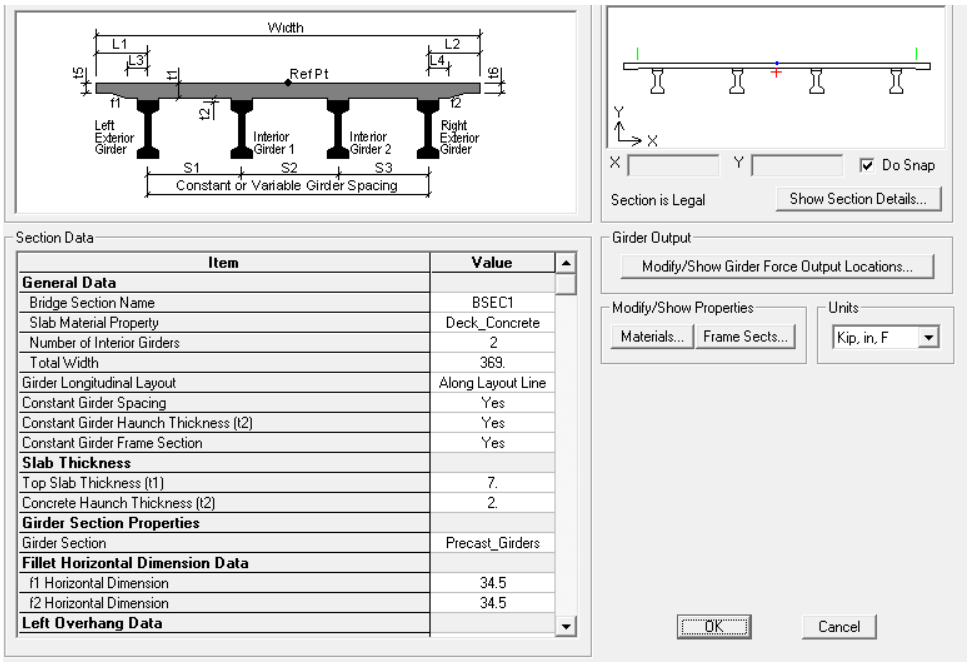

Figure 6-2 – CSiBridge Superstructure Input Dialog Box (2010)

After the superstructure was defined, the substructure components were generated using their respective input fields. The substructure includes the bearing pads, abutments and bents.

6.2.1.1 Bents

To model the bents, a frame element was created for the bent caps and frame elements were generated for the piles. The girders connecting to the bent cap were all defined as discontinuous from the superstructure. The column heights were appropriately defined based off the elevations in the plans and were fixed at ground level. In the plans for the bridge, the elevation was recorded for the top of each pile as well as the elevation for the ground line so it was known how long to define each pile.

For the encased piles, the section designer was required to achieve the proper geometry, as this section type is not a predefined frame section. Creating the piles in this manner required a verification of the cross section behavior to ensure it was behaving as intended. To accomplish this, a beam was created with the same geometry and material properties in SAP. It was fixed at one end and free at the other. A load of 1 kip was applied to the free end of the beam, and the resulting displacement is shown in Figure 6-3.

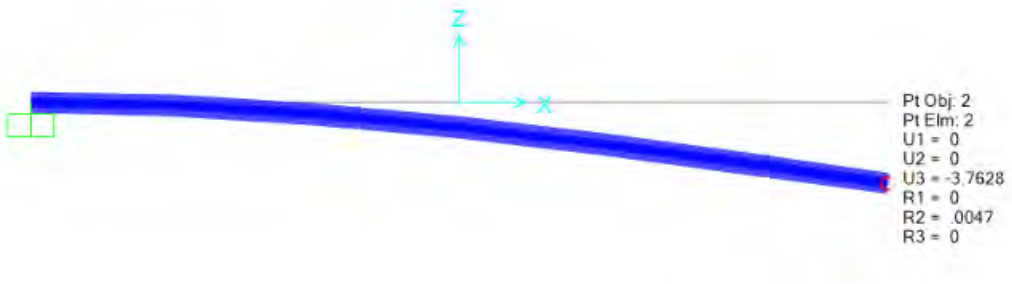

Figure 6-3 – SAP2000 Validation of Cross-Sectional Geometry of Pile

The deflection computed by SAP at the free end was 3.76 inches and the deflection computed by hand, considering flexural only deformations, was 3.71 inches. When computing by hand, the deflection equation used was

$$\Delta = \frac{PL^3}{3E_{concrete}I_{transformed}} \qquad \text{Equation 6-1}$$

Where

$$P = 1\ kip$$

$$L = 1200\ inches$$

$$E_{concrete} = 3320\ ksi$$

$$I_{transformed} = 46722\ in^4$$

Since the deflection reported by SAP was less than 1.5 percent greater than the flexure-only calculation, this method of defining the encased piles in CSI was deemed acceptable. The piles of bents 3 and 4 did not have to be verified since they were predefined sections in the software.

6.2.1.2 Abutments

The next substructure items defined were the abutments. These were frame elements that match the geometry of the abutment grade beam. The wall behind this beam was neglected in the model as were the piles since it was assumed the abutment was completely fixed. The connection to the girders was defined as “Connect to Girder Bottom Only.” The bottom of this beam was defined as fixed.

6.2.1.3 Bearing Pads

The stiffness of the bearing pads were instrumental in how the load would be transferred from the superstructure to the substructure. Therefore, much effort was placed in defining this

properly in the model and later calibrating to match the field results. In this bridge, elastomeric bearing pads, type 2, mark B1 with a total thickness of 0.75 in, length of 14.5 in and width of 9.0 in were used. There are two individual layers of elastomer and one 12-gauge steel shim plate between the layers. To model the properties of the bearing pad and represent the girder end fixities defined in the plans, three types of bearings were created in CSI. The fixities that had to be accounted for were

1. Expansion with no bolts to resist transverse movement, no direction fully restrained in this setup. Used on interior girders on ends designated expansion in the plans.
2. Expansion with bolts that provided transverse resistance, restraining only transverse translation. Used on exterior girders on ends designated expansion in the plans.
3. Fixed, restraining transverse and longitudinal translation. Used on interior and exterior girders as designated in the plans.

Using the equations defined in Chapter 2.6 for the pads and the bolt stiffness equation discussed below, the stiffness values were computed. For these equations, two characteristics of the bearing pad had to be assumed. The shear modulus of the elastomer was assumed to be 0.135 ksi and the modulus of elasticity was assumed to be 30 ksi as discussed in Chapter 2.6. The stiffness calculation for the girder ends that contained bolts included the shear and flexural resistance from the bolt in addition to the pad. The two components of the bolt stiffness act in series and Equation 6-2 is how the stiffness for a single bolt was calculated.

$$\frac{1}{k_{bolt}} = \frac{1}{k_{flexure}} + \frac{1}{k_{shear}} \qquad \text{Equation 6-2}$$

Where

$$k_{flexure} = \frac{3EI}{L^3} \qquad \text{Equation 6-3}$$

$$E = 29000\ ksi$$

$$I = 0.049\ in^4$$

$$L = 0.75\ in$$

$$k_{shear} = \frac{9}{10} * \frac{GA}{L} \qquad \text{Equation 6-4}$$

$$G = 11600\ ksi$$

$$A = 0.785\ in^2$$

$$L = 0.75\ in$$

With a bolt on each side of the girder acting in parallel with the bearing pad, the bolt stiffness value was doubled and added to the stiffness of the pad alone. A summary of the stiffnesses used are presented in Table 6-1.

Table 6-1 – Bearing Pad Stiffness Definitions for Girder End Fixities

Girder End Condition	Stiffness values (k/in)			Stiffness (k-in/rad)
	Longitudinal Direction	Transverse Direction	Vertical Direction	Rotation about Transverse Axis
Expansion with bolts	23.5	10000	5220	35240
Expansion, no bolts	23.5	23.5	5220	35240
Fixed	10000	10000	5220	35240

With the bearing pads defined properly, at this phase Figure 6-4 depicts the model upon completion of the preliminary stages of modeling utilizing the advantages of CSI Bridge. From here, this model was exported to SAP for refinement and to begin analysis.

Figure 6-4 – Initial Analytical Model as Constructed in CSI

6.3 Refinement of Model in SAP2000

It was determined that the entire length of the pile should be included and the influence from the soil along the pile modeled as well. After increasing the length of the piles to reflect their full length, the pile fixity was changed from completely fixed to restrained in the transverse and vertical directions and a spring added at the tip for partial fixity in the longitudinal direction. In addition, springs were added along the length of the pile to provide longitudinal stiffness, the amount of springs will be discussed in Section 6.3.1. To generate the soil springs, FB-MultiPier

was utilized to obtain P-y curves and create equivalent springs from this information. This procedure is presented in Section 6.3.1. Furthermore, in CSI Bridge the correct batter would not stay applied to the outer piles, so the appropriate slope of 1.5/12 was applied. Another modification was applied to the pile heights of Bent 4, these were altered to better match the field conditions as they varied from the plans. It was observed in the field that the ground level was no longer uniform at each pile. To obtain a more accurate ground level elevation for current conditions, the 1 ft increments that were marked on the piles while being driven were used. The 1 ft increments indicated how many feet from that line to the tip of the pile. Since the tip elevation is indicated in the plans, the amount of the pile below the ground line could be obtained based on what markings were visible in the field. The final major change in the model in SAP was in the bearing pads and their stiffnesses.

6.3.1 FB-MultiPier P-y Curve Generation for Soil Springs

For each bent, a model was created in FBMP (BSI, 2017). The boring log provided in the plans (ALDOT 2013) contained the information to create an accurate soil profile. The piles were discretized into 8 nodes along the free length and 16 nodes along the embedded length. Figure 6-5 and Figure 6-6 are representative of all 6 bents. All models can be found in Appendix A as well as the inputs for the soil properties.

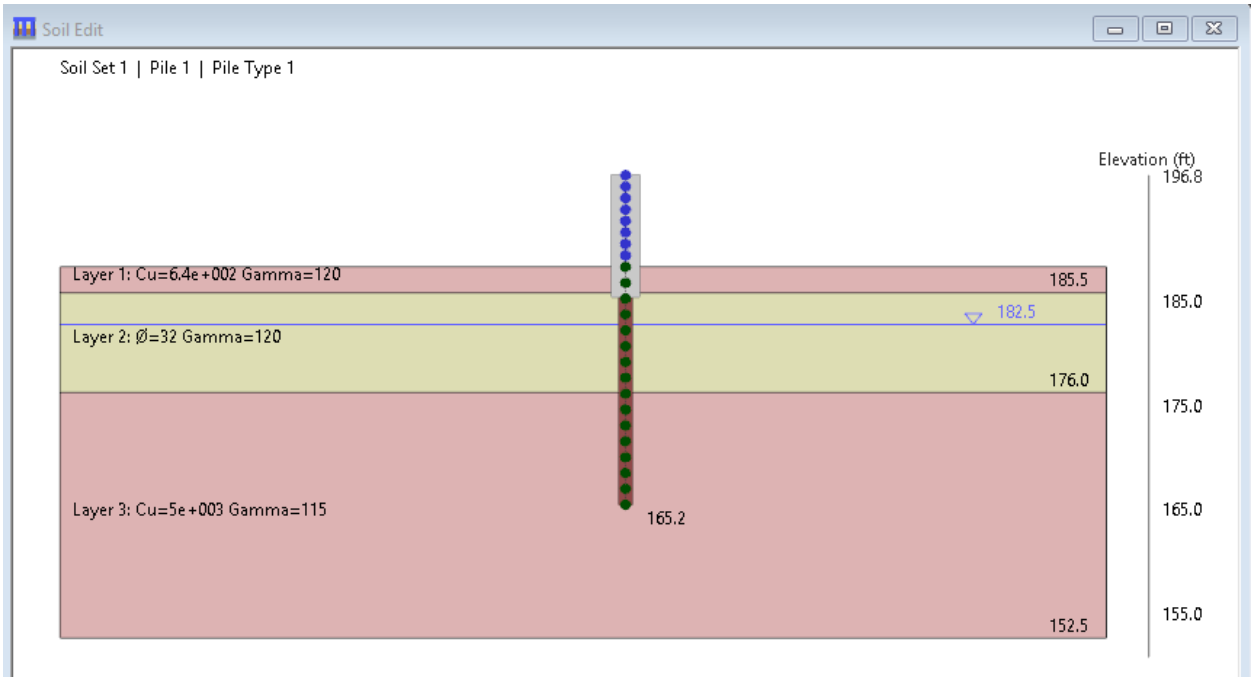

Figure 6-5 – Soil Profile and Elevations for Bent 2

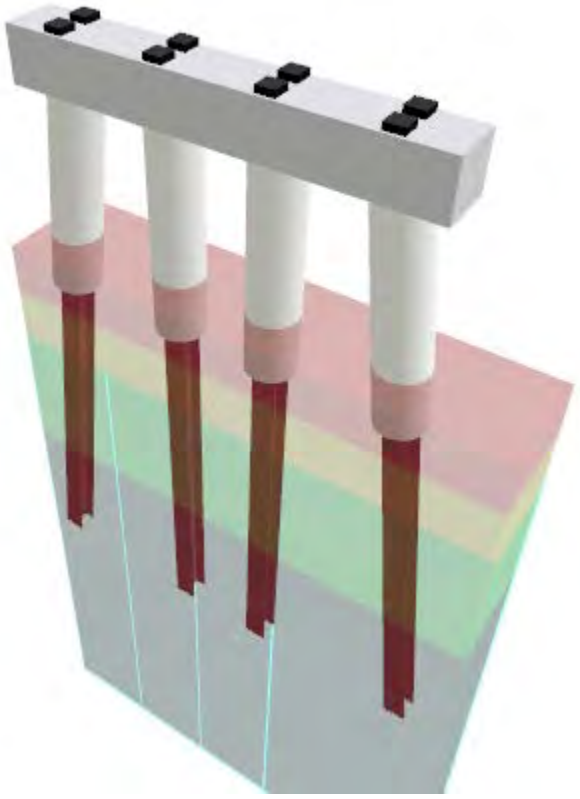

Figure 6-6 – 3-D View of Bent 2 in FB-MultiPier

Once the bent geometry and soil properties were input, FBMP automatically generates soil resistance plots for each layer and pile segment. Figure 6-7 is an example of the output for a P-y curve. For every pile, every soil layer, and both pile segments if evaluating the encased piles, a P-y curve was generated.

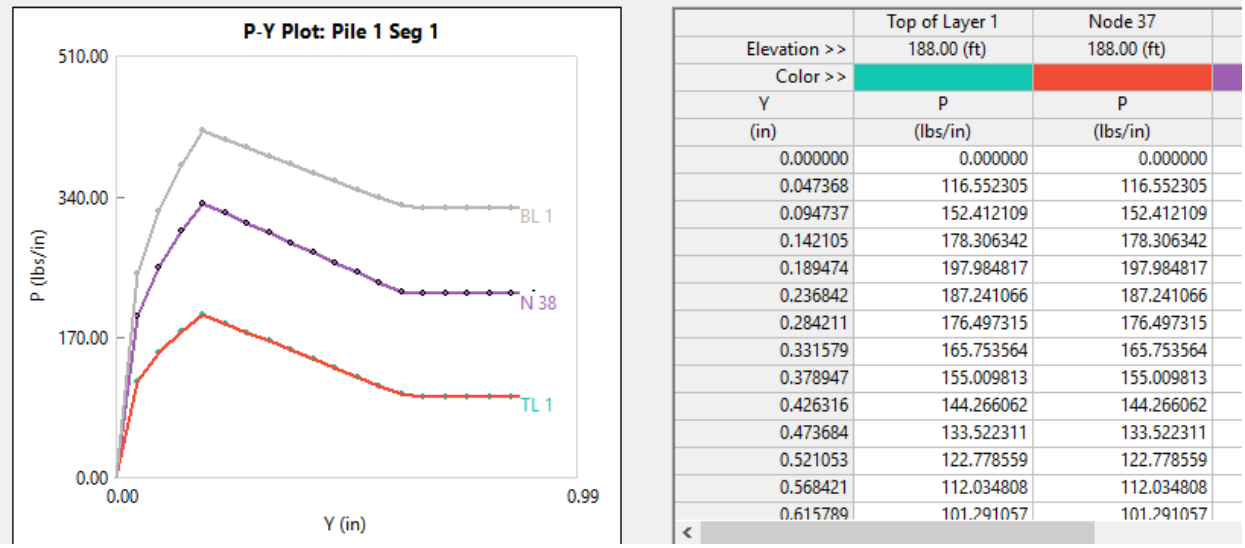

	Top of Layer 1	Node 37
Elevation >>	188.00 (ft)	188.00 (ft)
Color >>		
Y	P	P
(in)	(lbs/in)	(lbs/in)
0.000000	0.000000	0.000000
0.047368	116.552305	116.552305
0.094737	152.412109	152.412109
0.142105	178.306342	178.306342
0.189474	197.984817	197.984817
0.236842	187.241066	187.241066
0.284211	176.497315	176.497315
0.331579	165.753564	165.753564
0.378947	155.009813	155.009813
0.426316	144.266062	144.266062
0.473684	133.522311	133.522311
0.521053	122.778559	122.778559
0.568421	112.034808	112.034808
0.615789	101.291057	101.291057

Figure 6-7 – P-y Curve for the Nodes along the Encased Portion of the Pile within Layer 1

It was assumed that the soil-structure response remained linear under vehicular braking forces; therefore, to compute the spring stiffness all that was required was the slope of the linear portion of the P-y curve and the tributary length pile for each node. Table 6-2 gives an example of how the curve data was used to generate the springs. This procedure was followed for every bent, then the piles in the SAP model were discretized so that the elevations of the springs corresponded in both models and the springs defined accordingly.

Table 6-2 – Soil Layer 1 Spring Stiffness Computed from P-y Curve Data

Soil Layer 1 (Encased)									
	Top of Layer 1	Trib. Length (ft)	Elastic Region Slope for TL1	Node 38	Trib. Length (ft)	Elastic Region Slope for N38	Bottom of Layer 1	Trib. Length (ft)	Elastic Region Slope for BL1
Elevation	188.00 (ft)	0.765		186.47 (ft)	1.25		185.50 (ft)	0.485	
Y	P	P*TL		P	P*TL		P	P*TL	
(in)	(lbs/in)	(lbs)	(lbs/in)	(lbs/in)	(lbs)	(lbs/in)	(lbs/in)	(lbs)	(lbs/in)
0.047368	116.552305	1069.95	22588	196.493178	2947.40	62223	246.890714	1436.90	30335

To confirm the accuracy of these calculations, a static analysis was performed in FBMP. A load of 10 kips was applied to the center of the bent cap in the y-direction and lateral pile displacement results were generated. Figure 6-8 shows the discretized wire-frame version of bent 2 with the load applied and Figure 6-9 is a representation of the lateral deflection results obtained.

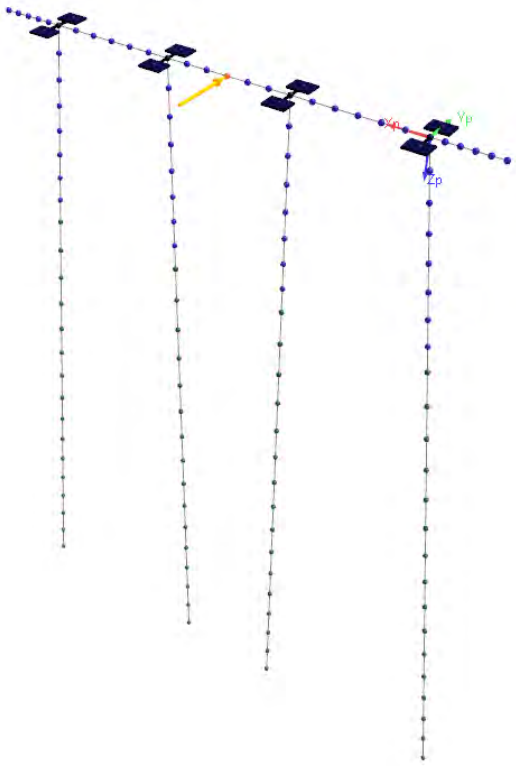

Figure 6-8 – FBMP Model of Bent 2 with 10 kips Applied to the Bent Cap

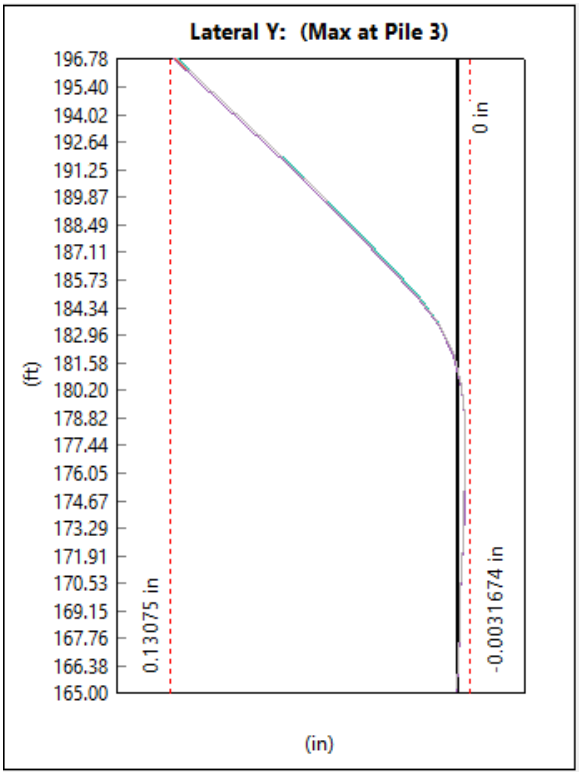

Figure 6-9 – Lateral Pile Displacements for all Piles in Bent 2

After this was completed in FBMP, the behavior of the springs needed to be checked in SAP. Each bent was isolated from the rest of the bridge in its own model and 10 kips was applied to the center of bent cap, in the same position as in FBMP. The displacement results from both models were graphed on the same plot to determine correlation. Figure 6-10 is Bent 2 with the springs added along the pile length and the 10 kip load applied to the bent cap. Figure 6-11 shows the displacements along the length of the left-most pile for both models and how well they match one another.

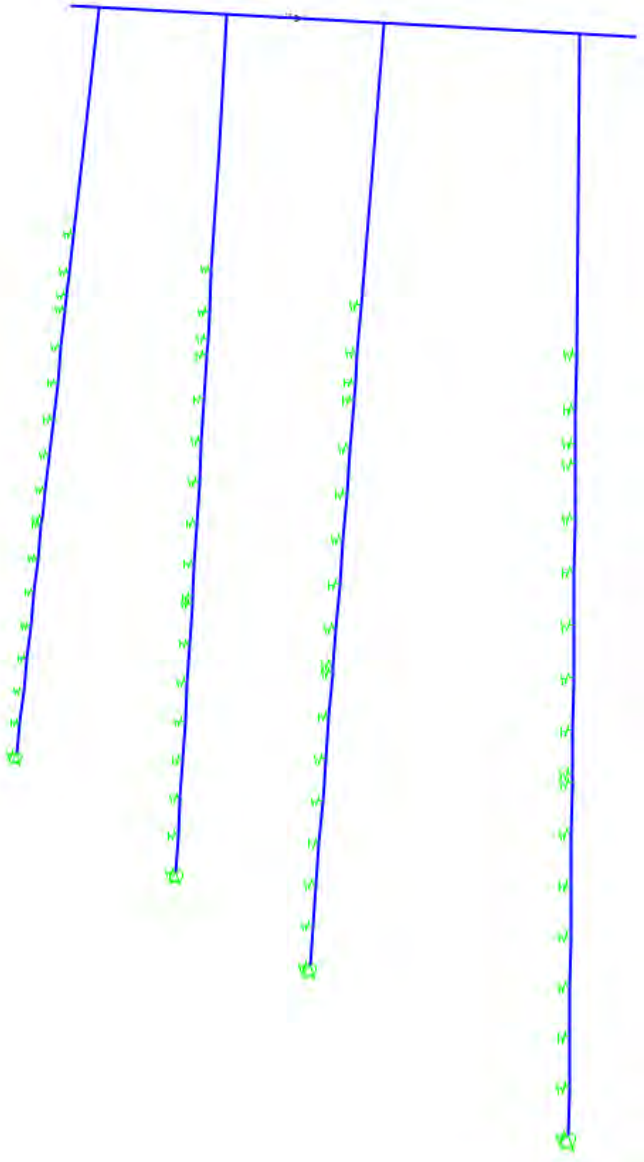

Figure 6-10 – Individual Model of Bent 2 for Static Loading Deflection Analysis

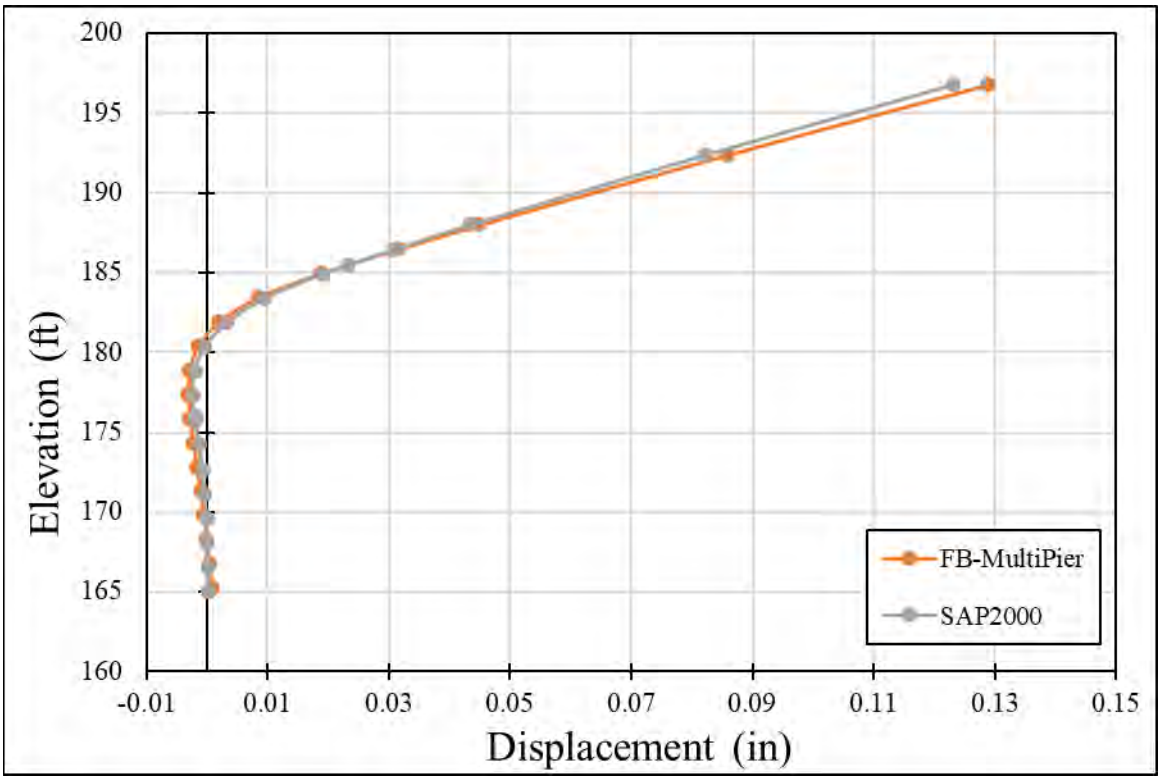

Figure 6-11 – Deflection Comparisons for Pile 1 of Bent 2

This verification was done for all 4 piles in all 5 bents, the results of which can be found in Appendix A. Pile 1 refers to the outer left pile, pile 2 is the middle-left pile, pile 3 is the right-middle pile, and pile 4 is the outer right pile.

6.3.2 Calibration of the Bearing Pad Stiffnesses

After comparing initial results from the static tests in the model, the stiffnesses of the bearing pads required adjustment to better represent what was happening in the field tests. When comparing joint displacements to field data, it was shown that the actual fixity of all the girders was closer to a version of expansion definitions 1 and 2, depending on interior or exterior girders, as defined in Section 6.2.1.3 for all joints rather than some being fixed and some being expansion as designated in the plans. The displacements of the girders relative to the bent caps were not matching expected values, and this was improved when all joints were changed to the appropriate expansion stiffness. This is a better representation of what was observed in the field. While in the field for testing it was realized that the nuts on the bolts were not tightened at either

the fixed or expansion ends of any of the spans. Without engaging the bolt through a snug tight nut, movement of the clip and ultimately the girder is permitted.

To determine the appropriate longitudinal stiffness to define all of the bearing pads, a series of different versions of the model where only the pad stiffness was changed were run so that the errors could be analyzed and reduced. By running models that varied the longitudinal stiffness from 23.5 k/in to 50 k/in, it was determined that 45 k/in produces the least sum of the squared error (SSE) value for span displacements. Varying the stiffness from 23.5 k/in to 50 k/in was done after 50 k/in was chosen to see how displacements compared to 23.5 k/in. A boundary needed to be created within which a reasonable amount of stiffnesses could be modeled to reduce error but be too arduous of a process to obtain a stiffness value for all the bearing pads. Table 6-3 includes the SSE for each stiffness value and span. Figure 6-12 illustrates how the SSE was relatively insensitive to pad stiffness for values between approximately 42 k/in and 50 k/in. Therefore, any value in this range is acceptable and should not alter the displacement or acceleration results significantly.

Table 6-3 – Longitudinal Stiffnesses and the Corresponding Sum of the Error Squared

Stiffness	**23.5 k/in**	**30 k/in**	**35 k/in**	**38 k/in**	**40 k/in**	**42 k/in**	**45 k/in**	**50 k/in**
SSE	0.01300	0.00681	0.00495	0.00439	0.00416	0.00402	0.00392	0.00397

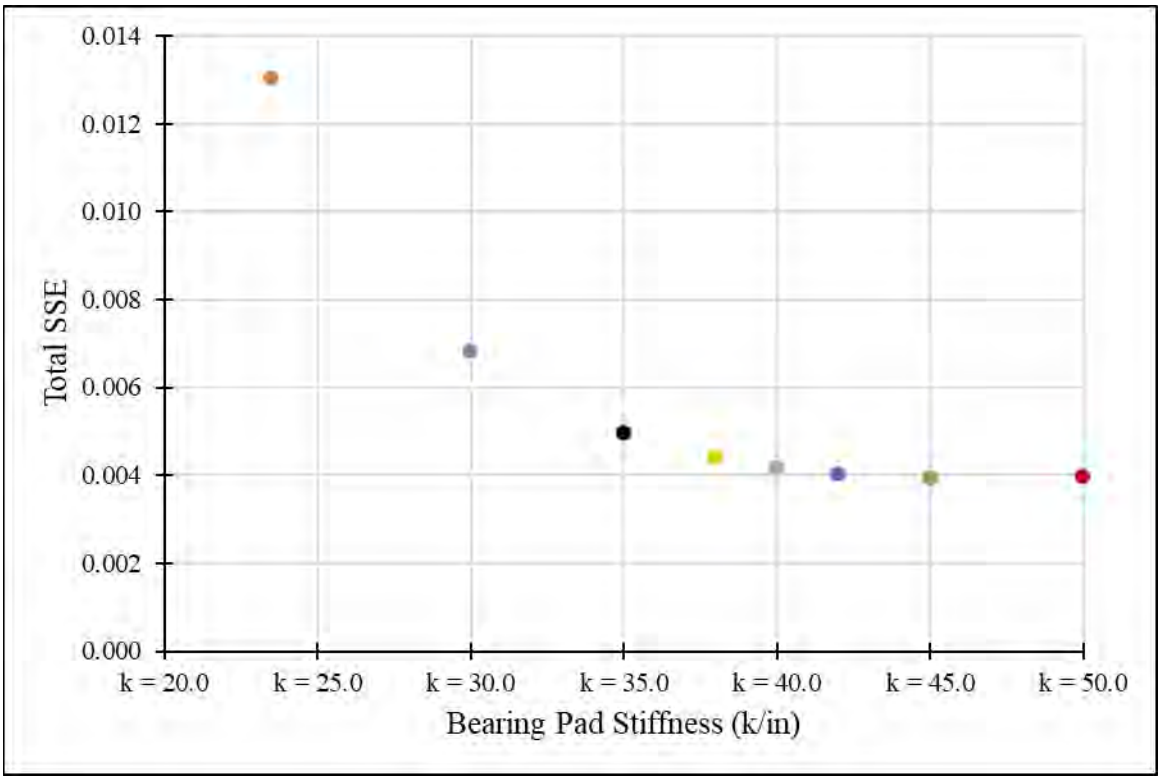

Figure 6-12 – Trend of Stiffness Values and When Reducing Error

After these adjustments were made, the final image of the model is as shown in Figure 6-13. The elements protruding from spans 2, 3 and 5 are weightless, rigid elements only intended to provide the necessary vertical offset for the mass of the truck when applied to the bridge for the dynamic analyses. They are 6 ft tall, an approximation of the height of the center of gravity of the truck and the height to offset the truck center of gravity in the LRFD Specification Section 3.5 (AASHTO, 2017).

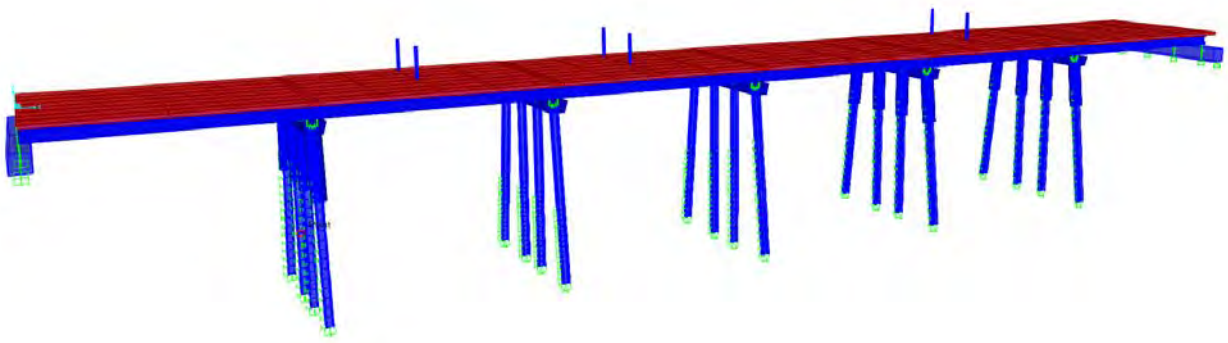

Figure 6-13 – Analytical Model After Imported to SAP and Modified

6.3.3 Static Analysis

After the field data was processed, it still required downsampling. From the downsampled data, two graphs were produced for each span's test as shown in Figure 6-14 and Figure 6-15. Similar graphs for spans 2-6 can be found in Appendix B. In Figure 6-14, the black line is the force recorded in the load cell over time. The colored lines are the displacement of the girder end relative to the bent cap, this is what extension or contraction was measured by the wire potentiometer over the same time period as the load cell. The labeling of components in the legend for both graphs are as follows

- AB-1 – Abutment 1
- B-2SB – South Side of Bent 2
- B-2NB – North Side of Bent 2
- B-3SB – South Side of Bent 3
- B-3NB – North Side of Bent 3
- B-4SB – South Side of Bent 4
- B-4NB – North Side of Bent 4
- B-5SB – South Side of Bent 5
- B-5NB – North Side of Bent 5
- B-6SB – South Side of Bent 6
- B-6NB –North Side of Bent 6
- AB-7 – Abutment 7

Figure 6-15 illustrates how the bridge components displaced during loading, increasing tension in the cable connected to the load truck, and during unloading, relieving of the tension in the cable. Both loading and unloading result in linear displacements, but the slope of the two differ. For every static test, the bents or abutment supporting the span that was loaded always displaced the most.

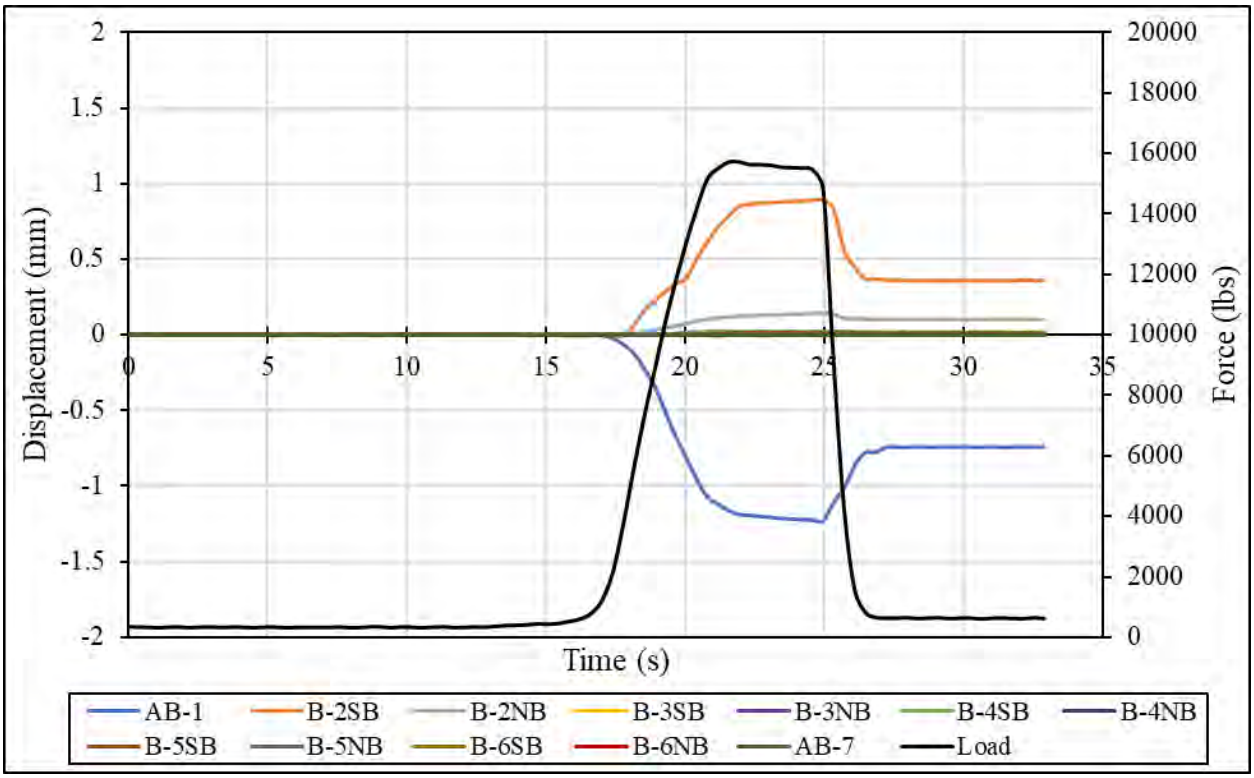

Figure 6-14 – Span 1 Displacement and Load vs Time for Static Pull Test

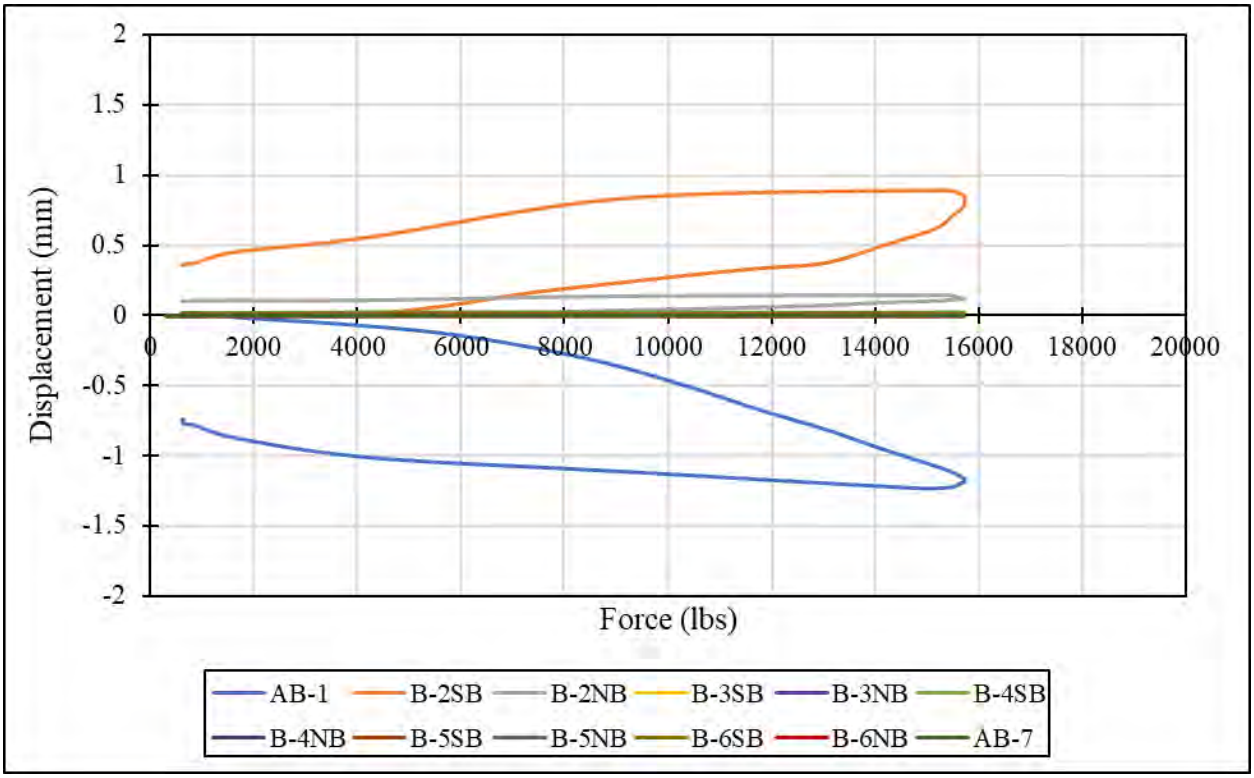

Figure 6-15 – Span 1 Displacements vs Applied Load

After reviewing the graphs, every test achieved at least 10 kips of tension with clear displacement results, based off this it was decided this would be a reasonable load to apply to the analytical model for comparisons.

Table 6-4 is the displacement data for Span 1 at the measured value closest to 10 kips and this data was compared to the model displacements under 10 kips of force. The data for Spans 2-5 can also be found in Appendix B. The change in force is listed also because the wire potentiometers were zeroed out between every test but the load cell was not. To account for this, the initial force recorded in the load cell was subtracted from all of the force values to get a change in force.

Table 6-4 – Wire Pot Readings and Displacements Relative to Abutment 1 for Span 1

At 10400 lbs (ΔF = 10054 lbs) applied to Span 1			
Data From Field Tests			
	Displacement of Girder End Relative to Cap (in)	Displacement Relative to AB1 (in)	
A1	-0.0199	delta_S1	-0.0199
B2S1	0.0113	delta_B2	-0.0086
B2S2	0.0019	delta_S2	-0.0068
B3S2	0.0000	delta_B3	-0.0068
B3S3	0.0001	delta_S3	-0.0067
B4S3	0.0002	delta_B4	-0.0065
B4S4	0.0000	delta_S4	-0.0065
B5S4	0.0000	delta_B5	-0.0066
B5S5	0.0000	delta_S5	-0.0066
B6S5	0.0000	delta_B6	-0.0066
B6S6	0.0000	delta_S6	-0.0067
A7	0.0000	delta_AB7	-0.0067

The wire potentiometers and accelerometers were along the left-center girder, so in the model the displacements recorded were from along the same girder-line. Additionally, the wire potentiometers were connected to an angle on the bottom of the girder and extended to a hook attached to the pedestal as shown in Figure 6-16, this had to be considered when evaluating results in the SAP model.

Figure 6-16 – Standard Wire Pot Set-Up

To account for this in the SAP model, the difference between the displacement at the top of the bearing pad link and the bottom of the bearing pad link was taken to replicate the field conditions. It was assumed there was no significant expansion or contraction of the girders when obtaining these displacement results from the model. The length of the link defined as the bearing pad was 0.75” to create the same displacement measurements in the model. Table 6-5 is representative of how the results were recorded and processed to produce values that were comparable to what was measured.

Table 6-5 – Span 1 SAP Results Processed to be Comparable to the Field Data

At 10 kips Statically Applied to Center of Span 1 in SAP Model									
Results from SAP2000 Along Girder Line 2 - All Bearing Pads 0.75"									
	Location	Joint	Global Displacement (in)	Global Rotation (rad)	Displacement between girder & support (in)	Displacement Relative to AB1 (in)		Location of Measurement	Total Displacement Relative to
AB1 (E)	Girder	135	-0.0399	-0.000014	-0.0399	delta_S1	-0.0399	$\Delta S1_a$	-0.0399
	Support	29	0.0000	0.000000				-	-
B2 SP1 (F)	Girder	151	-0.0403	0.000001	0.0158	delta_B2	-0.0241	$\Delta S1_b$	-0.0403
	Support	49	-0.0245	-0.000143				$\Delta B2_a$	-0.0245
B2 SP2 (E)	Girder	153	-0.0197	0.000006	0.0048	delta_S2	-0.0193	$\Delta S2_a$	-0.0197
	Support	48	-0.0245	-0.000143				$\Delta B2_b$	-0.0245
B3 SP2 (F)	Girder	191	-0.0195	0.000000	0.0049	delta_B3	-0.0144	$\Delta S2_b$	-0.0195
	Support	254	-0.0147	-0.000063				$\Delta B3_a$	-0.0147
B3 SP3 (E)	Girder	193	-0.0113	0.000004	0.0034	delta_S3	-0.0110	$\Delta S3_a$	-0.0113
	Support	56	-0.0147	-0.000063				$\Delta B3_b$	-0.0147
B4 SP3 (F)	Girder	211	-0.0111	-0.000001	0.0034	delta_B4	-0.0076	$\Delta S3_b$	-0.0111
	Support	260	-0.0077	-0.000039				$\Delta B4_a$	-0.0077
B4 SP4 (E)	Girder	217	-0.0054	0.000002	0.0023	delta_S4	-0.0053	$\Delta S4_a$	-0.0054
	Support	259	-0.0077	-0.000039				$\Delta B4_b$	-0.0077
B5 SP4 (F)	Girder	235	-0.0053	-0.000001	0.0023	delta_B5	-0.0031	$\Delta S4_b$	-0.0053
	Support	273	-0.0031	-0.000019				$\Delta B5_a$	-0.0031
B5 SP5 (E)	Girder	241	-0.0021	0.000001	0.0010	delta_S5	-0.0021	$\Delta S5_a$	-0.0021
	Support	299	-0.0031	-0.000019				$\Delta B5_b$	-0.0031
B6 SP5 (F)	Girder	235-1	-0.0020	0.000000	0.0010	delta_B6	-0.0011	$\Delta S5_b$	-0.0020
	Support	334	-0.0011	-0.000007				$\Delta B6_a$	-0.0011
B6 SP6 (F)	Girder	241-1	-0.0005	0.000000	0.0005	delta_S6	-0.0006	$\Delta S6_a$	-0.0005
	Support	332	-0.0011	-0.000007				$\Delta B6_b$	-0.0011
AB7 (E)	Girder	143	-0.0005	0.000000	0.0005	delta_AB7	-0.0001	$\Delta S6_b$	-0.0005
	Support	17	0.0000	0.000000				$\Delta AB7_a$	0.0000

The 10 kip load was applied in the center of the span, pointing in the same direction as the truck was being pulled as shown in Figure 6-17, where 10 kips is applied to Span 1. A static load case for each span was created so that 10 kips could be applied to each span and analyzed in the model.

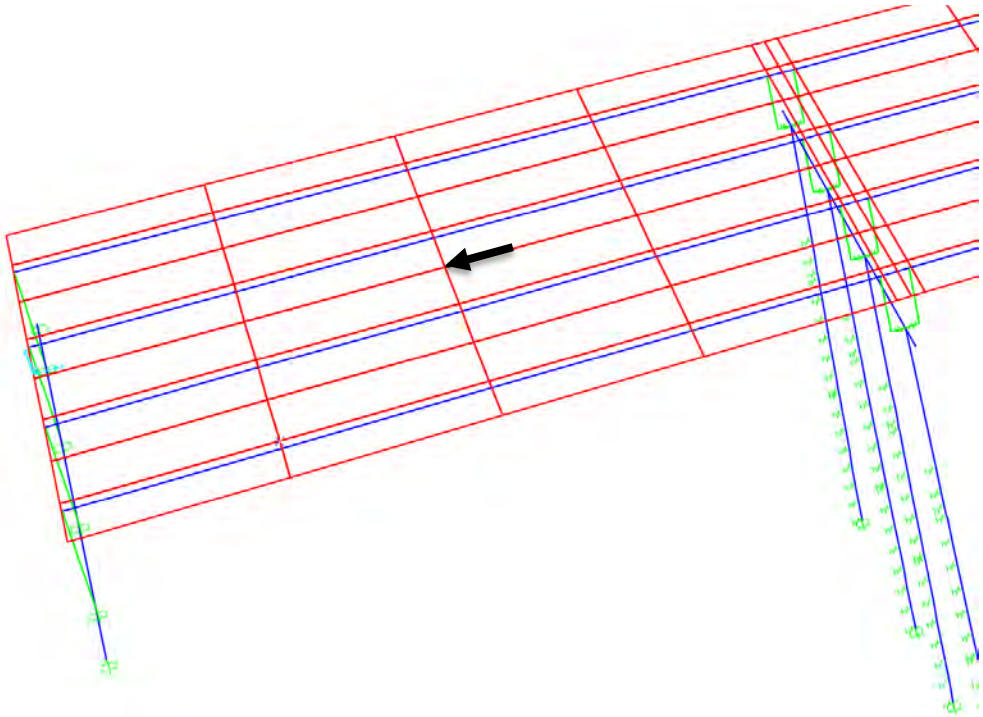

Figure 6-17 – SAP Model with 10 kip Static Load Applied to Span 1

6.3.4 Dynamic Analysis

To model the dynamic tests, the acceleration data from the field was most important. For each test, the acceleration in the longitudinal direction from the inertial measurement unit was used to obtain the braking maneuver profile. Figure 6-18 shows the IMU data from the tests that were deemed best. The designation of best was qualitative and meant: the truck approached the bridge at a constant speed and maintained this speed until reaching the span being tested, once fully in the span, the brakes were applied and a controlled stop was completed within the same span. For modeling purposes, each test was evaluated and its own braking force function defined to best match its IMU data. Figure 6-18 shows how similar the braking maneuvers were from test to test, but minor changes in intensity, build up, constant deceleration duration, and decline to zero acceleration impacted the results significantly so a single function could not be defined. In this graph, time zero is the instant that the brakes were applied so that this could be defined as a time-history analysis ramp function in SAP. On the graph, the C or R designates center or right of the

span, the first number is the span stopped on and the second number is the trial number on that span.

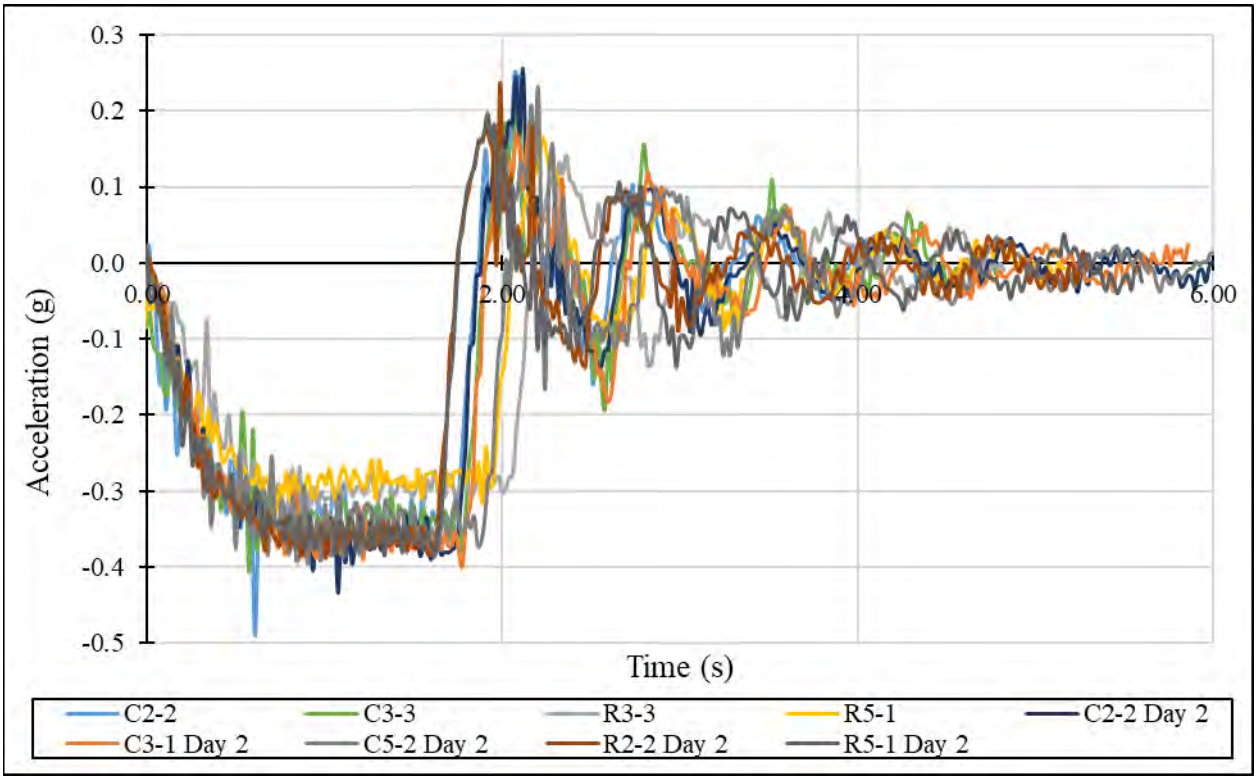

Figure 6-18 – IMU Acceleration Data for the Longitudinal Direction of the Load Truck

When comparing the measured values to the decelerations rates presented in Section 2.10, the correlation is good. Loaded single-unit trucks averaged 0.39g, unloaded truck tractors and single-unit trucks averaged 0.36g, and loaded truck tractors with an unbraked control trailer averaged 0.34g. The average deceleration rate for the center braking tests was 0.35g and the right-side braking tests averaged 0.30g. With the data matching the information in the literature reviewed well, this reinforced the foundational idea of this thesis that the amount of longitudinal force getting transmitted into the substructure during a braking force is dependent upon the friction between the road and tire interface. This frictional limitation results, ultimately, in the percentage of the truck weight that gets imparted on the bridge.

Figure 6-19 is a representation of how the different IMU data was defined in SAP. The test data and corresponding SAP ramp functions for every test can be found in Appendix C.

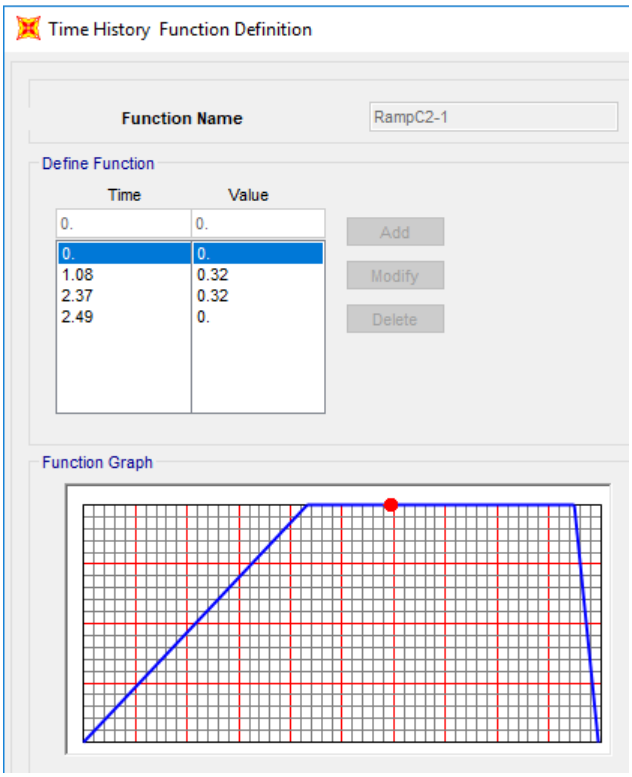

Figure 6-19 – SAP Ramp Function Defined for the Center of Span 2, Trial 1

After the ramp function was defined, it was added to the proper load case. Figure 6-20 shows the definition of the load case for the center of span 2 loading condition. Minor adjustments in rise time of the ramp resulted in changes in the results of the SAP acceleration data. By extending the ramp, there was more time before the oscillations began in the output data. Furthermore, modifying the maximum steady state deceleration resulted in changes to the magnitude of acceleration reported by the model.

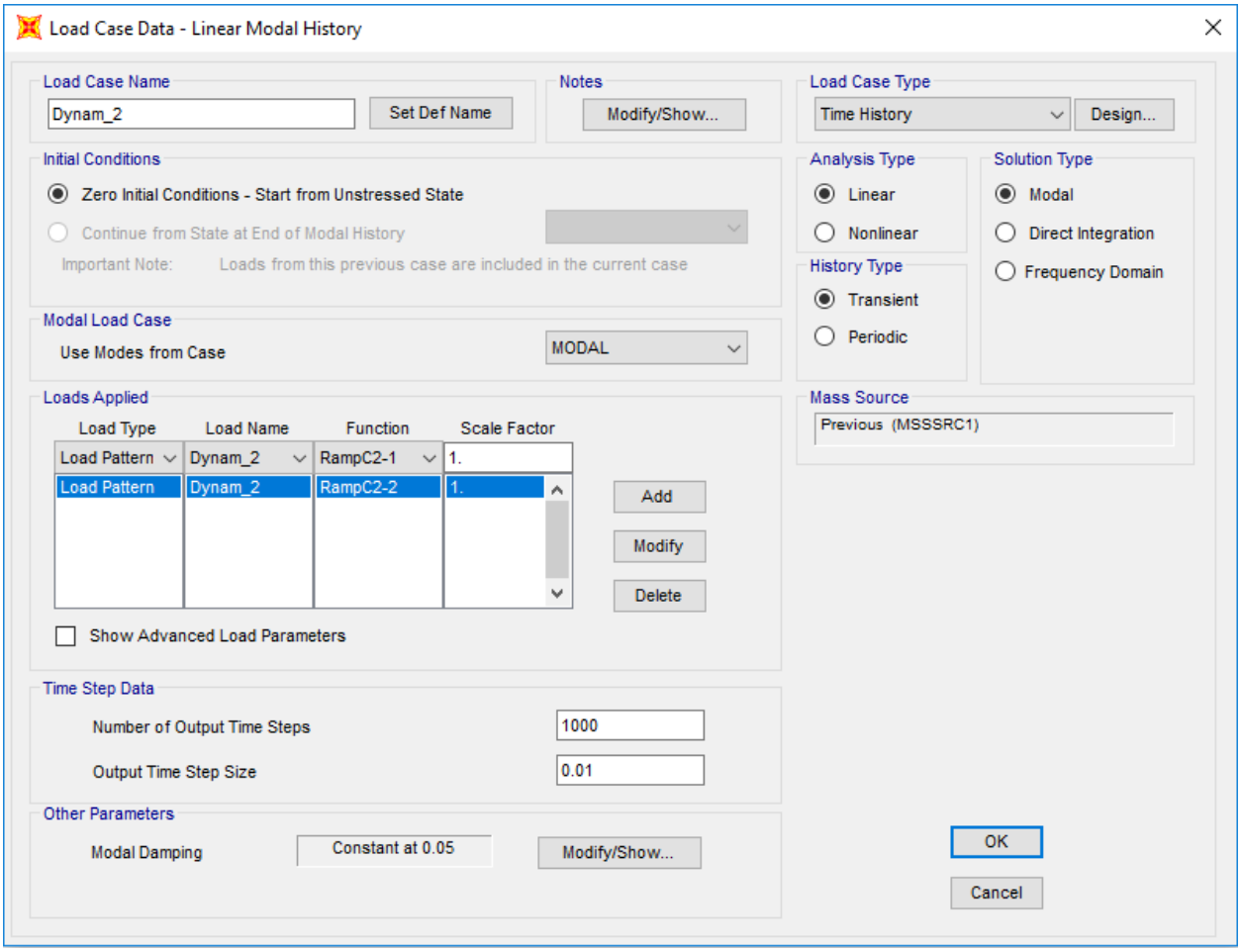

Figure 6-20 – Load Case Input for Span 2 Center Test

Every test condition had a load case defined similarly, the only change was what ramp function was used and where the load was applied on the bridge deck. For the cases where the truck stopped in the center of the span, 70.2 kips was applied in the center of the deck, the same location as the static load. When the truck stopped on the right side of the deck, the 70.2 kip force was positioned on the right side of the bridge, right above the exterior girder line. During the field testing, when the truck was braking on the right side the outside wheel was kept along the stripe painted on the bridge deck which was directly above the girder line.

In a dynamic analysis, mass has to be defined properly. The barriers on both sides of the bridge deck were not modeled, but their mass could not be neglected. From the geometry of the traffic barriers and the unit weight of reinforced concrete being 150 pounds per cubic foot, it was determined that the barriers weighed 305 lbs/ft each. This was discretized into point forces that were applied to joints in the model, in units of kips, in all three directions and SAP automatically

converted these weights to masses with units of k-s^2/in. The weight of the truck was applied to the rigid elements in terms of weight in all three directions as well. The truck weight was only applied to the span that was being tested and on the center or right side depending on the test. The rigid vertical element was required to elevate the mass to 6 ft off the bridge deck, 6 ft being an approximation of the center of the mass of the truck. Figure 6-21 displays the bridge with the point masses applied along both edges for the barrier rail mass and the mass of the truck applied to a single rigid element.

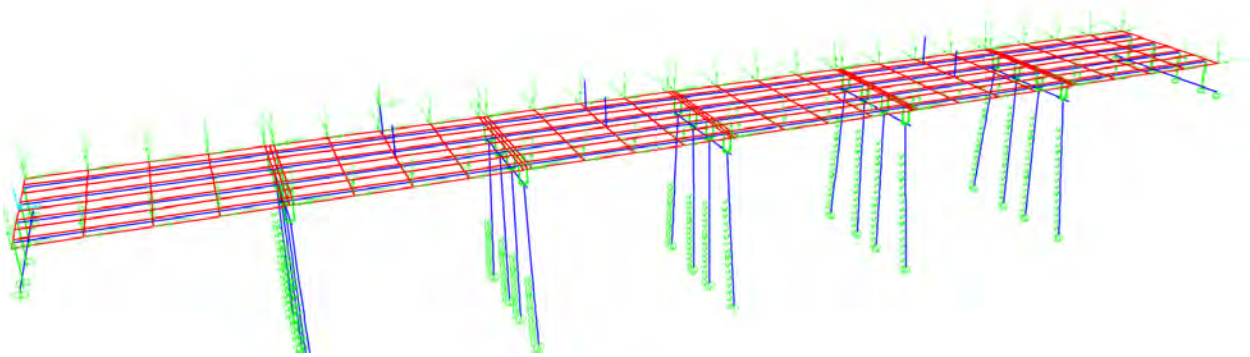

Figure 6-21 – Barrier Mass Applied along Full Length of Bridge and Truck Mass Applied to One Rigid Element

To ensure that enough of the modal mass was being included in the model, 20 modes were used. By using 20 modes, the total mass being captured in the X-direction was 93 percent. Beyond 20 modes, there was no significant increase in modal mass captured, therefore, no additional benefit to accuracy but there was an increase in computational duration. Throughout these 20 modes, 5 percent viscous damping was held constant. Additionally, due to limitations in the modeling software, certain time-dependent variables could not be modeled nor could they be measured in the field. Such variables include forms of hysteretic damping (friction, drag, material characteristics, etc.) instead of pure viscous damping like what is defined in SAP.

6.4 Static Test Results

6.4.1 Bridge Displacements Due to Static Loading

The results presented in this section illustrate the model displacements under 10 kips statically applied to each span compared to the displacements of the real bridge. This type of comparison allowed for the bearing pad stiffness to be refined. The stiffnesses played a major role in the displacement magnitudes. The error is minimized when a bearing pad stiffness of 45

k/in is utilized. The results of the analyses with this spring stiffness are satisfactory for this analysis given the amount of unknowns and assumptions behind the creation of the model. The benefit of the static tests was to aid in the calibration of the model. By removing the dynamic variables, it is easier to isolate components that need attention and modifications to improve behavior.

Figure 6-22 through Figure 6-27 present the relative displacements of the girder ends to the bent caps versus the displacements reported by SAP. Only the second trial from testing on span 5 was included in these results because it yielded more realistic data than the first test. The designations for the locations in the following figures are:

- A1 – relative displacement of Span 1 girder away from top of Abutment 1
- B2S1 – relative displacement of Span 1 girder away from top of Bent 2
- B2S2 – relative displacement of Span 2 girder away from top of Bent 2
- B3S2 – relative displacement of Span 2 girder away from top of Bent 3
- B3S3 – relative displacement of Span 3 girder away from top of Bent 3
- B4S3 – relative displacement of Span 3 girder away from top of Bent 4
- B4S4 – relative displacement of Span 4 girder away from top of Bent 4
- B5S4 – relative displacement of Span 4 girder away from top of Bent 5
- B5S5 – relative displacement of Span 5 girder away from top of Bent 5
- B6S5 – relative displacement of Span 5 girder away from top of Bent 6
- B6S6 – relative displacement of Span 6 girder away from top of Bent 6
- A7 – relative displacement of Span 6 girder away from top of Abutment 7

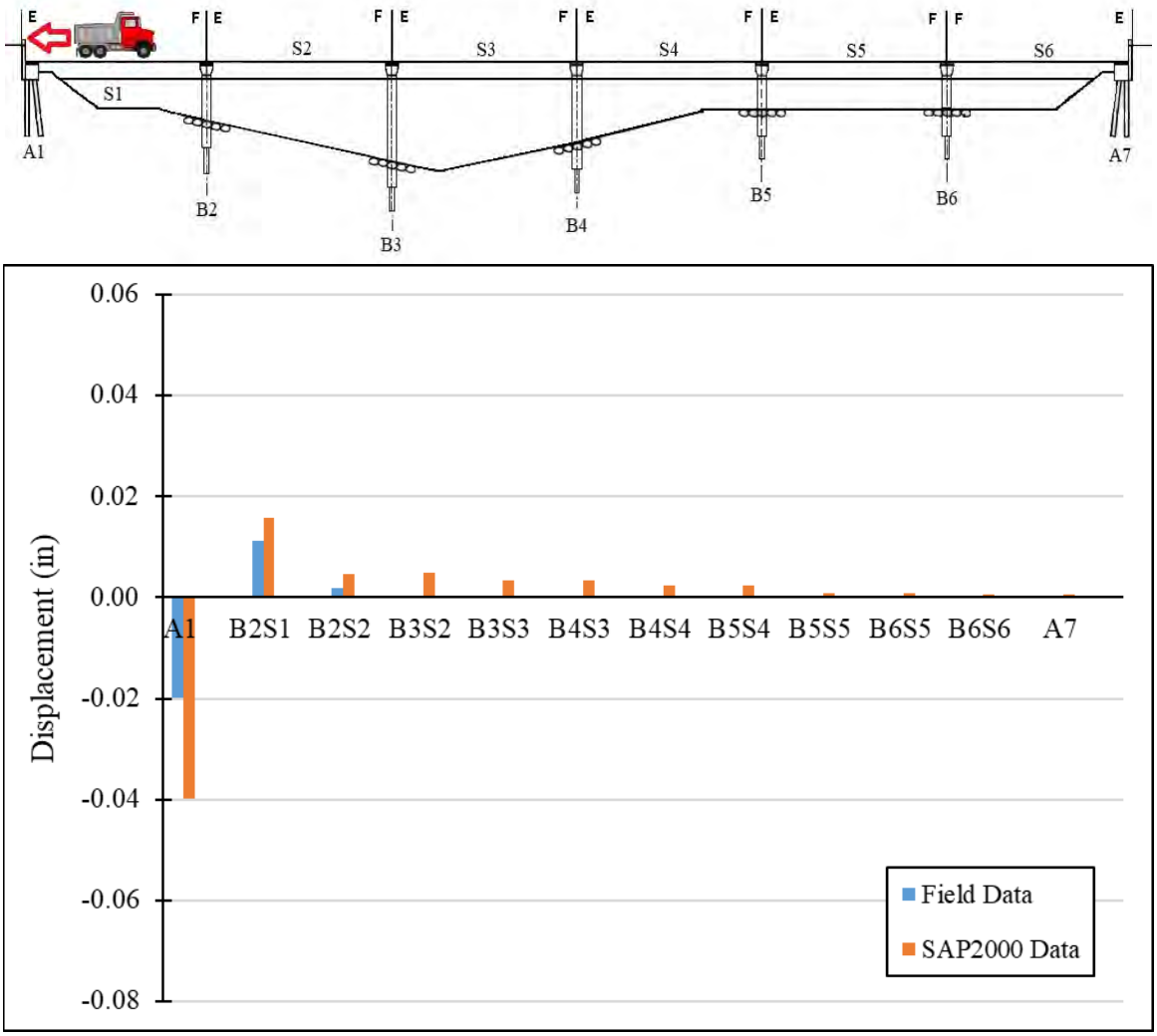

Figure 6-22 – Measured versus Model Displacements for Span 1 Static Loading

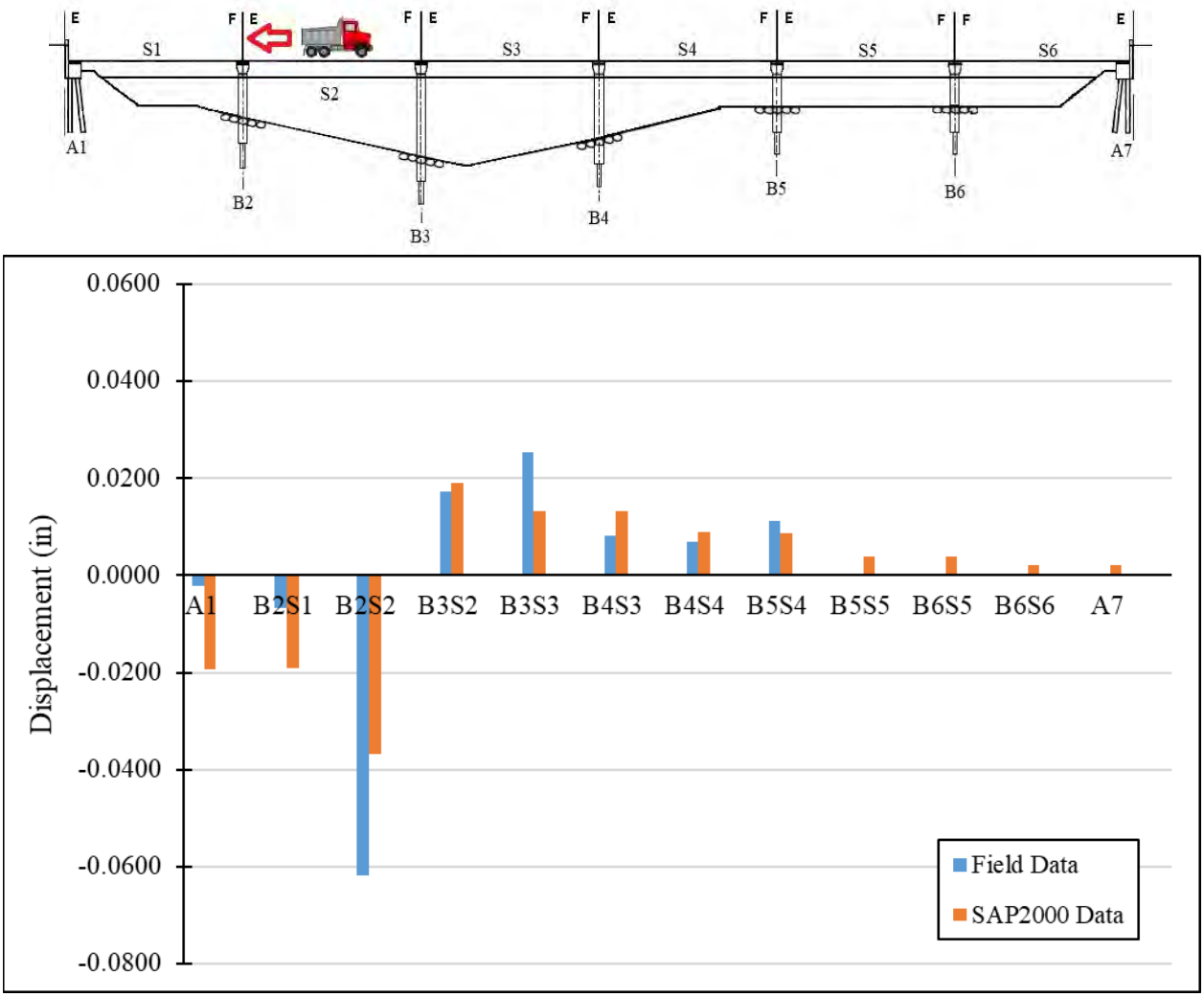

Figure 6-23 – Measured versus Model Displacements for Span 2 Static Loading

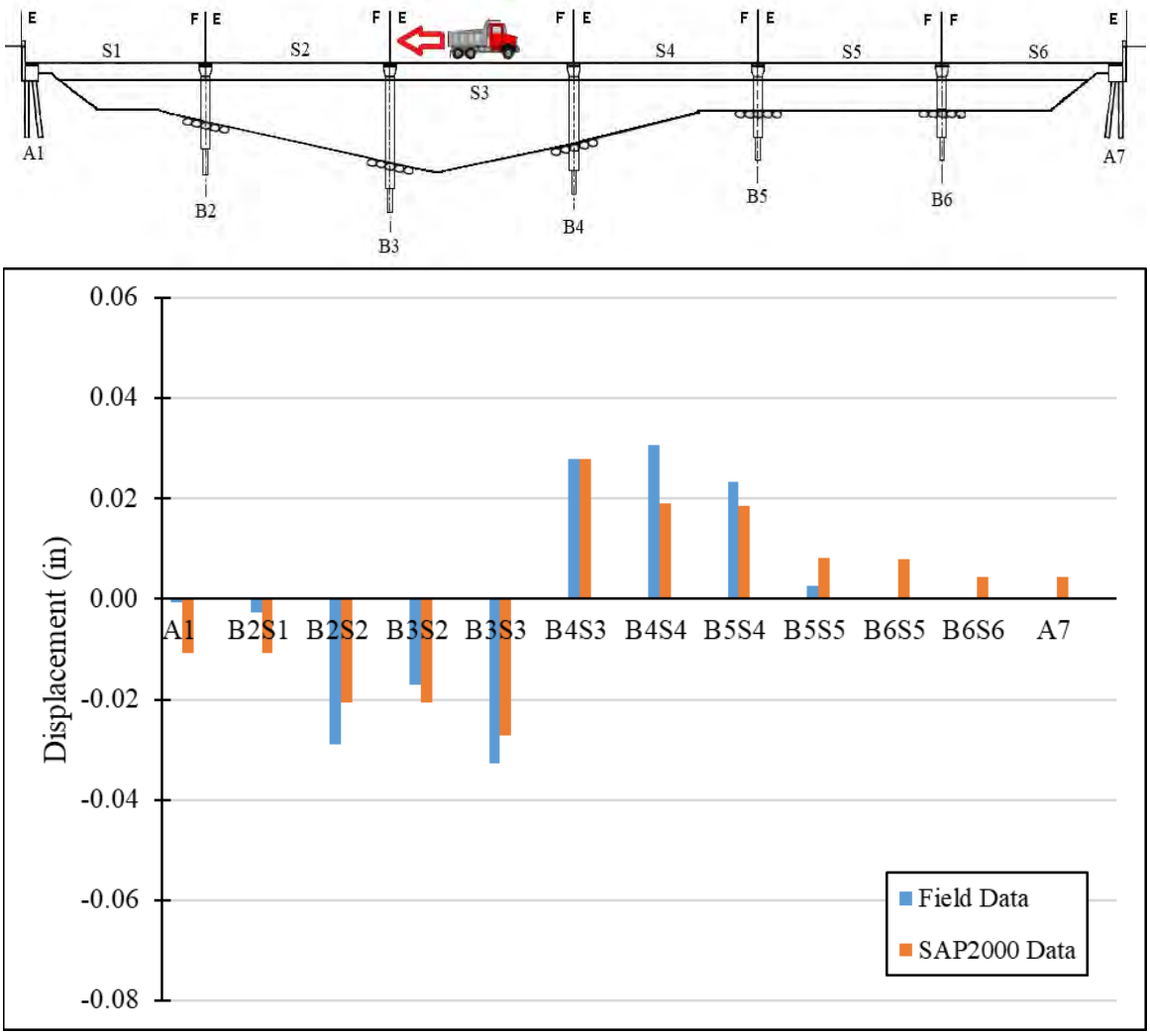

Figure 6-24 – Measured versus Model Displacements for Span 3 Static Loading

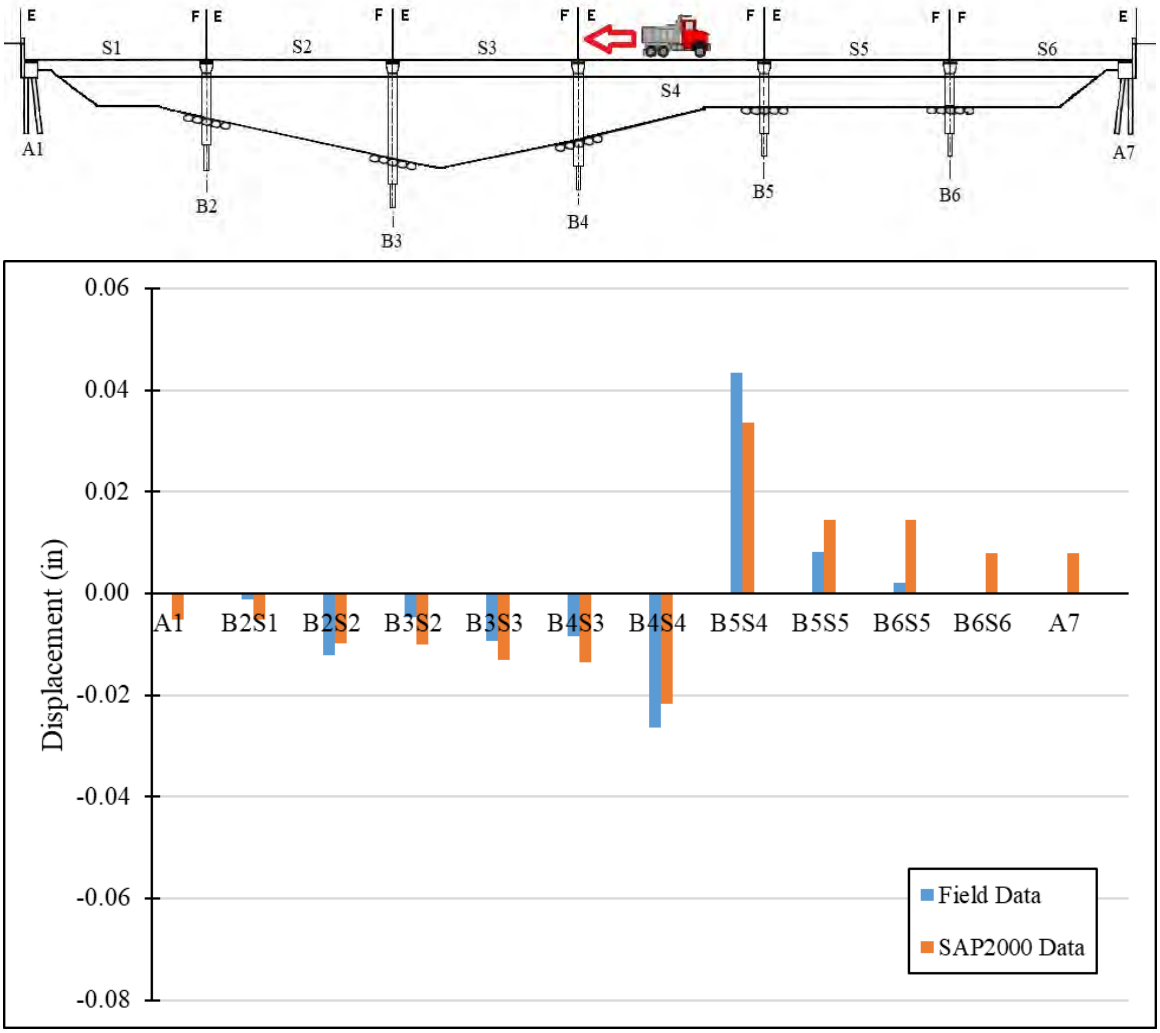

Figure 6-25 – Measured versus Model Displacements for Span 4 Static Loading

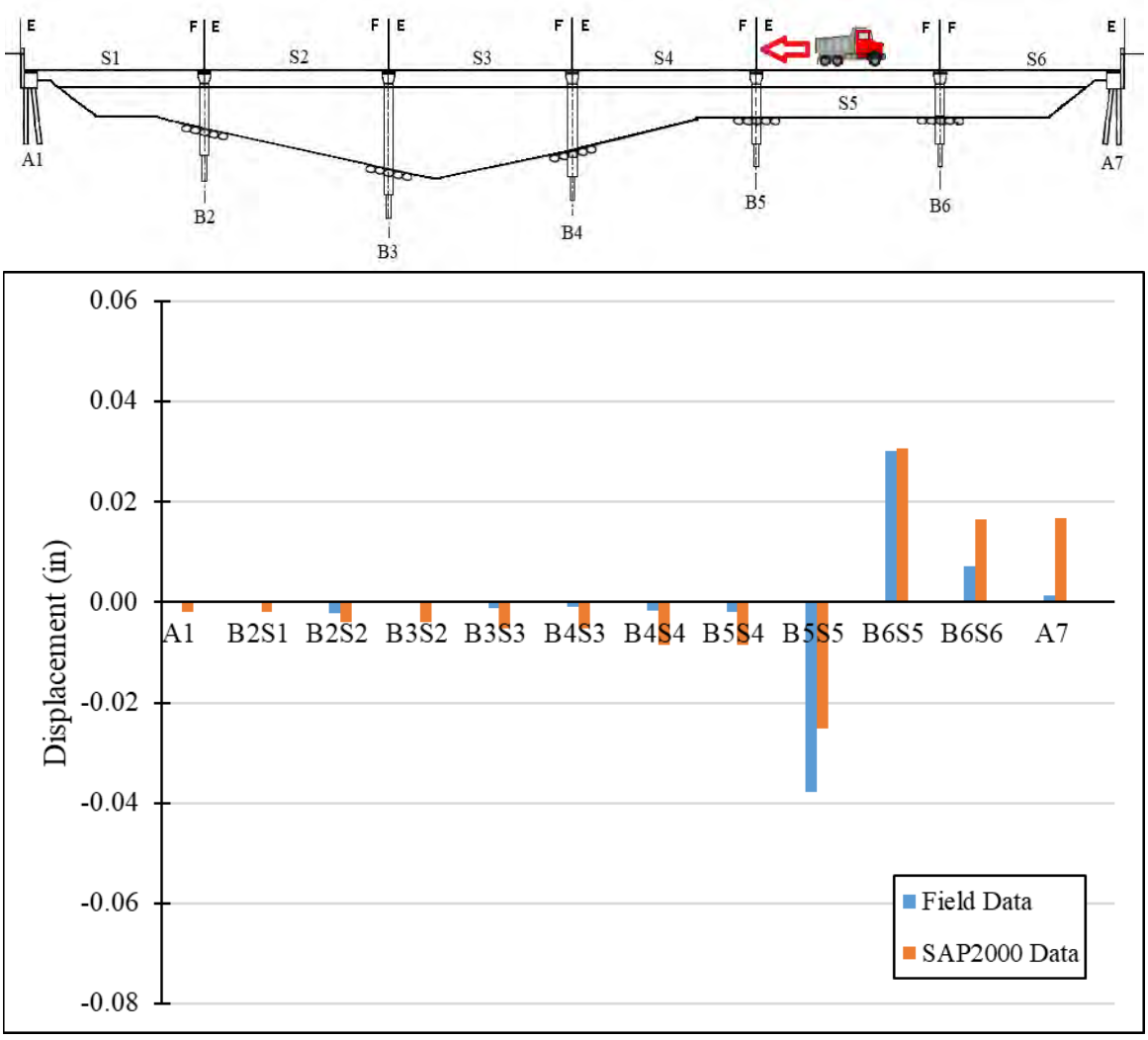

Figure 6-26 – Measured versus Model Displacements for Span 5 Static Loading

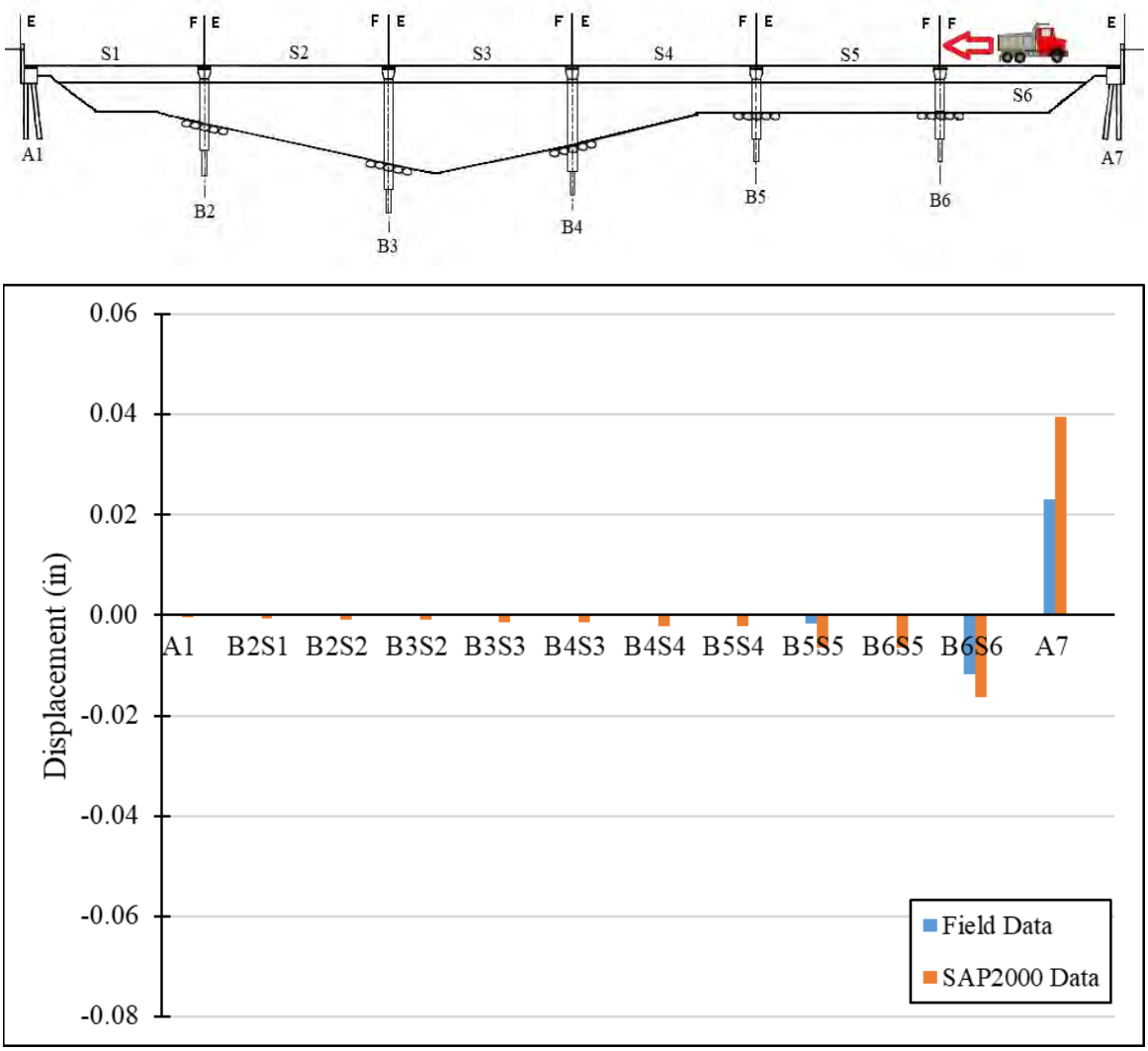

Figure 6-27 – Measured versus Model Displacements for Span 6 Static Loading

For every test case, the loaded span displaced the most. When the truck is positioned on Spans 3 and 4, the adjacent spans displace more than when the truck is on other spans. Bents 3 and 4 are the tallest and are the two bents that are not encased in concrete, making them less stiff relative to the other bents. For these reasons, more displacement of adjacent spans is expected when Spans 3 and 4 were tested.

Matching the displacements at the abutments proved difficult as well. At Abutments 1 and 7 the model reported more displacement then was recorded in the field. But, during other span loadings away from the ends of the bridge, many bents in the model reported smaller displacements then the field data. Therefore, a general determination of the bearings being

uniformly too stiff or too flexible was not possible. This is another reason for attempting to reduce the error in the displacement values mathematically since there is significant variability in the results where some locations are too flexible and some are too stiff.

6.4.2 Resulting Shear Force in Bridge Bents

Among the four piles within each bent, the shear force was fairly uniformly distributed in the model. This uniformity is an indication of the relative stiffness of the superstructure and the bent cap. Bent 4 was the only exception to this, but the pile heights within this bent varied due to the changing ground level in the field so this was expected as well. All other piles had uniform ground elevation for all four piles, preventing this variability in force distribution.

Since this uniformity in force among piles in a bent was occurring, only the percentage of shear force going into each substructure assembly (abutment or bent) are reported in Figures 6-28 through 6-33.

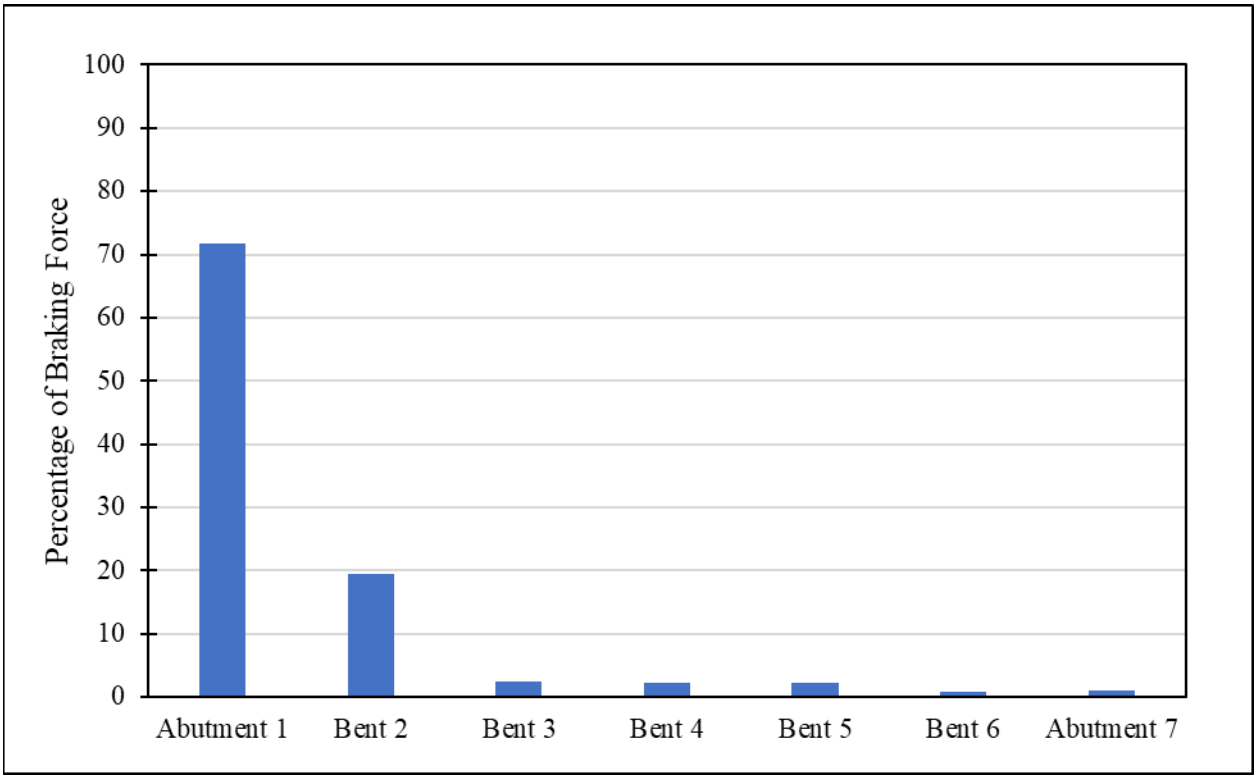

Figure 6-28 – Force Distribution in Substructure from Span 1 Loading

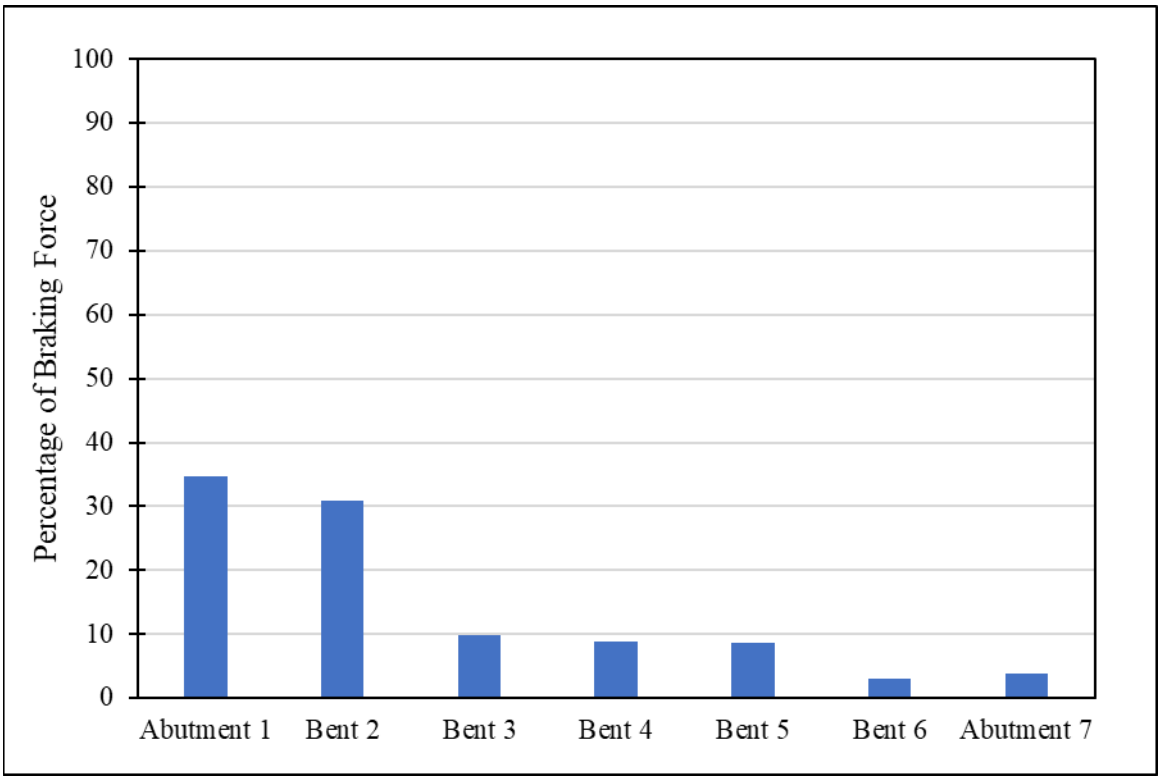

Figure 6-29 – Force Distribution in Substructure from Span 2 Loading

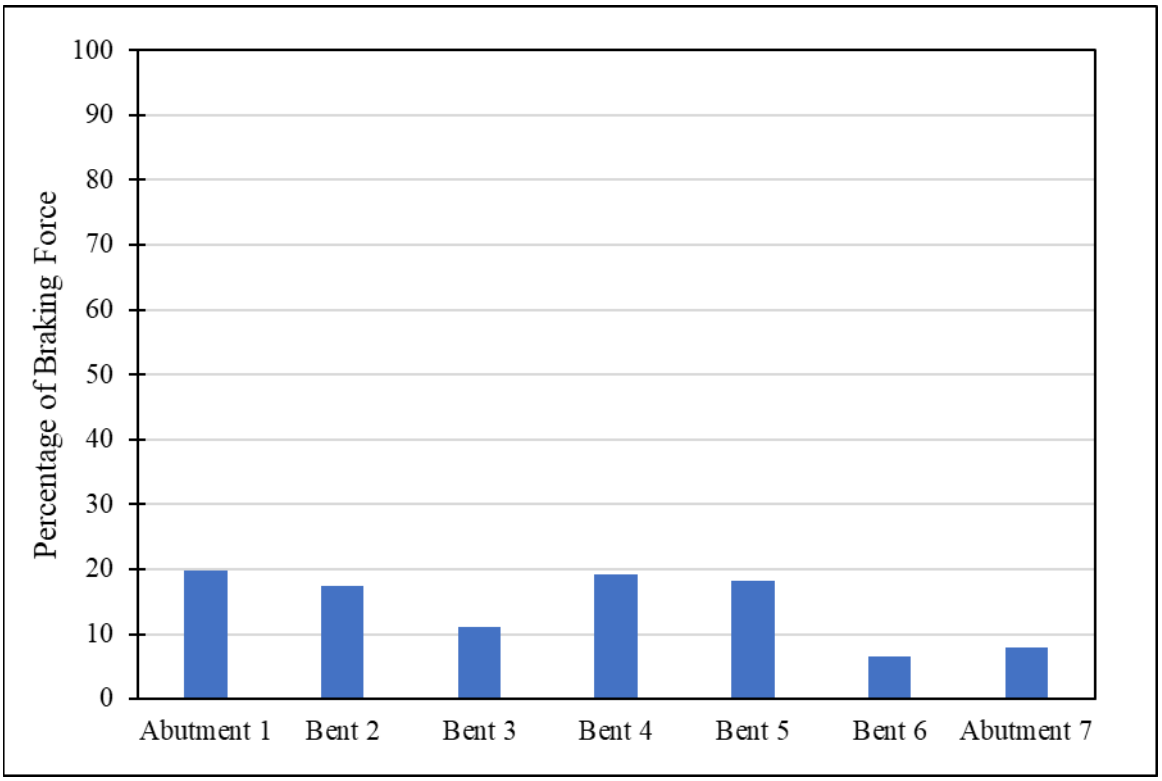

Figure 6-30 – Force Distribution in Substructure from Span 3 Loading

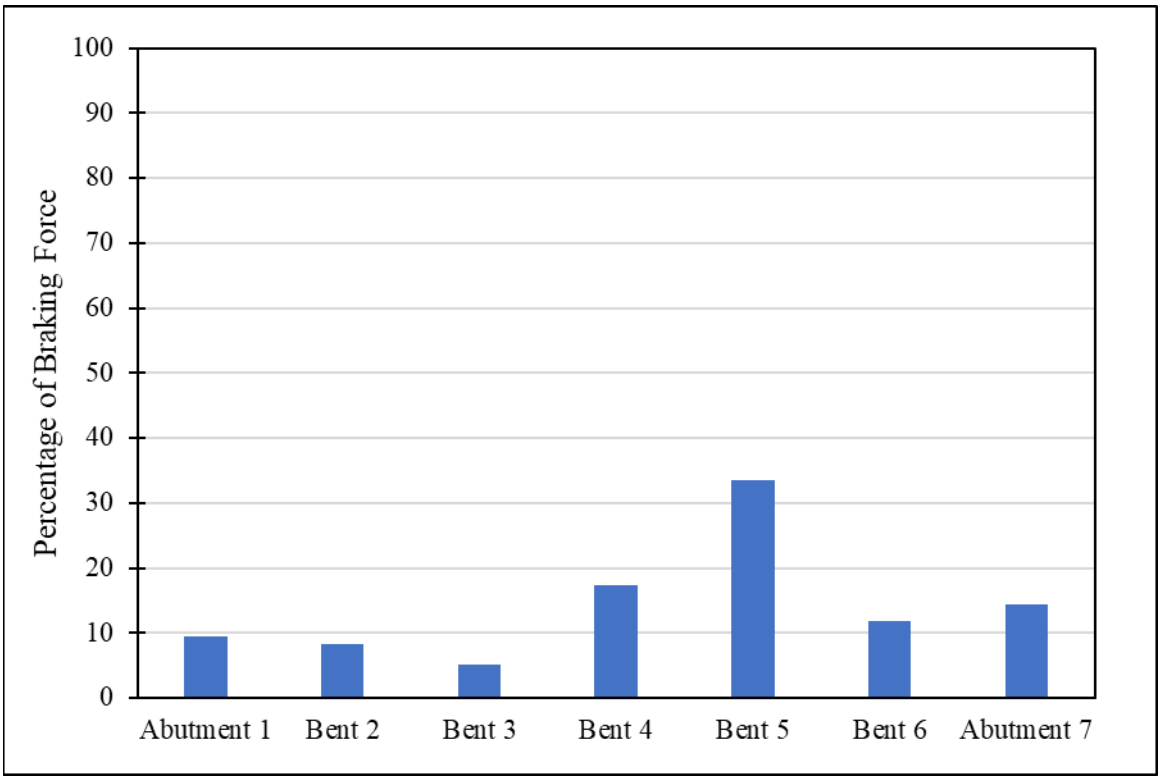

Figure 6-31 – Force Distribution in Substructure from Span 4 Loading

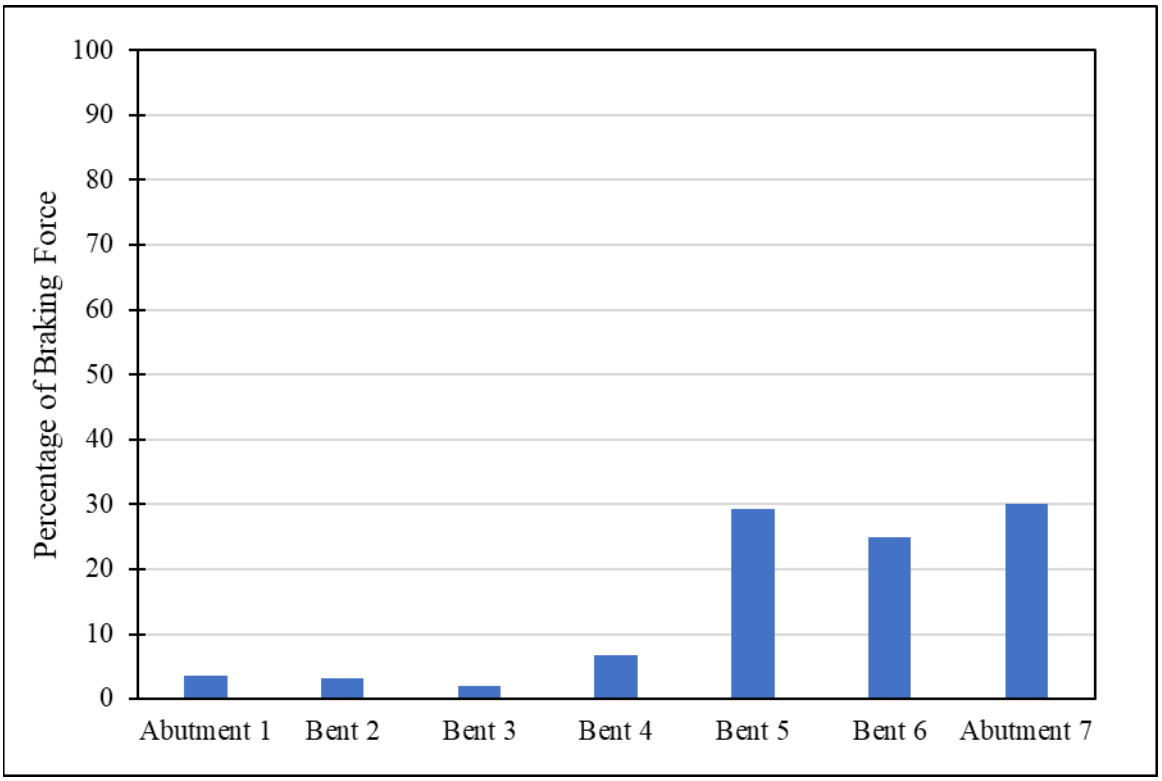

Figure 6-32 – Force Distribution in Substructure from Span 5 Loading

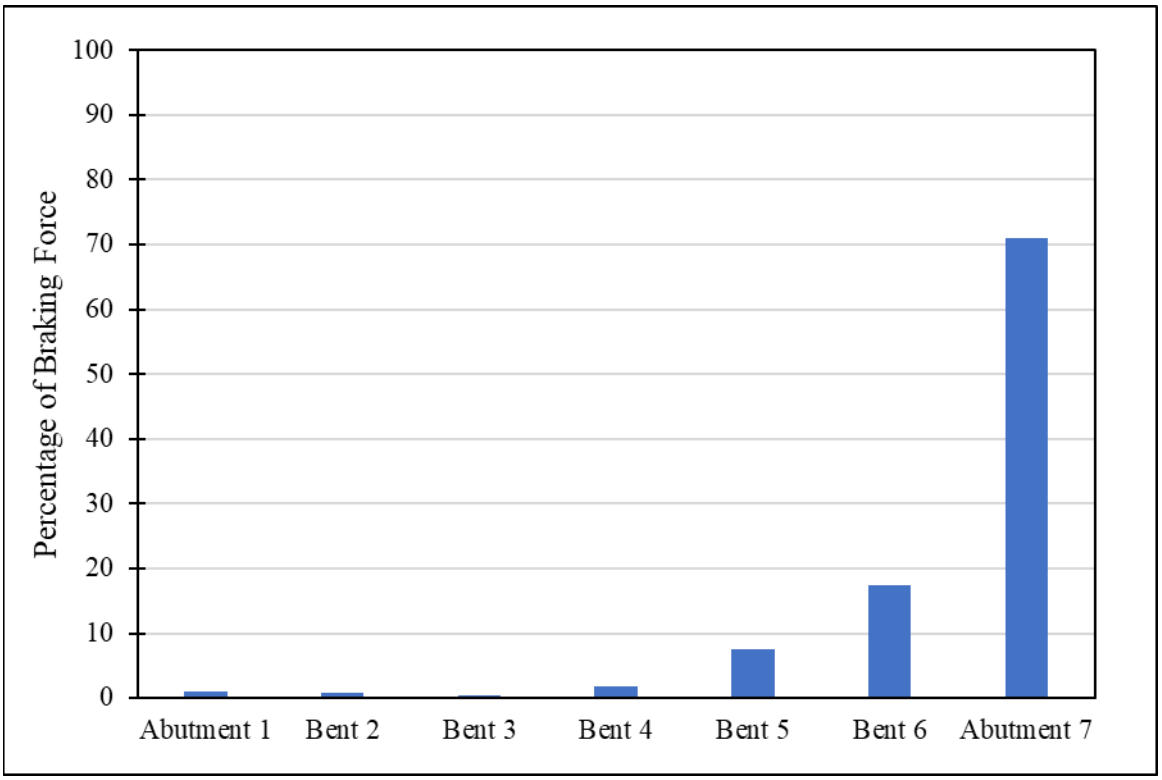

Figure 6-33 – Force Distribution in Substructure from Span 6 Loading

6.4.3 Analysis of Static Force Distribution

In every test, the total magnitude of the braking force on the bridge in the longitudinal direction is distributed among all of the supporting substructure in various amounts depending on the location. The total shear distribution should sum to the applied force.

As the static horizontal braking forces moves away from the abutment, the force becomes more evenly distributed among the other bents, especially in the middle spans of the bridge. As the force gets closer to the other abutment, the distribution of the total force becomes less throughout all bents again and the majority goes into the nearest abutment. The abutments draw large portions of the force due to their relative stiffness being so much greater than the bents.

When the load was applied to Spans 1 or 6, slightly over 70 percent of the entire force went into the abutments. For Spans 2, 3, 4, and 5, each substructure component resisted less than 40 percent of the entire force. When Spans 3 and 5 were loaded, the substructure components resisted less than 30 percent. Therefore, as the load is applied further and further away from the

ends of the bridge, the more distributed the total applied force is to the substructure, reducing the component force that must be resisted by individual elements.

During the loading of Spans 3 and 4, the bent at the end of the span where the front of the truck was positioned experienced a greater amount of shear force than the other bent supporting that span. For these tests, these were also the bents that displaced the most. For every test, if it was not an abutment that experienced the greatest amount of force, the bent that displaced the most was also the bent that experienced the most shear force. Moreover, it was always one of the bents supporting the loaded span.

6.5 Dynamic Test Results

6.5.1 Bridge Accelerations Due to Dynamic Loading

When comparing the dynamic model to the field data, the accelerations of each were evaluated. Figure 6-34 through Figure 6-44 are the measured accelerations compared to the model accelerations. In order to alleviate the amount of data displayed on each graph and to provide clarity for comparisons, the only accelerations included were from the span that was tested, the two adjacent spans and the bents supporting the test span. The accelerometers were located at each end of the girder that was designated fixed on the plans and the accelerometers on the bents were centered on the top of the bent cap. The only exception to this was accelerometer B-3a, it was placed on the outer face of bent cap of bent 3. The side it was placed on was also the same side the right side tests were conducted on. In the figures, Field Sp-1, Field B-2, etc. is the naming convention for field accelerometer on Span 1, Bent 2, etc. and the same naming convention is used for SAP. For each test, the diagram above the acceleration graph shows the location of the truck, peak deceleration rate and the truck weight. Additionally, where the braking of the truck began and the time when the truck was completely stopped are called out on the figures. For the exact times used, the time history functions for each test case are located in Appendix C.

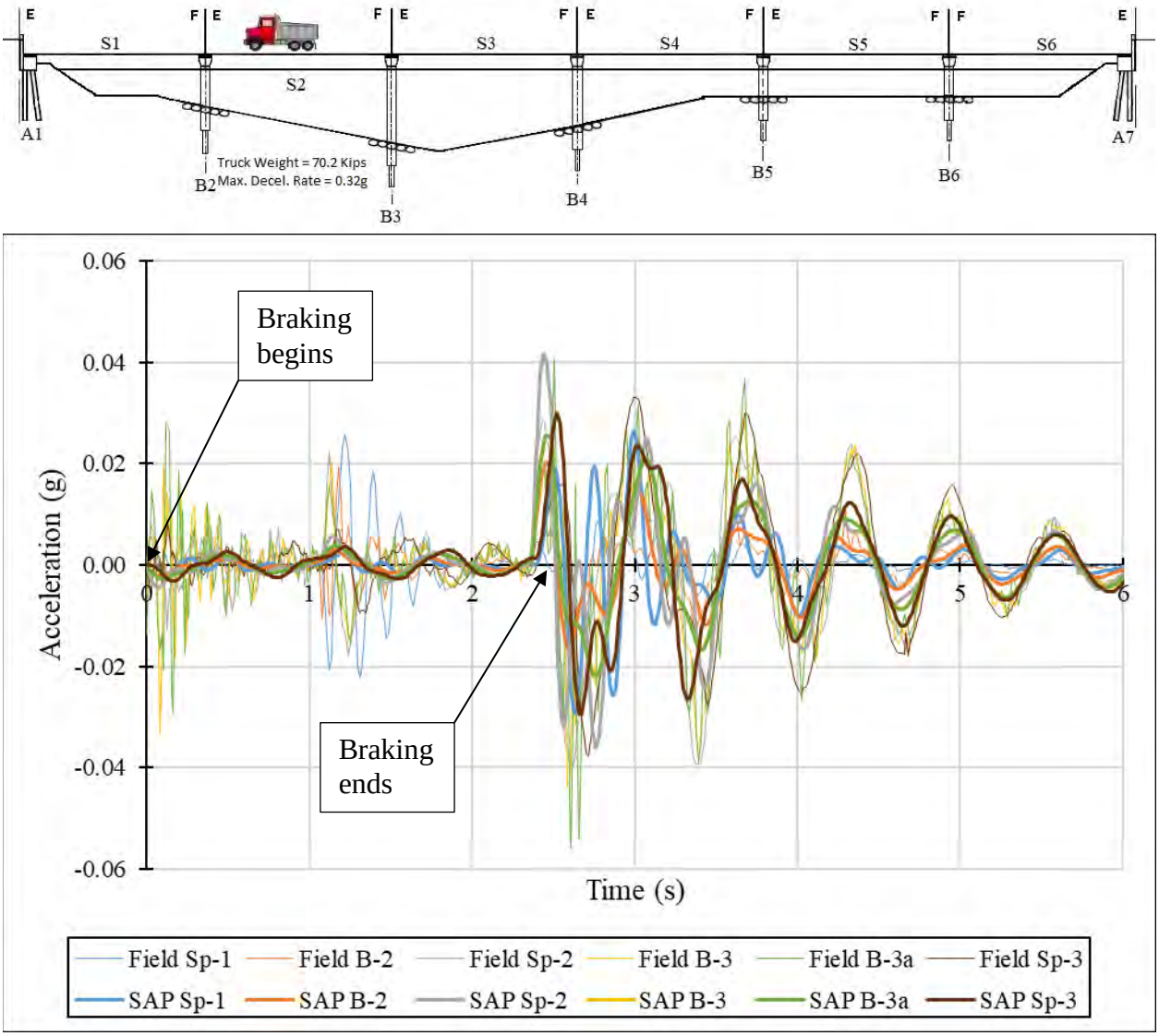

Figure 6-34 – Field and Model Accelerations for Test 1 on Center of Span 2

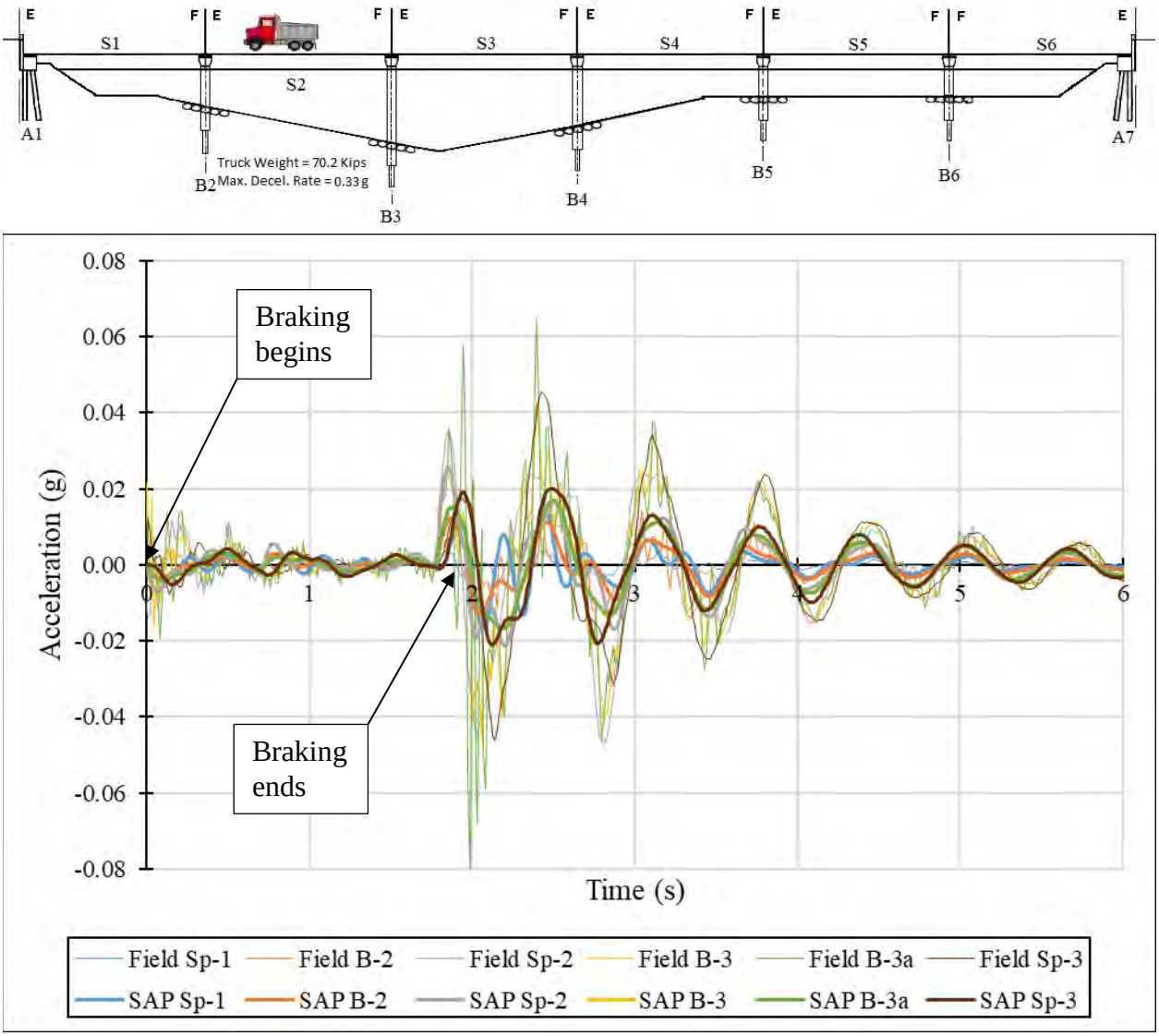

Figure 6-35 – Field and Model Accelerations for Test 2 on Center of Span 2

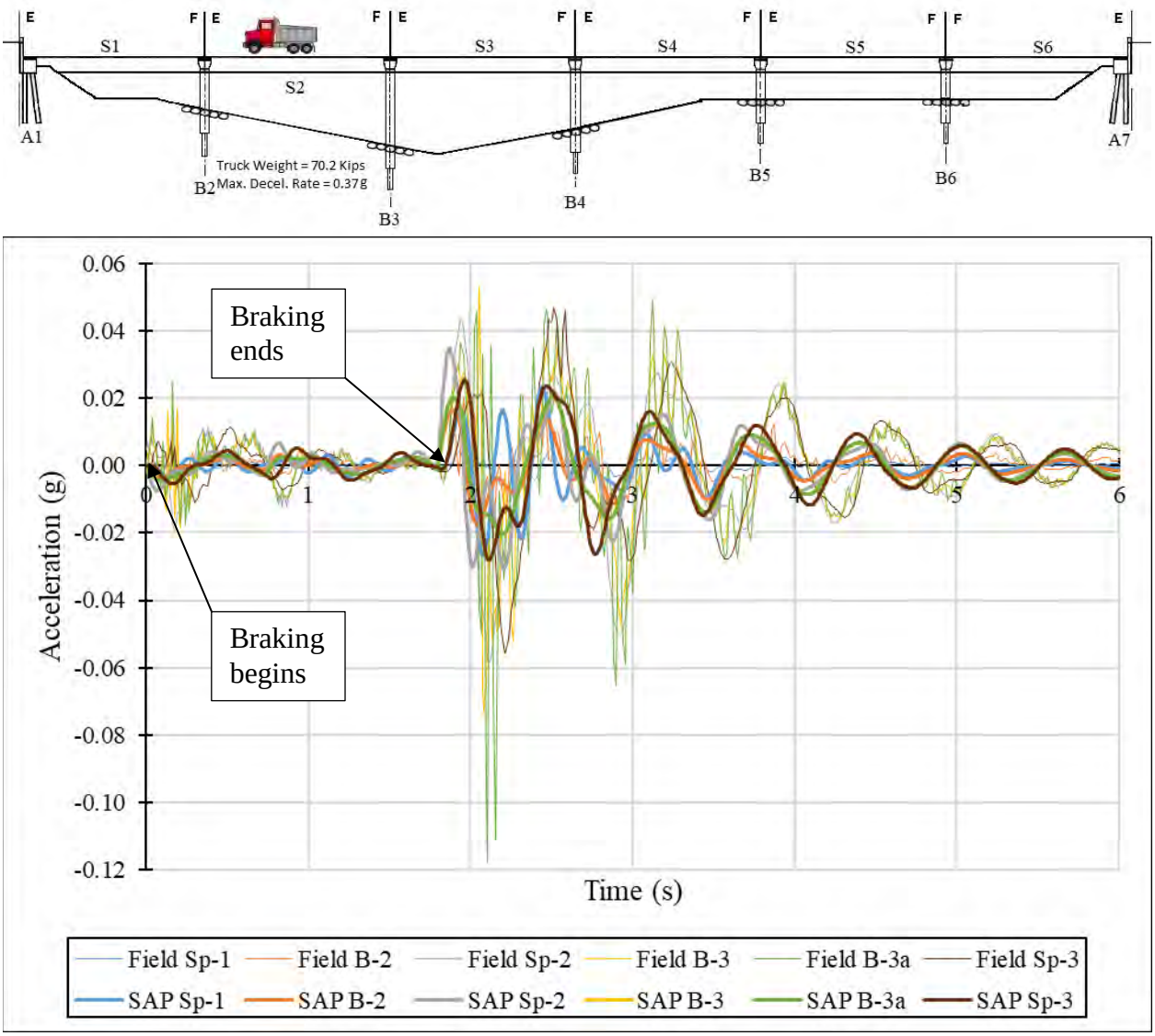

Figure 6-36 – Field and Model Accelerations for Test 3 on Center of Span 2

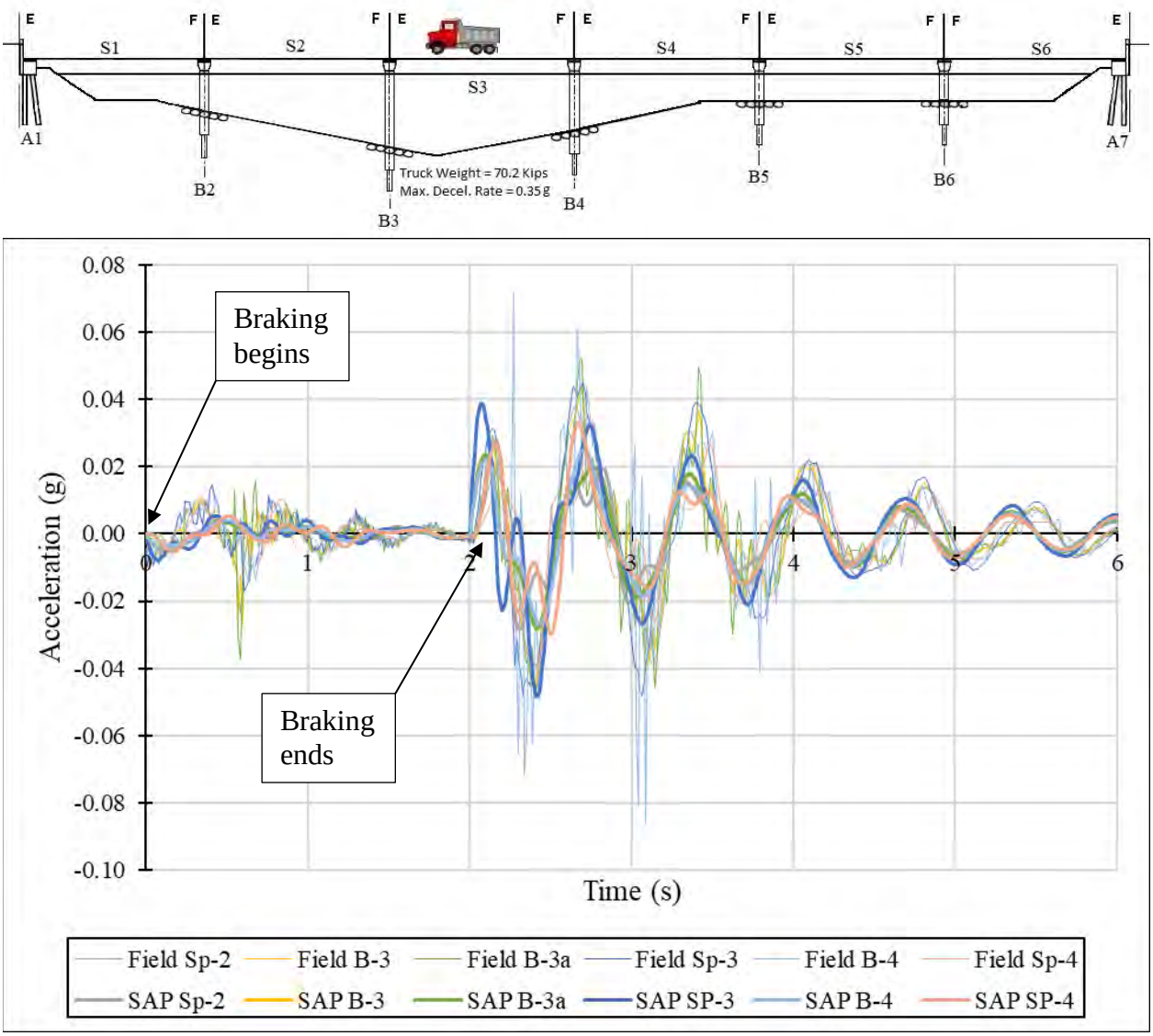

Figure 6-37 – Field and Model Accelerations for Test 1 on Center of Span 3

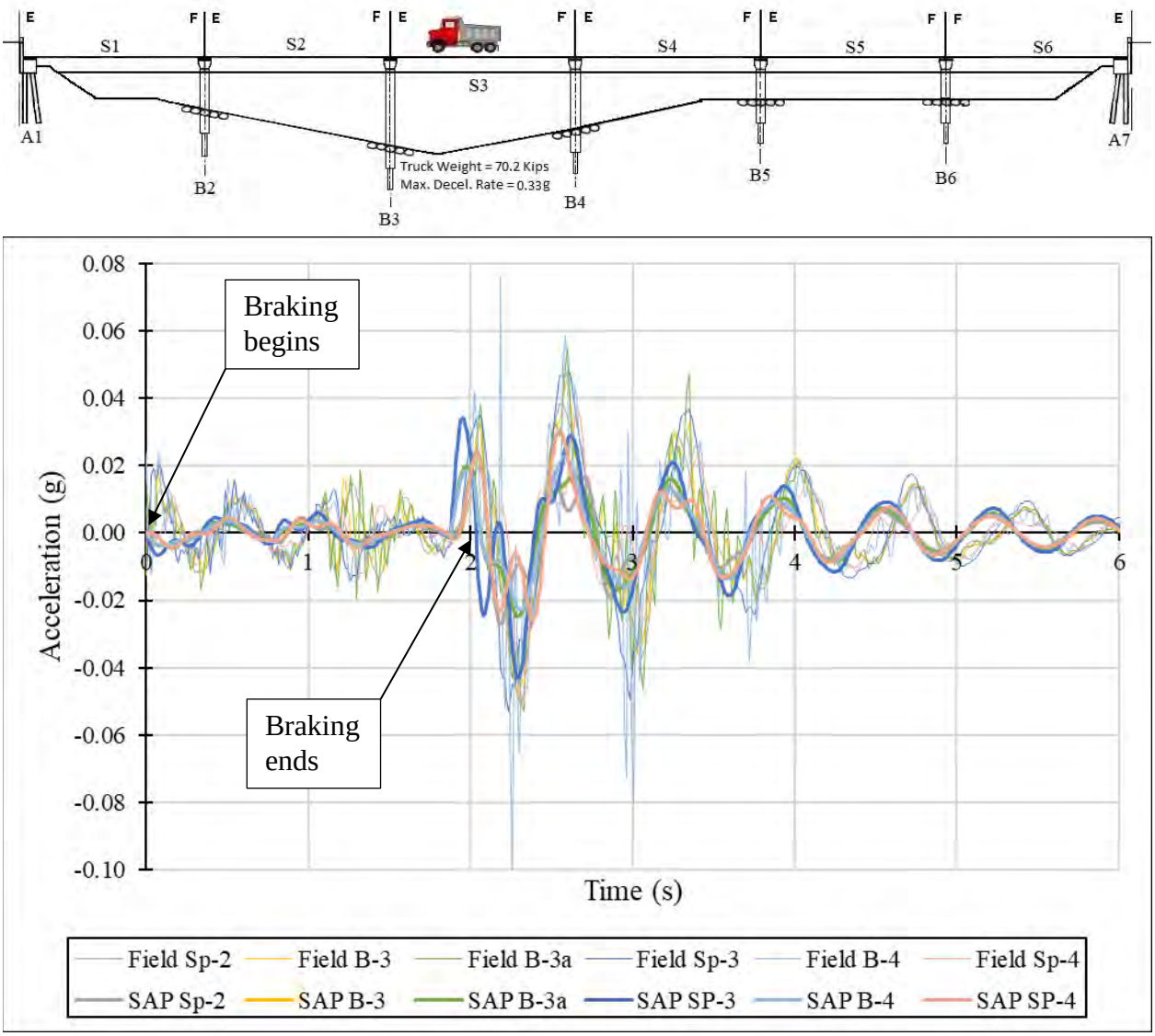

Figure 6-38 – Field and Model Accelerations for Test 3 on Center of Span 3

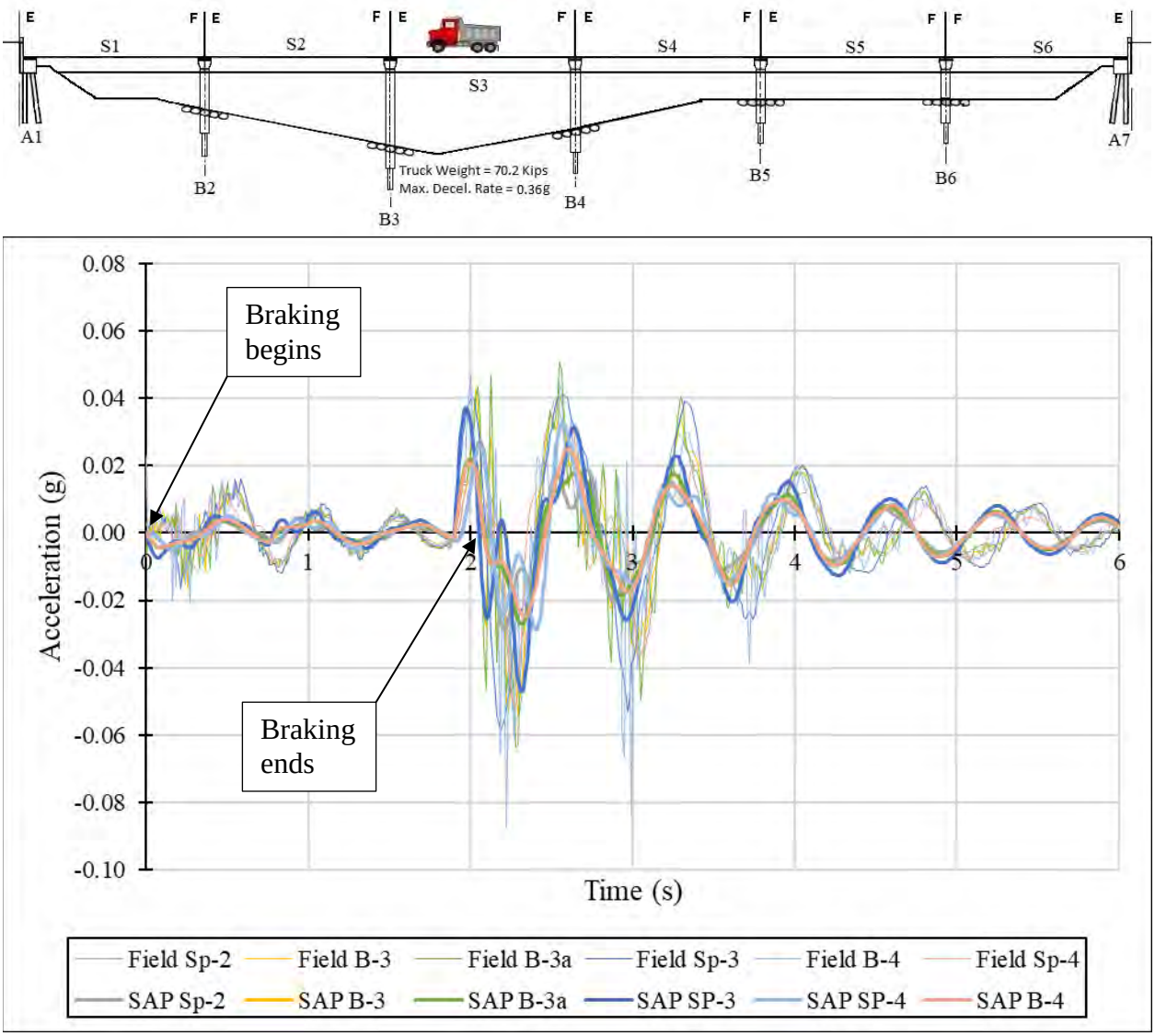

Figure 6-39 – Field and Model Accelerations for Test 4 on Center of Span 3

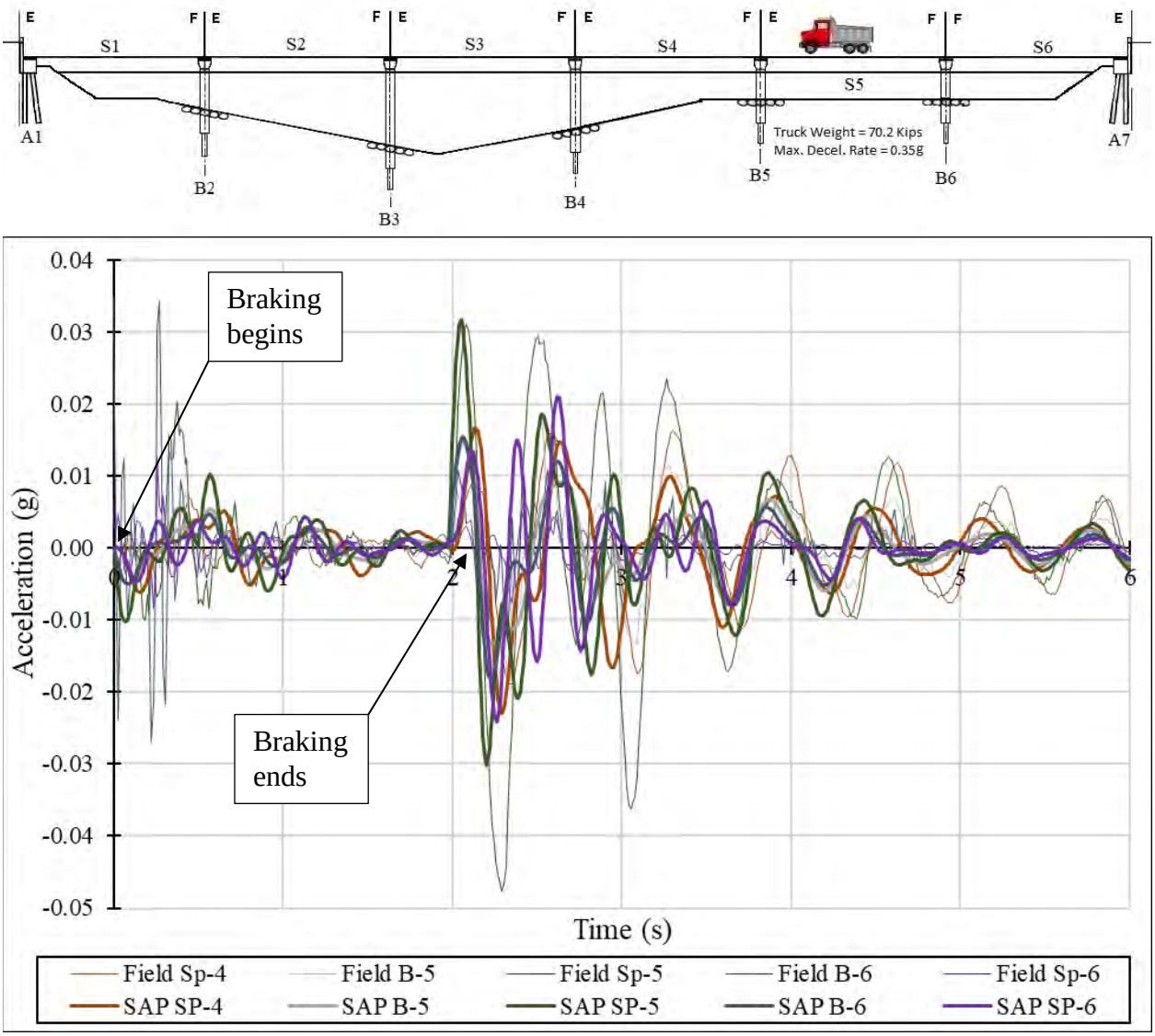

Figure 6-40 – Field and Model Accelerations for Test 2 on Center of Span 5

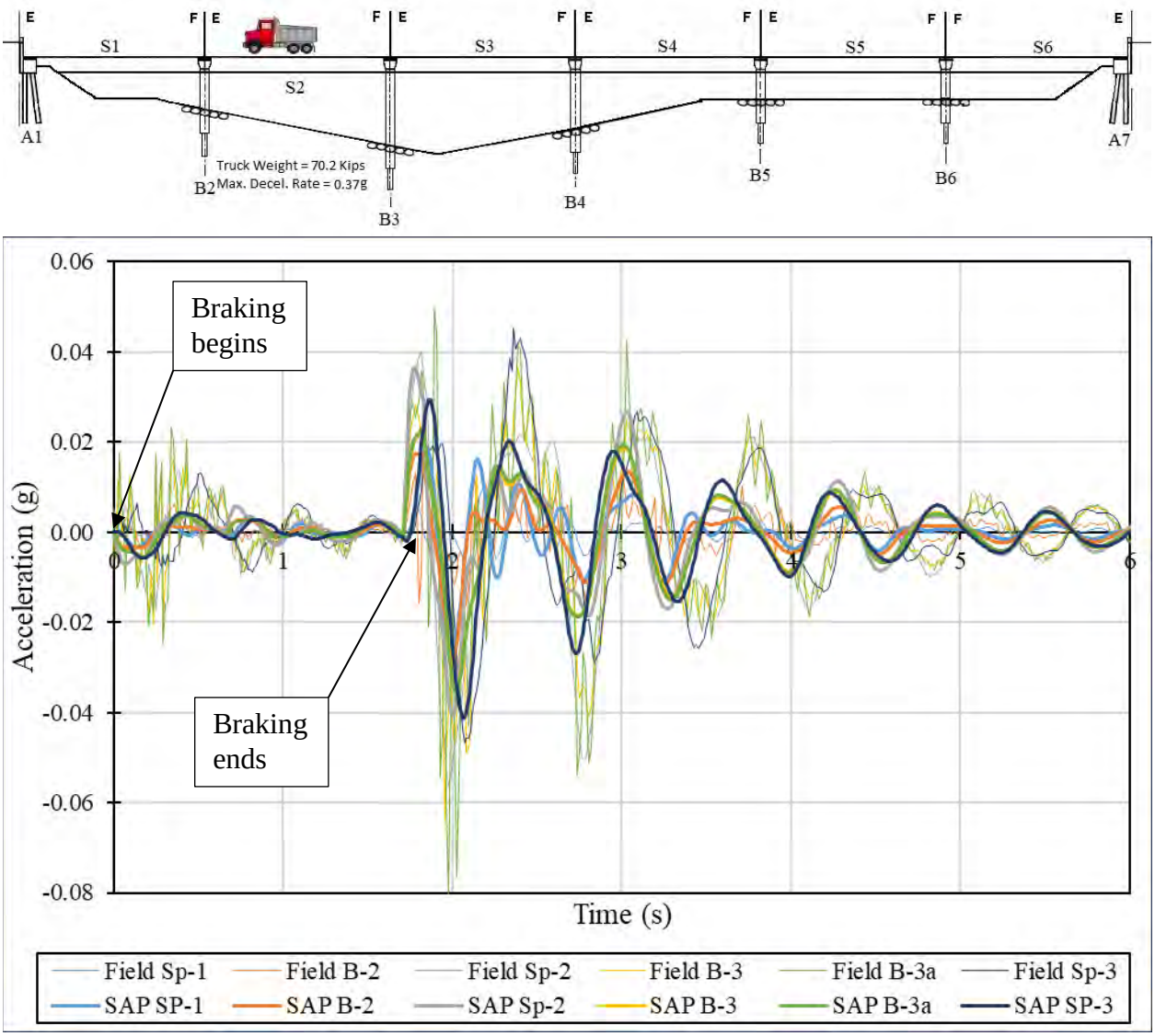

Figure 6-41 – Field and Model Accelerations for Test 2 on the Right Side of Span 2

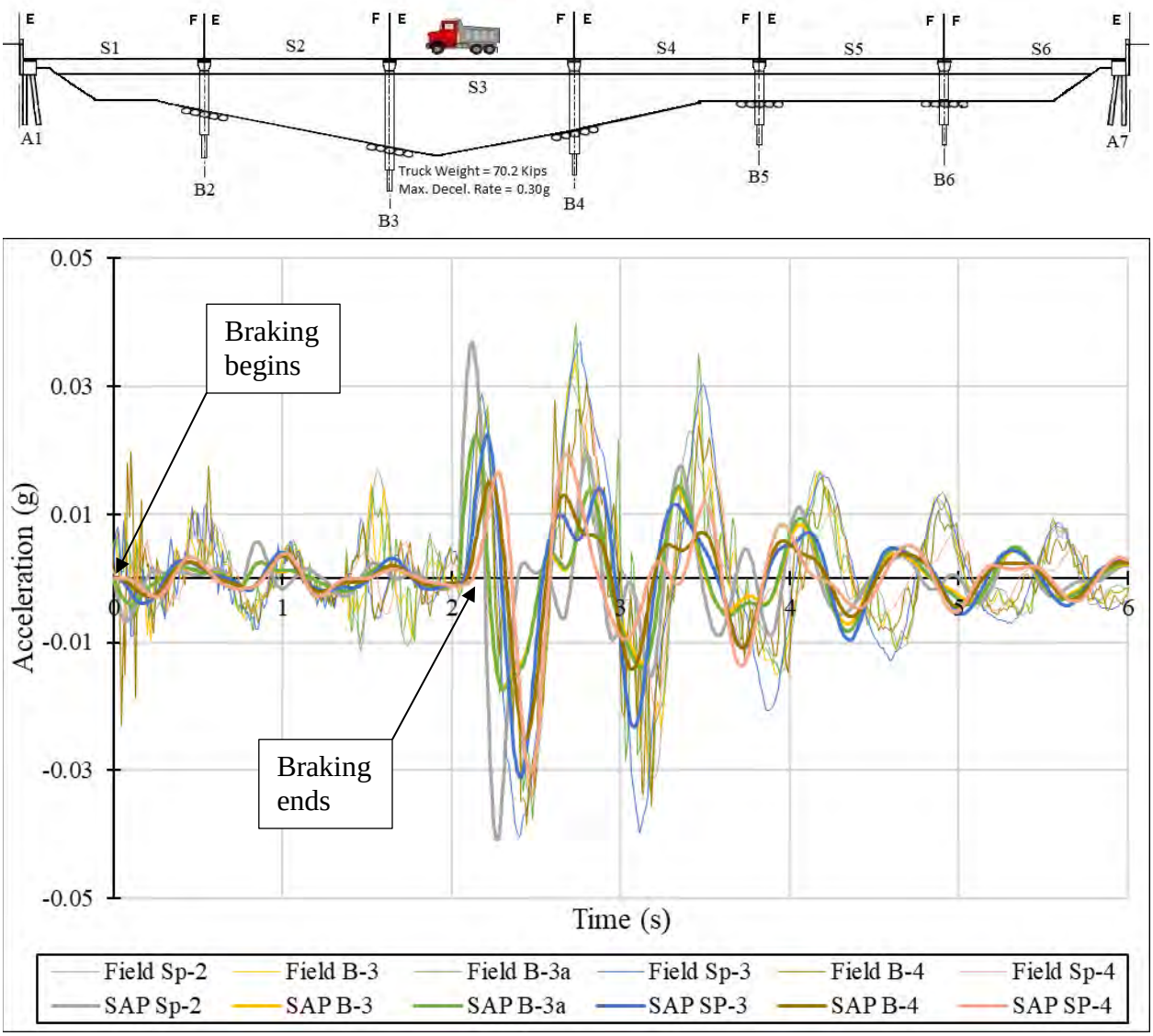

Figure 6-42 – Field and Model Accelerations for Test 3 on the Right Side of Span 3

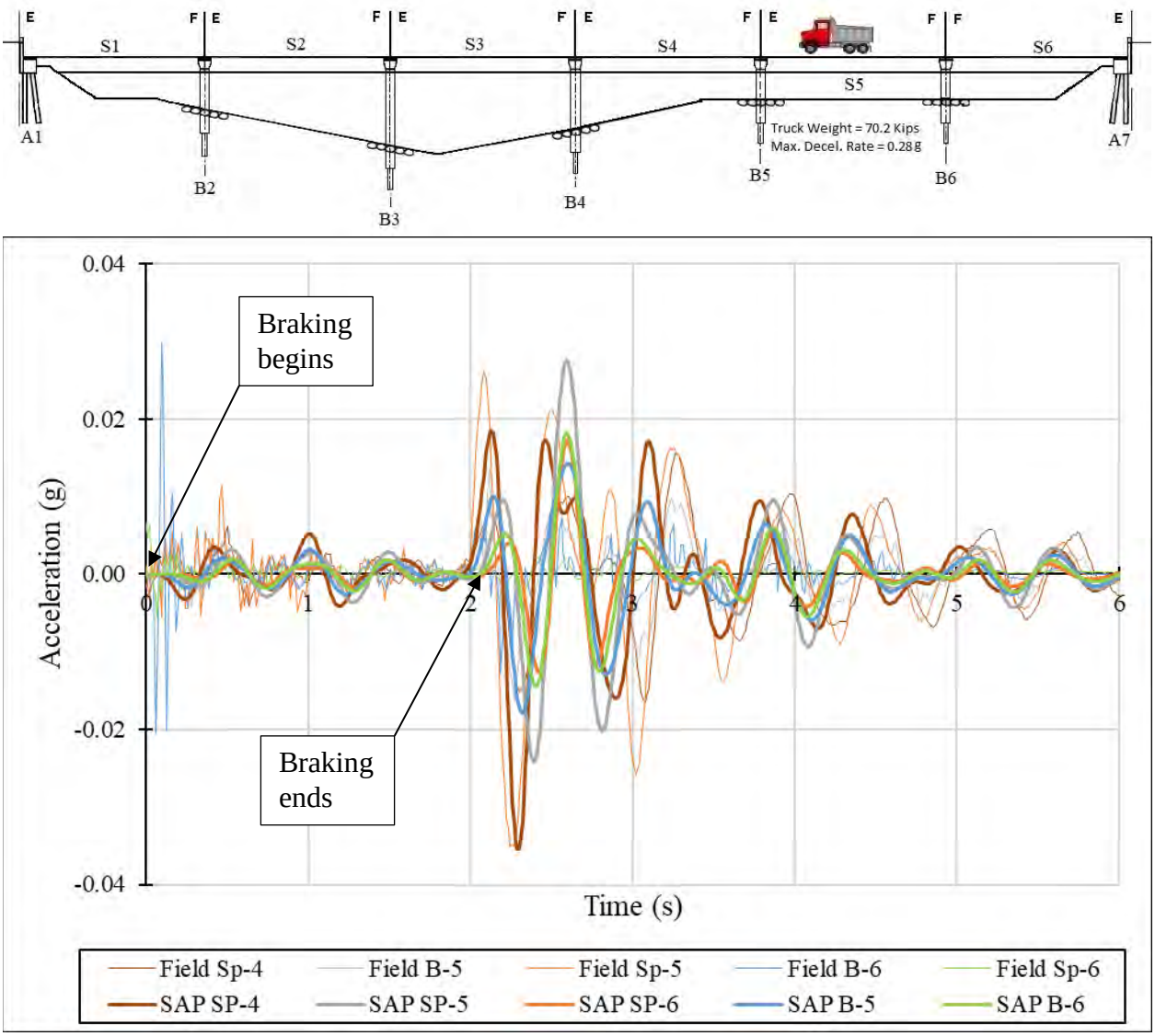

Figure 6-43 – Field and Model Accelerations for Test 1 on the Right Side of Span 5

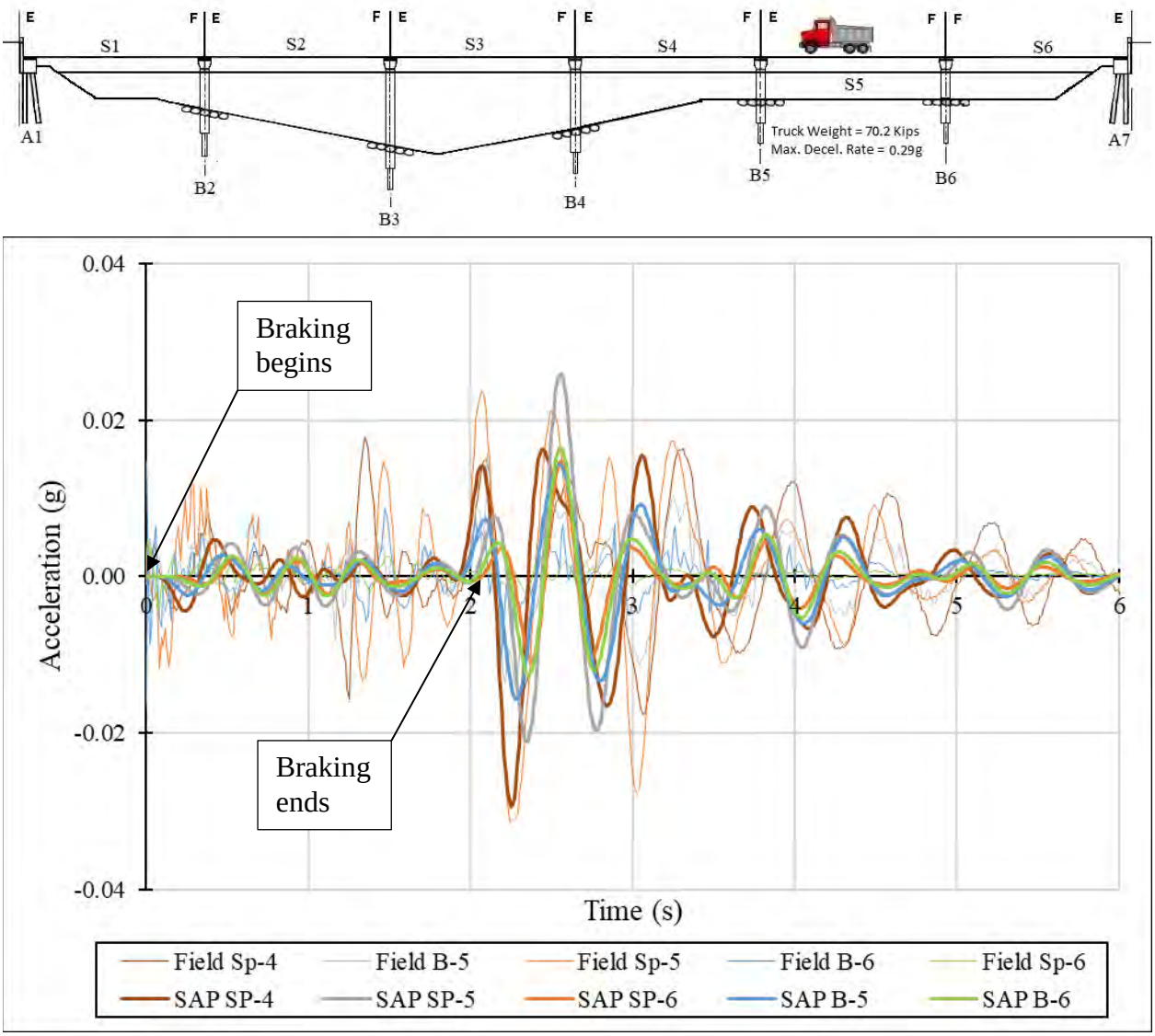

Figure 6-44 – Field and Model Accelerations for Test 3 on the Right Side of Span 5

With each of these tests, after the initial free response phase the peaks and troughs appear to become out of phase between the field data and the SAP data. But, the period and frequency of vibration between both remained similar. These response properties are more telling of the correlation despite them being slightly out of phase.

6.5.2 Analysis of Bridge Substructure Accelerations

To understand the maximum amount the bridge substructure elements were accelerating in relation to the maximum truck deceleration, Figure 6-45 through Figure 6-50 were produced. Despite there being negative accelerations, the absolute values were taken to find the highest magnitude of acceleration for a bridge span.

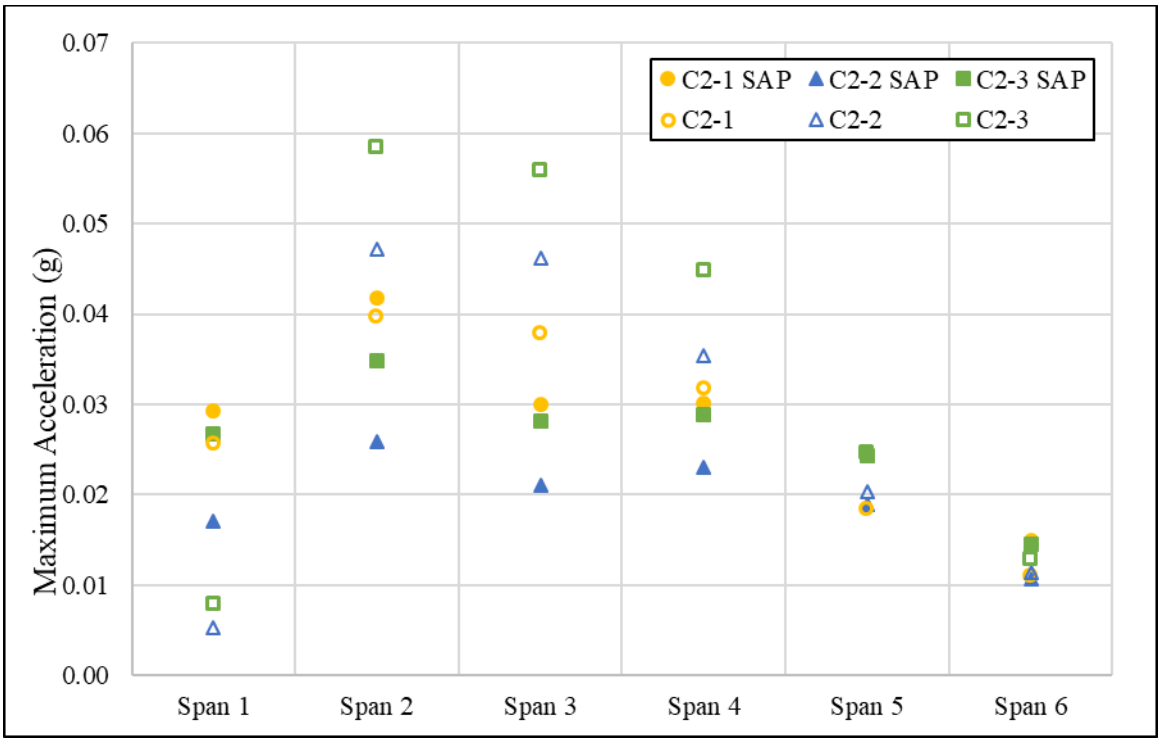

Figure 6-45 – Maximum Acceleration per Span from Field Test & Model for Span 2 Center Braking

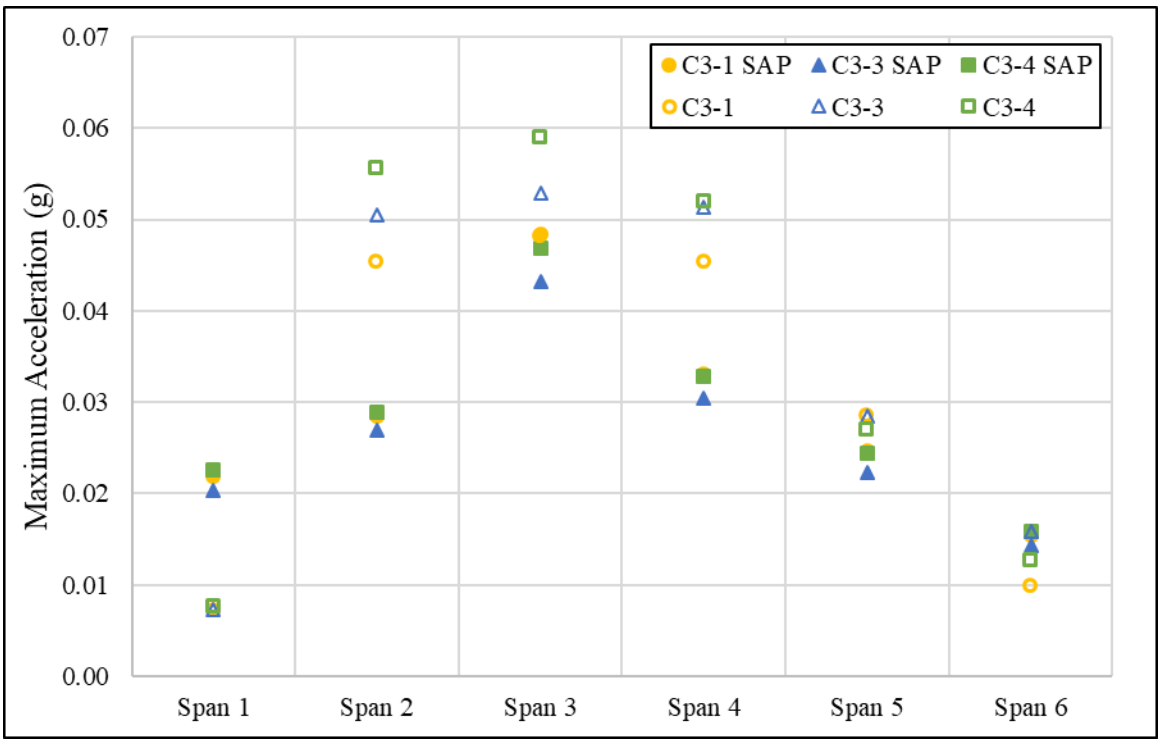

Figure 6-46 – Maximum Acceleration per Span from Field Test & Model for Span 3 Center Braking

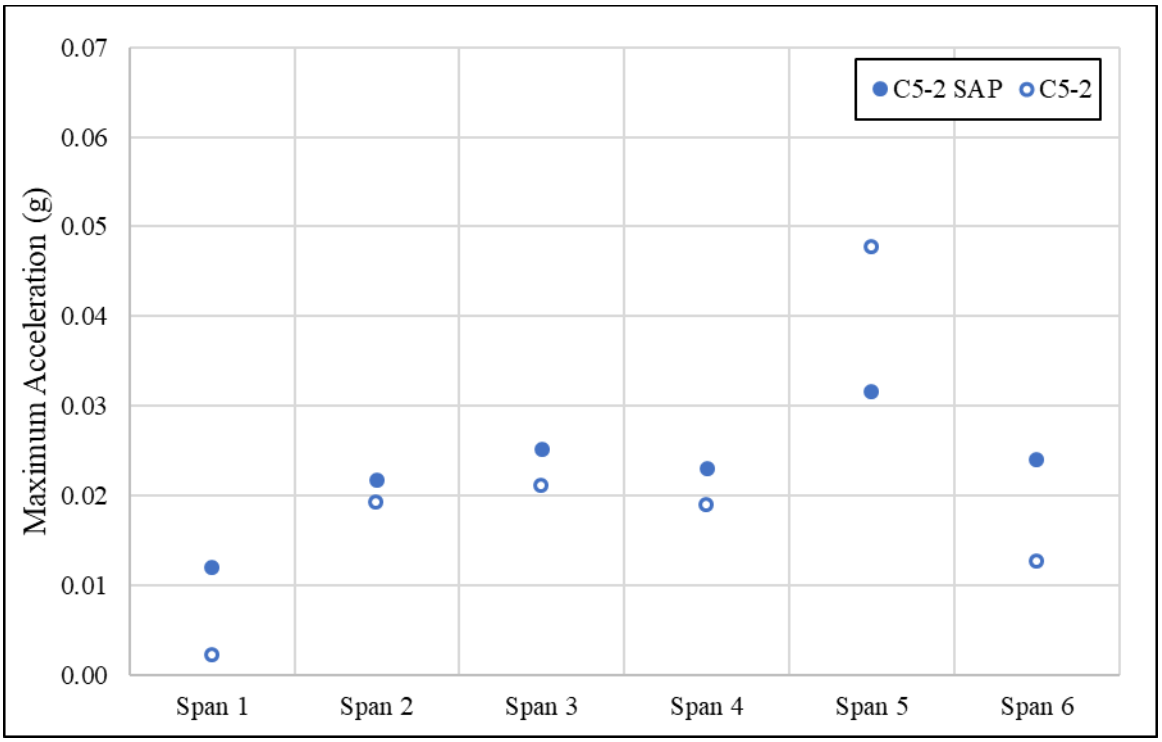

Figure 6-47 – Maximum Acceleration per Span from Field Test & Model for Span 5 Center Braking

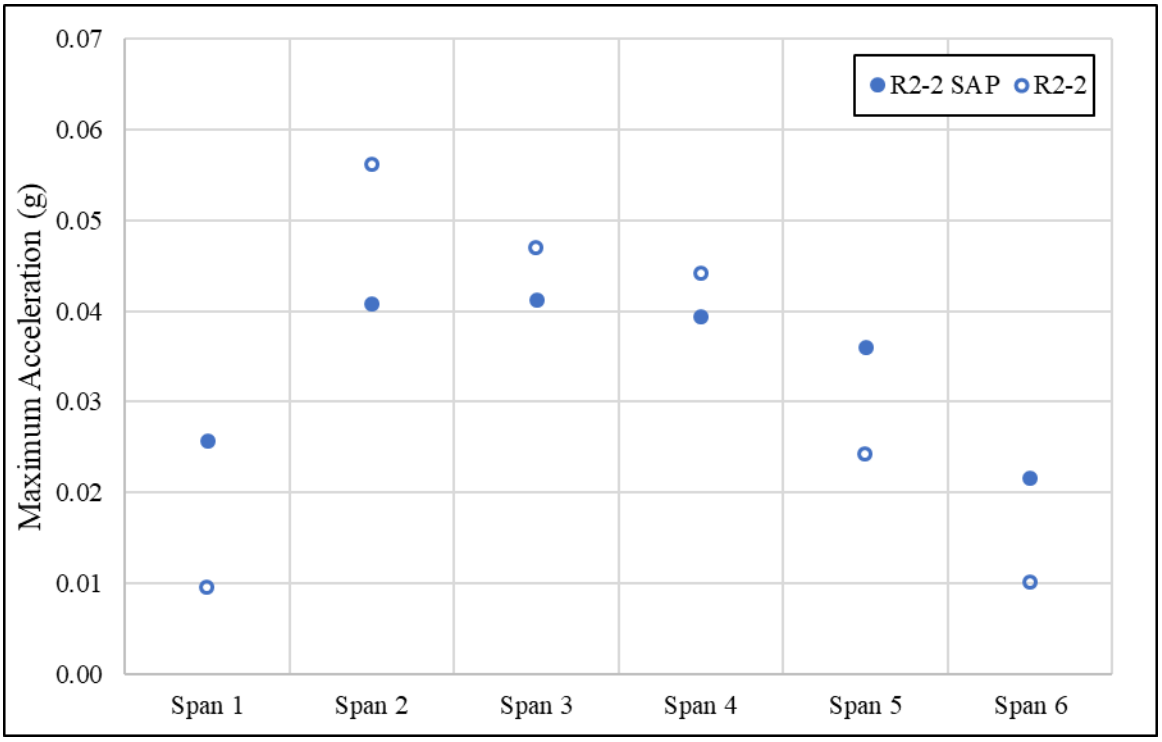

Figure 6-48 – Maximum Acceleration per Span from Field Test & Model for Span 2 Right Side Braking

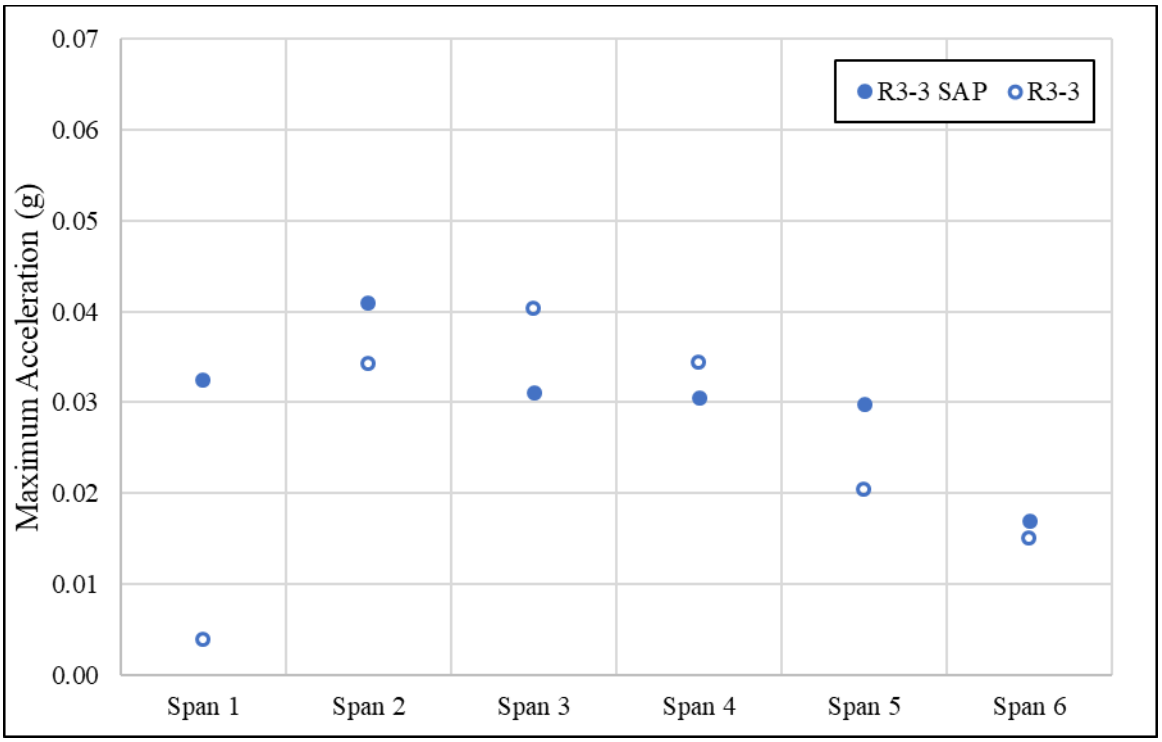

Figure 6-49 – Maximum Acceleration per Span from Field Test & Model for Span 3 Right Side Braking

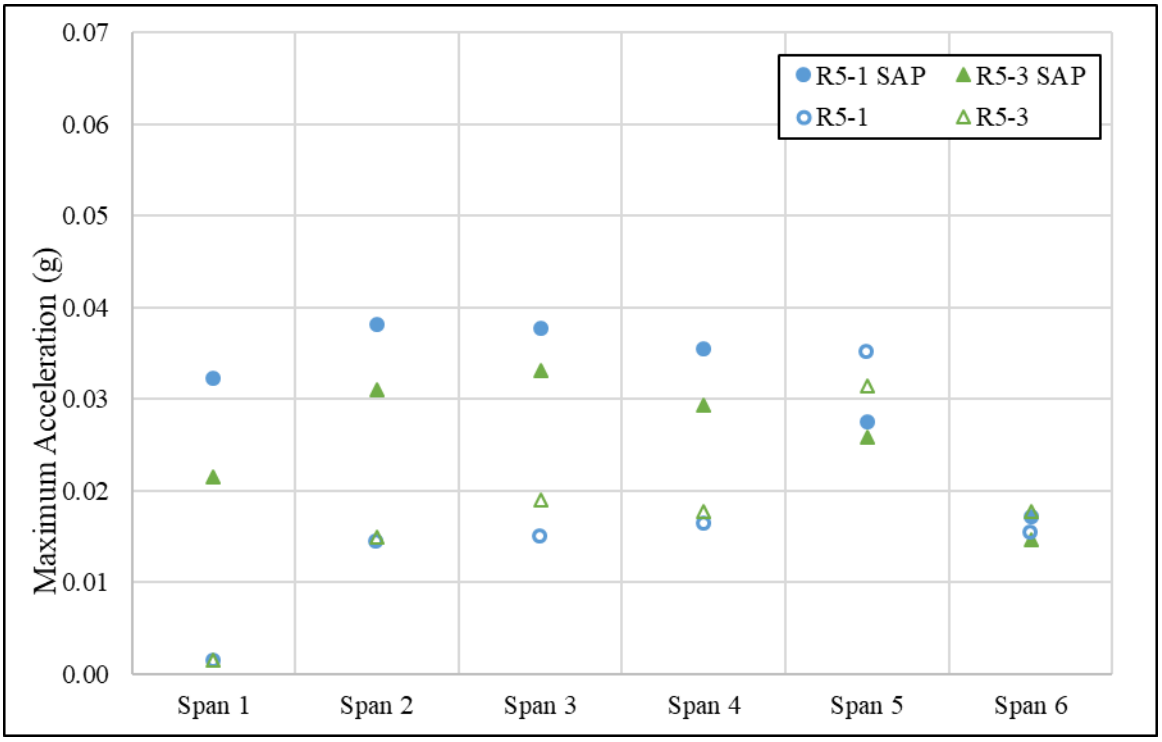

Figure 6-50 – Maximum Acceleration per Span from Field Test & Model for Span 5 Right Side Braking

In every test but Span 3 when braking occurred on the right side, the span that the truck stopped on experienced the greatest acceleration.

6.5.3 Shear Forces in Bents from Dynamic Braking Tests

For each model loading condition, Figure 6-51 through Figure 6-61 illustrate the total shear force over time that the entire bridge substructure (bents and abutments) experienced. The maximum total horizontal force is developed during the length of time that the brakes are applied (the first few seconds). The magnitude of this force is approximately equal to the maximum deceleration rate times the mass of the truck. For example, Figure 6-51 shows the total shear force in the substructure from braking on the center of Span 2, Test 1. In that test, the maximum deceleration rate was 0.32g and the truck mass was 70.2 kips, therefore, the approximate maximum total horizontal force is assumed to be 22.5 kips as a result of the truck deceleration. This simple calculation does not account for any dynamic amplification or the inertia of the bridge, but is an estimation of the maximum that is expected in a static braking force. The calculation for the approximate maximum horizontal force is included on each figure. It is also important to note that the total shear force in the substructure does not ever get above the total shear force during the braking event. As soon as the braking maneuver is completed, the bridge acceleration is already damping out during free response and the forces are dissipating.

Unlike the static tests where the amount of force for each component was presented, only the total shear force for each test is included since these tests were time dependent and are not easily combined in one figure.

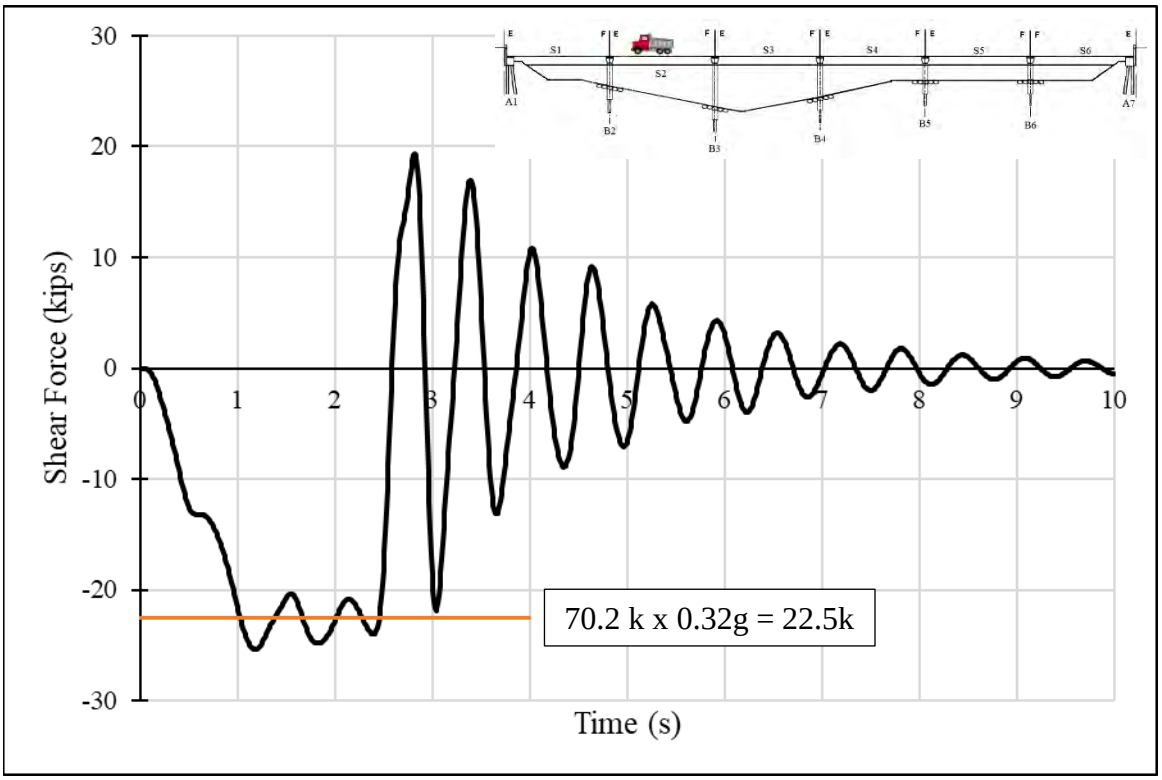

Figure 6-51 – Shear Force in Substructure from Center of Span 2 Braking Test 1

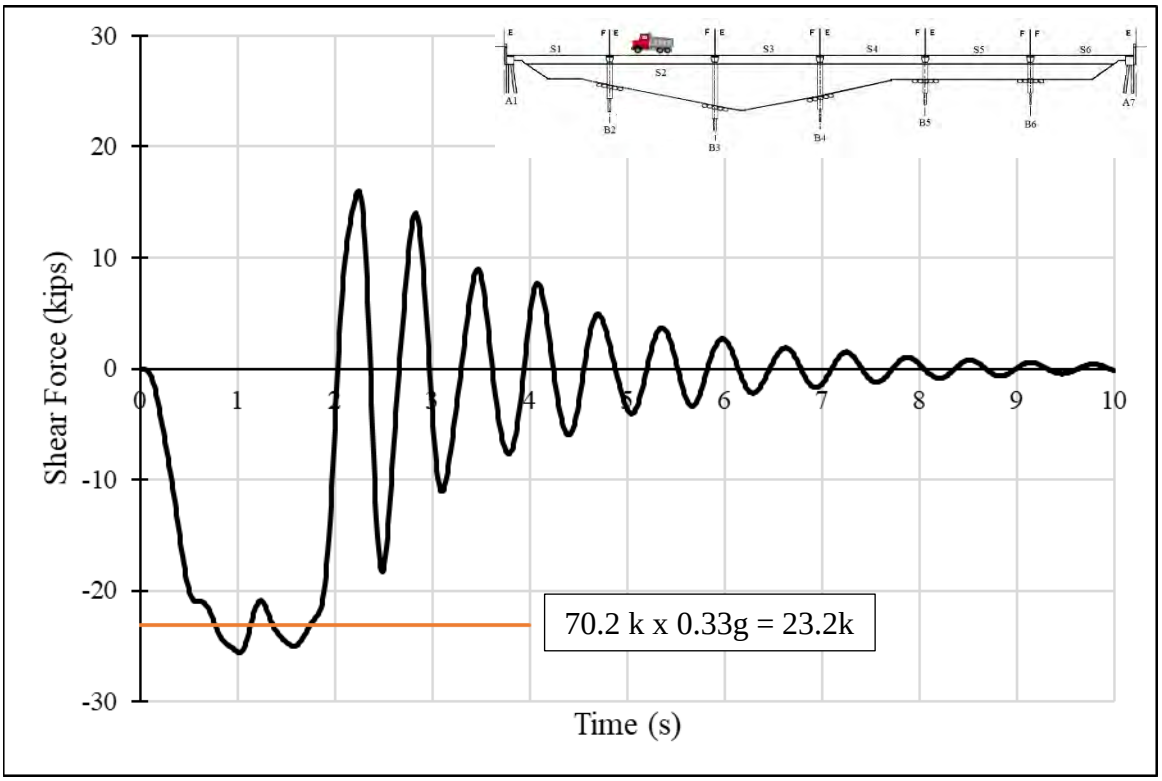

Figure 6-52 – Shear Force in Substructure from Center of Span 2 Braking Test 2

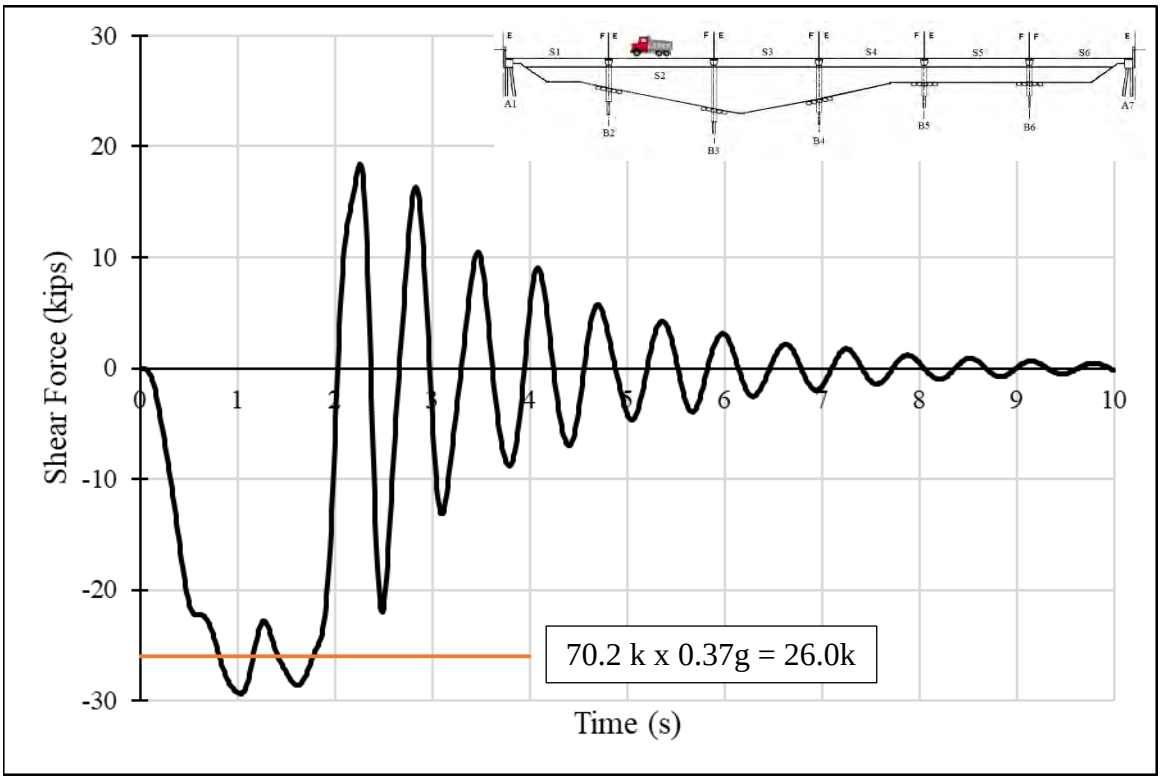

Figure 6-53 – Shear Force in Substructure from Center of Span 2 Braking Test 3

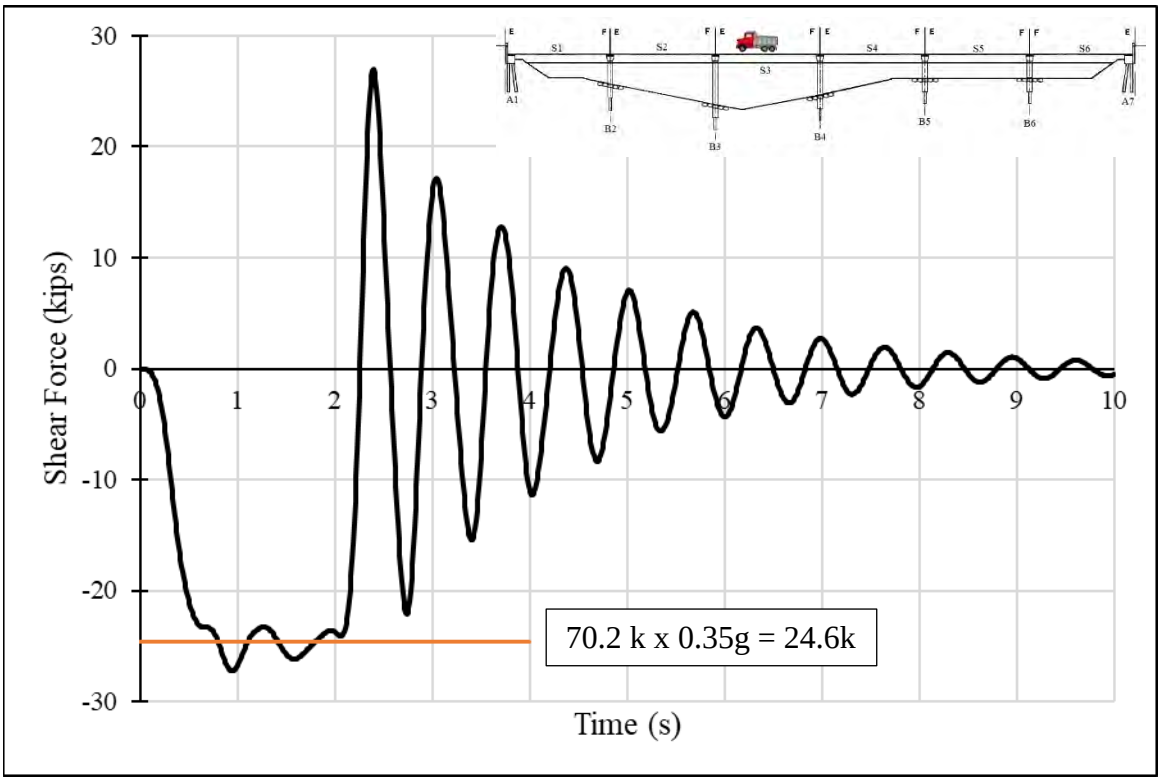

Figure 6-54 – Shear Force in Substructure from Center of Span 3 Braking Test 1

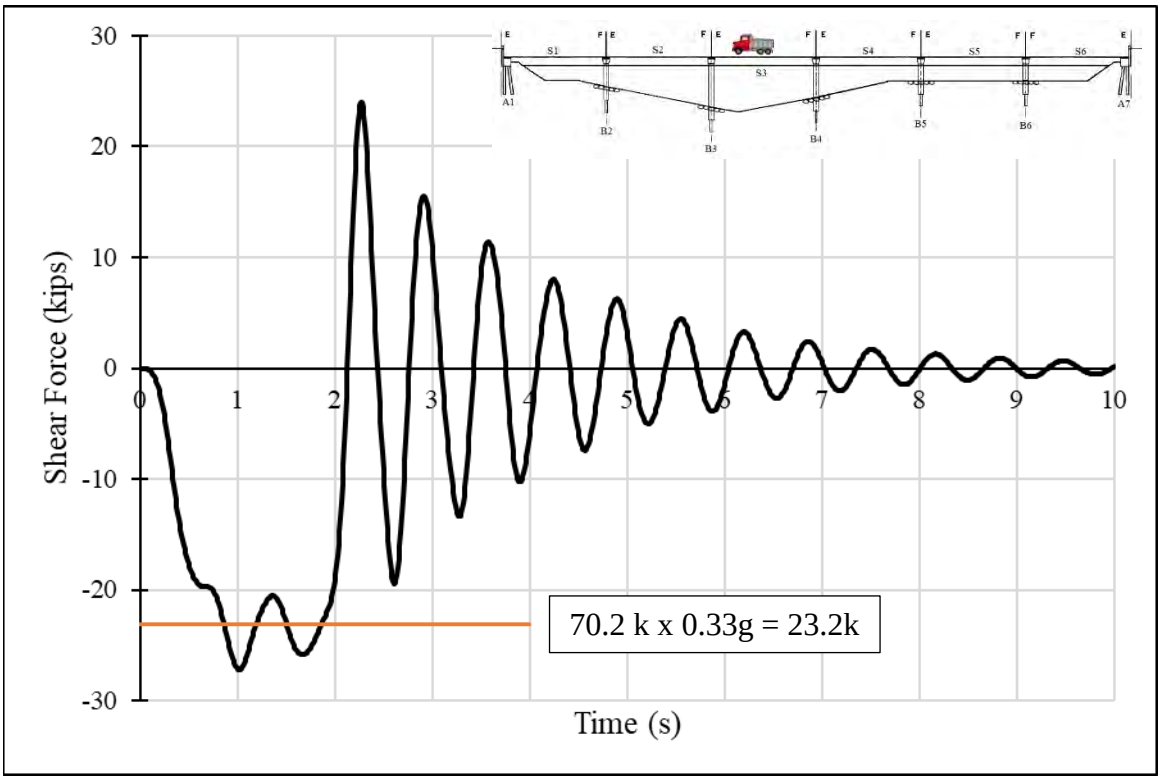

Figure 6-55 – Shear Force in Substructure from Center of Span 3 Braking Test 3

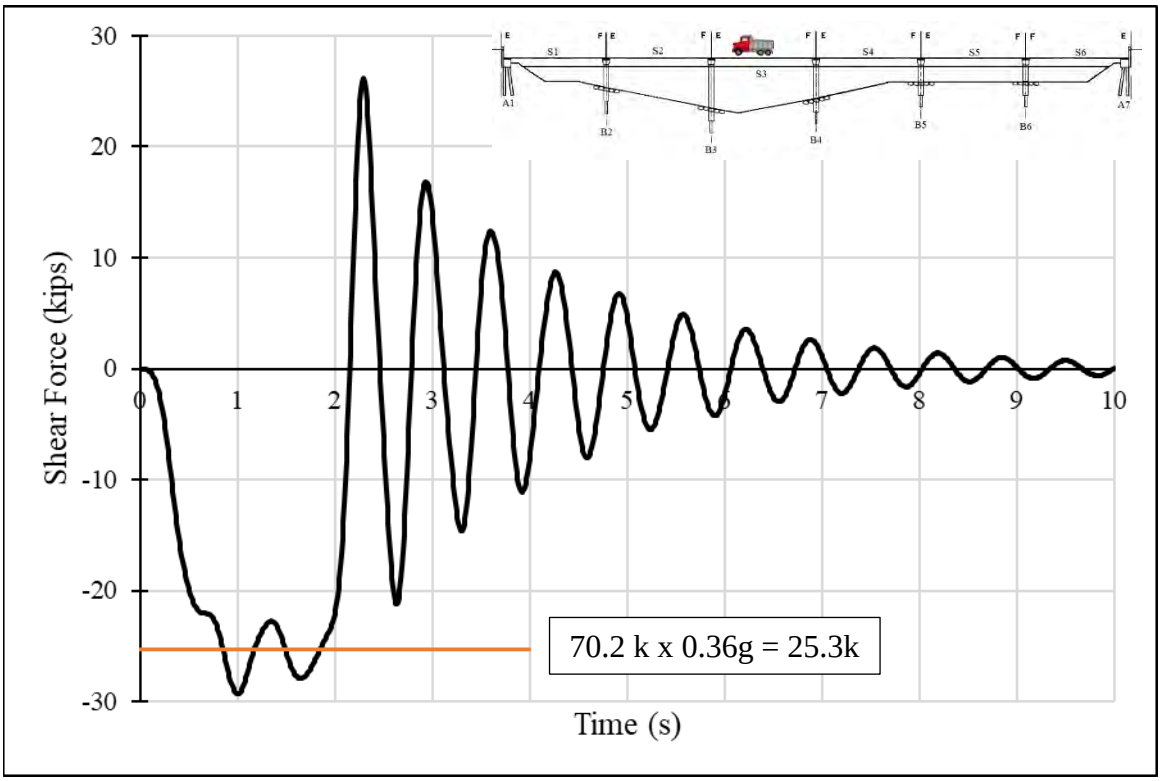

Figure 6-56 – Shear Force in Substructure from Center of Span 3 Braking Test 4

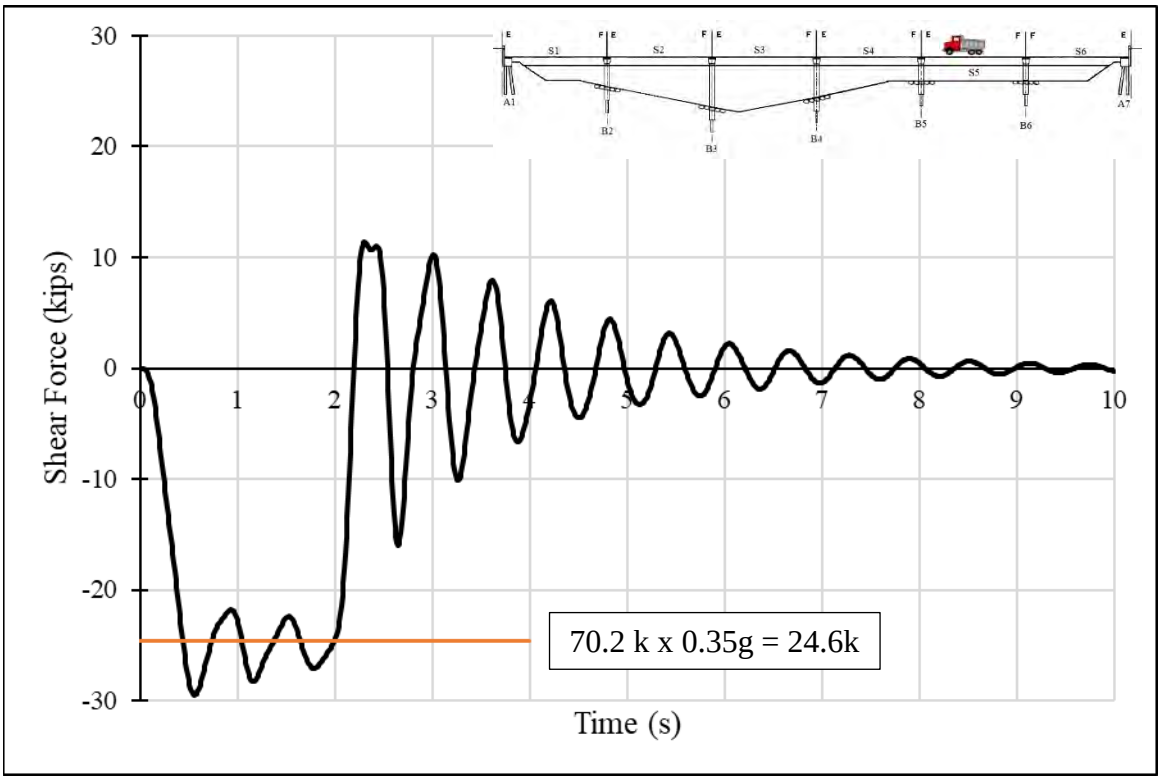

Figure 6-57 – Shear Force in Substructure from Center of Span 5 Braking Test 2

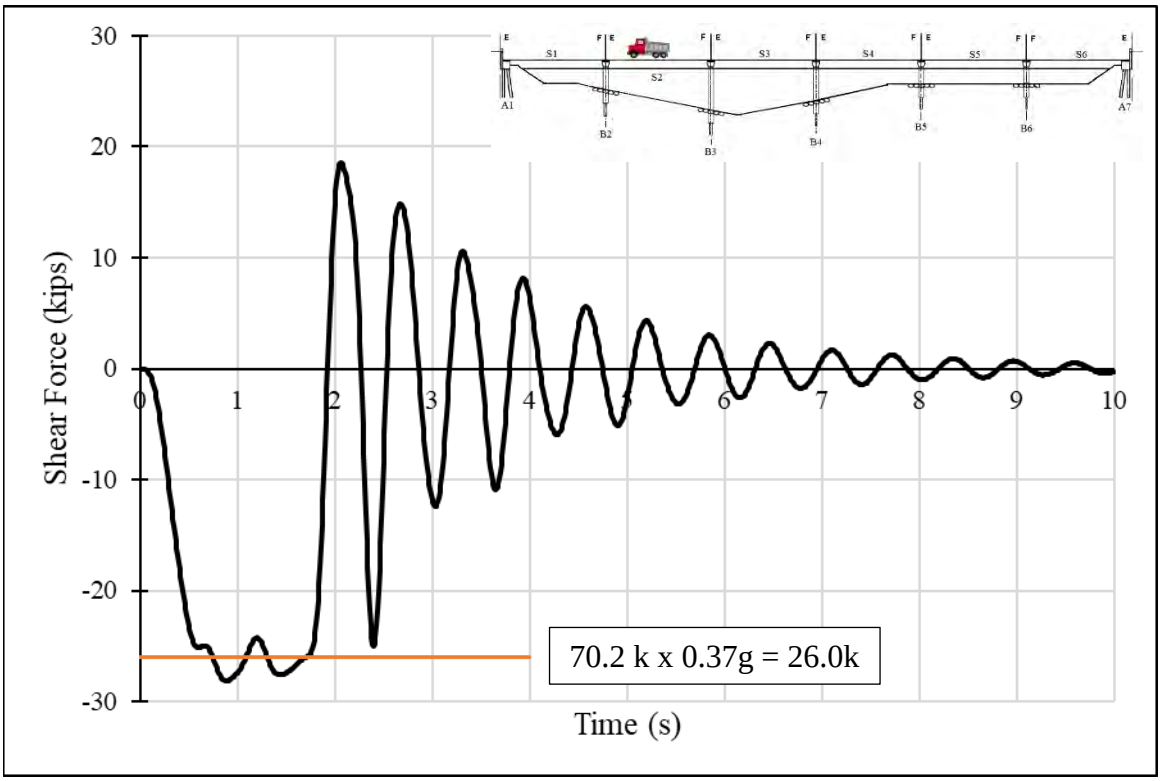

Figure 6-58 – Shear Force in Substructure from the Right Side of Span 2 Braking Test 2

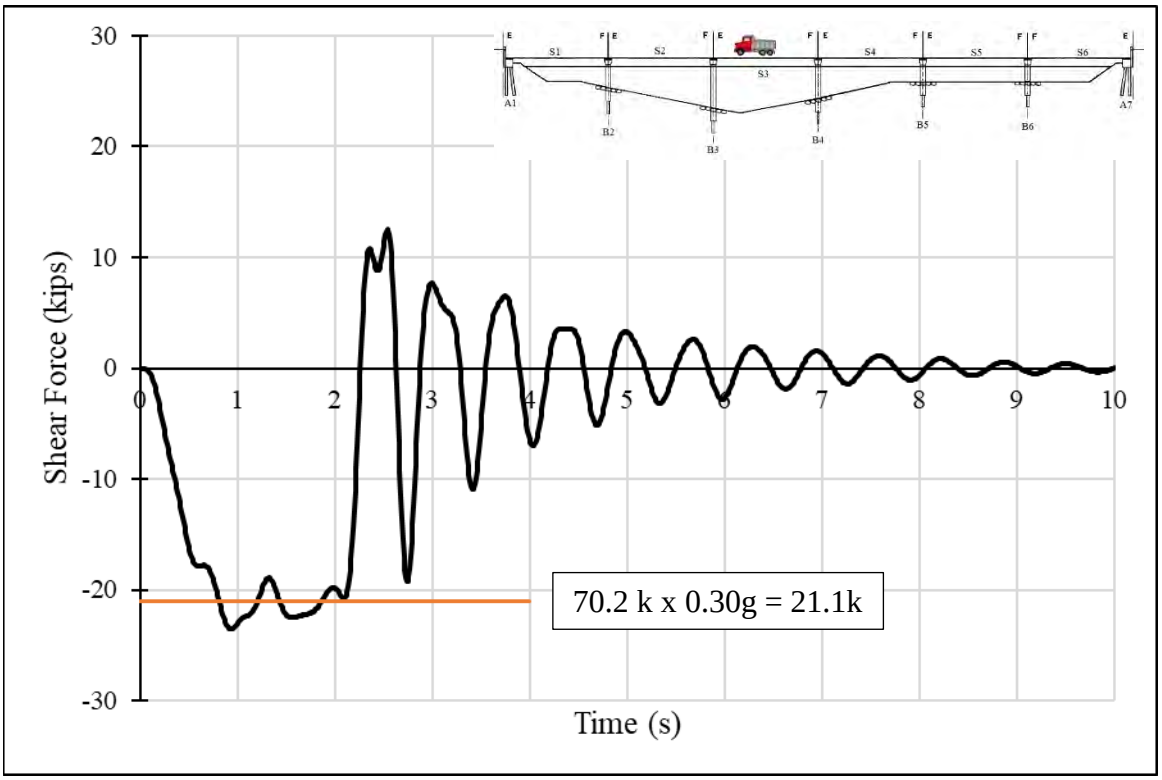

Figure 6-59 – Shear Force in Substructure from the Right Side of Span 3 Braking Test 3

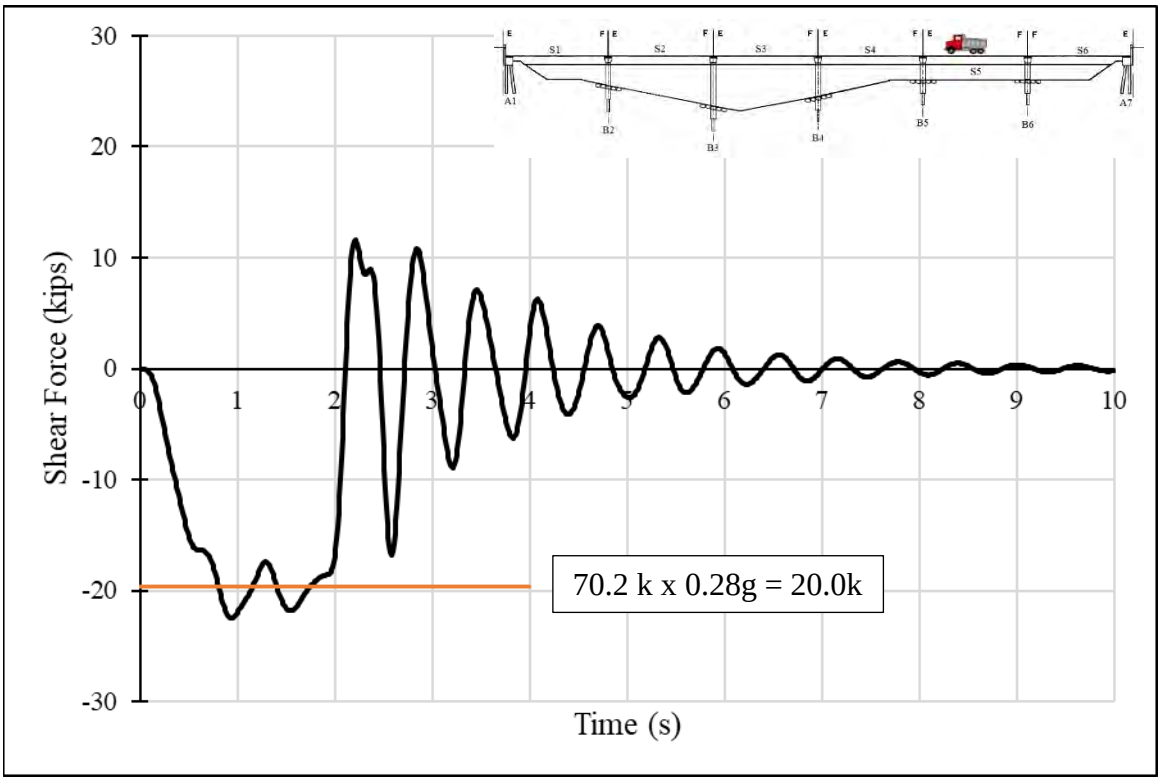

Figure 6-60 – Shear Force in Substructure from the Right Side of Span 5 Braking Test 1

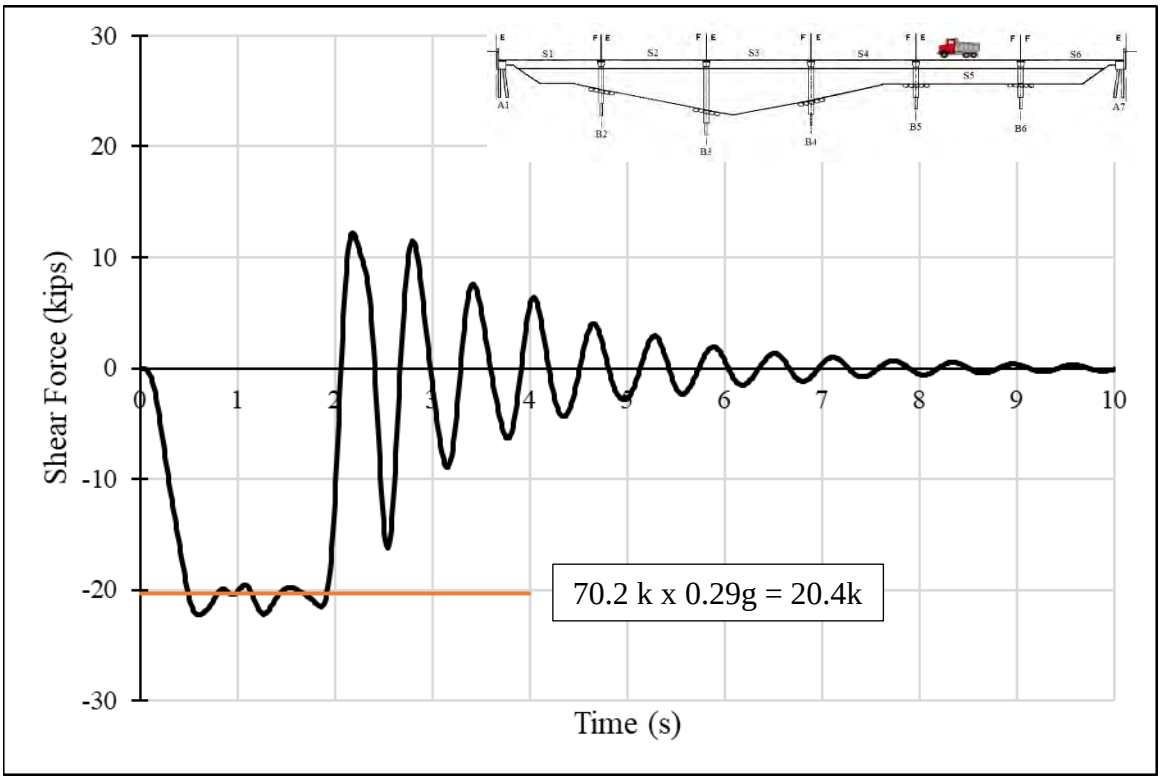

Figure 6-61 – Shear Force in Substructure from the Right Side of Span 5 Braking Test 3

6.5.4 Analysis of Dynamic Force Distribution

When analyzing each test's shear force, the peak value is approximately equal to the static horizontal braking force. The distribution of the total force among the components is more difficult to track in a dynamic situation. Figure 6-62 through Figure 6-103 show the shear forces of each abutment or bent compared to the total shear force experienced by the entire substructure for the test deemed best from every span loading condition. The jumps in percentages and occasional steep drop offs in the percentage of force felt by the member results from the total amount of force in the entire substructure being very small, therefore, that component at that time step could be responsible for almost the entire force even though it is experiencing a small shear force itself.

The best test was selected by which model corresponded best to the field data, and in the situation where only one trial was conducted for a given loading condition this was because only the best test from the field data was processed and available for comparisons. The tests that were determined best were: center of Span 2 Test 1, center of Span 3 Test 4, center of Span 5 Test 2,

the right side of Span 2 Test 2, the right side of Span 3 Test 3, and the right side of Span 5 Test 1.

6.5.4.1 Horizontal Substructure Forces Resulting from Braking at Center of Span 2

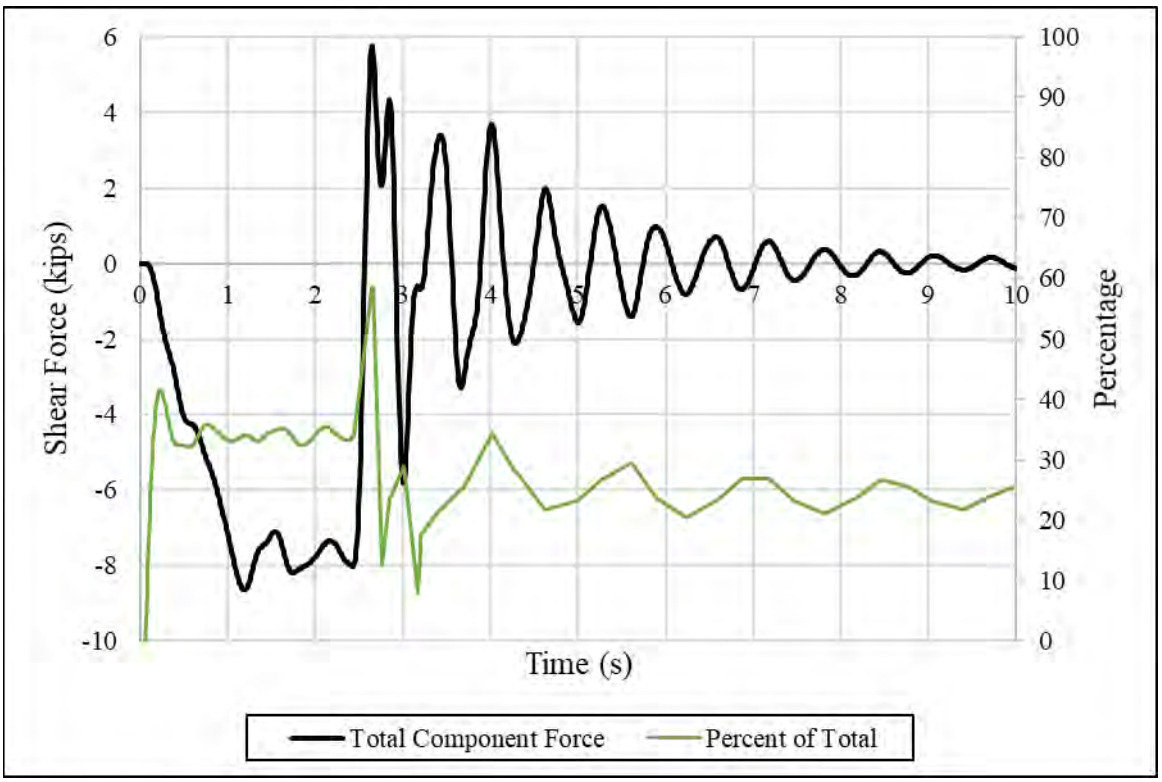

Figure 6-62 – Abutment 1 Horizontal Force due to Braking at Center of Span 2

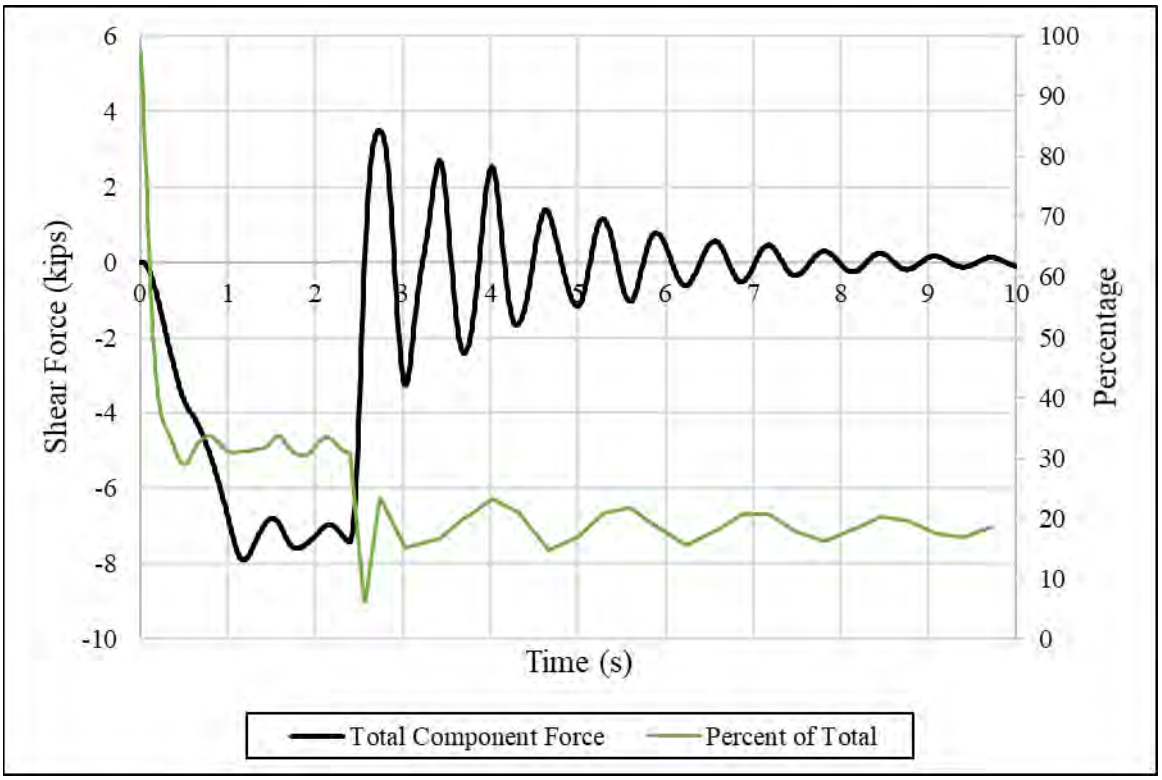

Figure 6-63 – Bent 2 Horizontal Force due to Braking at Center of Span 2

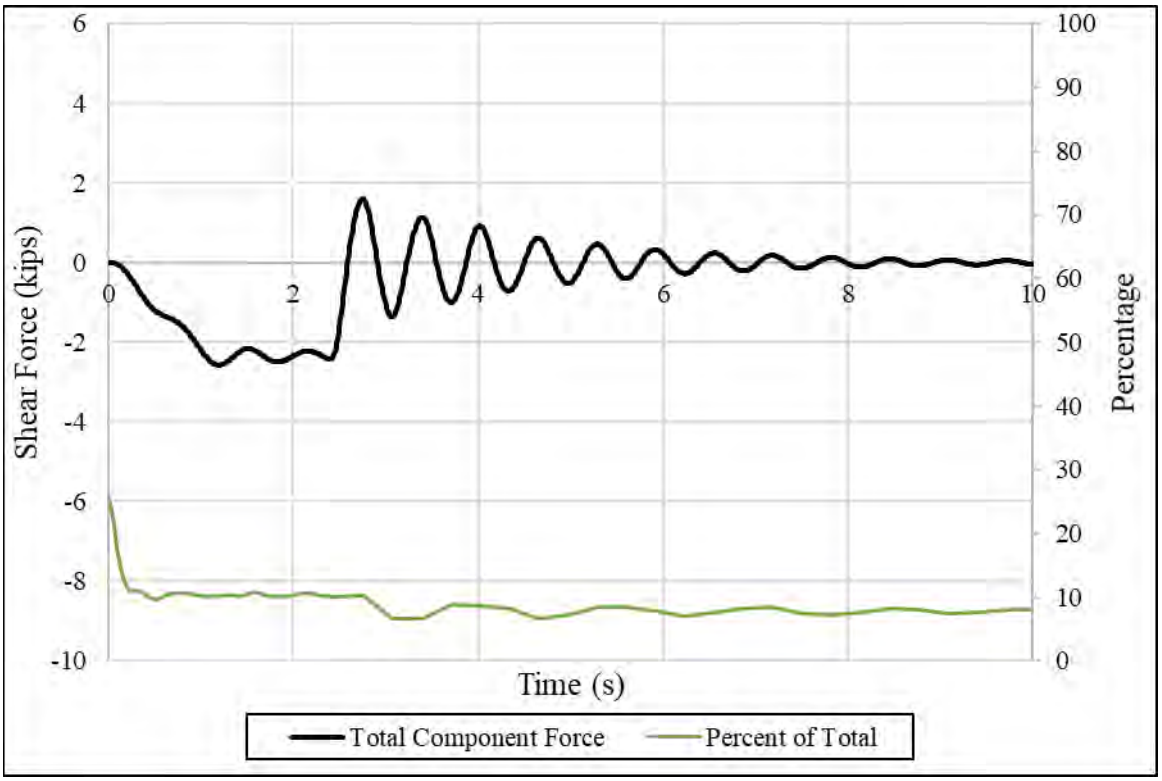

Figure 6-64 – Bent 3 Horizontal Force due to Braking at Center of Span 2

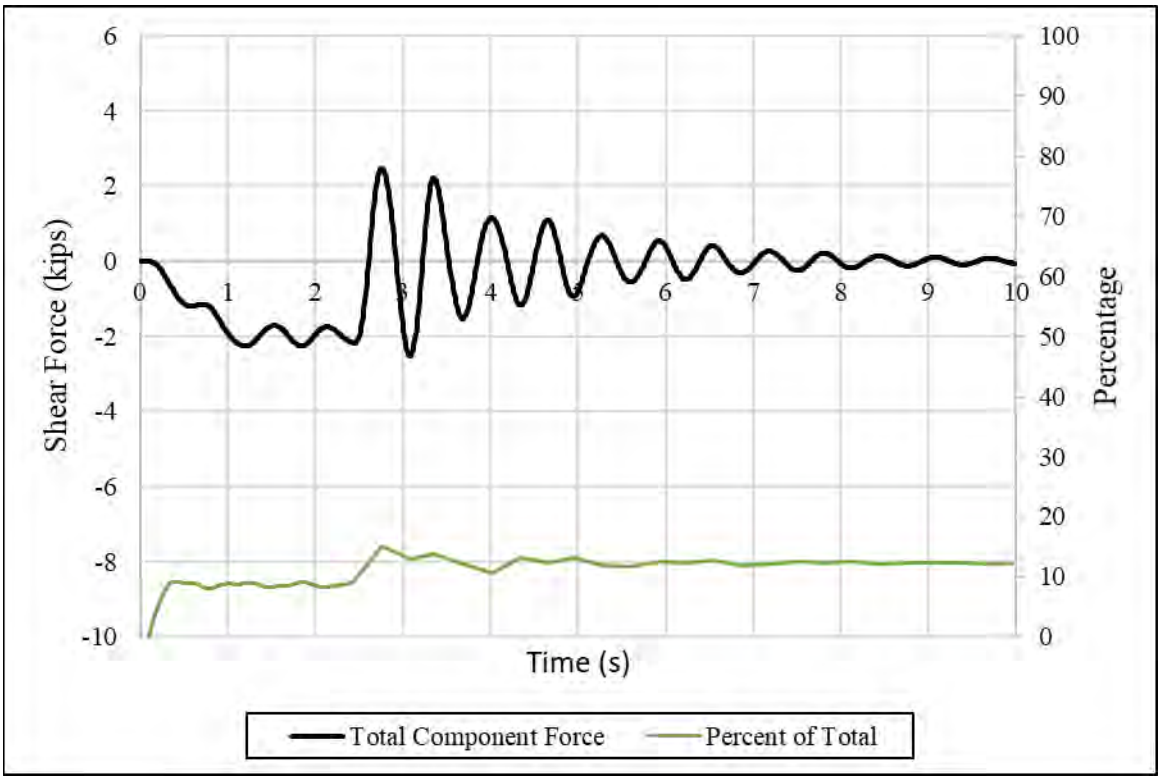

Figure 6-65 – Bent 4 Horizontal Force due to Braking at Center of Span 2

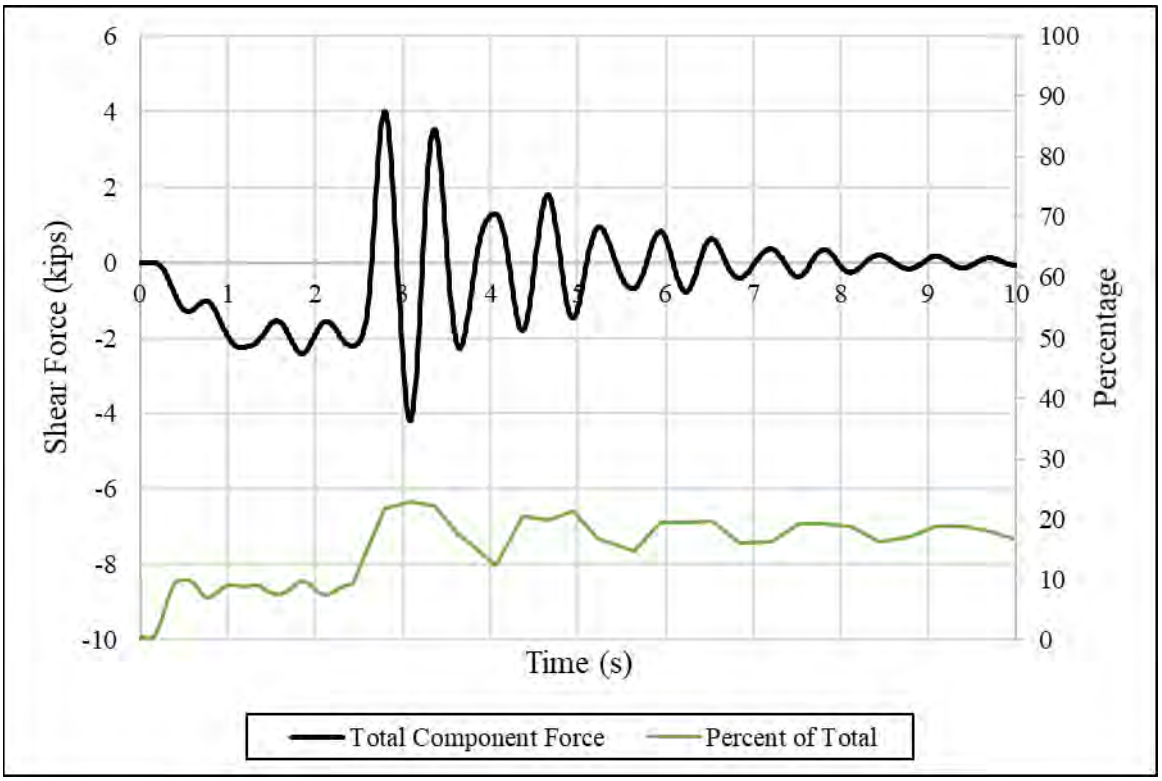

Figure 6-66 – Bent 5 Horizontal Force due to Braking at Center of Span 2

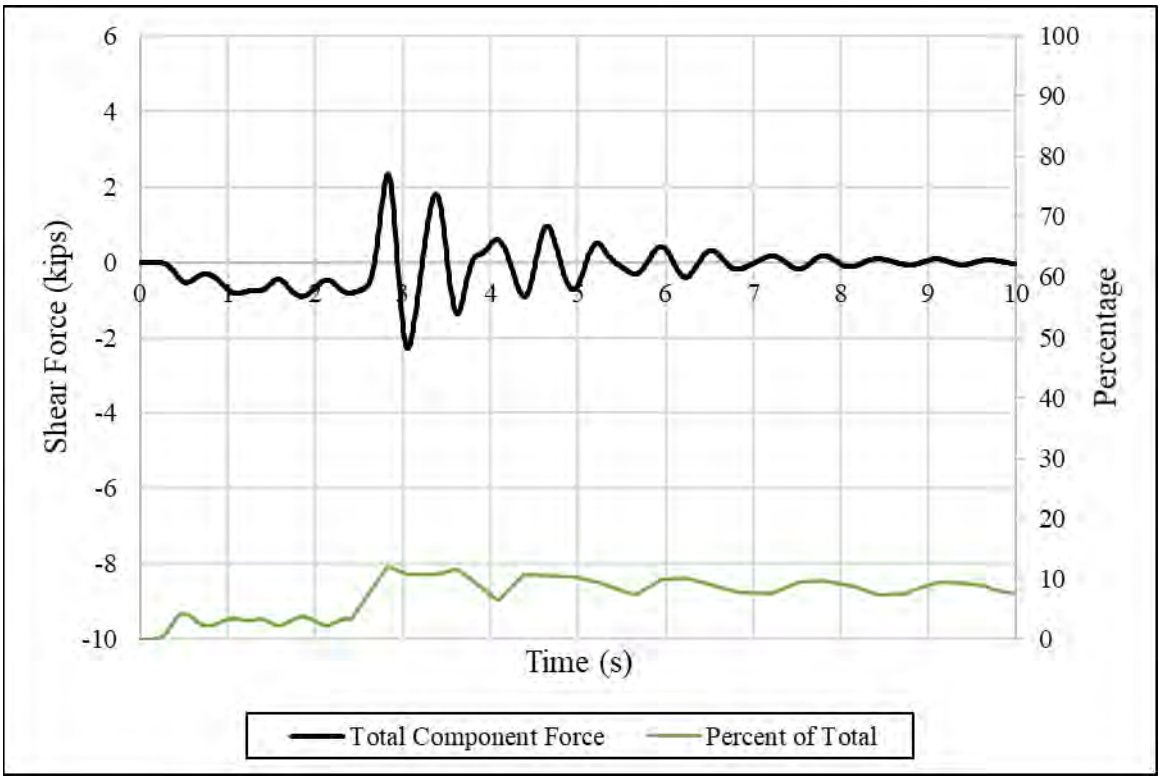

Figure 6-67 – Bent 6 Horizontal Force due to Braking at Center of Span 2

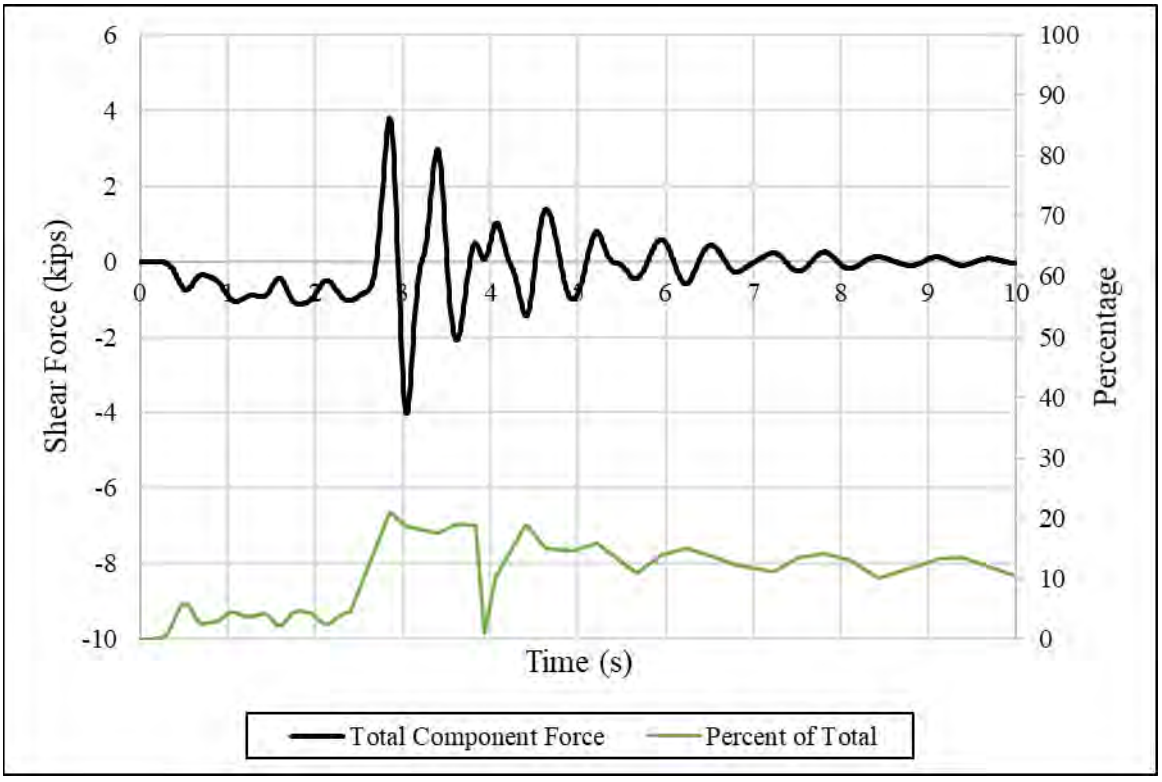

Figure 6-68 – Abutment 7 Horizontal Force due to Braking at Center of Span 2

For this test, the maximum total horizontal shear force from the truck braking from the entire substructure was approximately 23 kips. When broken down by component, Abutment 1 and Bent 2 carried the greatest portion of the applied force. Abutment 1 peaked at approximately 31 percent, 7.9 kips, and Bent 2 peaked at approximately 31 percent of the total, 7.5 kips. This is similar to the static test where Abutment 1 felt the greatest shear force, closely followed by the amount of force in Bent 2. Beyond the span that the braking occurred on, the amount of individual bent or abutment shear force remained relatively low, at or below 20 percent of the entire force in the whole substructure.

6.5.4.2 Horizontal Substructure Forces Resulting from Braking at Center of Span 3

From the three tests conducted on Span 3, the third test provided the best data. Figure 6-69 through Figure 6-75 presents the horizontal shear force in each bent or abutment compared to the total horizontal shear force experienced by the entire substructure for this test.

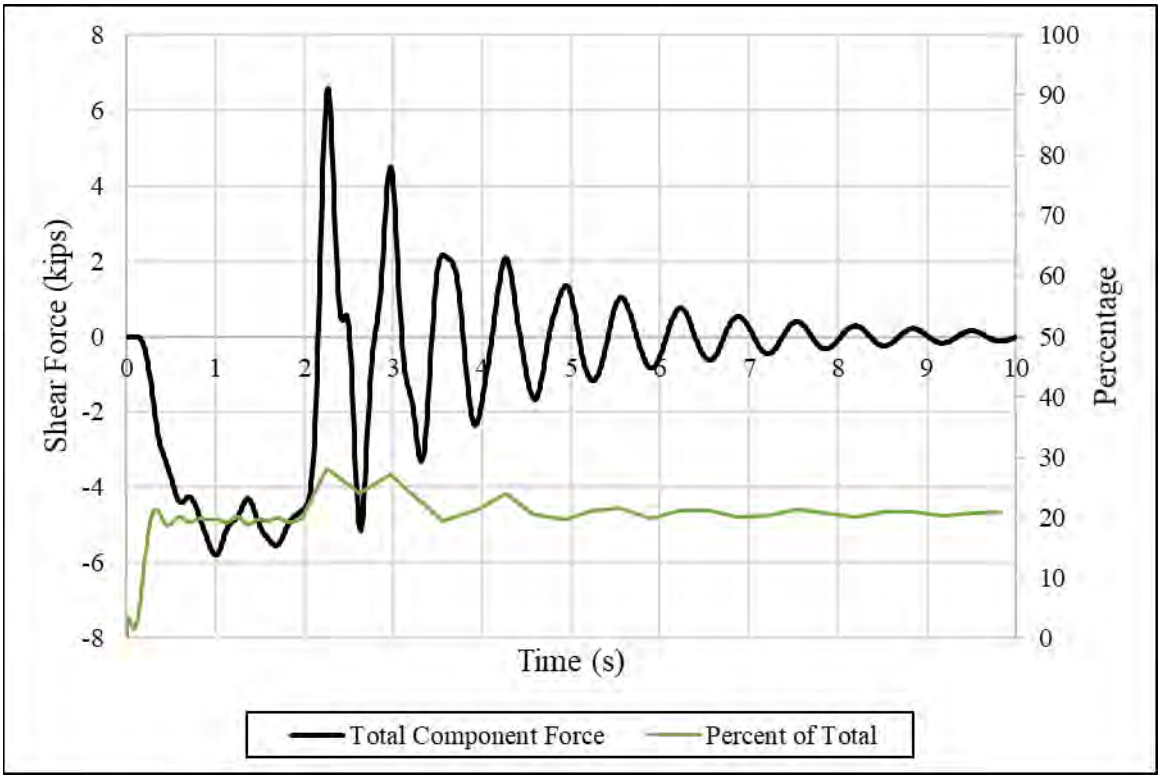

Figure 6-69 – Abutment 1 Horizontal Force due to Braking at Center of Span 3

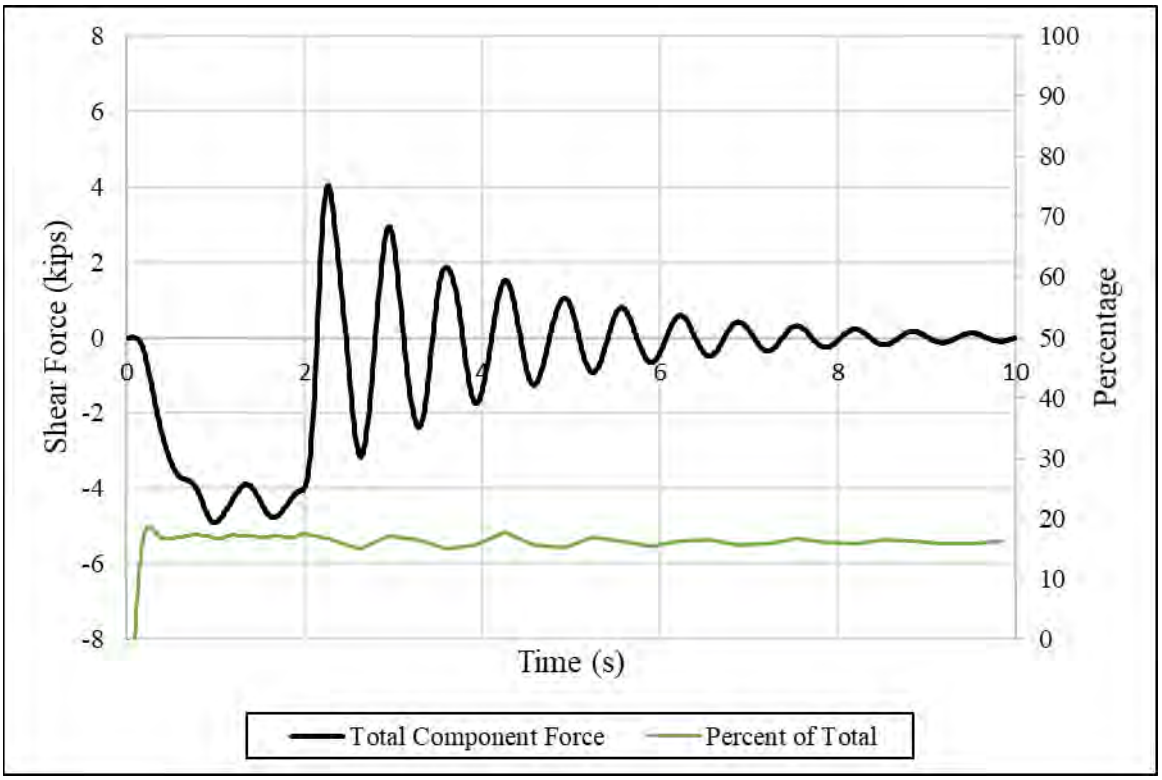

Figure 6-70 – Bent 2 Horizontal Force due to Braking at Center of Span 3

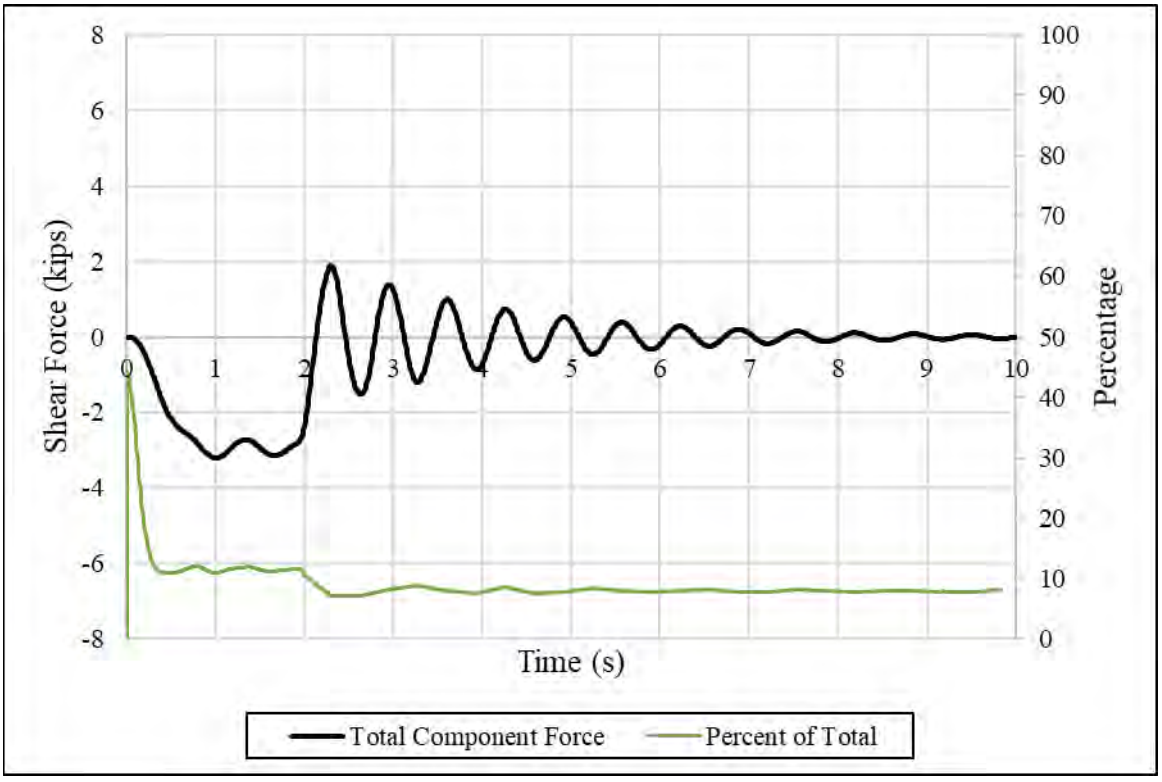

Figure 6-71 – Bent 3 Horizontal Force due to Braking at Center of Span 3

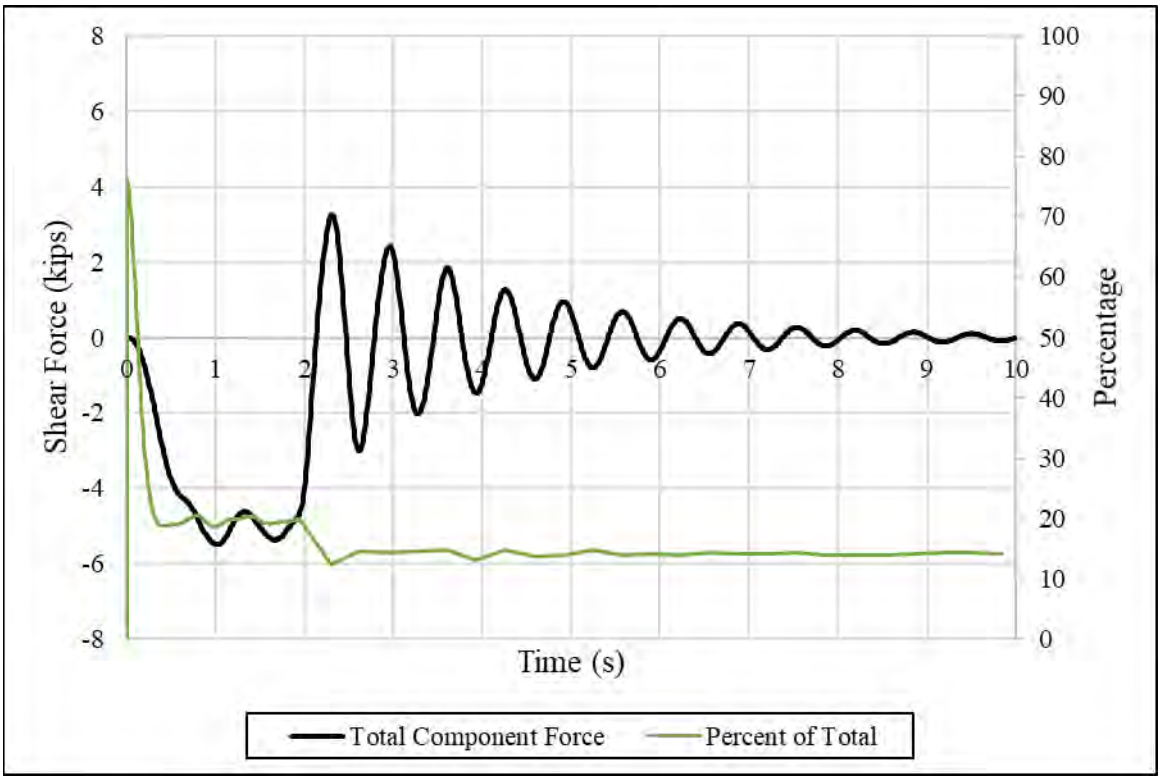

Figure 6-72 – Bent 4 Horizontal Force due to Braking at Center of Span 3

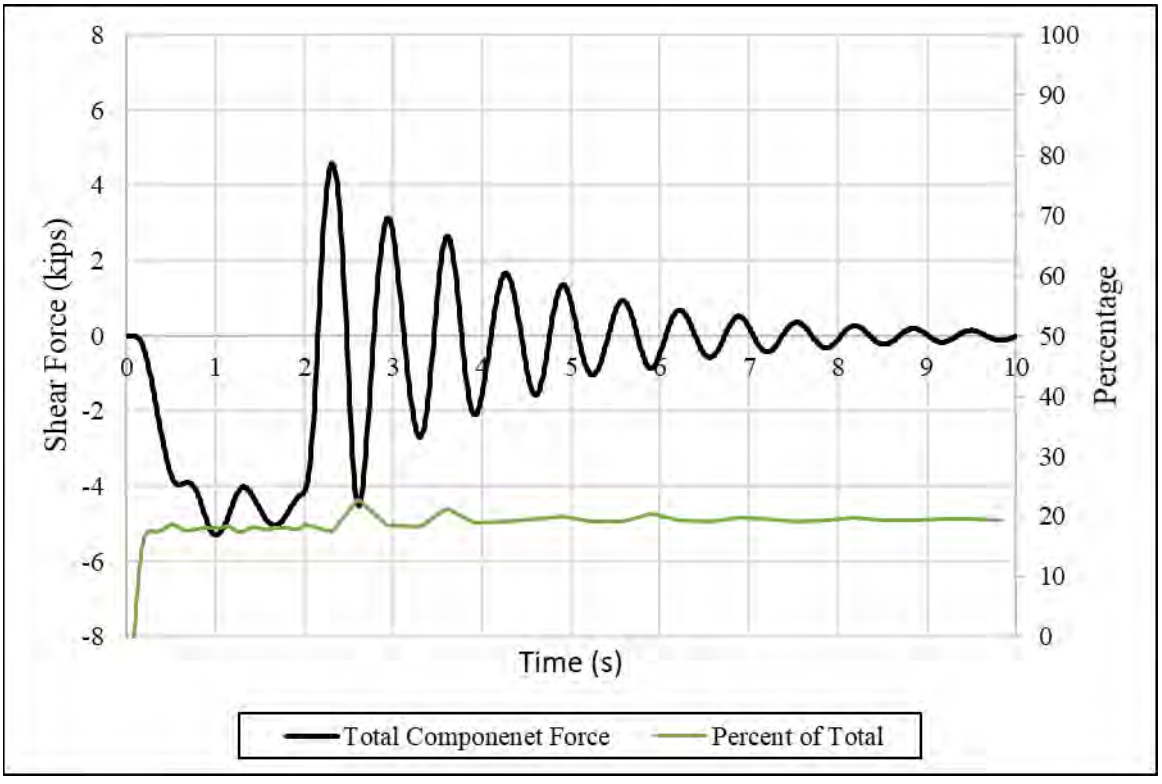

Figure 6-73 – Bent 5 Horizontal Force due to Braking at Center of Span 3

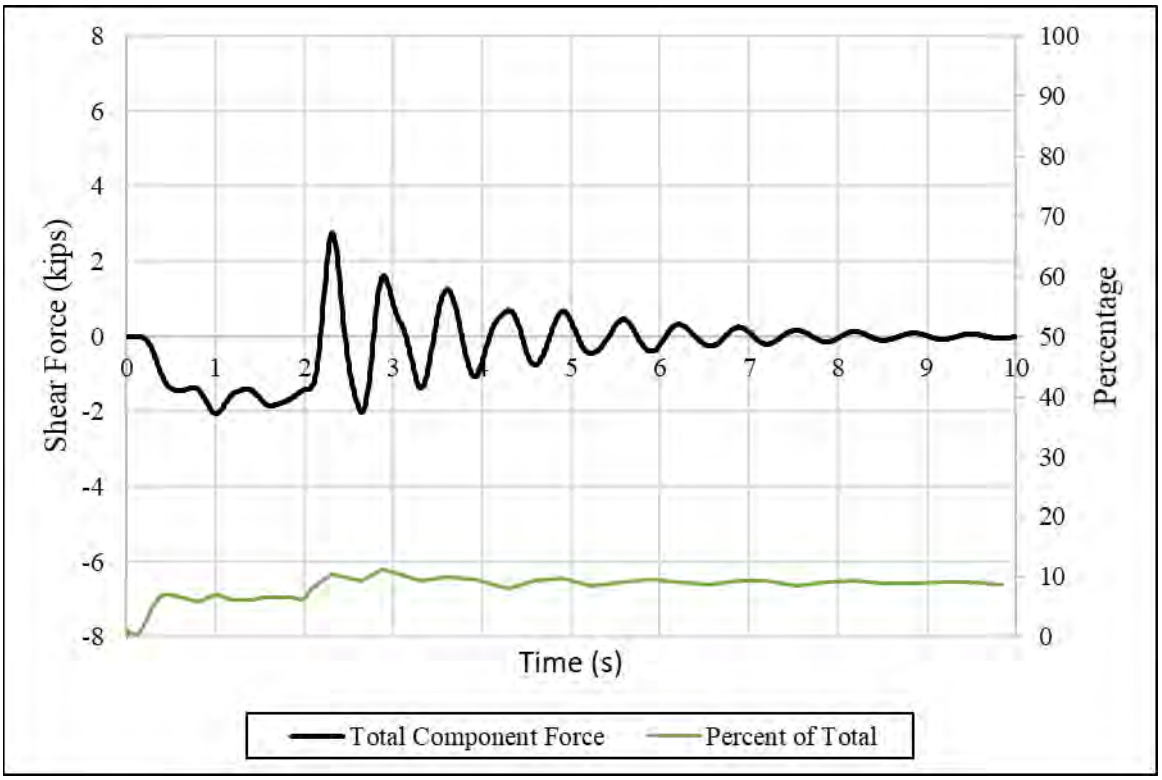

Figure 6-74 – Bent 6 Horizontal Force due to Braking at Center of Span 3

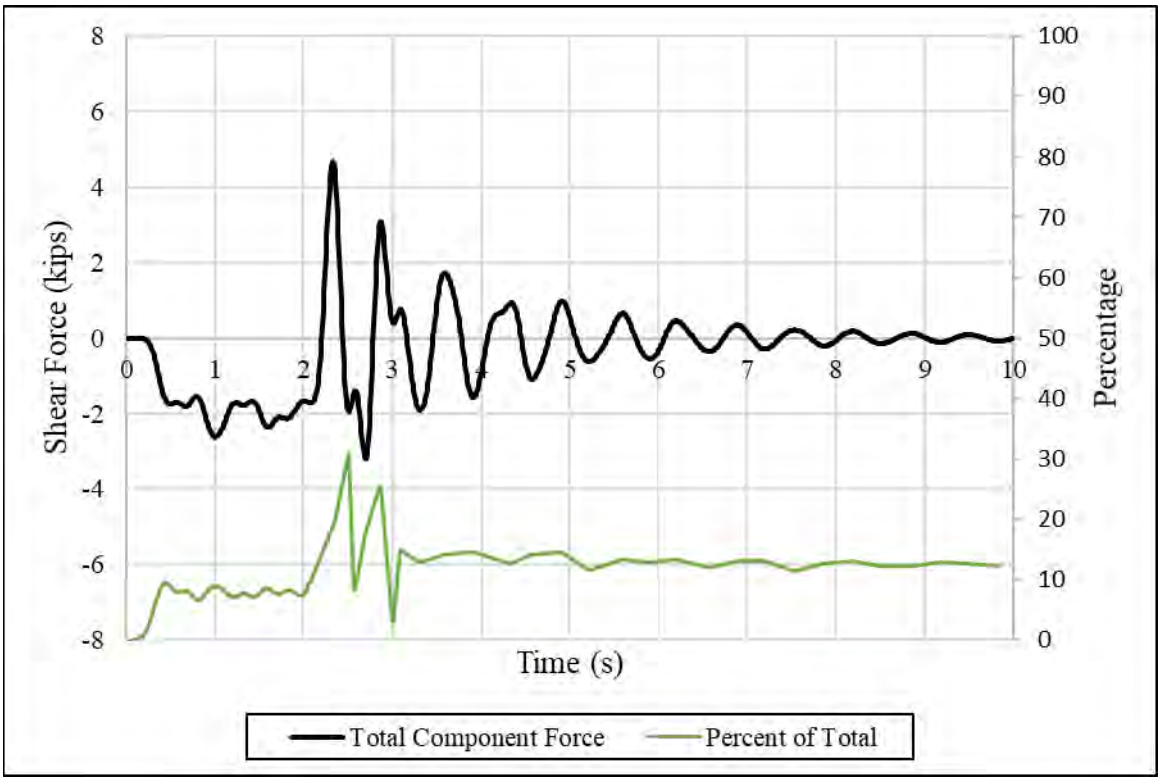

Figure 6-75 – Abutment 7 Horizontal Force due to Braking at Center of Span 3

On Test 4 of the center of Span 3, Abutment 1 and Bent 4 were the components that experienced the highest horizontal shear force. Abutment 1 experienced 6.6 kips, approximately 24 percent, and Bent 4 felt approximately 20 percent of the total force, resulting in about 5 kips in each member. The maximum total horizontal force experienced during this test was approximately 25 kips. During the free response phase, all components remained at or below 20 percent shear force distributed to them. This, again, corresponds to the static tests where one of the bents supporting the span that was loaded experienced a larger amount of force then other members.

6.5.4.3 Horizontal Substructure Forces Resulting from Braking at Center of Span 5

From the tests conducted on Span 5, the second test provided the best data. Figure 6-76 through Figure 6-82 present the horizontal shear force in each bent or abutment compared to the total horizontal shear force experienced by the entire substructure for this test.

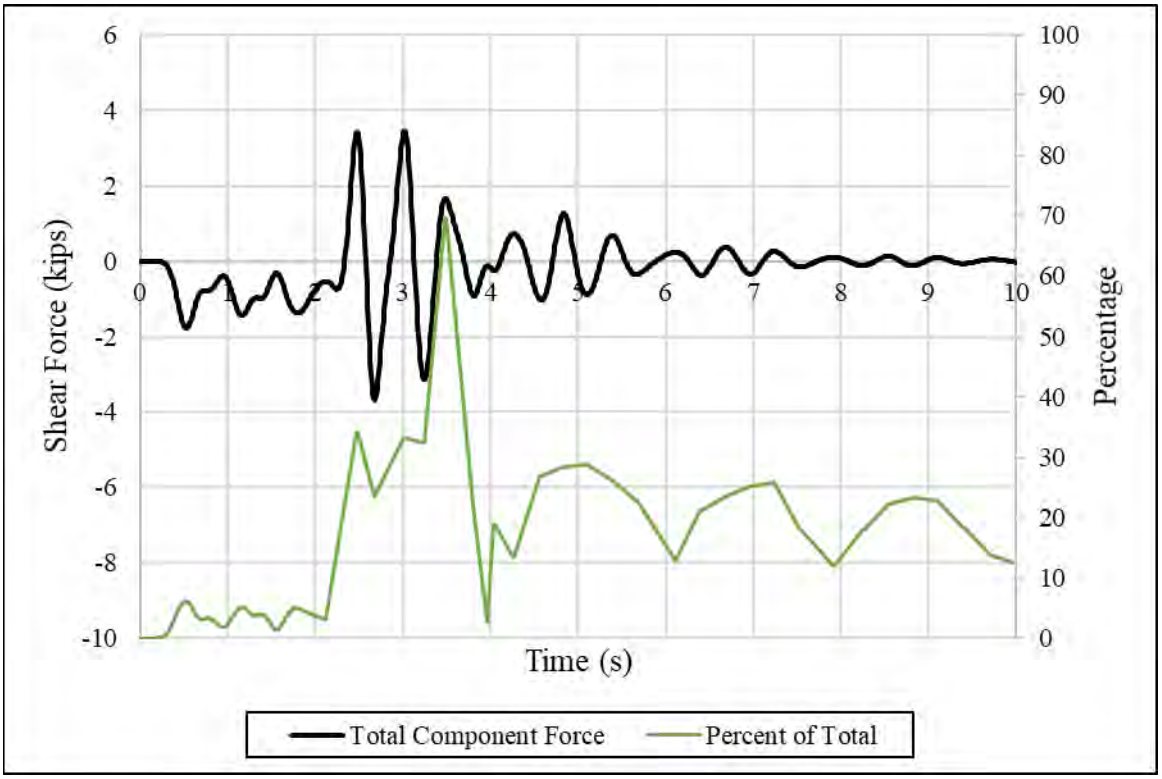

Figure 6-76 – Abutment 1 Horizontal Force due to Braking at Center of Span 5

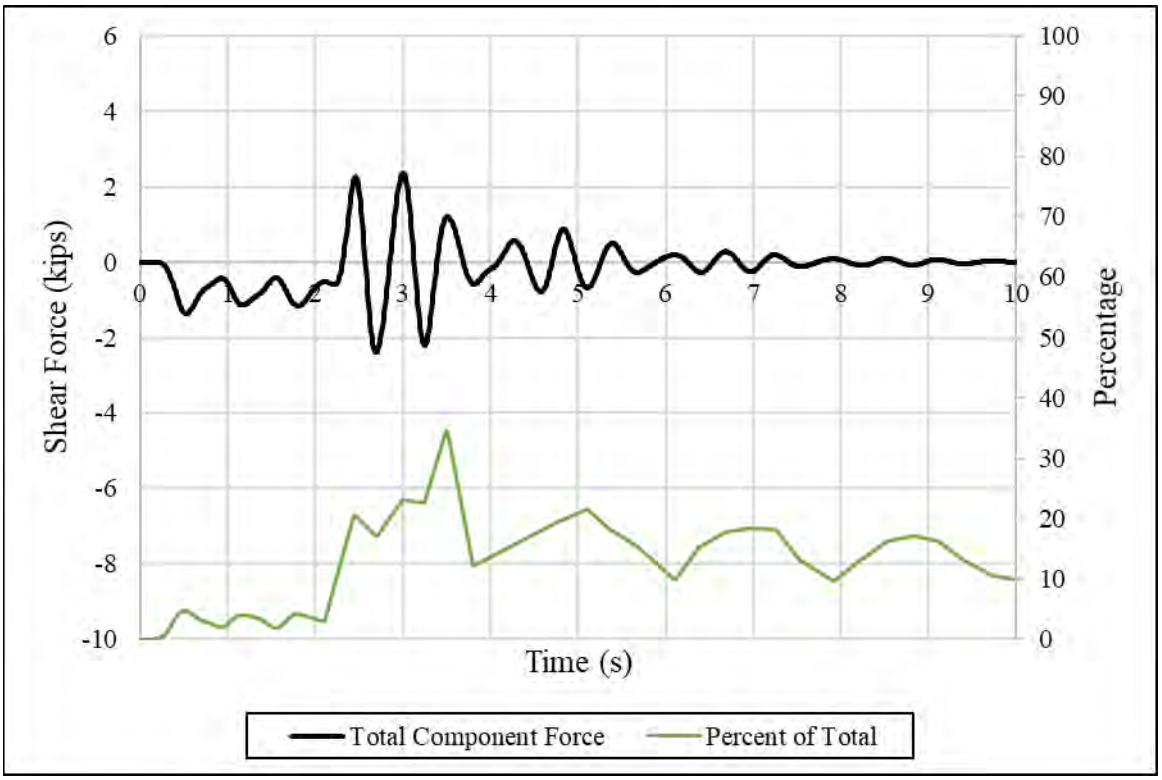

Figure 6-77 – Bent 2 Horizontal Force due to Braking at Center of Span 5

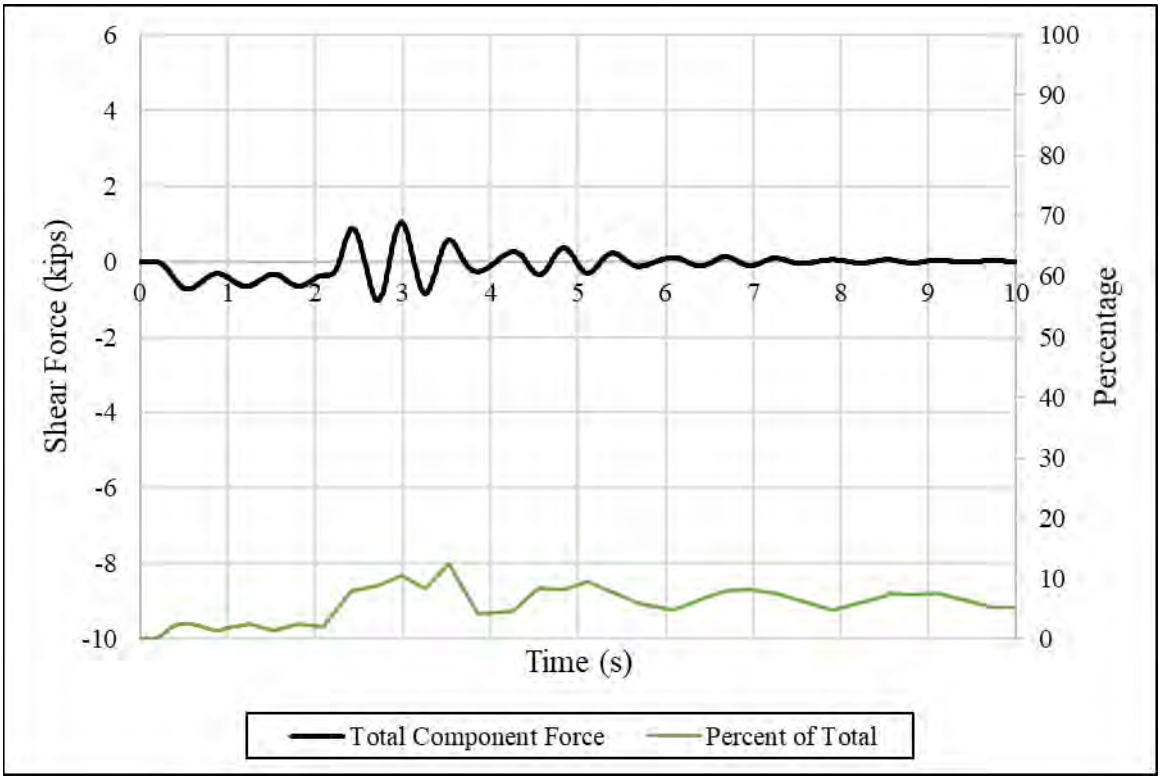

Figure 6-78 – Bent 3 Horizontal Force due to Braking at Center of Span 5

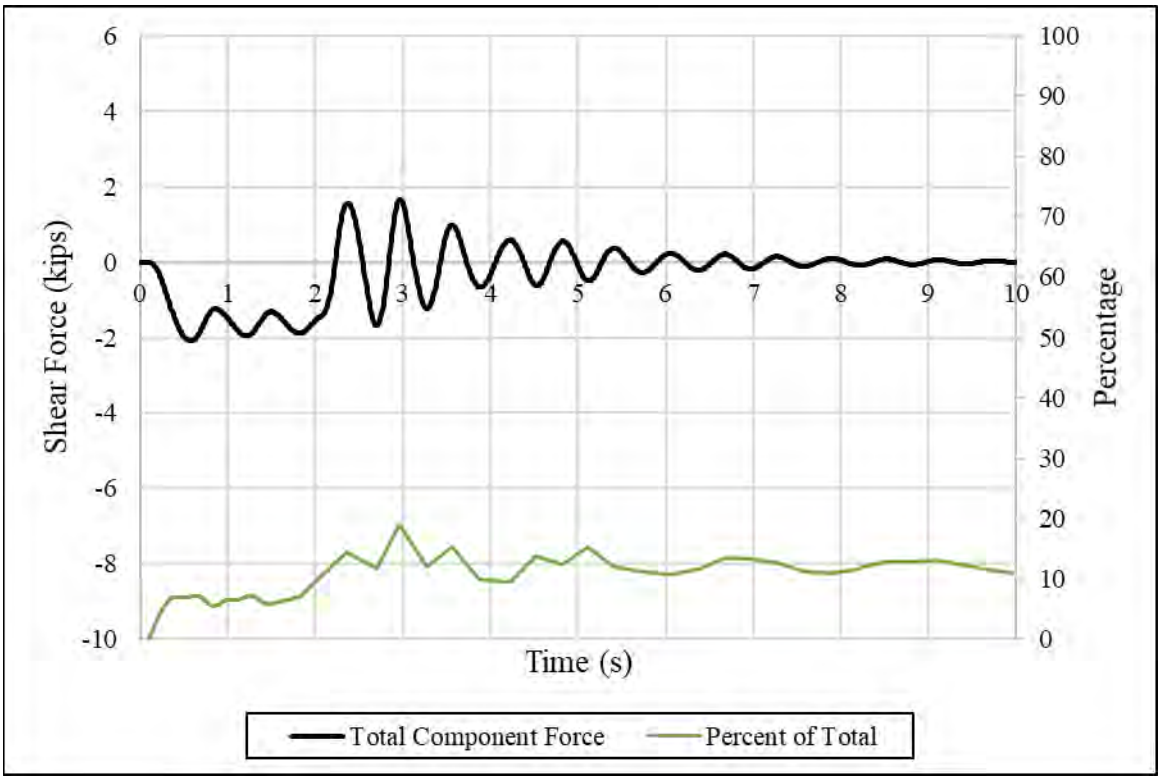

Figure 6-79 – Bent 4 Horizontal Force due to Braking at Center of Span 5

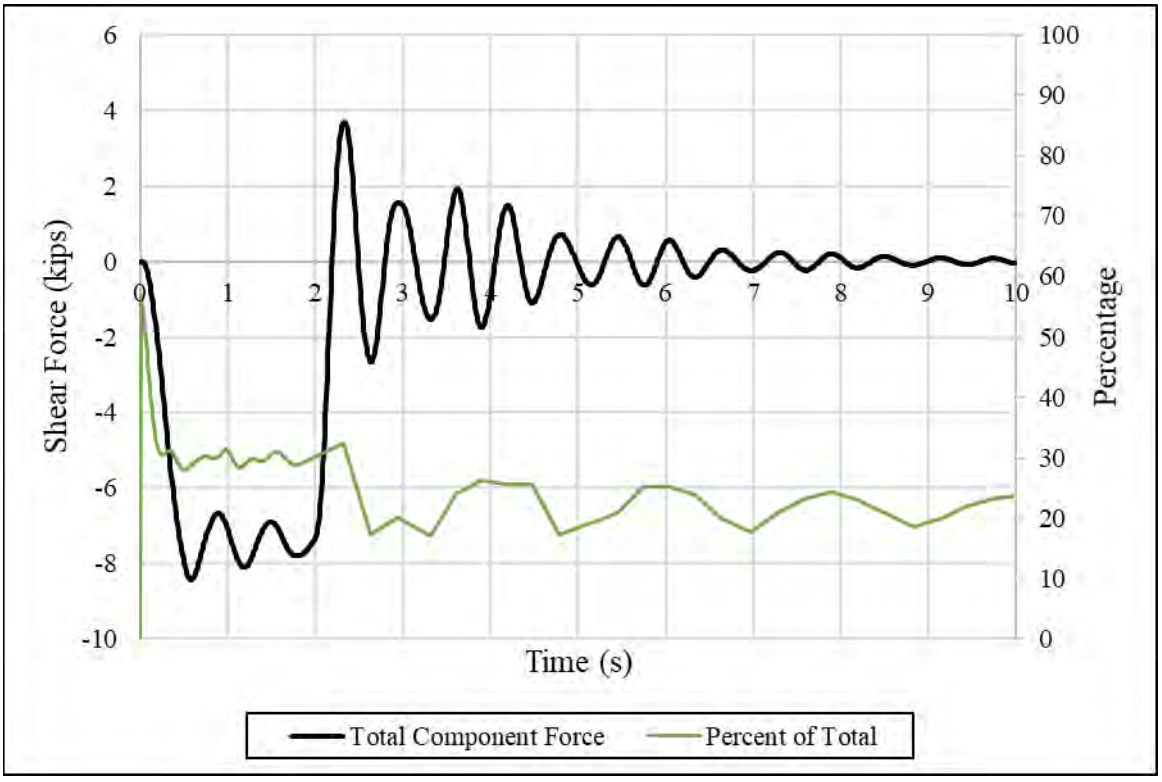

Figure 6-80 – Bent 5 Horizontal Force due to Braking at Center of Span 5

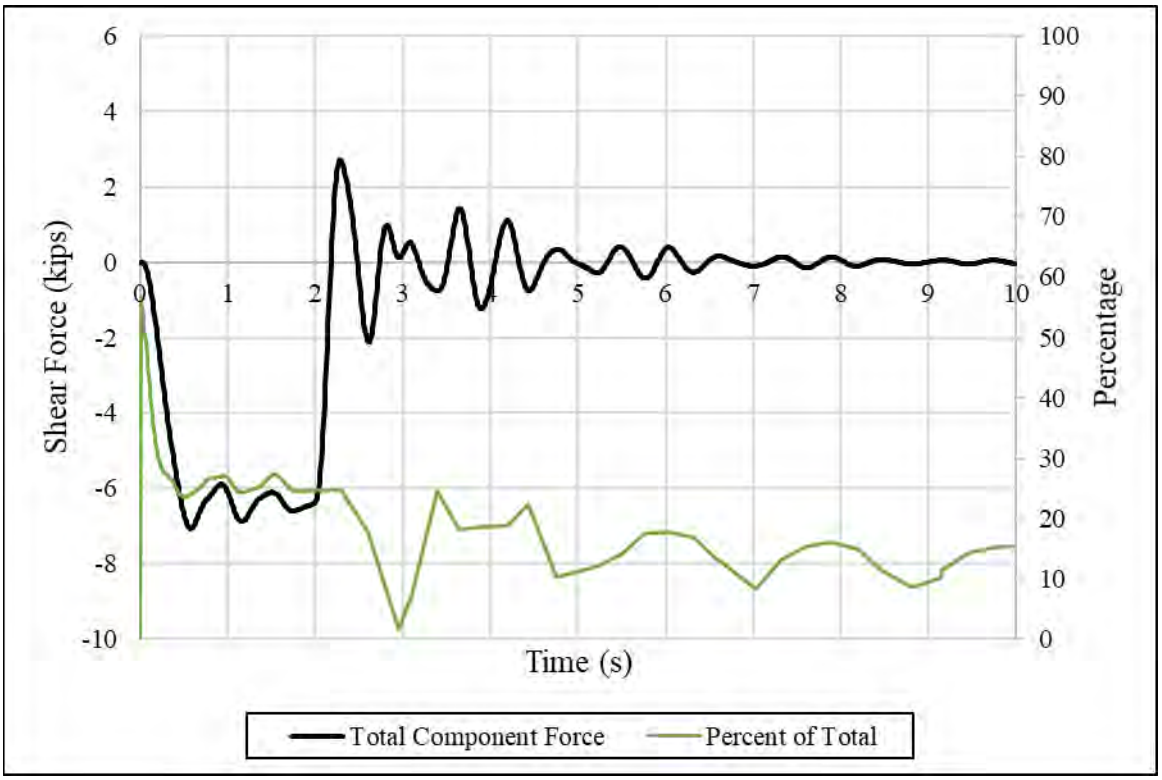

Figure 6-81 – Bent 6 Horizontal Force due to Braking at Center of Span 5

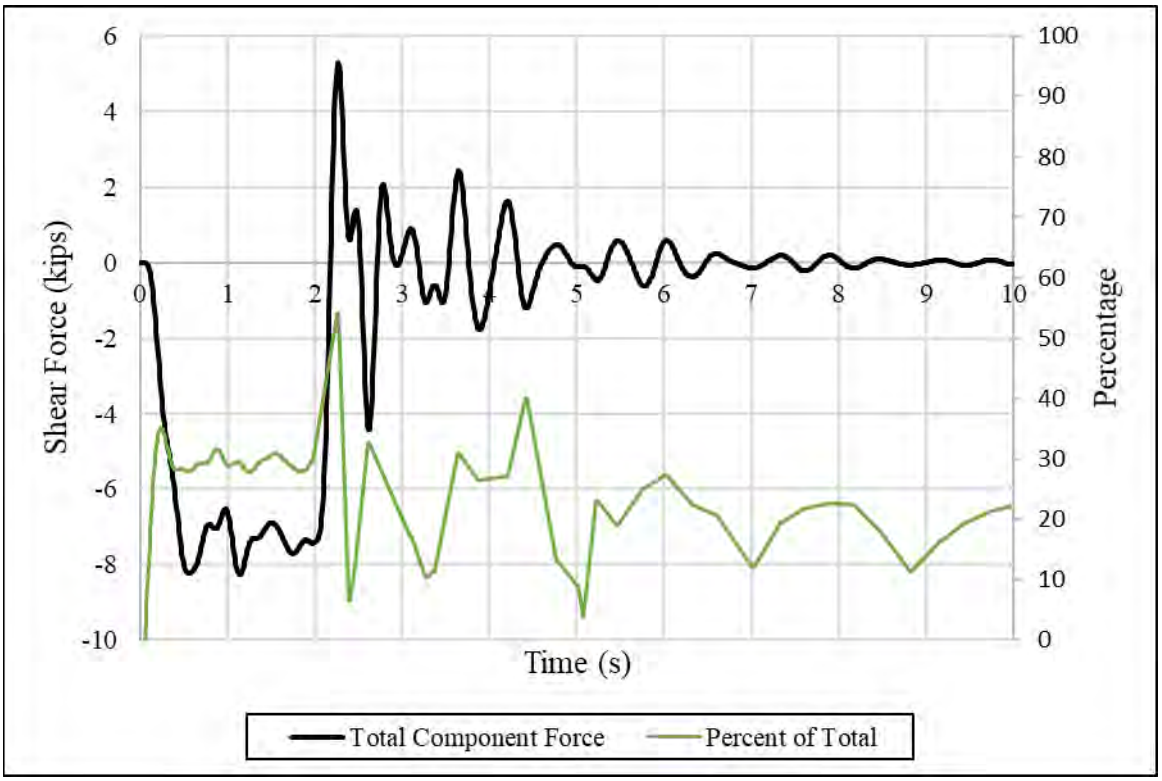

Figure 6-82 – Abutment 7 Horizontal Force due to Braking at Center of Span 5

With braking on Span 5, the maximum total horizontal shear force that was experienced in the entire substructure was approximately 25 kips. As with the previous two braking tests, one of the abutments experienced the greatest amount of force, for this test it was Abutment 7 since the braking occurred further down the bridge. Abutment 7 felt 30 percent of the total force from the entire substructure during the constant deceleration phase and approximately 7.6 kips at the maximum with a jump up to 53 percent of the total overall force during the initial phase of free response. Also, Bent 5 experienced a maximum of about 7.5 kips and experienced 30 percent of the total force.

6.5.4.4 Horizontal Substructure Forces Resulting from Braking on Right of Span 2

From the tests conducted on the right side of Span 2, the second test provided the best data. Figure 6-83 through Figure 6-89 presents the horizontal shear force in each bent or abutment compared to the total horizontal shear force experienced by the entire substructure for this test.

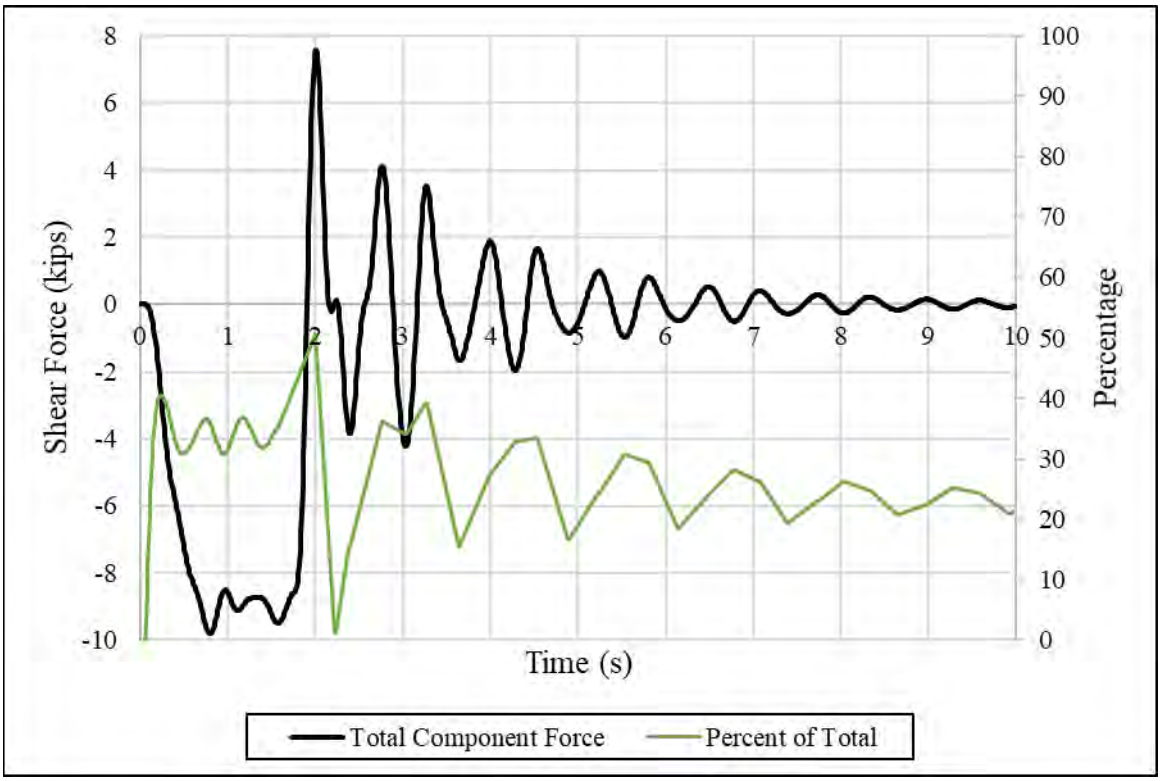

Figure 6-83 – Abutment 1 Horizontal Force due to Braking on Right of Span 2

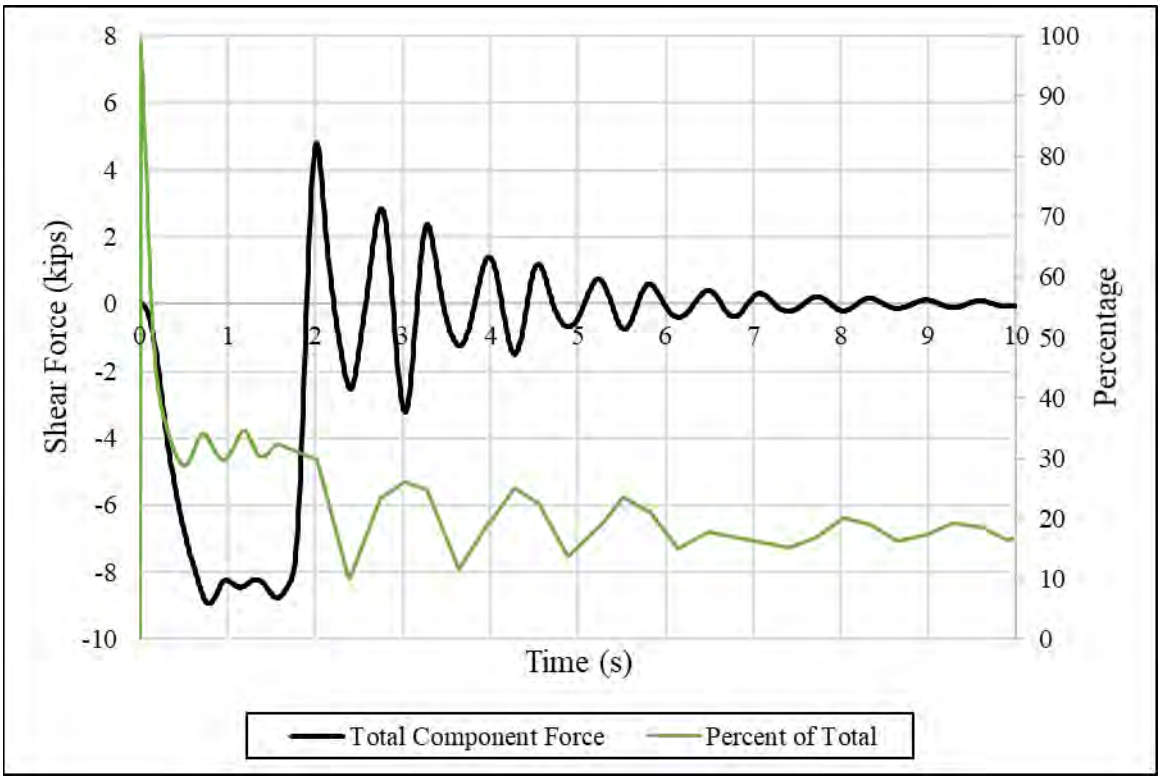

Figure 6-84 – Bent 2 Horizontal Force due to Braking on Right of Span 2

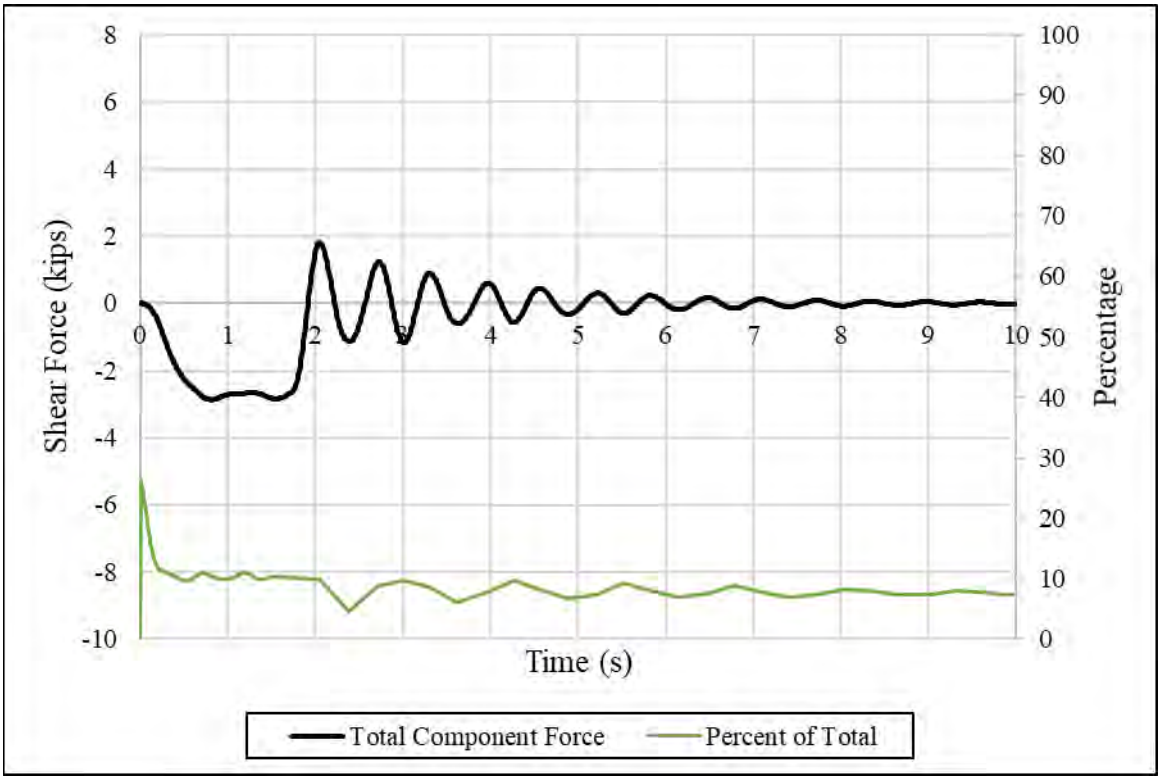

Figure 6-85 – Bent 3 Horizontal Force due to Braking on Right of Span 2

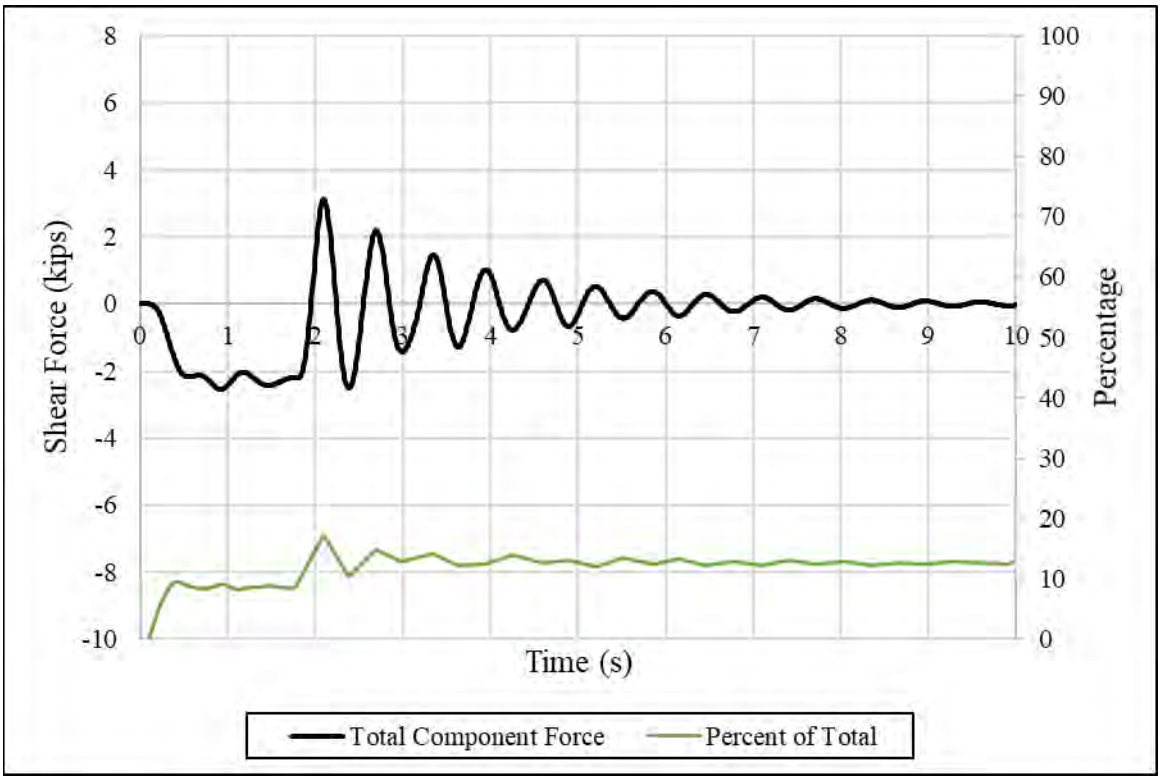

Figure 6-86 – Bent 4 Horizontal Force due to Braking on Right of Span 2

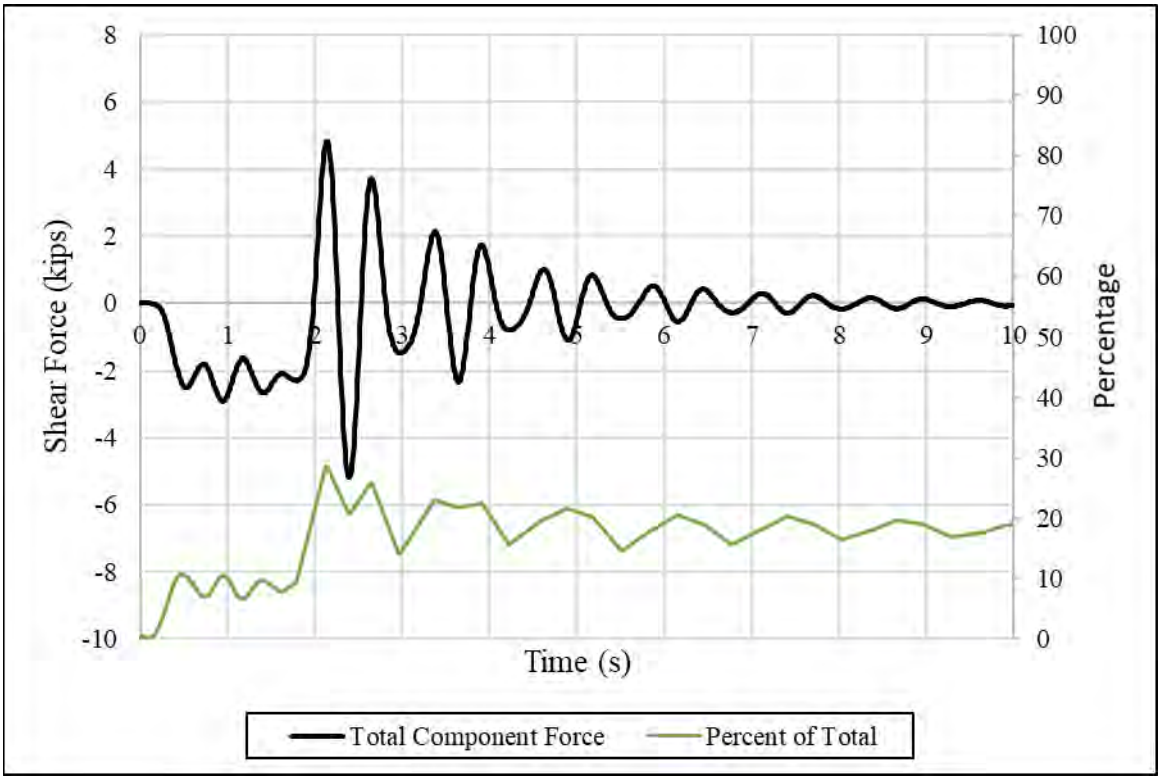

Figure 6-87 – Bent 5 Horizontal Force due to Braking on Right of Span 2

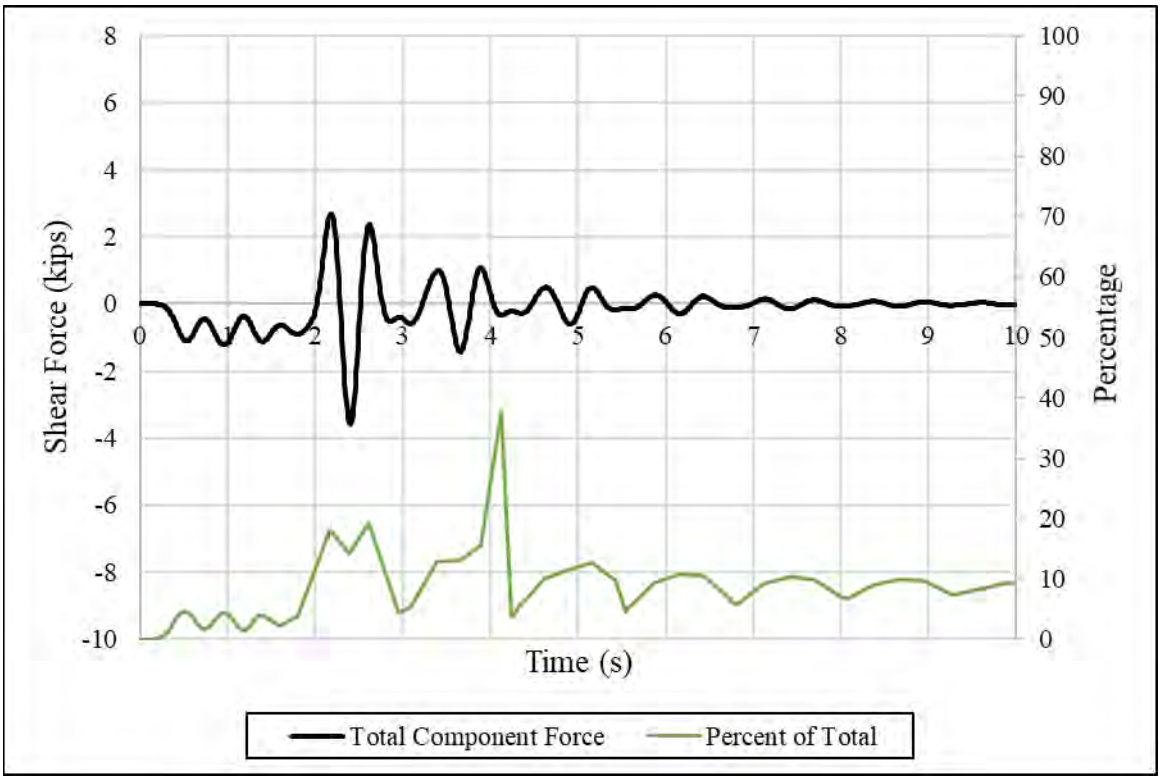

Figure 6-88 – Bent 6 Horizontal Force due to Braking on Right of Span 2

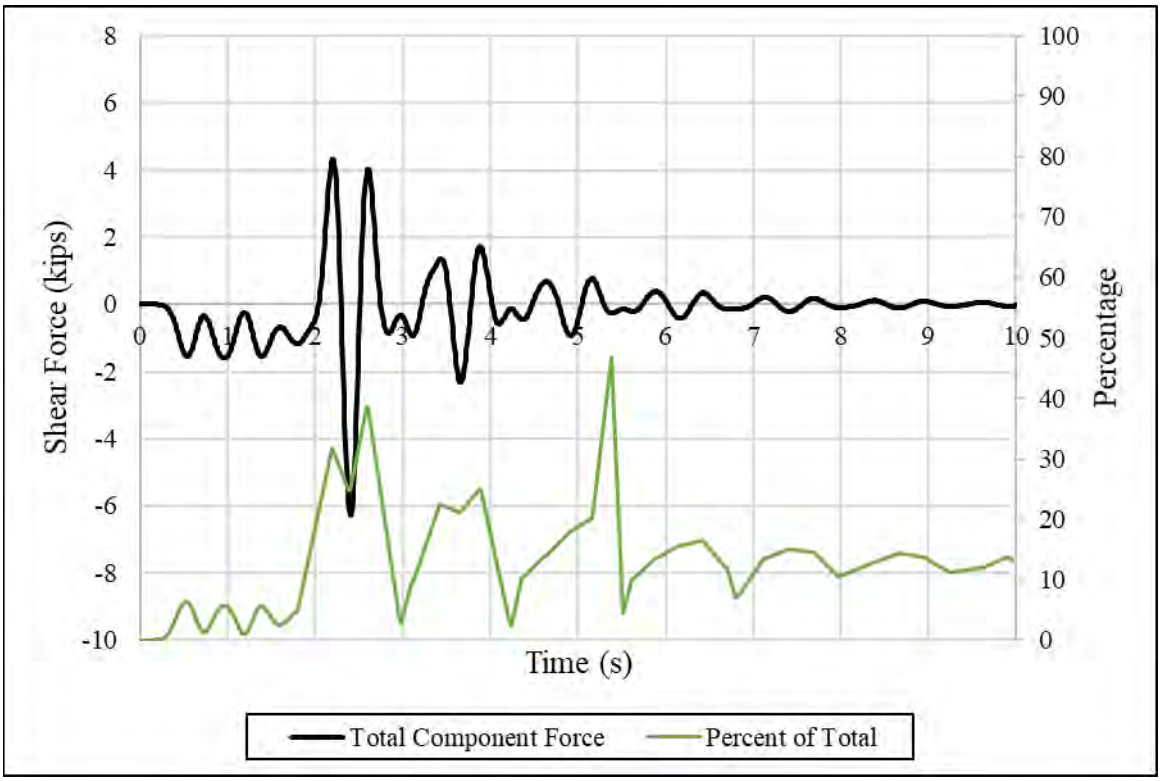

Figure 6-89 – Abutment 7 Horizontal Force due to Braking on Right of Span 2

Just as when braking occurred on Span 2 center, when braking on the right side, Abutment 1 and Bent 2 experienced the highest percentage of the overall force. Abutment 1 experienced a maximum of 33 percent, 8.9 kips, during braking and Bent 2 experienced 31 percent, 8.5 kips, respectively. The maximum total horizontal shear force experienced by the whole substructure during this test was approximately 26 kips.

6.5.4.5 Horizontal Substructure Forces Resulting from Braking on Right of Span 3

From the tests conducted on the right side of span 3, the third test provided the best data. Figure 6-90 through Figure 6-96 present the horizontal shear force in each bent or abutment compared to the total horizontal shear force experienced by the entire substructure for this test.

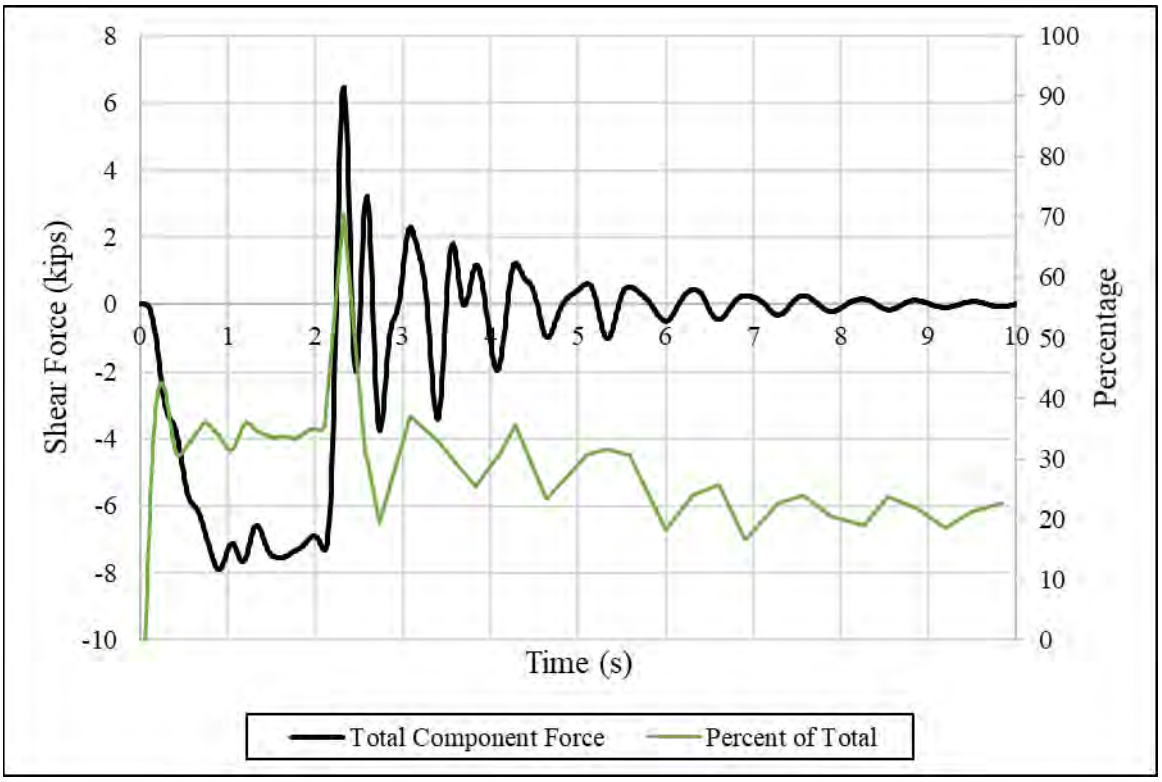

Figure 6-90 – Abutment 1 Horizontal Force due to Braking on Right of Span 3

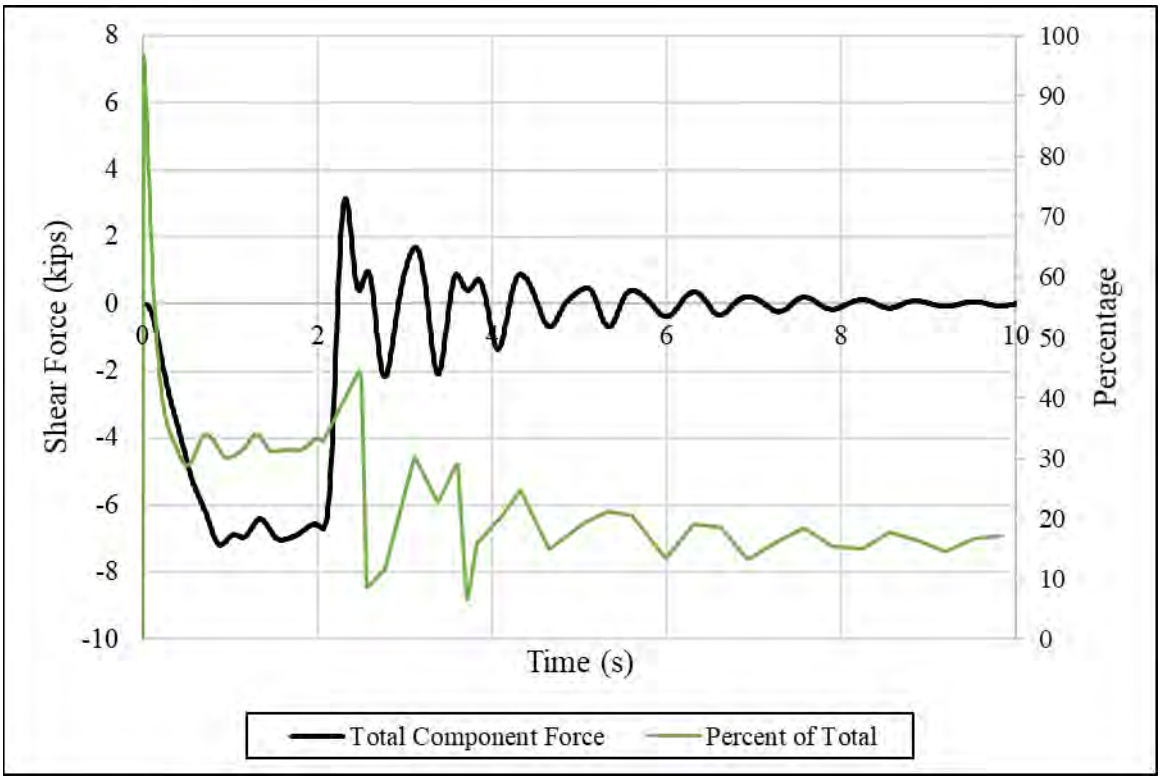

Figure 6-91 – Bent 2 Horizontal Force due to Braking on Right of Span 3

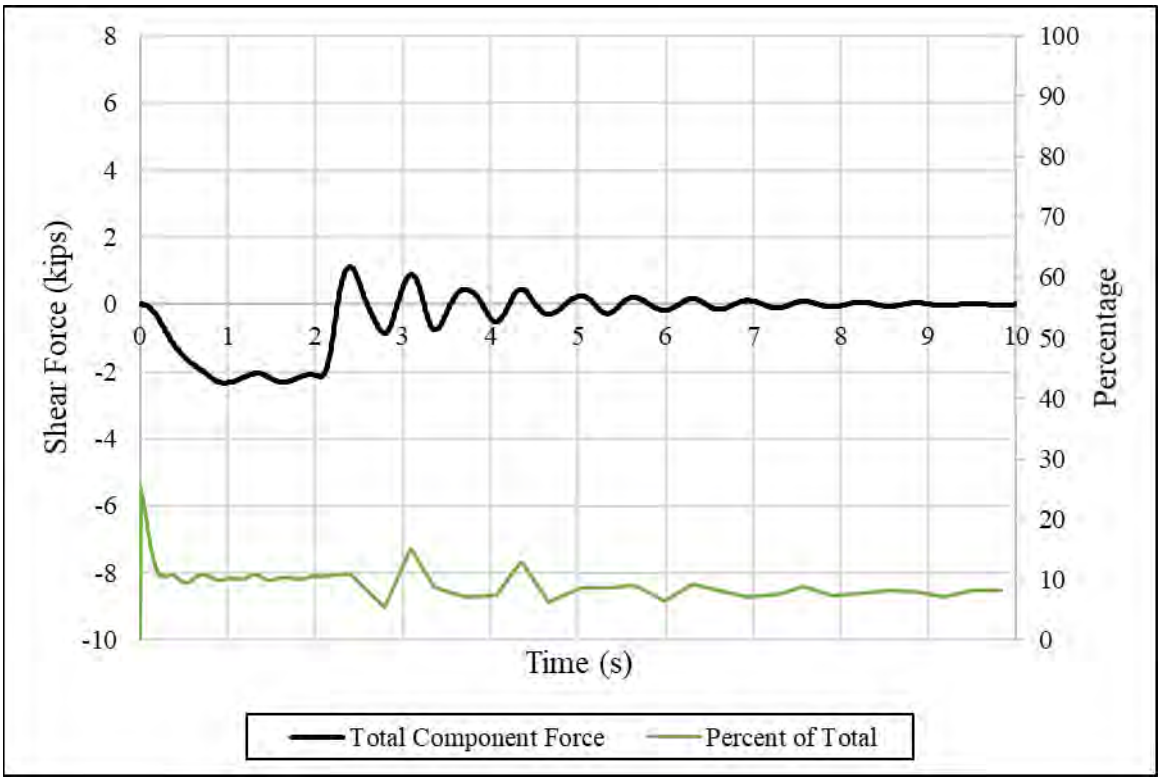

Figure 6-92 – Bent 3 Horizontal Force due to Braking on Right of Span 3

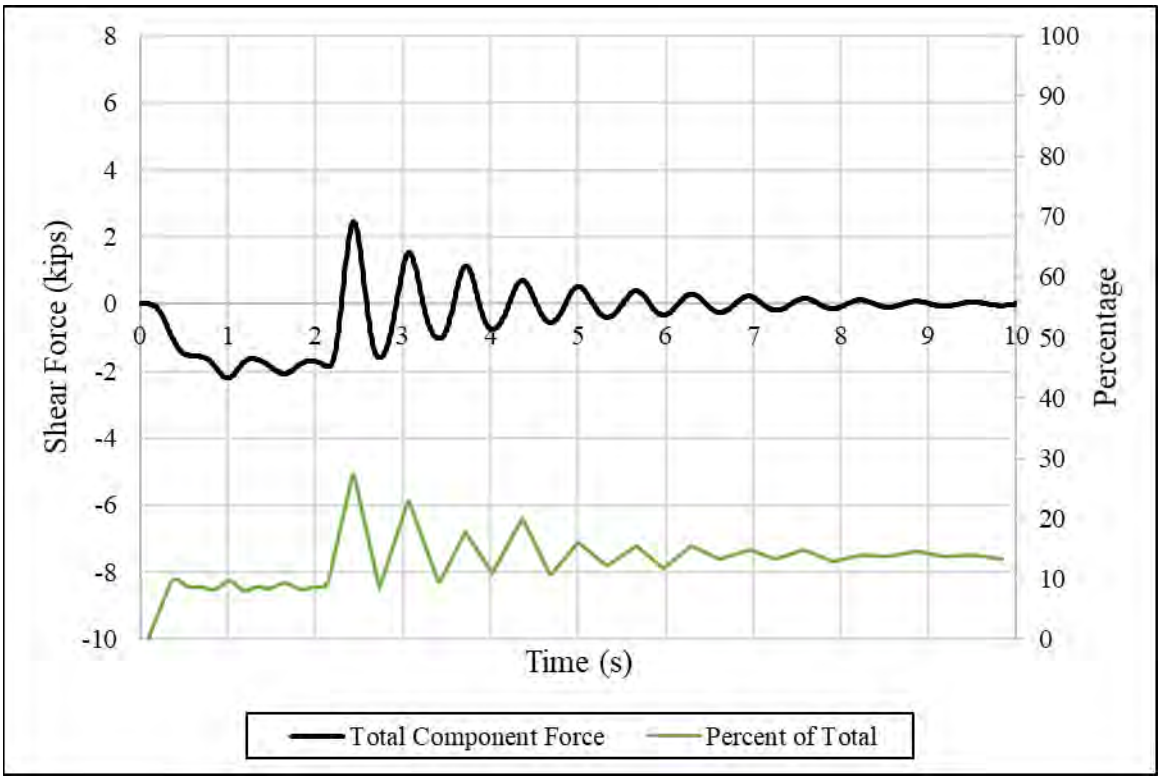

Figure 6-93 – Bent 4 Horizontal Force due to Braking on Right of Span 3

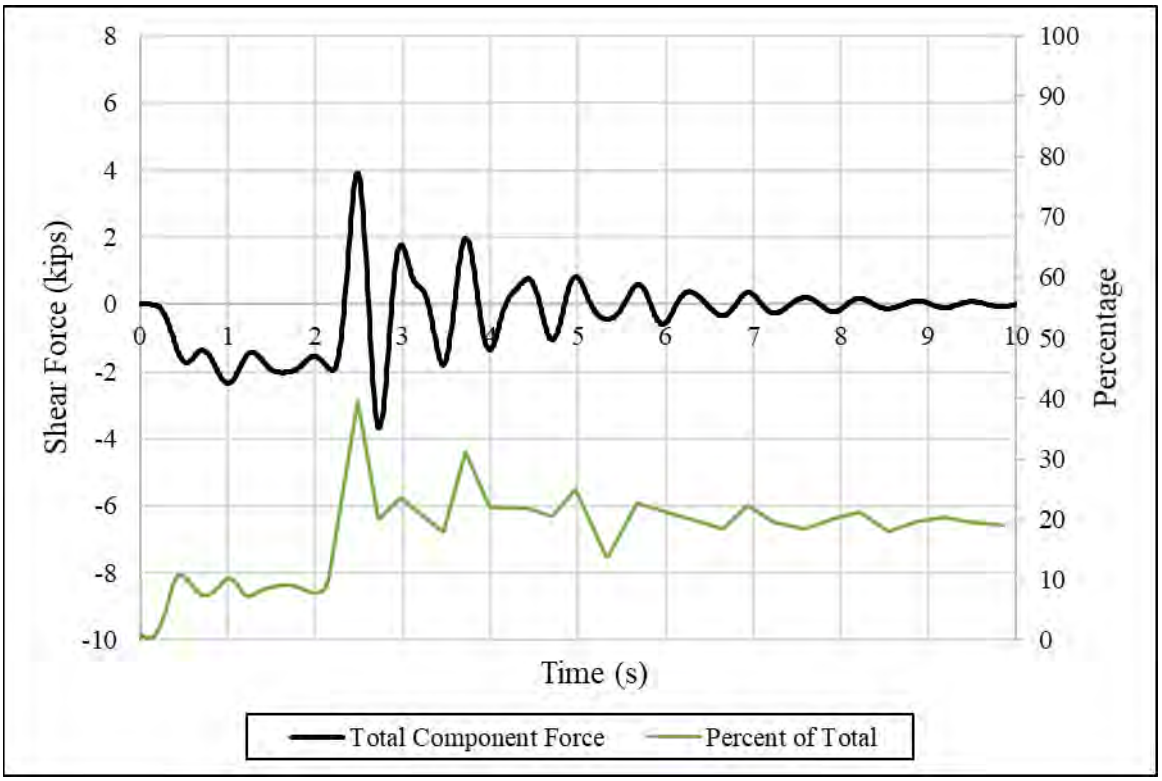

Figure 6-94 – Bent 5 Horizontal Force due to Braking on Right of Span 3

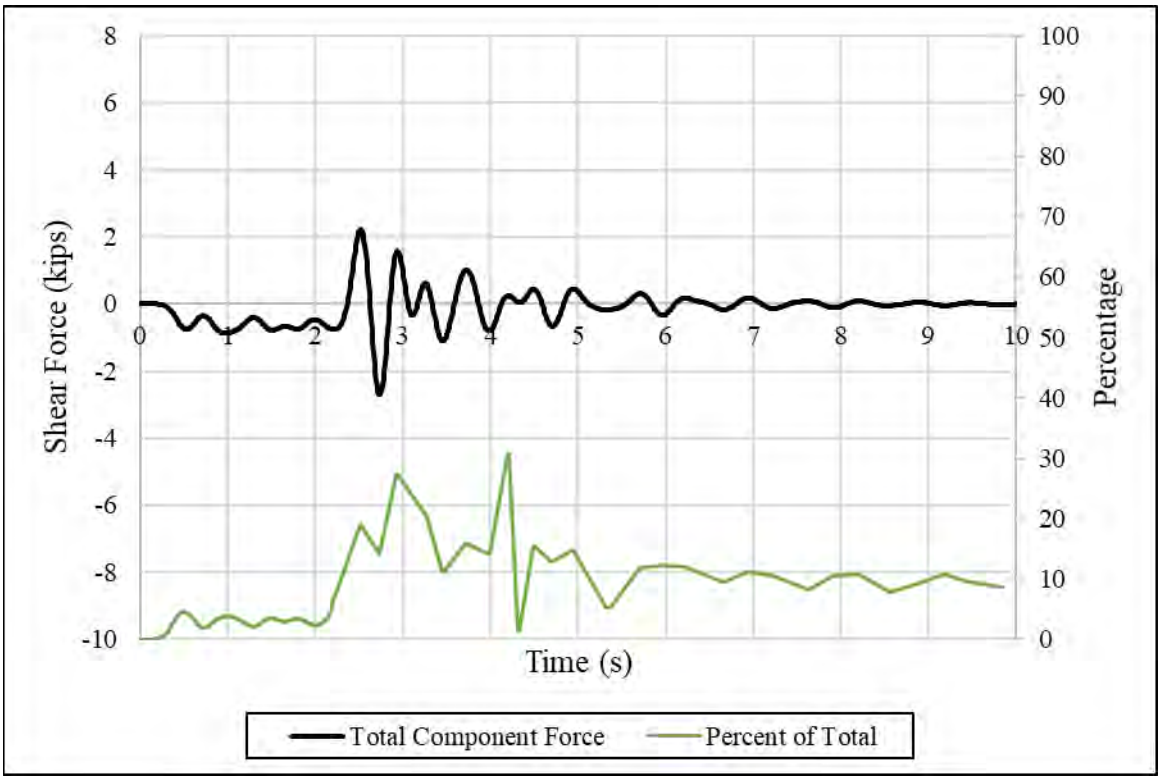

Figure 6-95 – Bent 6 Horizontal Force due to Braking on Right of Span 3

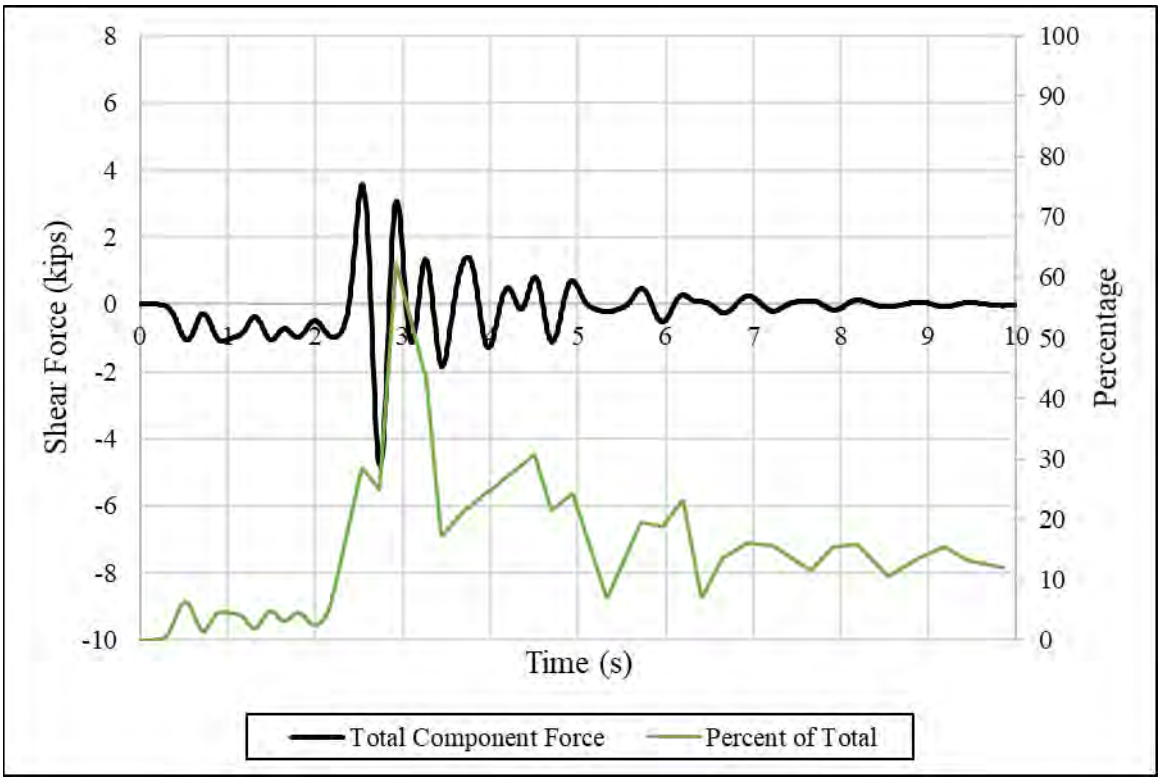

Figure 6-96 – Abutment 7 Horizontal Force due to Braking on Right of Span 3

As with Span 2 loaded on the right, when braking on the right side of Span 3, Abutment 1 and Bent 2 experienced the highest percentage of the horizontal shear force. Abutment 1 experienced a maximum of 34 percent and approximately 7.3 kips and Bent 2 experienced 31 percent, 6.7 kips, respectively. The maximum total horizontal shear force experienced by the whole substructure was approximately 21 kips.

6.5.4.6 Horizontal Substructure Forces Resulting from Braking on Right of Span 5

From the tests conducted on the right side of Span 5, the first provided the best data. Figure 6-97 through Figure 6-103 present the horizontal shear force in each bent or abutment compared to the total horizontal shear force experienced by the entire substructure for this test.

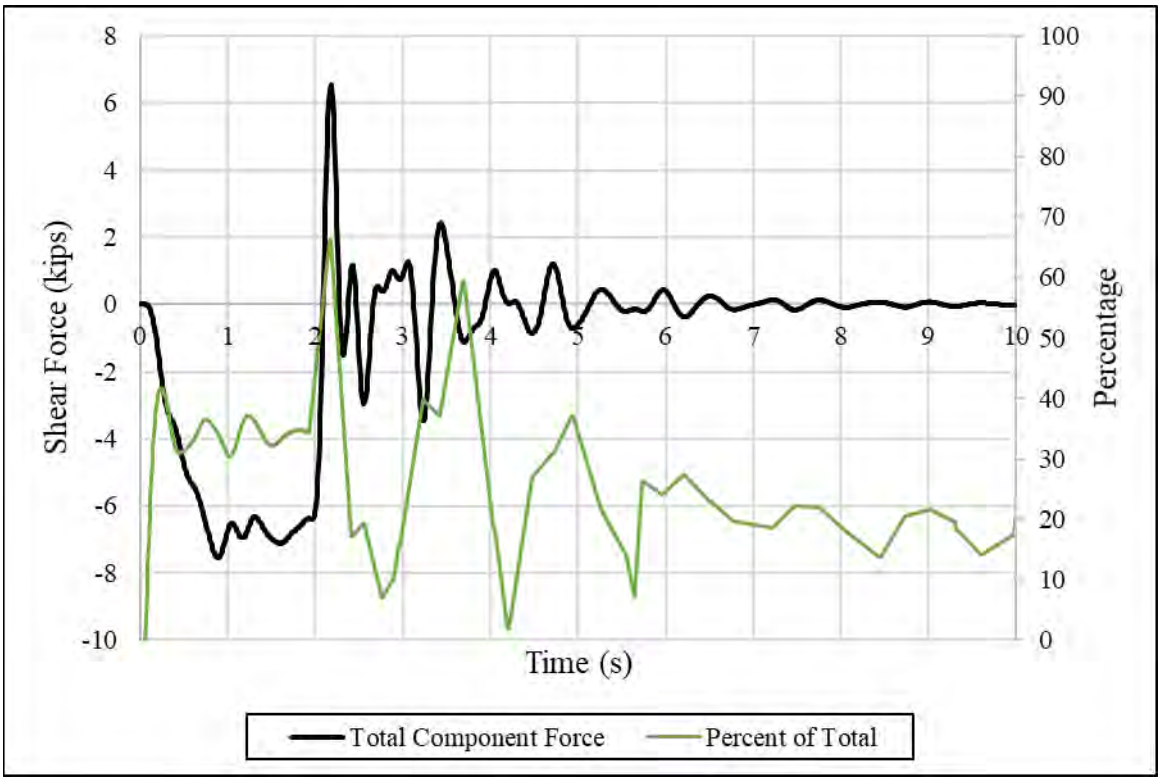

Figure 6-97 – Abutment 1 Horizontal Force due to Braking on Right of Span 5

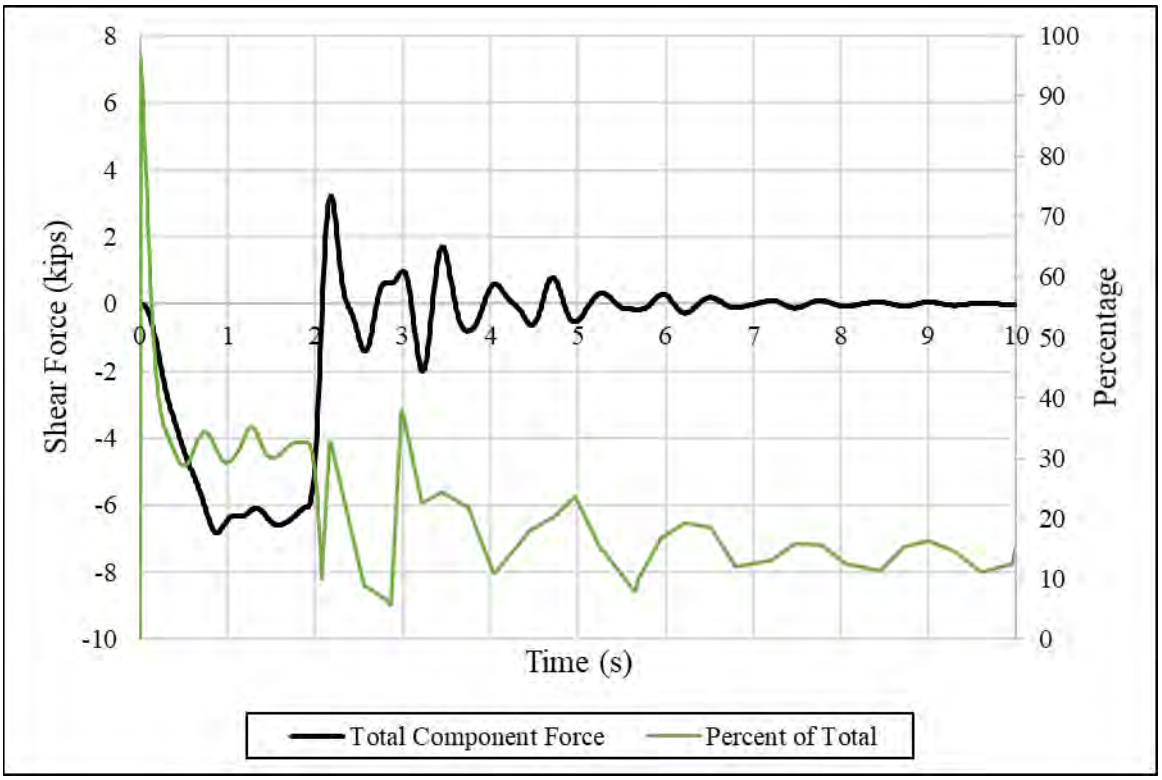

Figure 6-98 – Bent 2 Horizontal Force due to Braking on Right of Span 5

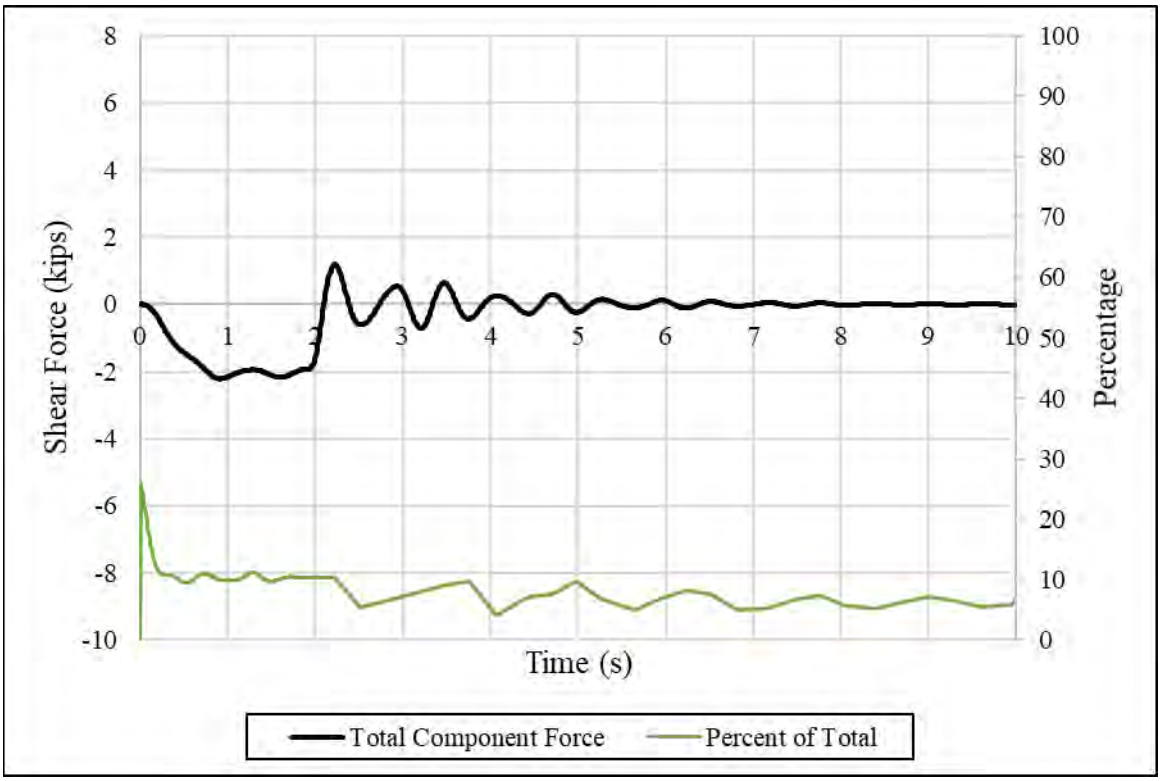

Figure 6-99 – Bent 3 Horizontal Force due to Braking on Right of Span 5

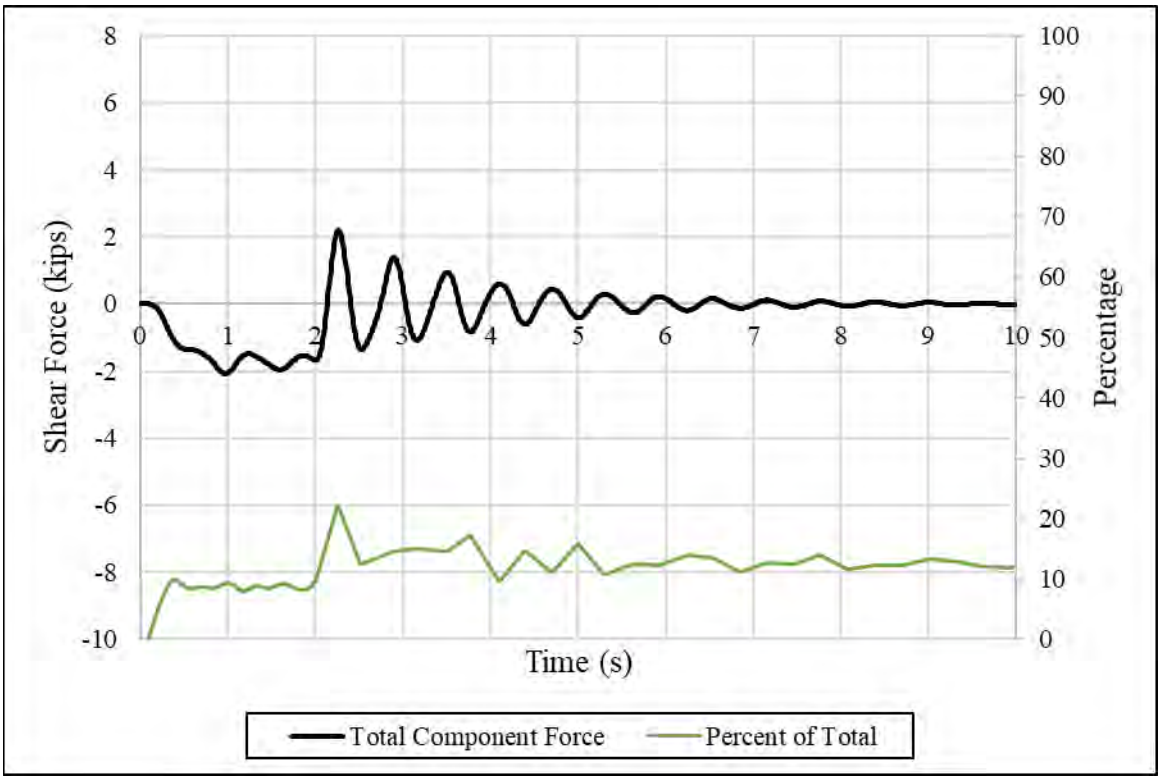

Figure 6-100 – Bent 4 Horizontal Force due to Braking on Right of Span 5

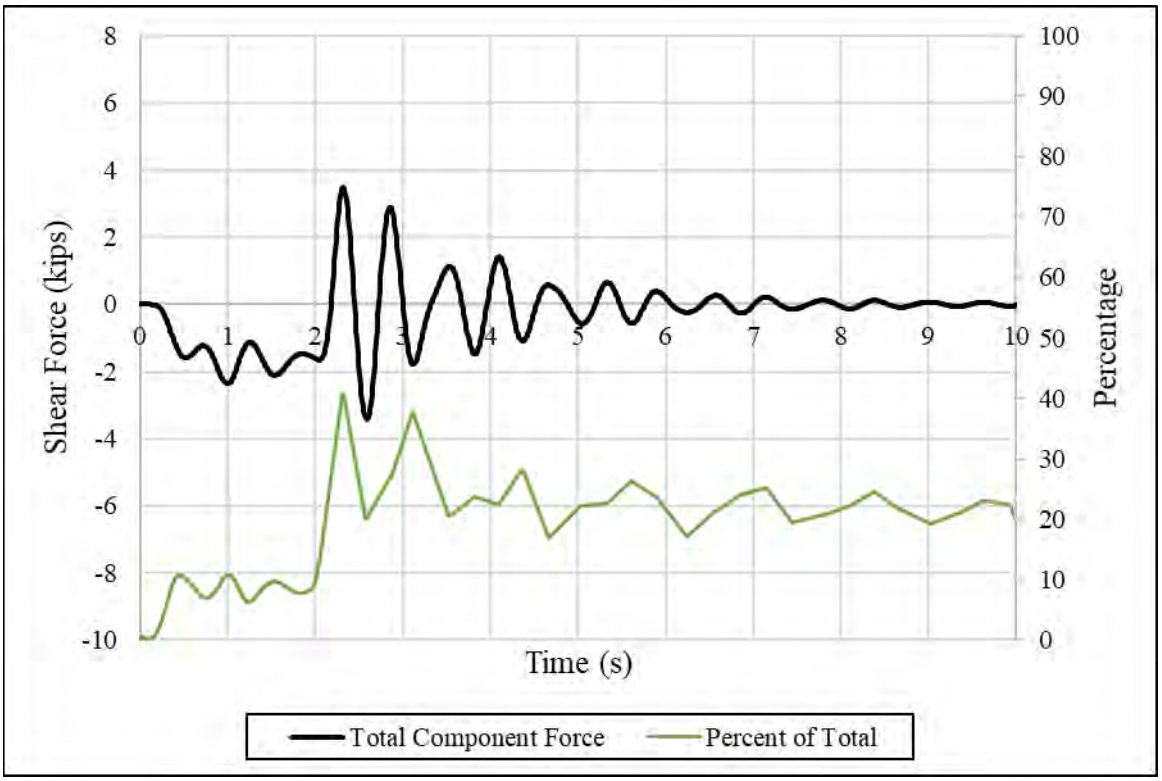

Figure 6-101 – Bent 5 Horizontal Force due to Braking on Right of Span 5

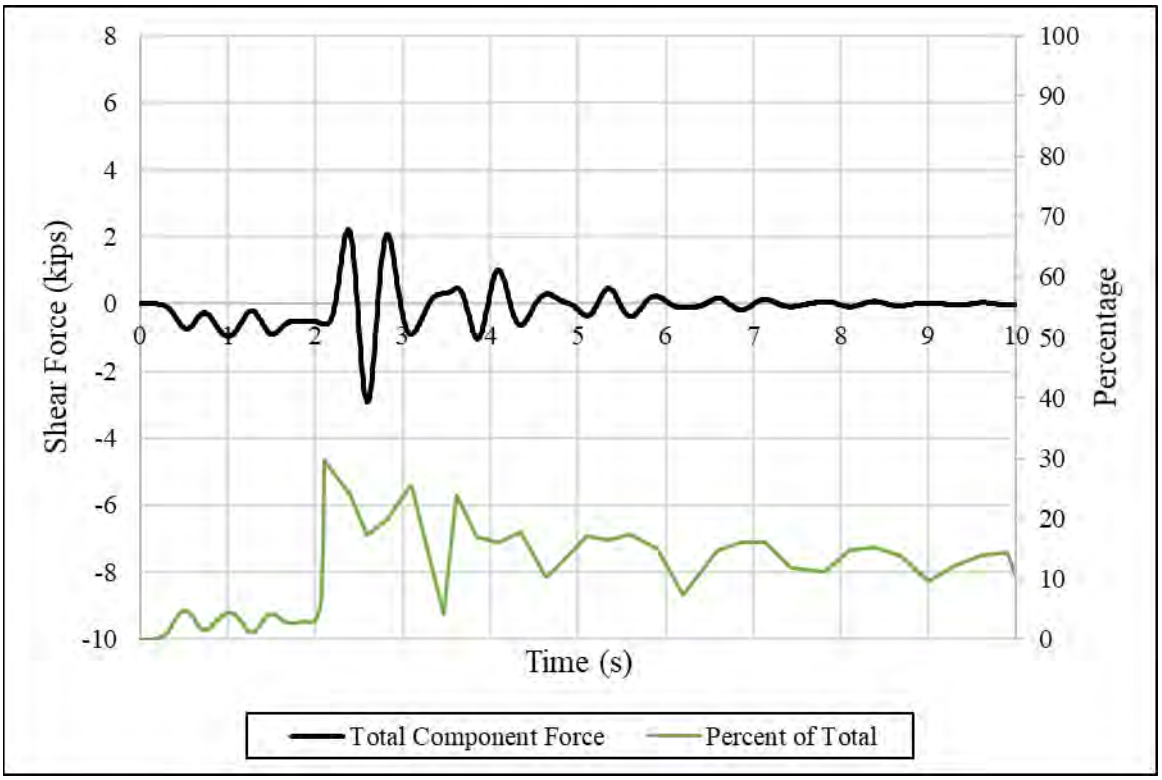

Figure 6-102 – Bent 6 Horizontal Force due to Braking on Right of Span 5

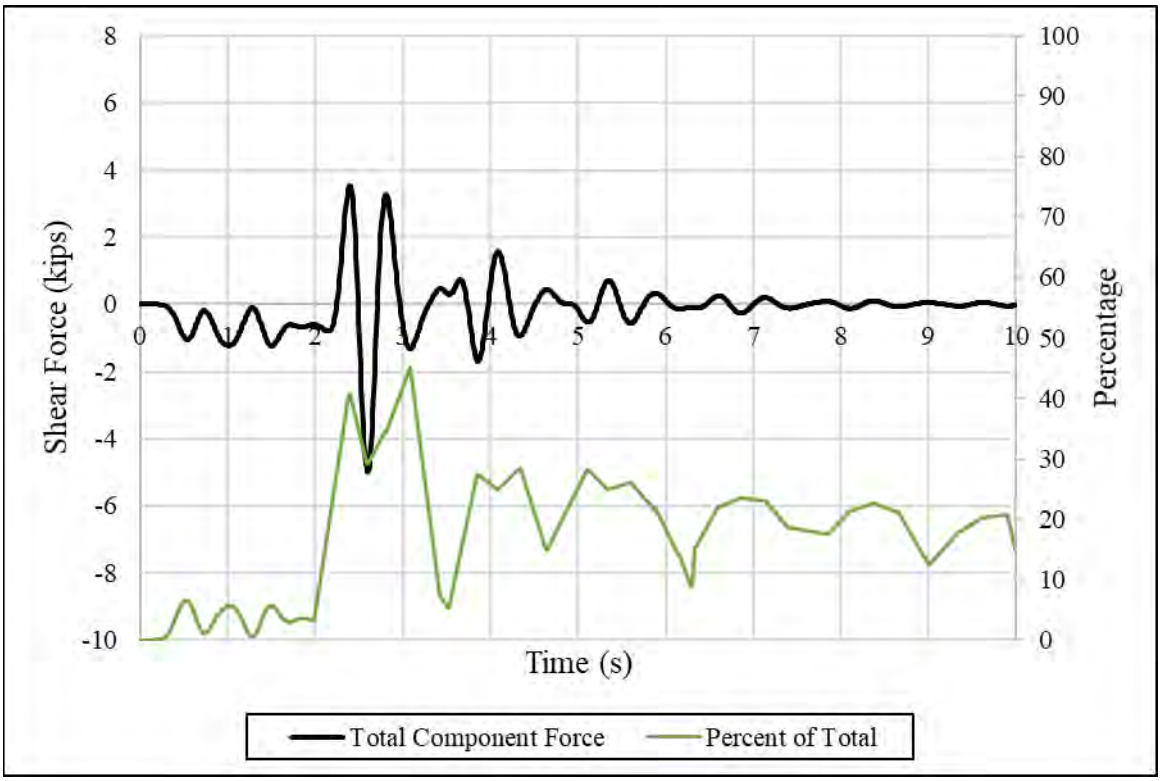

Figure 6-103 – Abutment 7 Horizontal Force due to Braking on Right of Span 5

Again, with Span 5 during braking on the right of the span, Abutment 1 and Bent 2 experienced the highest percentage of the horizontal shear force. Abutment 1 experienced a maximum of 33 percent at approximately 6.8 kips and Bent 2 experienced 32 percent at 6.4 kips. The maximum total horizontal shear force experienced by the whole substructure was approximately 20 kips. With this test occurring on the right side and at a smaller maximum deceleration rate compared to the center tests, it is reasonable for the overall magnitudes of the forces to be less and the distribution to be different than when the span was braked on in the center.

6.6 Summary of Results

To summarize the results of the horizontal shear forces, Table 6-6 contains the approximate maximum horizontal shear force expected in a static loading based off the truck mass and maximum deceleration rate, the maximum total horizontal shear force in the entire substructure from the model, and the maximum horizontal shear force in each bent or abutment. The bolded entry in each of the columns shows the maximum value of all the tests for the given component. Despite the maximum horizontal shear force for the entire substructure always occurring during braking of the truck, each component did not always experience its maximum horizontal shear force during braking. In several tests, a bent or abutment experienced its maximum horizontal shear force during the free response period of vibration. If this was the case, each component that experienced its greatest force during free response is marked in the table by an asterisk. Even though this occurred, it is of importance to note that the maximum horizontal force was not significantly greater than the amount of horizontal shear force experienced during braking. The shaded cells indicate the substructure components that are directly supporting the loaded span and could be expected to experience the greatest horizontal shear force based on which span was loaded. It is also important to note that the element experiencing the maximum component demand always occurred when the component directly supported the span on which braking occurred and this maximum occurred during the braking phase (forced vibration). Even though not every span was loaded, this was consistent for all of the loaded spans.

Table 6-6 – Maximum Total and Component Horizontal Shear Force for each Dynamic Test

Braking Position	Maximum Static Horizontal Shear (kips)	Maximum Dynamic Horizontal Shear (kips)	Maximum Component Shear Force (kips)						
			Abutment 1	Bent 2	Bent 3	Bent 4	Bent 5	Bent 6	Abutment 7
Center Span 2	22.5	22.7	7.9	7.5	2.4	2.5*	4.2*	2.3*	4.0*
Right Span 2	26.0	26.5	**8.9**	**8.5**	2.7	3.0*	5.2*	3.6*	6.3*
Center Span 3	25.3	26.3	6.6*	4.6	**3.0**	**5.1**	4.7	2.7*	4.7*
Right Span 3	21.1	21.2	7.3	6.7	2.2	2.4*	3.9*	2.7*	4.7*
Center Span 5	24.6	25.4	3.7*	2.4*	1.0*	1.7	**7.5**	**6.5**	**7.6**
Right Span 5	20.0	19.7	6.8	6.4	2.0	2.3*	3.4*	2.9*	5.0*

For every test, the maximum total horizontal force in the model was very close to the maximum horizontal force computed statically. There was some oscillation around this maximum value due to the dynamic response of the bridge, but all values were within a few kips of the average that was recorded.

To understand how the forces reported in the model compare to the maximum static horizontal shear force, Table 6-7 was utilized. The table shows how the maximum horizontal shear force in the model was comparable to the static value and it shows how the component maximum shear forces are distributed. Knowing what load magnitude and location will produce the greatest shear force in that individual component is an invaluable aspect to designers who have to design based on demand.

Table 6-7 – Percentage of Maximum Total Shear Force Computed Statically to Maximum Shear Force Reported in Model

	Maximum Static Horizontal Shear Force (kips)	Maximum Total Horizontal Shear Force in Model	Abutment 1	Bent 2	Bent 3	Bent 4	Bent 5	Bent 6	Abutment 7
Center of Span 2	22.5	101%	35%	33%	11%	11%	19%	10%	18%
Right Side of Span 2	26.0	102%	34%	33%	10%	12%	20%	14%	24%
Center of Span 3	25.3	104%	26%	18%	12%	20%	19%	11%	19%
Right Side of Span 3	21.1	100%	35%	32%	10%	11%	18%	13%	22%
Center of Span 5	24.6	103%	15%	10%	4%	7%	30%	26%	31%
Right Side of Span 5	20.0	99%	34%	32%	10%	12%	17%	15%	25%

In every case, the magnitude of the total horizontal shear force is directly related to the maximum braking deceleration. If the maximum deceleration was 0.33g, then the magnitude of the maximum total horizontal force in the bents and abutments of the bridge was equal to 33 percent of the truck weight. All of the center test deceleration rates were comparable to the deceleration rates expected based on previous studies. In the Federal Motor Vehicle Safety Standard 121 (NHTSA 2008), the average maximum deceleration rates were 0.39g, 0.36g, and 0.34g for the various truck types. In this study, the average maximum deceleration rate was 0.35g for all the center braking tests and 0.31g for all the right side braking tests. Thus, if the total maximum horizontal shear force that will be transmitted to the substructure of the bridge is ultimately equal to the achievable deceleration rate, the 25 percent of the truck weight provision in the LRFD Specification gives a force less than the *total* horizontal force on the entire bridge substructure.

When reviewing the effect of off-center braking, for Spans 3 and 5 at lower total maximum forces, Abutment 1 and Bent 2 experienced greater forces then when braking occurred in the center of the span. Abutment 1 and Bent 2 experienced greater forces from the right side braking then from the center, but at a higher total maximum horizontal force. These bents and abutments could be experiencing greater forces as a result of resisting some tendency of the bridge to want to twist as a result of the eccentric load in the plan dimension. Regardless of

braking location, the maximum deceleration rate is the determining factor in the magnitude of the total maximum horizontal shear force that must be resisted by the entire bridge substructure.

Based on these results, the total maximum horizontal shear force that the all the bents and abutments combined experience can be determined by performing a static analysis. Multiplying the design truck weight multiplied by a reasonable achievable deceleration rate, like the values presented in this chapter, gives an accurate estimate of the total maximum horizontal shear force. If the horizontal shear force that the individual bents or abutments must resist is the desired value, a static analysis is sufficient and will have reasonable accuracy if the loading is applied on the span supported by the component (column or abutment). The percentage of the horizontal shear force that a component must resist is variable. Numerous factors such as stiffness, length, number of piles in a bent, and soil-structure interaction will affect the amount of horizontal shear force and as shown in Table 6-6 and Table 6-7.

Chapter 7 Parametric Study of Braking Force Distribution

7.1 Introduction

In this chapter, the objective is to investigate shear force distribution along bridges in the longitudinal direction by using a limited parametric study that includes 23 bridge different models. Development of a numerical model for Macon County Road 9 Bridge using CSIBridge and SAP2000 was discussed in previous chapters. This numerical model was validated by comparing the simulation results with the field measurements from the static and dynamic bridge testing. The modeling assumptions and parameters for the parametric study primarily follow the previous chapters with some small modifications.

According to the experimental testing, the total truck braking force is approximately 32 percent of the truck weight. After a truck brakes, the braking force will be transferred to the bridge deck at which point it will follow a load path including the bridge deck, girders, bearings, bents/abutments and foundations. Therefore, the relative stiffnesses of these elements have a significant impact on the distribution of braking force among the abutments and bents. Among these elements, the differences between bearing pad stiffnesses are relatively small compared with the differences between the bent column and foundation stiffnesses since these vary considerably with site layout and column geometry. Column stiffness, which is heavily influenced by the column height, has a significant effect on the braking force distribution. Soil-structure interaction also has a large impact on column stiffness and hence braking force distribution. Modeling of soil-structure interaction is highly variable and uncertain and has not been considered in this parametric study.

7.2 Parametric Study

A parametric study was performed with multiple variables. The first variable is column stiffness (three values), the second is the number of spans (3, 6, and 12 spans), and the third is the position of the braking vehicle. Each of the 23 models were analyzed using both a static load and a dynamic forcing function to investigate the difference in the way the forces are distributed in the different analyses. For loading, each span was loaded individually to capture the overall shear force distribution based on different braking locations. Simultaneous braking force on multiple spans was not investigated in this study.

The three levels of column stiffness are based on upper and lower limits for column stiffness for typical bridges and one intermediate value. These three values for column stiffness were generated by implementing three different column heights and an associated column cross section. The shortest column (8 ft) has the greatest stiffness and the tallest column (24 ft) the lowest stiffness. The model assumes all the columns framing into the same cap beam have the same height and cross section. A span of 80 ft is utilized for all the bridges. Three baseline models with a 12 ft column height (intermediate stiffness value) along the bridge were built first, including a three-span bridge, a six-span bridge and a twelve-span bridge (Cases 1, 4, and 11). Figures 7-1, 7-2 and 7-3 show the baseline three-span, six-span and twelve-span bridges with notation used in this parametric study.

Tables 7-1, 7-2, and 7-3 show detailed column height information for each bent cap beam along the bridge in the longitudinal direction for three-span, six-span and twelve-span bridges, respectively. The numbers in bold text indicate the column that has been changed from baseline models. Among these bridge models, Cases 1, 4 and 11 are baseline models of three-span, six-span and twelve-span bridges, respectively. The basis of this study is investigating the effect of the relative stiffness of an individual bent on the distribution of longitudinal braking force. As such, each case results from changing a single bent from the baseline configuration with the intermediate value for stiffness to a more flexible column bent or to a column bent with greater stiffness. As an example, for the three-span cases, Case 1 is the baseline version with all intermediate stiffness columns. As the case numbers increase, a single column is changed from intermediate stiffness of high stiffness or low stiffness. The higher the case number, the further the column is from Abutment 1. The exceptions to this are Cases 20 through 23 (Table 7-2) for the six-span bridge. Cases 20 and 21 are similar to the baseline cases but with all stiff or all flexible bents to ascertain how the distribution of the braking force to the abutments is affected by the total stiffness of all the column bents. Cases 22 and 23 are individual scenarios with alternating stiff and flexible column bents.

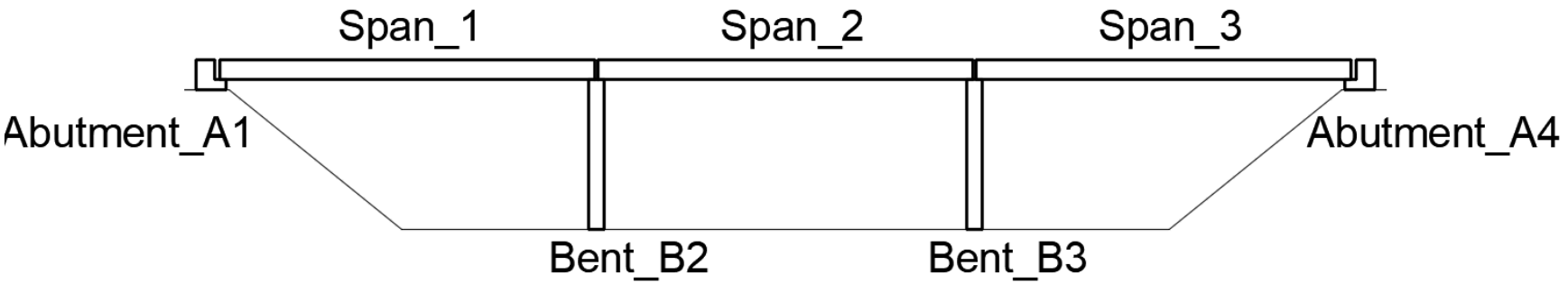

Figure 7-1 Annotated Three-Span Bridge Model

Table 7-1 Column Height Information for Three-Span Bridge Cases

Case Number	Column Height (ft)	
	B2	B3
1 (Baseline)	12	12
2	**8**	12
3	**24**	12

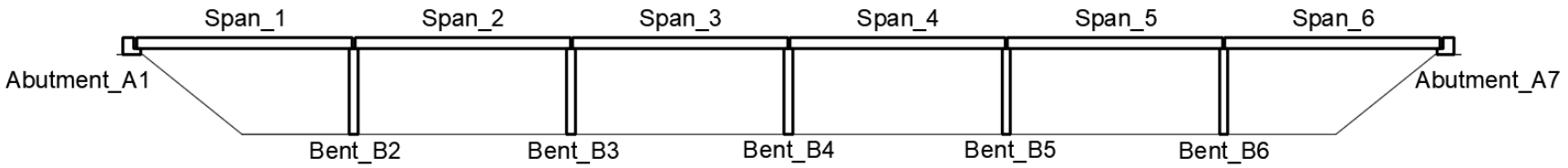

Figure 7-2 Annotated Six-Span Bridge Model

Table 7-2 Column Height Information for Six-Span Bridge Cases

Case Number	Column Height (ft)				
	B2	B3	B4	B5	B6
4 (Baseline)	12	12	12	12	12
5	**8**	12	12	12	12
6	**24**	12	12	12	12
7	12	**8**	12	12	12
8	12	**24**	12	12	12
9	12	12	**8**	12	12
10	12	12	**24**	12	12
20 (All Stiff Columns)	**8**	**8**	**8**	**8**	**8**
21 (All Flexible Columns)	**24**	**24**	**24**	**24**	**24**
22 (Alternating Stiffness)	**8**	**24**	**8**	**24**	**8**
23 (Alternating Stiffness)	**24**	**8**	**24**	**8**	**24**

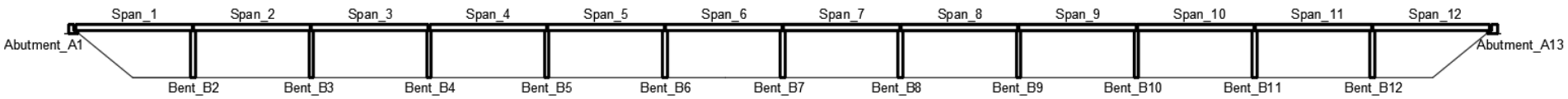

Figure 7-3 Annotated Twelve-Span Bridge

Table 7-3 Column Height Information for Twelve-Span Bridge Cases

Case Number	Column Height (ft)									
	B2	B3	B4	B5	B6	B7	B8	B9	B11	B12
11 (Baseline)	12	12	12	12	12	12	12	12	12	12
12	**8**	12	12	12	12	12	12	12	12	12
13	**24**	12	12	12	12	12	12	12	12	12
14	12	12	**8**	12	12	12	12	12	12	12
15	12	12	**24**	12	12	12	12	12	12	12
16	12	12	12	**8**	12	12	12	12	12	12
17	12	12	12	**24**	12	12	12	12	12	12
18	12	12	12	12	12	**8**	12	12	12	12
19	12	12	12	12	12	**24**	12	12	12	12

7.3 Numerical Model Description

7.3.1 Superstructure Modeling

The superstructure of highway bridges includes the bridge deck and bridge girders. They were modelled using information provided by ALDOT. All the spans in this study were simple spans with 1.5 in expansion joints between spans. The expansion joint was assumed to have no stiffness. The modeling process for the cross section and length of the superstructure for the bridges in this parametric study are the same as for the validated bridge model in Chapter 6. The deck width is 30.75 ft with a thickness of 7 inches, which is supported by four AASHTO standard bridge girders (Type III). The bridge girder spacing is 8 ft. The span length in this study is 80 ft for all bridges. The concrete haunch thickness is 2 inches. The cast-in-place bridge deck and concrete haunch in this project were constructed with 4,000 psi concrete while the precast, prestressed concrete girders were modeled as 6,000 psi concrete.

7.3.2 Substructure Modeling

The highway bridge substructure includes the cap beam, columns, abutments, and foundations. In this study, a substructure with four-pier bents was used for all bridge cases. All the cap beams were modelled as linear elastic beam elements with a solid rectangular cross section. The depth of the cap beam is 2 ft while the width is 3.5 ft. The cap beam was made of cast-in-place 4,000 psi concrete. Columns below the cap beams represented the only variables in the model: stiffness (height and section) and location. All the columns were assumed to be A992 steel (F_y = 50 ksi). The column cross section is combined with a specific column height to provide the desired stiffness value. All columns under the same bent cap beam have the same stiffness (height and cross section). Table 7-4 shows the relation between the column height and cross-sectional properties as well as the equivalent cantilever column stiffness for reference. The 8 ft column height represents a very stiff column bent while the 24 ft height represents a very flexible column bent near the height limit where a tower type bent would be required. The 12 ft column height represents an intermediate value of column lateral stiffness. Soil-structure interaction is not included in this parametric study, and the columns are assumed fixed at the base. The column height is measured from the bottom of the bent cap to the fixed support at the foundation.

Table 7-4 Relationship between Column Height and Cross Section

Column Height (ft)	Column Cross Section	Column Stiffness $[3EI/L^3]$ (k/in)
8	HP 10X57	28.9
12	HP 12X74	16.6
24	HP 12X53	1.4

The abutment is one of the substructure components that resists the earth pressure, lateral forces, and vertical loading at the end of the bridge. The dimension of the cross section of the abutment in this study was 3 ft by 3 ft. The length of the abutment was 30.75 ft which was the same as the bridge deck. The abutment was modeled using cast-in-place 3,000 psi concrete and pin supports. Because of this simplification, the forces at the abutments are likely greater than in reality because they would have a small amount of flexibility due to the drilled shafts directly supporting the abutment. Each of the bridge girders is connected to the abutment using the same link elements representing the bearing pads as for the bents.

7.3.3 Connection Modeling

Connection behavior between the superstructure and substructure was also considered in this analysis because it was evident in the field testing that the connections were important. All the bridges in this study all contain a girder-to-elastomeric bearing pad connection at the end of each span. These connections were found to behave as an “expansion” (allowing horizontal translation) bearing even at the span supports that are considered a “fixed” (no-translation) bearing. A link element in the analysis model was created to represent the connection between girders and cap beams (or abutments). The stiffness of the link element in both the longitudinal and transverse directions was defined as 45 kips/in. This spring constant is a modified value of that calculated based on the properties of the bearing pad after comparing numerical results to field test data. Figure 7-4 shows a typical six-span bridge model from CSIBridge.

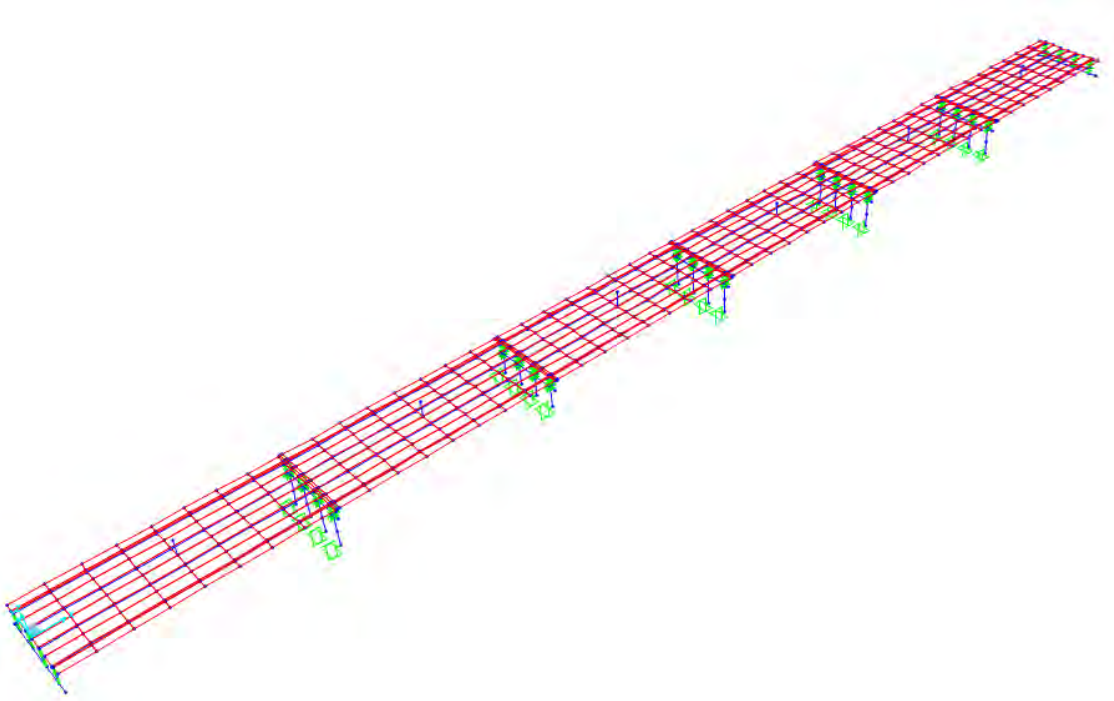

Figure 7-4 Typical Six-Span Highway Bridge CSIBridge Model

7.3.4 Loading Condition and Analysis Method

For all bridges, static and dynamic loads were each applied at the midspan of the braking span at the top of an element included to apply the load at the approximate vertical center of mass of the truck. For each case, the load was applied on each span. Both static and dynamic analyses were linear elastic since none of the elements in the bridge model are expected to have inelastic behavior under braking forces. Linear response history analysis based on modal superposition analysis was used to simulate the dynamic behavior of the bridges under braking force. At least forty modes needed to be calculated in the modal analysis to capture the full dynamic behavior. The time history function, which is defined as a ramp function in CSIBridge, is same as the function shown in Figure 6-19. The static and dynamic braking load in this study are both 22.5 kips which is 32 percent of truck gravity load based on the field tests. Modal damping was used by defining the mass and stiffness proportional coefficients based on the modal analysis results for each bridge model.

7.4 Results and Discussion of Results

After conducting static and dynamic load analysis on the numerical models, both maximum shear force in each bent and abutment and the maximum overall shear force are recorded. Figures 7-5 through 7-10 show the normalized shear forces under static and dynamic load on the different models for the baseline three-span (Case 1), six-span (Case 4) and twelve-span (Case 11) bridge models. The span number in the legend refers to the span where the braking force is applied as identified in Figures 7-1 through 7-3 and Tables 7-1 through 7-3. The normalized shear forces are calculated as the maximum value normalized by the braking force applied to the structure. Under static loading, the sum of the normalized shear forces in each bent and both abutments is equal to one. However, under dynamic loading, the sum of the maximum normalized shear in each bent and the abutments is greater than one. This occurs because the maximum shear in each bent does not happen simultaneously.

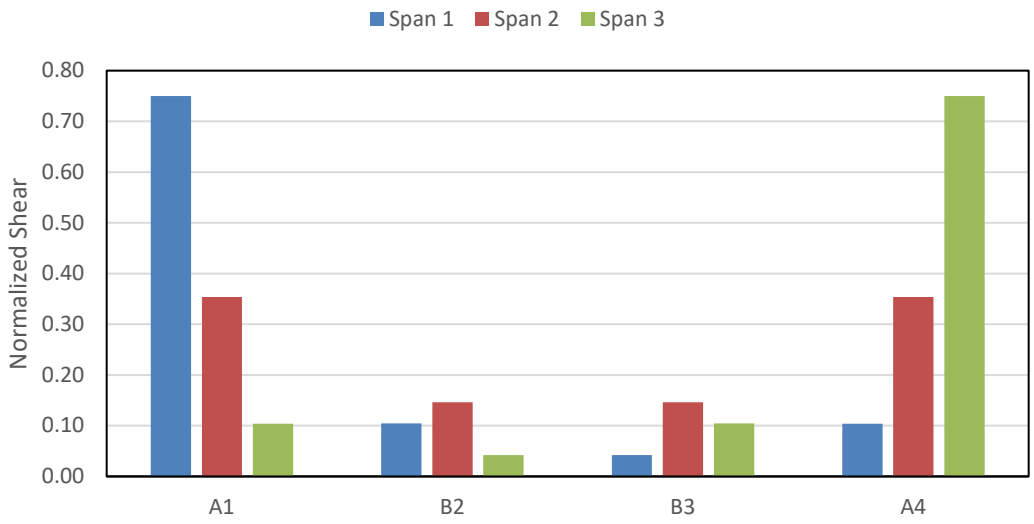

Figure 7-5 Normalized Shear Force under Static Load for Case 1 Bridge

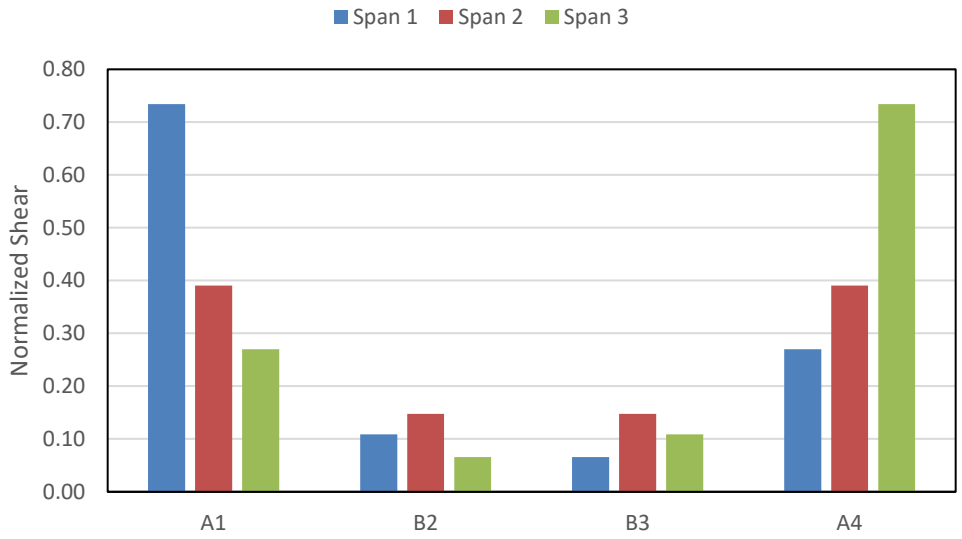

Figure 7-6 Normalized Shear Force under Dynamic Load for Case 1 Bridge

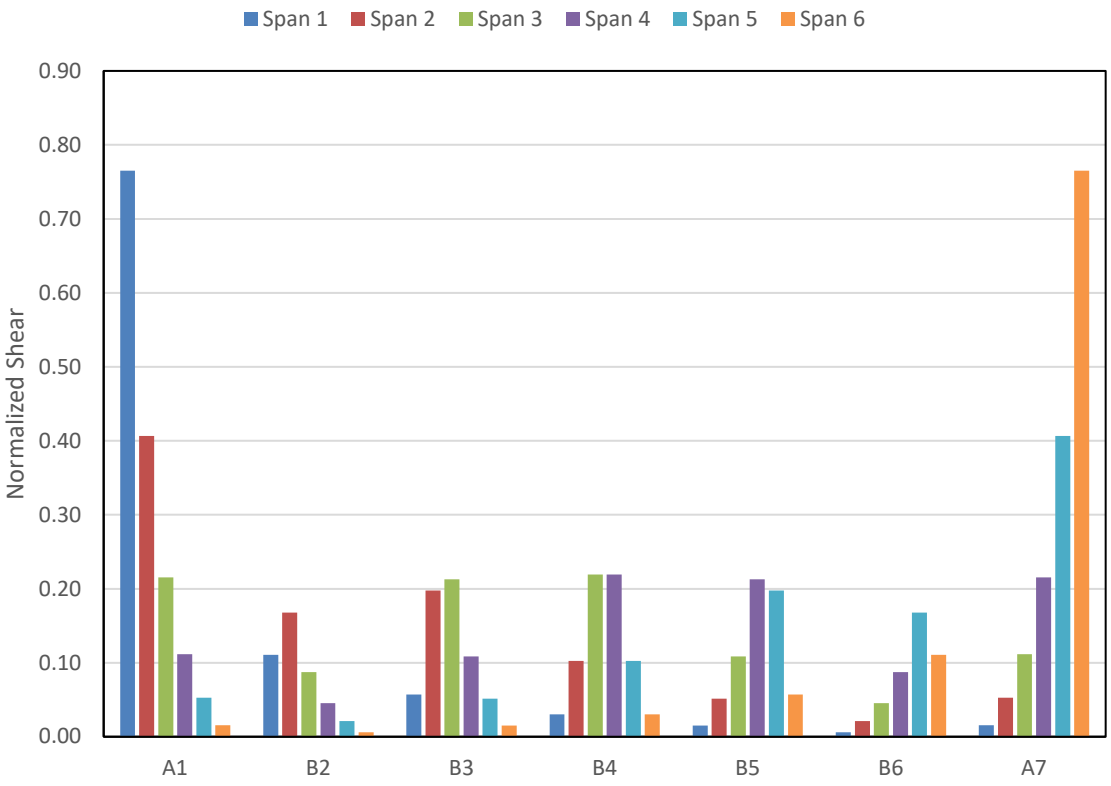

Figure 7-7 Normalized Shear Force under Static Load for Case 4 Bridge

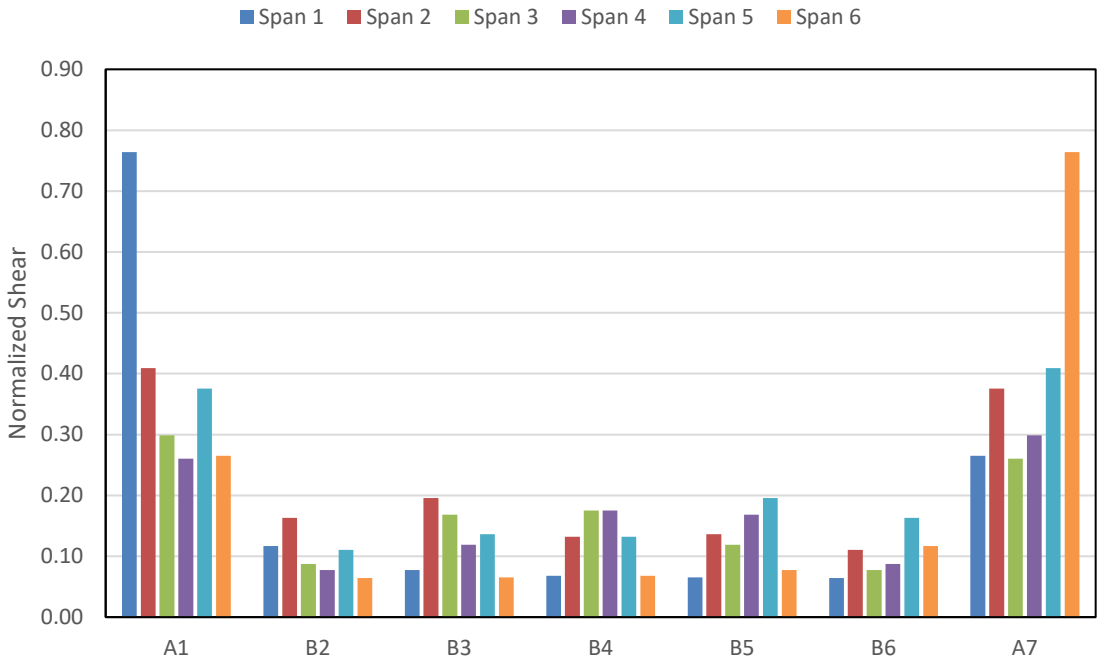

Figure 7-8 Normalized Shear Force under Dynamic Load for Case 4 Bridge

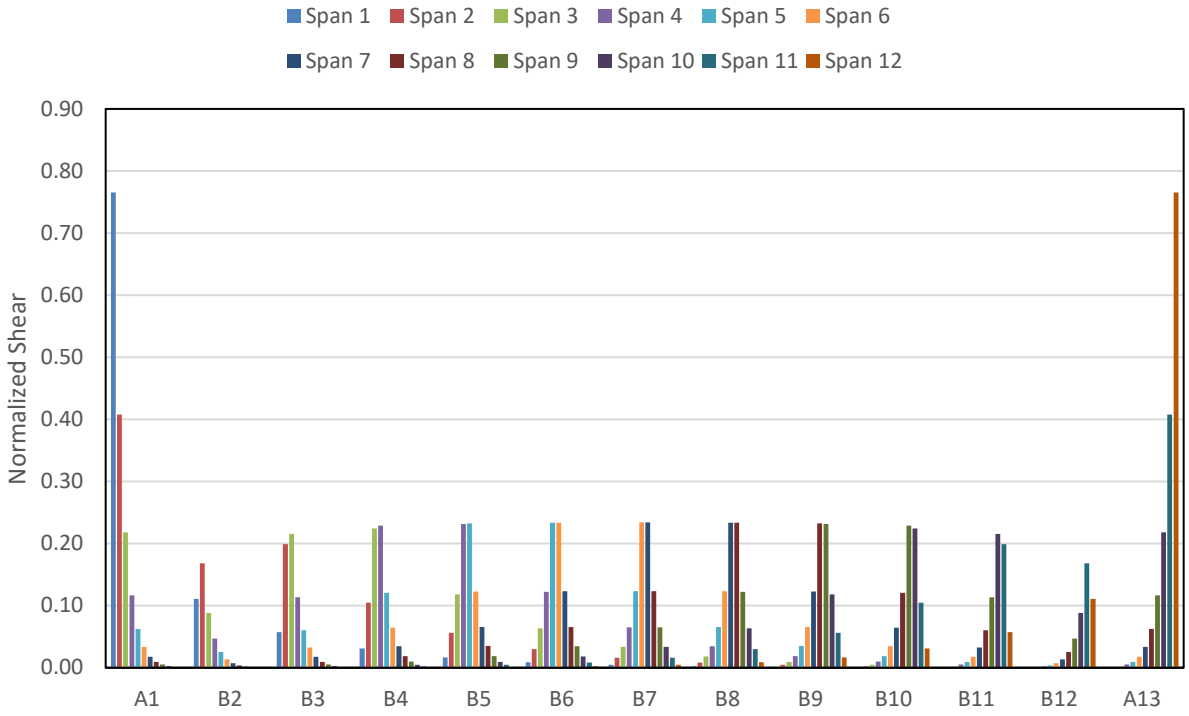

Figure 7-9 Normalized Shear Force under Static Load for Case 11 Bridge

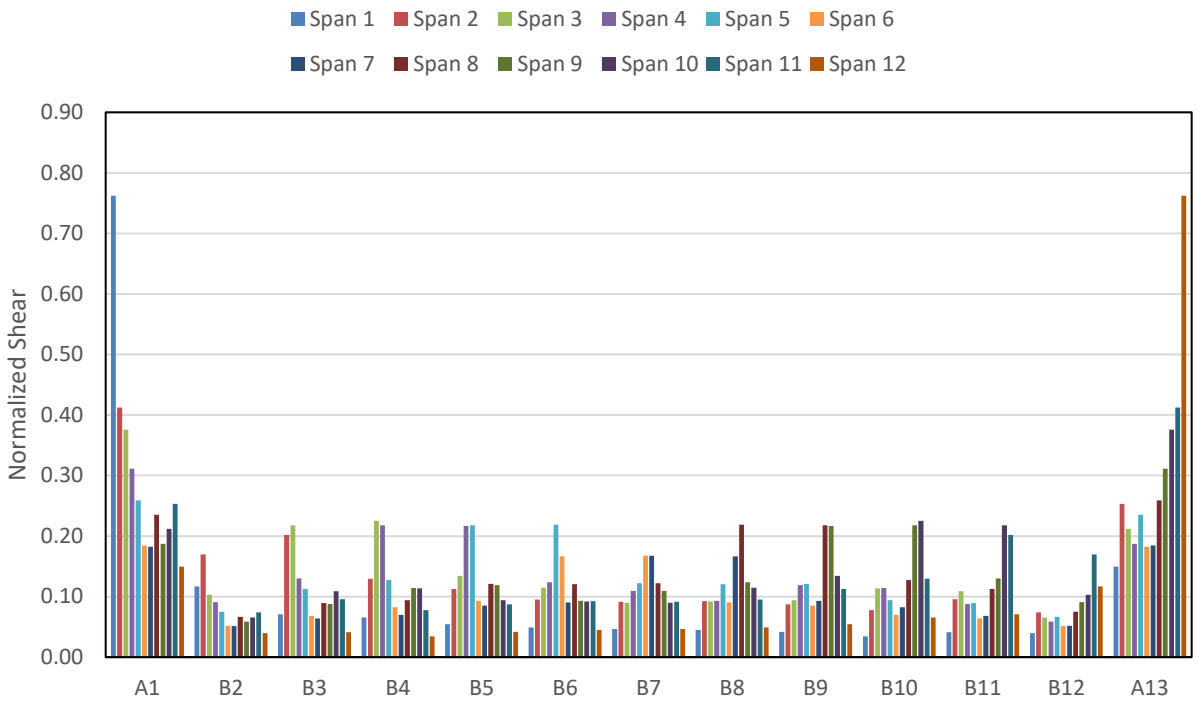

Figure 7-10 Normalized Shear Force under Dynamic Load for Case 11 Bridge

What is clear from Figures 7-5 through 7-10 is that the abutments take a significant portion of the braking force, even when the loading is not adjacent to the abutment. In addition, it is clear that for an individual column bent, the maximum shear occurs when the loading is on an adjacent span. Based on Figures 7-5, 7-7 and 7-9 which are static analysis results, normalized shear force for all the bents and abutments reached the maximum value when braking force was applied on the adjacent spans and decreased when braking force moved away from the bent. According to Figures 7-6, 7-8 and 7-10, the results of dynamic analysis were similar to the static results but there are some differences between the two. The maximum normalized shear force in a bent in both cases still occurs when the braking force is applied on the adjacent spans and the magnitude is similar. The difference is the normalized bent shear as the loaded span was further away from the bent. Due to the vibrational dynamics of the models, as the braking force moves away from a given bent, the demand initially goes down but when the symmetric opposite span is loaded a larger demand occurs. This can be seen in Figure 7-8 in the results for B2. The maximum demand occurs when Span 2 is loaded and then the demand decreases for Spans 3 and 4. When Span 5 is loaded (the symmetric opposite of Span 2) the demand increases again. This behavior is most evident in the six-span and twelve-span models.

Figure 7-11 shows the comparison of normalized shear force in Bent 2 (B2) between static and dynamic analysis on the six-span Case 5 bridge. It clearly shows that the difference between static and dynamic analysis in Bent 2 is small when braking force was applied on Spans 1 and 2 which are adjacent to Bent 2. The difference is large when braking force was applied on Spans 5 and 6 which are two corresponding symmetric spans. The abutments always take a significant portion of shear force in the dynamic analysis while the shear force can be very small in the far abutment in the static analysis.

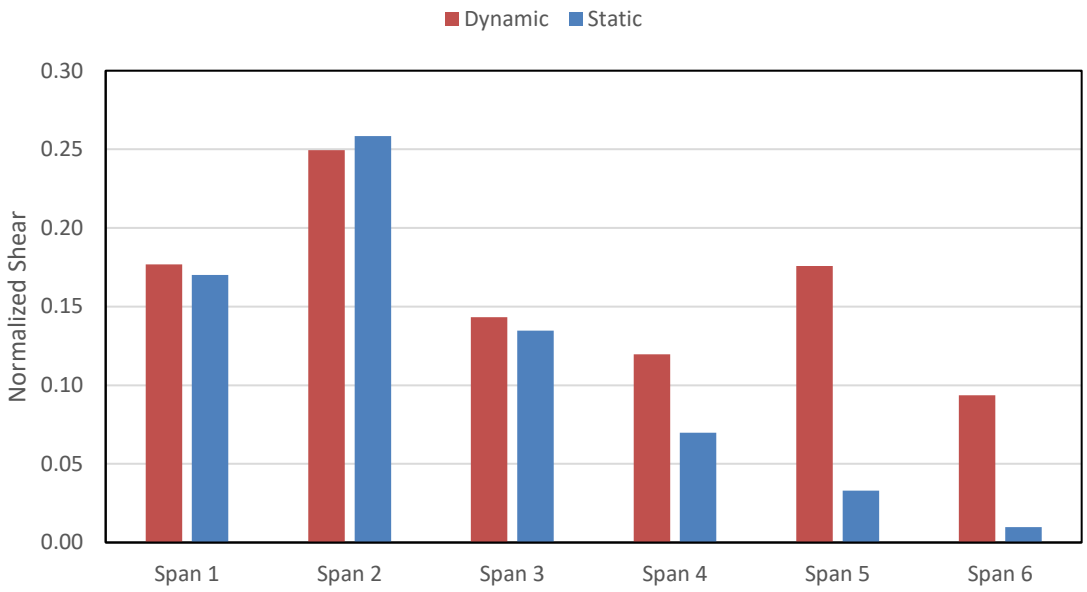

Figure 7-11 Shear Force Comparison between Static and Dynamic Analysis in Bent 2 on the Six-Span Case 5 Bridge

For static loading in Figure 7-5 the sum of the values representing loading in Span 1 on each of the elements are 0.75 + 0.10 + 0.04 + 0.10 = 1.00. For dynamic loading in Figure 7-6, the sum of the values representing loading in Span 1 are 0.73 + 0.11 + 0.07 + 0.27 = 1.18. This shows that the dynamic analysis will show higher maximum forces in individual bents than the static analysis for columns or abutments further away from the loading but the values for the support elements adjacent to the loaded spans have approximately the same magnitude. The magnitude of the ratio of dynamic-to-static forces for the different bridge cases and different loading locations varies. For the three-span bridge configurations the range of ratios is from 1.04 to 1.28. The six-span bridge configuration ratios range from 1.14 to 1.60. For the twelve-span bridge configurations, the values range from 1.30 to 2.04. Figures 7-12, 7-13 and 7-14 show the

ratio of dynamic-to-static forces for the three-span, six-span and twelve-span, respectively. From this it is clear that the greater the number of spans, the greater the ratio of dynamic to static forces. It is also clear that the loading the center spans of the bridge also results in a higher dynamic-to-static shear force ratio. However, the static analysis results are adequate for design purposes since the results of maximum shear force in each bent in static and dynamic analysis are similar when considering bents adjacent to the loaded span.

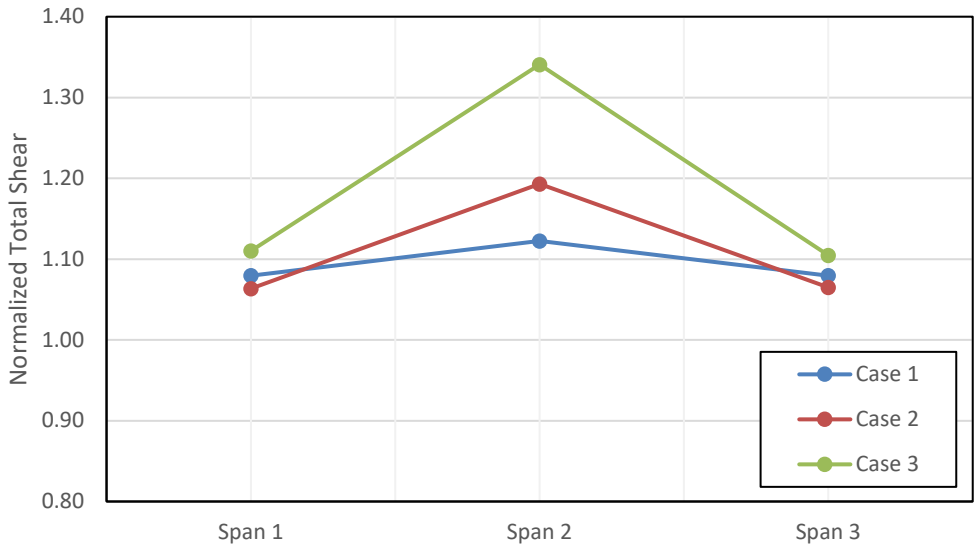

Figure 7-12 Normalized Total Shear Force under Braking Load for Three-Span Bridges

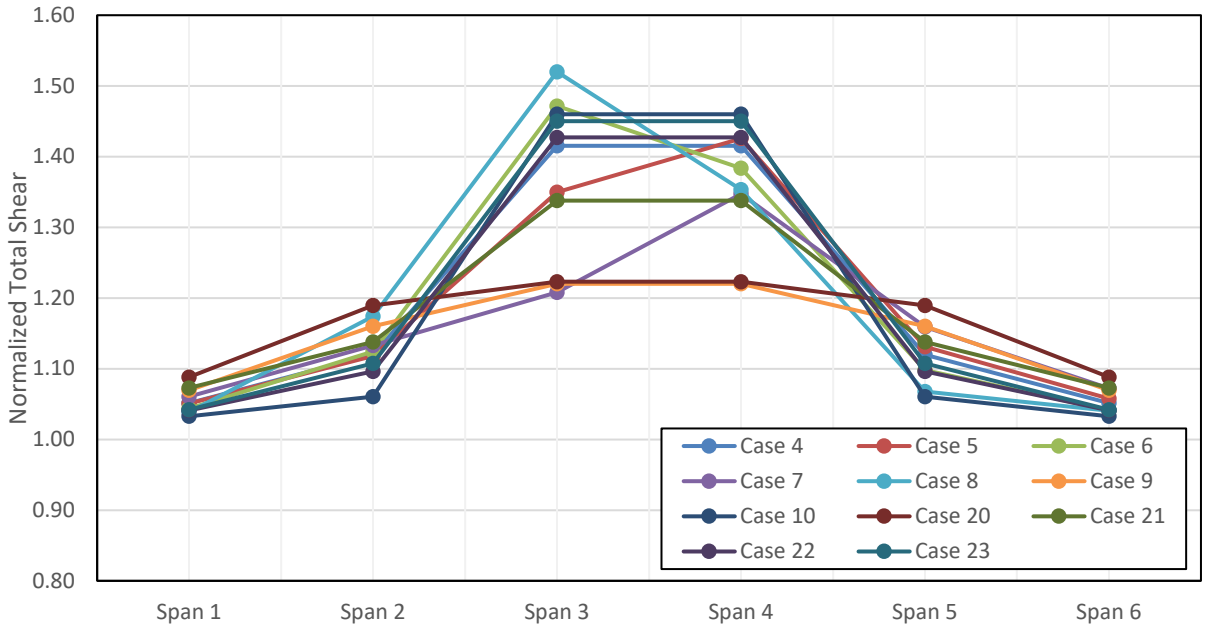

Figure 7-13 Normalized Total Shear Force under Braking Load for Six-Span Bridges

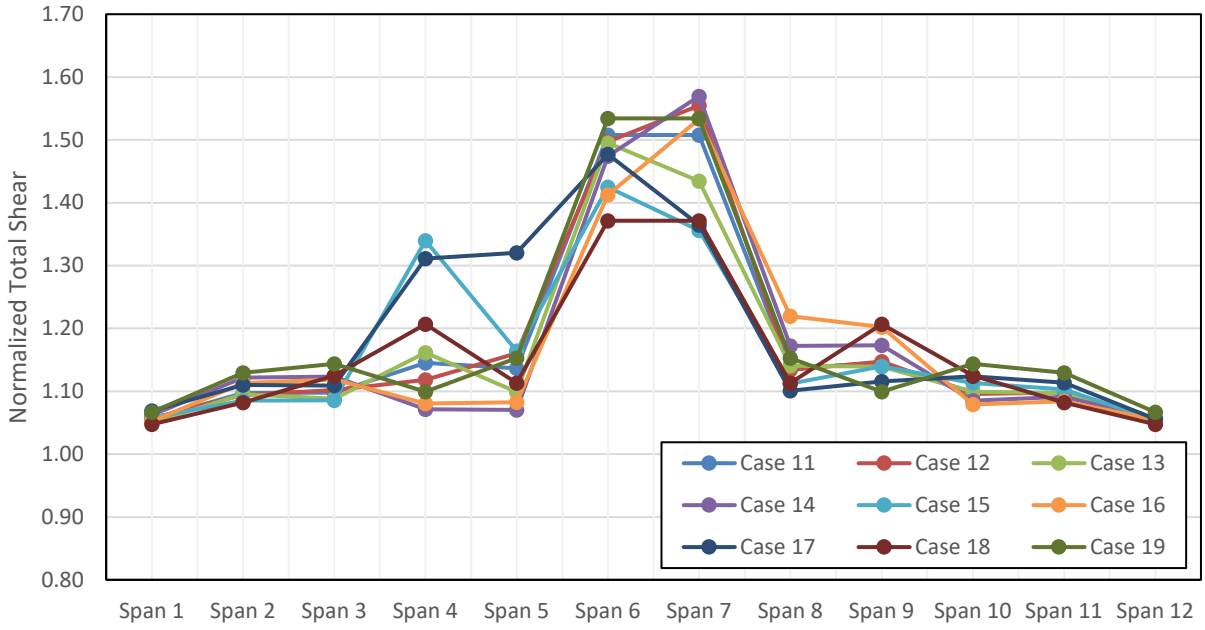

Figure 7-14 Normalized Total Shear Force under Braking Load for Twelve-Span Bridges

Overall, the results of dynamic analysis are considered more accurate when compared with the result from static analysis. The dynamic analysis more accurately simulates the process

of how braking force was applied to the bridge and how the bridge actually responds based on the field test. The following discussion of results will focus on the dynamic results.

Further results of normalized shear force distribution among different bridge cases using two types of comparisons are now presented. First, the position of the braking force will be fixed. A Span 2 loading condition was selected to represent these comparisons. Figures 7-15, 7-16 and 7-17 show the normalized shear force comparison under Span 2 loading condition among three-span, six-span and twelve-span bridges, respectively. As a reminder, Cases 1, 4 and 11 are the baseline cases with all column bents at the intermediate stiffness value. As the case number increases, individual bents are changed from intermediate to low or high stiffness values in accordance with

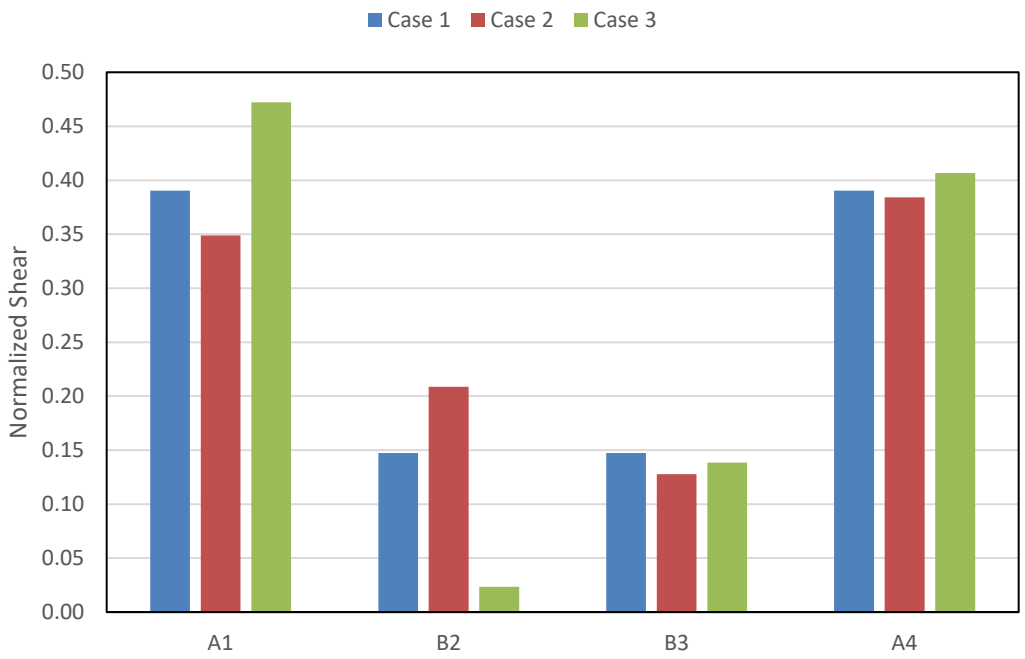

Figure 7-15 Normalized Shear Force Comparison under Span 2 Loading Condition among Three-Span Bridges

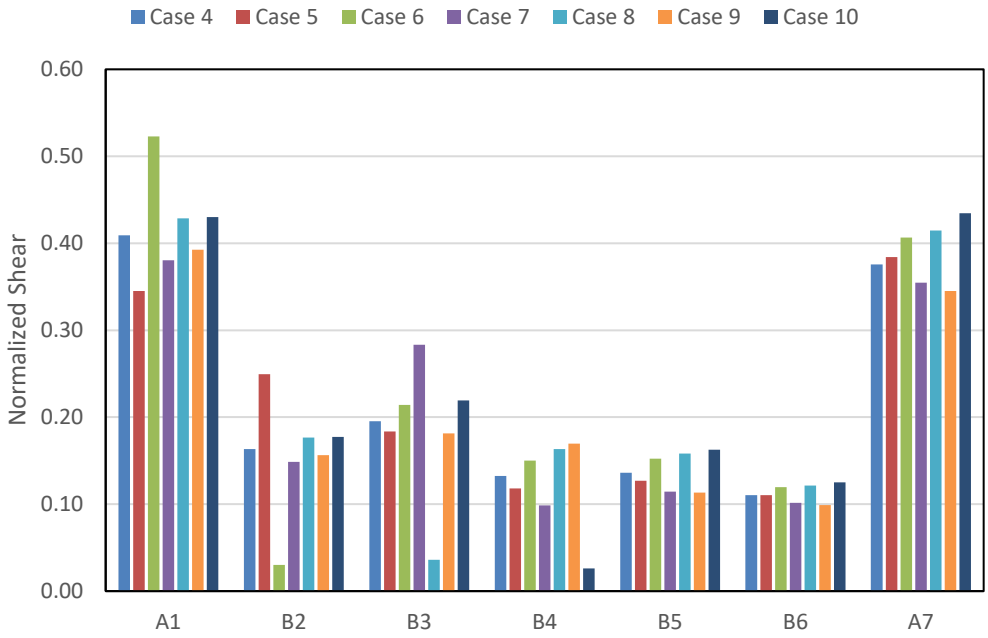

Figure 7-16 Normalized Shear Force Comparison under Span 2 Loading Condition among Six-Span Bridges

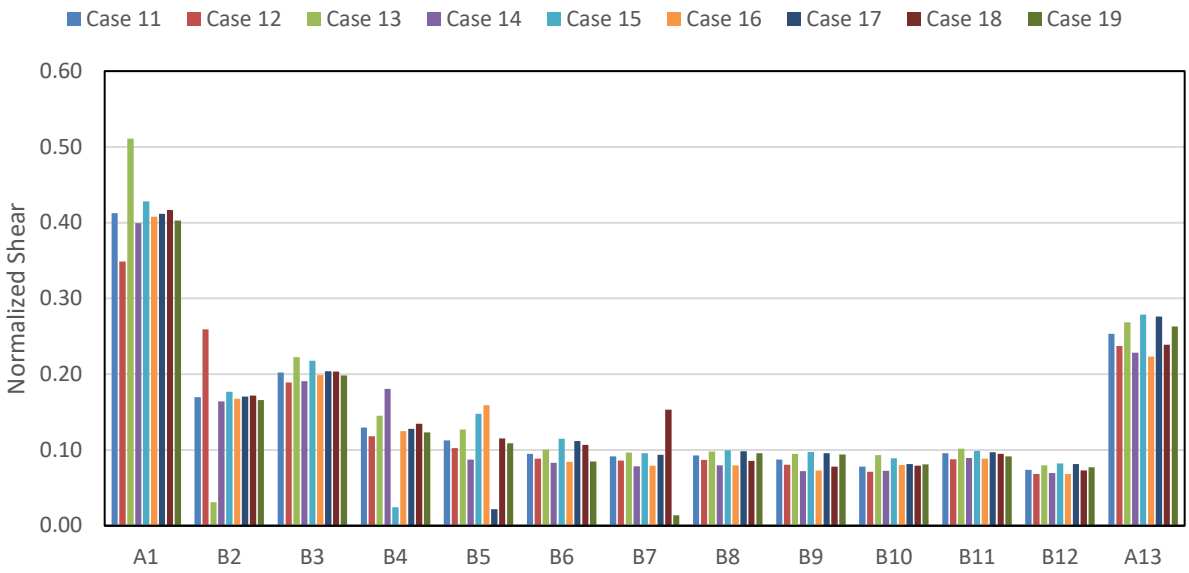

Figure 7-17 Normalized Shear Force Comparison under Span 2 Loading Condition among Twelve-Span Bridges

Based on Figures 7-15, 7-16 and 7-17, changing the stiffness of a single column bent can cause a significant change of normalized shear force in the bents and abutments. Considering Case 11 as the baseline with all bents at the intermediate bent stiffness the change of bent

stiffness of B2 are Cases 12 (high stiffness value) and 13 (low stiffness value). For these figures, all the results are based on braking force being applied to Span 2. This can be seen best in the results for B2. The second bar in each Case represents column B2 with a higher stiffness (Case 12) and hence a higher shear demand. The third bar of the B2 results shows the effect of the column bent stiffness being reduced with a smaller shear demand (Case 13). The overall trend is that columns with larger relative stiffness will have larger normalized shear force while column bents with smaller relative stiffness will have smaller normalized shear force. In the case of a column bent with a smaller relative stiffness, the abutments and remaining bents will take additional shear demand. The normalized shear force in abutments and bents that are adjacent to or within two spans from the modified bent will still experience a change in shear demand, but it will be smaller than for adjacent elements. The normalized shear force in abutments and bents that are more than two spans away from the modified bent are not sensitive to changing an individual column stiffness.

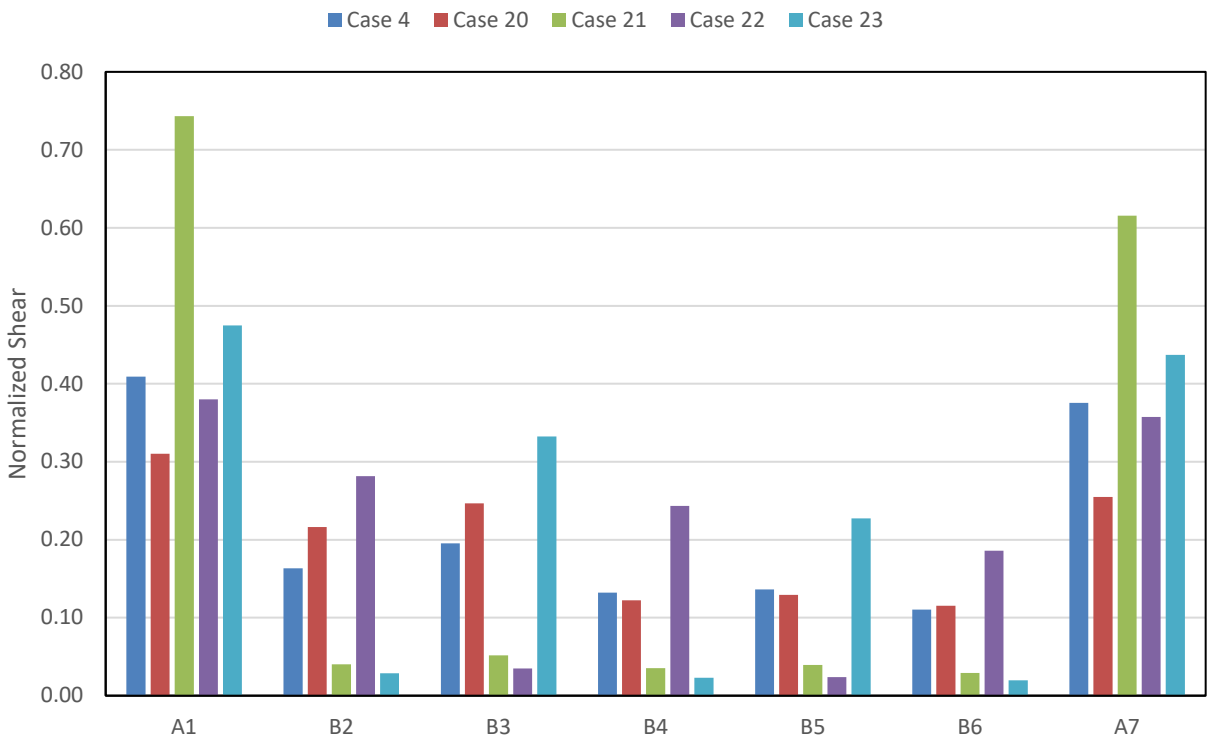

Figure 7-18 Normalized Shear Force Comparison under Span 2 Loading Condition among Six-Span Bridges with Multiple Column Stiffness Changes

Figure 7-18 shows the normalized shear force comparison under a Span 2 loading condition among six-span bridges where multiple column stiffness values were changed between cases. This confirms the same results as the previous figures. The second data bar for B2 shows the increase in shear demand that results from all the column bents having higher stiffness. Data bar 3 of B2 shows the effect of all columns being more flexible. The third and fourth bars demonstrate the same trends as the fourth bar has B2 as a stiff element and the fifth bar has B2 as a flexible condition. Overall, when the relative stiffness of a column bent is changed, the normalized shear force in the modified bent will change significantly especially when the loading is in an adjacent span. The normalized shear force in the bents or abutments that are adjacent or within two spans of the modified bent will have a significant change. The normalized shear force in the bents or abutments that are more than two spans away from the modified bent will have a very small change. These results can be explained using the second type of comparison by fixing the bent or abutment and only looking at the effect of changing loading position and column stiffness.

When considering the maximum normalized shear demand that occurs in a bent, the value ranges based on the column stiffness and location. Considering Cases 4 (intermediate column stiffness), 20 (high column stiffness) and 21 (low column stiffness) where all the columns were the same height. For these cases, the shear demand is the highest in the center columns (B3, B4, and B5). The least magnitude of the normalized shear demand is 0.05, for the most flexible column height, and the highest shear demand is 0.28, for the highest stiffness column. The baseline six-span (Case 4) has a maximum normalized bent shear demand of 0.22. This provides a range for the maximum shear demand in a column when there is generally consistent column stiffness along the length of the bridge.

Figures 7-19, 7-20 and 7-21 show the normalized shear force in Bent 2 (B2) under braking force on each span for the three-span, six-span and twelve-span bridges, respectively. Figures 7-19 and 7-20 show the normalized shear force in Bent 6 (B6) and Abutment 7 (A7) under braking force on each span of the six-span bridges, respectively.

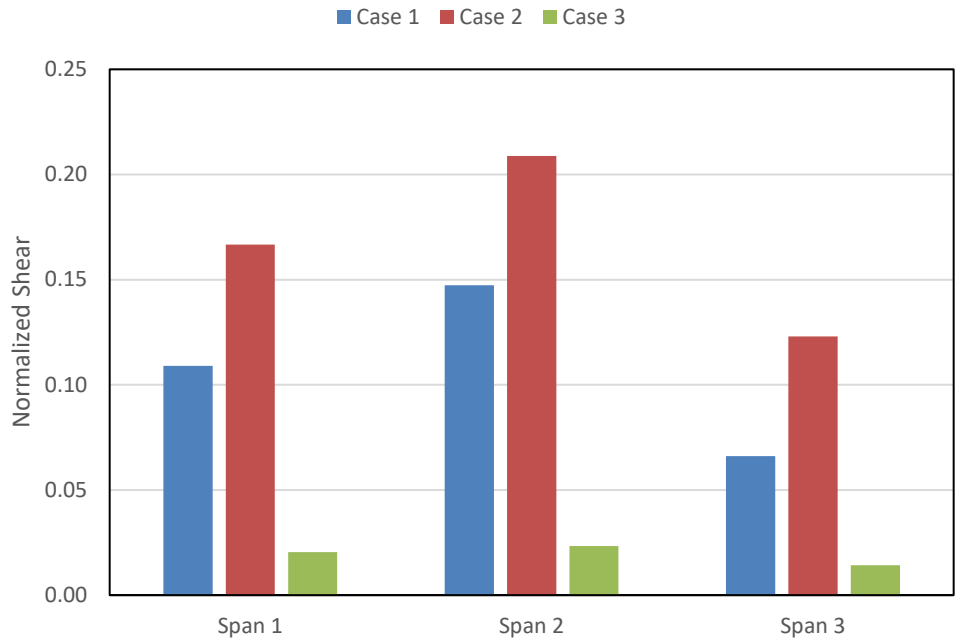

Figure 7-19 Normalized Shear Force in Bent 2 (B2) under Braking Force on Each Span for Three-Span Bridges

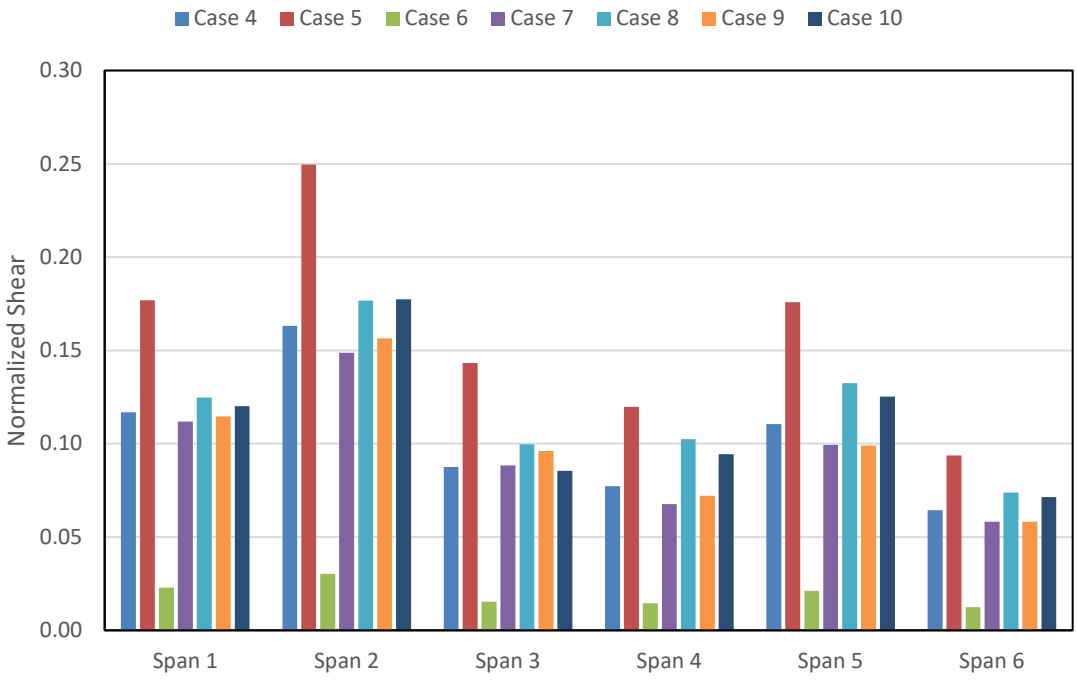

Figure 7-20 Normalized Shear Force in Bent 2 (B2) under Braking Force on Each Span for Six-Span Bridges

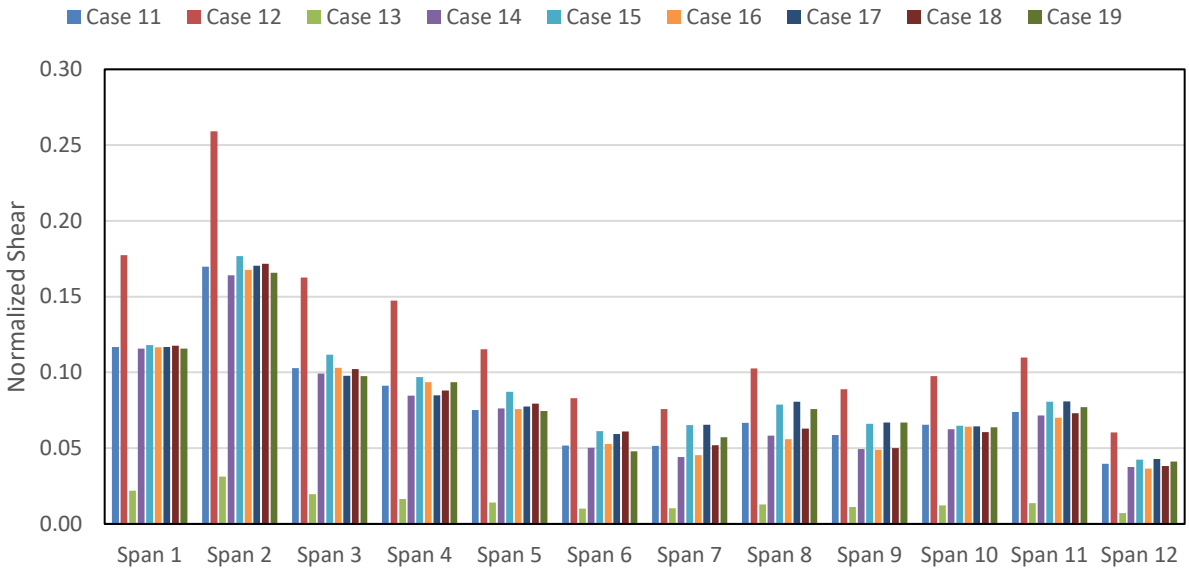

Figure 7-21 Normalized Shear Force in Bent 2 (B2) under Braking Force on Each Span for Twelve-Span Bridges

Based on Figures 7-19 - 7-21, it is further reinforced that the largest impact on shear force demand in a given bent is based on the relative stiffness of that bent. This is most prominent in Figure 7-19. The significant jump in values between Cases 1, 2, and 3 indicate that the stiffening of Bent 2 causes a jump from 0.11 to 0.17 for Span 1 loading due to the stiffening of Bent 2. The same effect is seen when the stiffness of Bent 2 is reduced from the baseline with values going from 0.11 to 0.02. Similar trends can be seen in Figures 7-20 and 7-21 on each of the bents where stiffness changes are considered. This can be seen most easily by the spike in the Case 5 values on Figure 7-20 and the Case 12 values on Figure 7-21.

Normalized shear force in Bent 6 and Abutment 7 on six-span bridges are shown in Figures 7-22 and 7-23. A similar conclusion can be made here for Bent 6. Cases 8, 9 and 10 indicate a significant change of normalized shear force since the change of column height occurs under Bent 4 which is two spans away from Bent 6. When considering the demand on Abutment 7, the influence of the changes in column stiffness do not have a significant impact as the modified columns are not adjacent to the abutment. The most influential parameter in this case is the proximity to the loading. Even when the loading is on the opposite side of the bridge, at least 20 percent of the normalized shear demand is in Abutment 7.

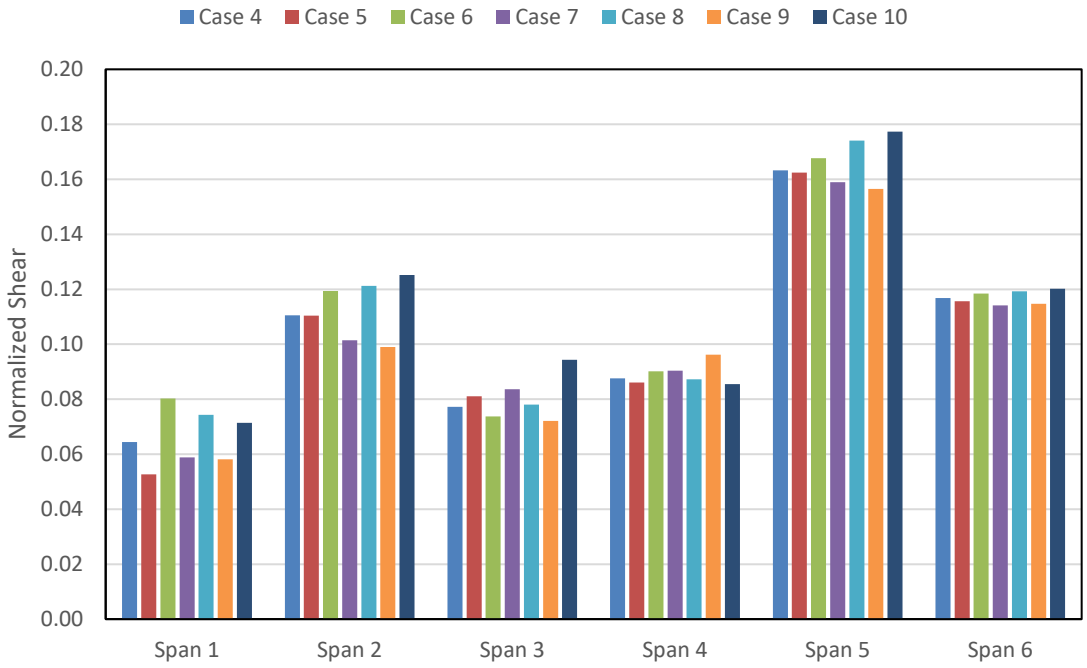

Figure 7-22 Normalized Shear Force in Bent 6 (B6) under Braking Force on Each Span for Six-Span Bridges

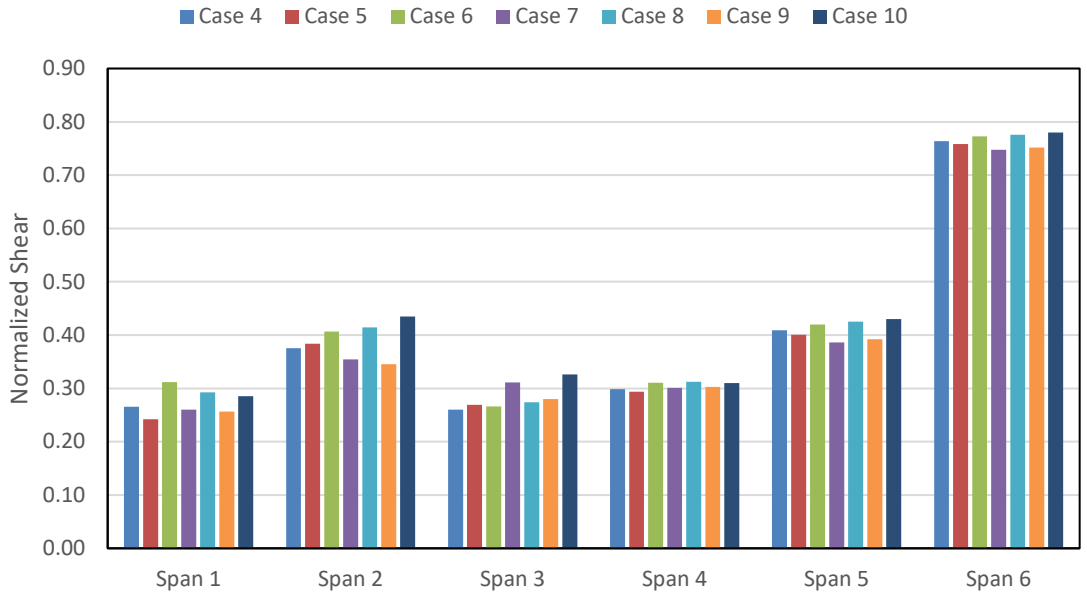

Figure 7-23 Normalized Shear Force in Abutment 7 (A7) under Braking Force on Each Span for Six-Span Bridges

Figures 7-24 and 7-25 show the effect of an individual column with high stiffness that is several spans away from the abutments. Figure 7-24 shows the Case 9 (high stiffness in Bent 4) results for a six-span bridge. Figure 7-25 shows the Case 14 (high stiffness in Bent 4) results for a twelve-span bridge. The important lesson from these plots is the upper limit on the shear demand that occurred in individual bents. For the six-span condition (Figure 7-24), the maximum normalized shear demand is 0.30. For the twelve-span condition (Figure 7-25), the maximum normalized shear demand is 0.34, which is approximately the same as for Cases 16 and 18. Basically, the maximum normalized shear demand for an individual column, which has a higher stiffness than adjacent column bents is approximately 0.34 for a twelve-span and 0.30 for a six-span bridge.

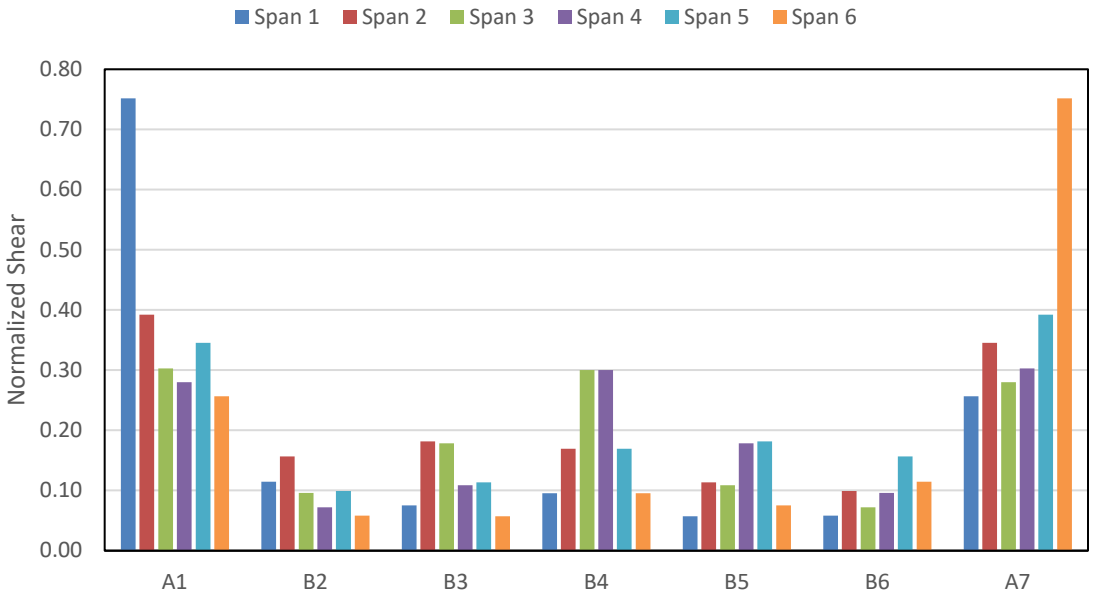

Figure 7-24 Normalized Shear Force for Six-Span Bridge Case 9

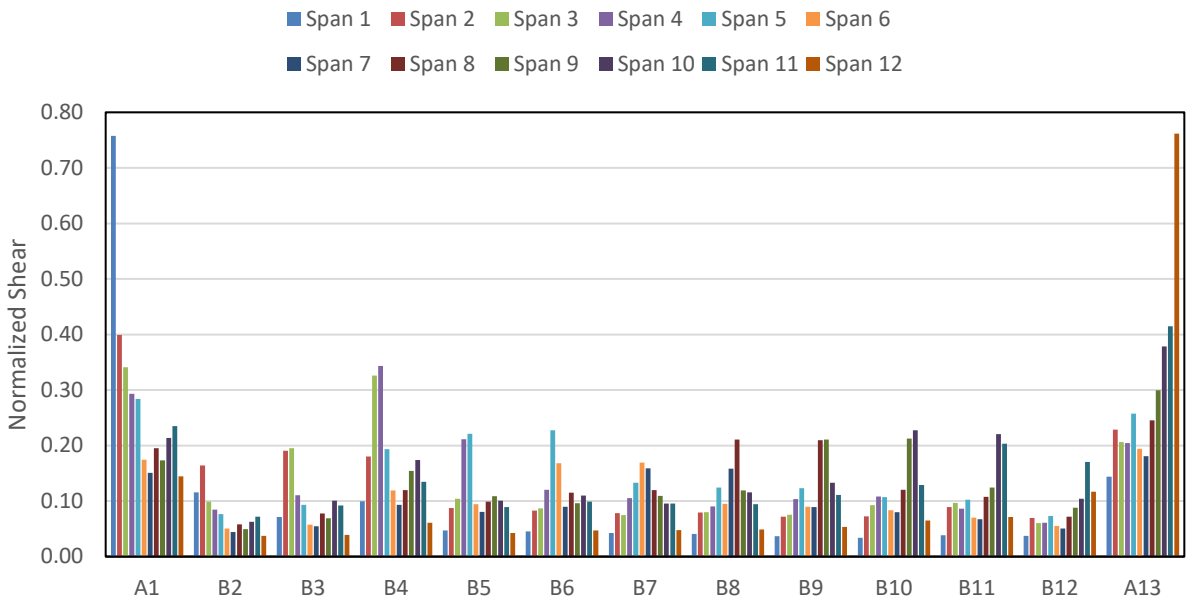

Figure 7-25 Normalized Shear Force for Twelve-Span Bridge Case 14

7.5 Chapter Summary and Conclusions

This limited parametric study provides a better understanding of the distribution of shear demand due to the application of braking force in the longitudinal direction of a bridge. These studies only apply to simply supported bridges bearing on elastomeric bearings that fall within the bounds of the parameters investigated. Several parameters (span length, bridge width, bent type, bridge girder type, girder support condition, bridge continuity) that may have an impact on braking force distribution have not been included in this study but should be considered in future research efforts. The magnitude of the braking force demand in a given bridge substructure component depends on several different conditions. Based on the results of this limited parametric study, the following conclusions can be drawn:

- Independent of the location of braking force application, the abutments take a significant portion of the braking force. The closer the abutment is to the applied force the larger the demand on the abutment. In general, when the braking force is applied to the end span, the adjacent abutment normalized shear demand is approximately 0.70 – 0.80. A dynamic analysis will result in about 0.20 – 0.30 of the normalized shear demand in the

far abutment while a static analysis will show very little normalized demand in the opposite abutment (< 0.05).

- The controlling shear demand in a given substructure element occurs when the braking force is applied to an adjacent span when the closest abutment is on the other side of the bent (i.e. Bent 2 gets the max demand from the loading on Span 2). The magnitude of the normalized shear depends greatly on the relative stiffness of the individual column bent.
- When the distribution of column bent stiffness along the length of a bridge is relatively consistent the upper limit of the normalized column shear demand is 0.28, which corresponds to a very stiff column. The intermediate column stiffness condition results in a normalized column shear demand of 0.22.
- An individual column with a significant difference in stiffness between adjacent column bents results in a significant difference in the shear demand. The upper limit normalized shear demand for a column that has a higher relative stiffness in relation to adjacent columns in this study was 0.34. A column that is very flexible with respect to adjacent columns can have very low values for normalized shear demand which can be less than 0.05.
- Statically applied braking forces provide a good prediction of the shear demand in a column bent provided the force is applied in an adjacent span.
- As most bridges do not have a consistent column stiffness along the length, a static analysis is recommended to determine the shear demand in the individual column bent. The placement of the braking force to determine the controlling column shear demand will result from forces placed in the adjacent spans.

Chapter 8 Summary and Conclusions

8.1 Summary

The research conducted in this project was undertaken to gain insight into to the load path and intensity of the longitudinal braking force in highway bridge substructures, specifically shorter span, simply-supported bridges. With the LRFD Specifications requiring a larger magnitude of force to be designed for than the Standard Specifications, it became necessary to better understand the implications of braking and what magnitude of forces are going to be generated.

To evaluate braking force magnitude and distribution, two types of field tests were conducted. First, static pull tests were conducted on each span with enough force generated to either reach 20 kips of tension in the cable connecting the tow truck and the load truck or the load truck brakes unable to resist the pulling force and the truck beginning to slide. Second, dynamic braking tests were conducted on the center and right side of spans 2, 3 and 5.

From these field tests, the data was processed and an analytical model was created and calibrated to the field data. Directly measuring the amount of shear force in the bridge bents was not possible, therefore, calibrating the displacements and accelerations of the bridge between the field data and model results was crucial to be able to validate the accuracy of the model results.

Bent shear forces from the static and dynamic tests were recorded and analyzed to determine how they compared to code provisions in regards to magnitude. The code does not specially state how the force should be distributed among substructure elements, so the breakdown of total force imparted on the bridge in the longitudinal directions compared to how much of that force each component experienced was analyzed.

The last component of the research project was a limited parametric study which further studied the distribution of the longitudinal braking force based on the position of the loading and the stiffness of the substructure element for simply supported spans typically constructed in Alabama.

8.2 Conclusions

- The static tests demonstrated that the largest deformations occurred in the bents or abutments supporting the loaded spans. Especially when the loaded span is near the abutment, a large

percentage of the deformation (and shear demand) goes into the abutment. When the braking force is on a span near the middle of the bridge, more of the braking force is shared with adjacent bents. Bents not supporting the loaded span experienced much smaller deformations.

- From the experimental tests, the maximum deceleration rate of the vehicle, as well as the vehicle weight, are the deciding factors in the total amount of longitudinal force imparted into the bridge. The average maximum achievable deceleration rate for braking tests on the center of the span was 0.35g and braking tests conducted on the right side averaged 0.31g. This deceleration rate is ultimately the percentage of the truck mass that potentially must be accounted for in design. Given the results of these tests, when compared to the LRFD Specification of 25 percent of the truck weight (the controlling provision for short-span bridges), LRFD does not appear to be overly conservative for determining the total horizontal force imparted to the bridge.
- Determination of the braking force demand in a bridge substructure element can be adequately determined using a static analysis when the substructure element is within close proximity to the loaded span.
- The distribution of the longitudinal braking force is controlled by the position of the braking vehicle and the lateral stiffness of an individual substructure component relative to the other substructure components. Even when the braking vehicle is near the center of a multi-span bridge, the abutments still resist approximately 20 percent of the total braking force due to their high relative stiffness.
- An individual bent will draw braking force shear demand based on the relative stiffness of the bent under consideration. The largest shear demand will occur when the braking vehicle is on an adjacent span. For a column bent flexible with respect to other bents the braking force ratio (bent shear as a ratio of total horizontal shear) is approximately 0.05 while a very stiff column can achieve normalized demands of up to 0.34.

8.3 Recommendations for Design Engineers

- The total longitudinal force on the bridge due to a braking vehicle can be determined by taking the total vehicle weight and multiplying it by the deceleration rate (in units of g). In this research the average deceleration was approximately 0.3 g.
- Distribute the total force among all substructure elements in accordance with the relative stiffness of the substructure elements. For abutments, the design-critical shear force will be based on braking occurring on the end spans of the bridge. For column bents, the design-critical shear demand will result from braking on an adjacent span.
- For the typical bridges analyzed in this study, the maximum force imparted to an abutment is approximately 75 percent of the total braking force. The maximum braking force imparted to an individual bent is approximately 35 percent of the total braking force.
- If able, perform a more rigorous analysis using a structural analysis software and analyze braking conditions on each span to determine the maximum amount of shear force per substructure component that must be resisted. This analysis should apply the braking force at the appropriate height above the deck and account for the support conditions of the bridge girders.
- While not discussed in this research, the moment that is generated at the base of the column based on the shear demand in the column is based on the load path for the braking force. Determining the moment demand at the base of the column using the total height between the applied braking force and the column base is highly conservative.

8.4 Recommendations for Future Research

The results and conclusions presented in this report provide a fundamental basis for the distribution and magnitude of longitudinal braking forces for simple span bridges constructed using ALDOTs typical practices. However, further research would be valuable to confirm these observations and to study the sensitivity of the magnitude of forces in the bridge when changes are made. Topics that could be further investigated are

- Evaluation of how sensitive the bridge is to change in bent stiffness, bent height, bent size, bearing pad stiffness, etc.,
- Evaluation of braking force distribution for bridges that are continuous over supports (i.e. continuous for live load or steel plate girders),

- Investigation on how braking force in longer span bridges is distributed and what magnitudes of longitudinal force are expected,
- The effect of off-center braking on different types of substructures, and
- The accuracy of static analysis versus dynamic analysis of the bridge response when focusing on determination of the maximum design force for an individual substructure component.

References

AASHTO. 2017. *AASHTO LRFD Bridge Design Specifications: Customary U.S. Units.* 8th. Washington D.C.: American Association of State Highway and Transportation Officials.

AASHTO. 2002. *Standard Specification for Highway Bridges.* 17th. Washington D.C.: American Association of State Highway and Transportation Officials.

ALDOT. 2013. *Bridge over Old Town Creek on County Road 9 (Site #2).* Montgomery, AL.

ALDOT. 2018. *Load Case Drawings.*

ALDOT. 2013. "Standard for Standard Details Drawing No. I-131."

Anderson, J. B. 1997. "A Laterally Loaded Pile Database." Masters Thesis, University of Florida.

BSI (2017). Bridge Software Institute, FB-MultiPier, https://bsi.ce.ufl.edu/products/overview.aspx?software=7.

Cai, C. S., S. Eddy, and N. Yazdani. 2000. "Effect of Bearing Pads on Precast Prestressed Concrete Bridges." *Journal of Bridge Engineering* (ASCE) 5 (3): 224-232.

Caltrans. 1994. "Memo to Designers 7-1." 1-7.

Campbell, J.A. (2016). "*Experimental Testing and Analytical Modeling of Driven Steel Pile Bridge Bents*." M.S. Thesis, Auburn University.

Chen, W., and L. Duan. 1999. *Bridge Engineering Handbook.* 1st. CRC Press.

Chopra, A. K. 2017. *Dynamics of Structures: Theory and Applications to Earthquake Engineering.* 5th. Hoboken, NJ: Pearson Education, Inc.

Computers and Structures, Inc. 2018. *CSi Knowledge Base.* Accessed February 24, 2019.

CSI. 2010. *CSiBridge 15.2.0.* Berkely, CA: Computers and Structures, Inc. .

CSI. 2012. *SAP2000 Ultimate Version 20.2.0.* Berkley, CA: Computers and Structures, Inc.

Deng, L., F. Wang, and W. He. 2015. "Dynamic Impact Factors for Simply-Supported Bridges Due to Vehicle Braking." *Advances in Structural Engineering* 18: 791-801.

Garrott, W. R., M. Heitz, and B. Bean. 2011. *Experimental Measurement of the Stopping Performance of a Tractor-Semitrailer From Multiple Speeds.* NHTSA.

Hetenyi, M. (1946). *Beams on Elastic Foundation*. Michigan: University of Michigan Press.

Hsiung, Y., & Chen, Y. (1997). *Simplified Method for Analyzing Laterally Loaded Single Piles in Clays*. Journal of Geotechnical and Environmental Engineering, ASCE, 1018-1029.

McCarthy, D. F. (2007). *Essentials of Soil Mechanics and Foundations Seventh Edition*. Upper Saddle River, New Jersey: Pearson Prentice Hall.

NHTSA. 2008. *Federal Motor Vehicle Safety Standard 121*. Washington, D.C.: National Highway Traffic Safety Administration.

Panzer, J. L. 2013. "Evaluation of Critical and Essential Concrete Highway Bridges in a Moderate Seismic Hazard." Masters Thesis.

Poulos, H G, and E H. Davis. *Pile Foundation Analysis and Design*. New York: Wiley, 1980. Print.

Reese, L. C., and S-T Wang. 1993. *Laterally Loaded Pile Analysis Program for the Microcomputer, Version 2.0. Final Report.* Washington, DC: Federal Highway Administration.

Robertson, P. K., Davies, M. P., & Campanella, R. G. (1989). *Design of Laterally Loaded Driven Piles Using the Flat Dilatometer*. Geotechnical Testing Journal, 30-38.

Skinner, Z. C. (2016). "*Theoretical Modeling and Lateral Load Testing of Driven Steel Pile Bridge Bents*." M.S. Thesis, Auburn University.

Smith, S.W. (1997). *The Scientist and Engineer's Guide to Digital Signal Processing*. California: California Technical Pub.

Snare, M. C. 2002. "Dynamics Model for Predicting Maximum and Typical Acceleration Rates of Passenger Vehicles." Master's Thesis, Virginia Polytechnic Institute and State Univeristy, Blacksburg, VA.

Torbic, D. J., D. W. Harwood, K. R. Richard, W. D. Glauz, and L. Elefteriadou. 2003. *NCHRP Report 505: Review of Truck Characteristics as Factors in Roadway Design.* Washington, D.C.: National Cooperative Highway Research Program.

Yazdani, N., S. Eddy, and C. S. Cai. 2000. "Effect of Bearing Pads on Precast Prestressed Concrete Bridges." *Journal of Bridge Engineering* 224-232.

Appendix A. FB-MULTIPIER and SAP2000 Soil Spring Verification

Table A-1 – Soil Layer Definitions Used for All Bents

Soil Layer Table

Soil Set	Soil Layer	Soil Type	Top Layer Elevation (ft)	Bottom Layer Elevation (ft)	Lateral Model	Axial Model	Torsional Model	Tip Model	Unit Weight (Top) (pcf)
1	1	Cohesive	190.00	185.50	Clay (O'Neill)	Driven Pile	Hyperbolic	Driven Pile	120.000
1	2	Cohesionless	185.50	176.00	Sand (Reese)	Driven Pile	Hyperbolic	Driven Pile	120.000
1	3	Cohesive	176.00	152.50	Clay (O'Neill)	Driven Pile	Hyperbolic	Driven Pile	115.000

Table A-2 – Lateral Model Properties Used for All Bents

Lateral Model Table

Soil Set	Soil Layer	Lateral Model	Internal Friction Angle (deg)	Subgrade Modulus (lb/in^3)	Undrained Shear Strength (psf)	Major Principal Strain @50%	Major Principal Strain @100%
1	1	Clay (O'Neill)			635.0000	0.0006	0.0008
1	2	Sand (Reese)	32.0000	260.4000			
1	3	Clay (O'Neill)			5000.0000	0.0100	0.0200

Table A-3 – Axial Model Properties Used for All Bents

Axial Model Table

Soil Set	Soil Layer	Axial Model	Internal Friction Angle (deg)	Shear Modulus (ksi)	Poisson's Ratio	Undrained Shear Strength (psf)	Unconfined Compressive Strength (psf)	Mass Modulus (Em) (ksi)	Modulus Ratio (Em/Ei)	Surface	Split Tensile Strength (psf)	Pile Concrete Unit Weight (pcf)	Slump (in)	Ultimate Unit Skin Friction (psf)
1	1	Driven Pile		3.50	0.30									3000.00
1	2	Driven Pile		3.50	0.30									3000.00
1	3	Driven Pile		3.50	0.30									3000.00

Table A-4 – Torsional Model Properties Used for All Bents

Torsional Model Table

Soil Set	Soil Layer	Torsional Model	Internal Friction Angle (deg)	Undrained Shear Strength (psf)	Shear Modulus (ksi)	Torsional Shear Stress (psf)
1	1	Hyperbolic		635.00	3.50	3000.00
1	2	Hyperbolic	32.00		3.50	3000.00
1	3	Hyperbolic		5000.00	3.50	3000.00

Table A-5 – Tip Model Properties Used for All Bents

Tip Model Table

Soil Set	Soil Layer	Tip Model	Internal Friction Angle (deg)	Shear Modulus (ksi)	Poisson's Ratio	Axial Bearing Failure (kips)
1	3	Driven Pile		3.5000	0.3500	144.0000

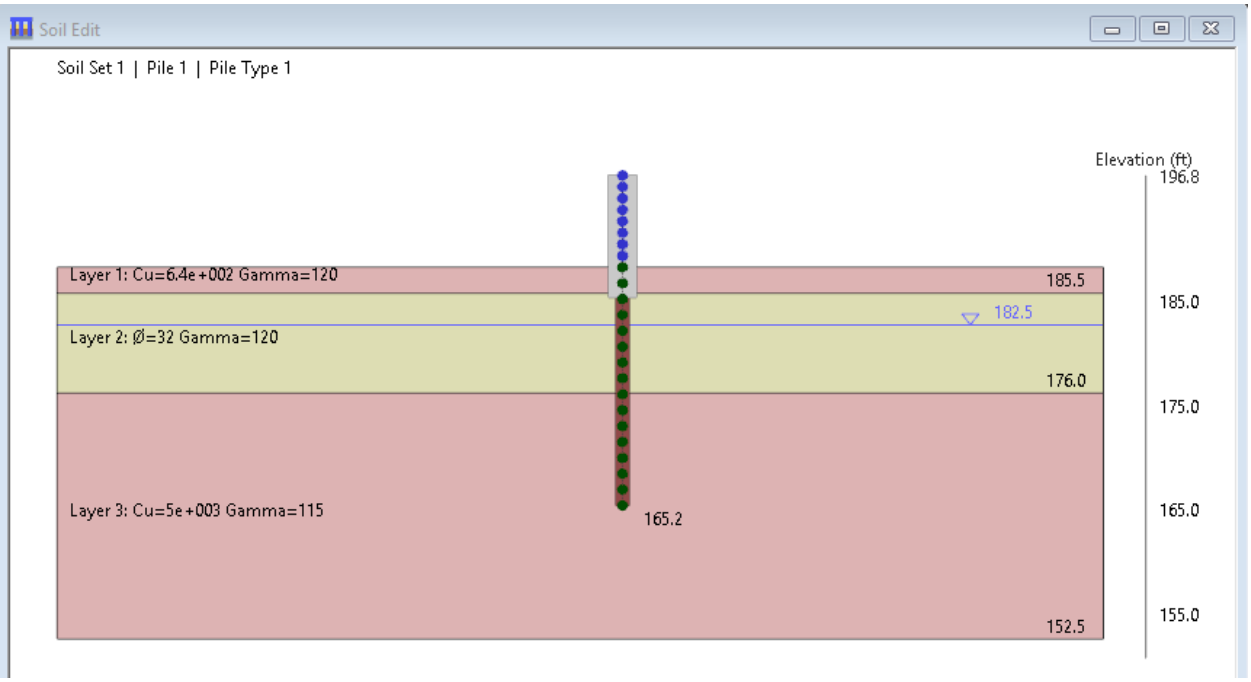

Figure A-1 – Bent 2 Elevation View in FBMP

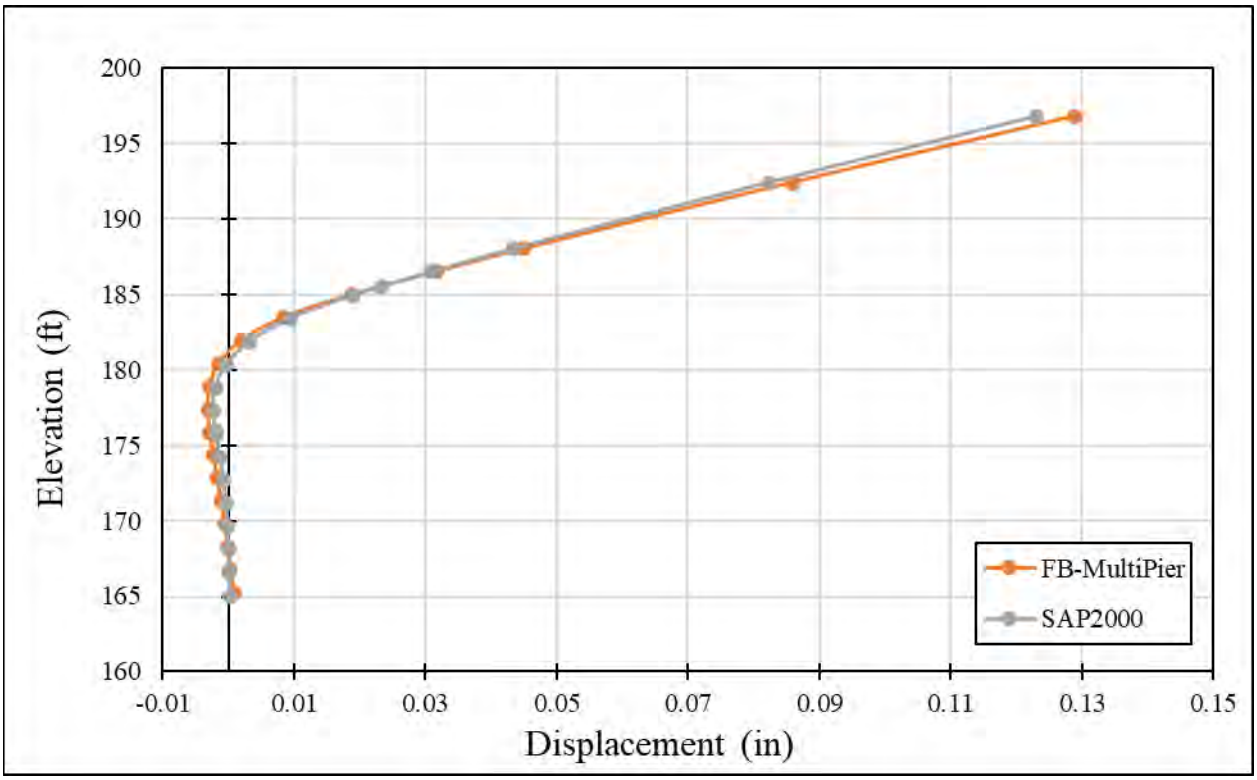

Figure A-2 – Displacement Comparisons for Pile 1 of Bent 2

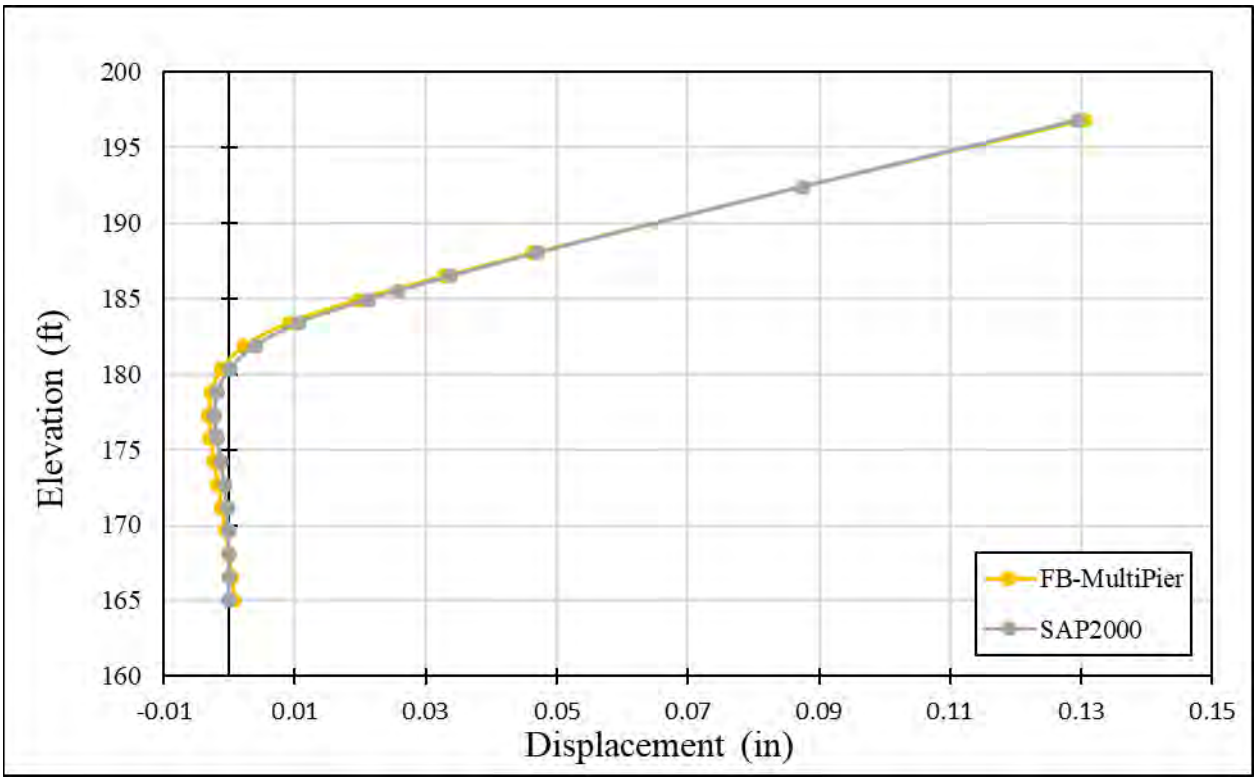

Figure A-3 – Displacement Comparisons for Pile 2 of Bent 2

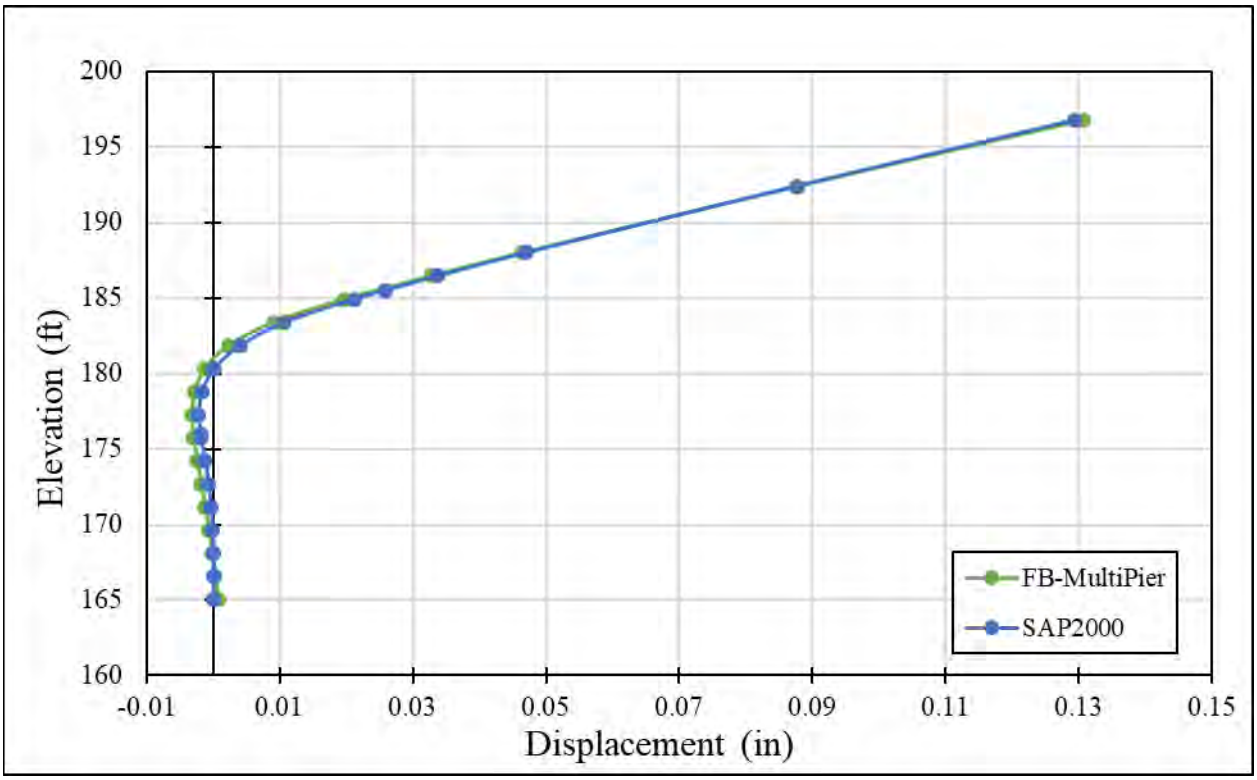

Figure A-4 – Displacement Comparisons for Pile 3 of Bent 2

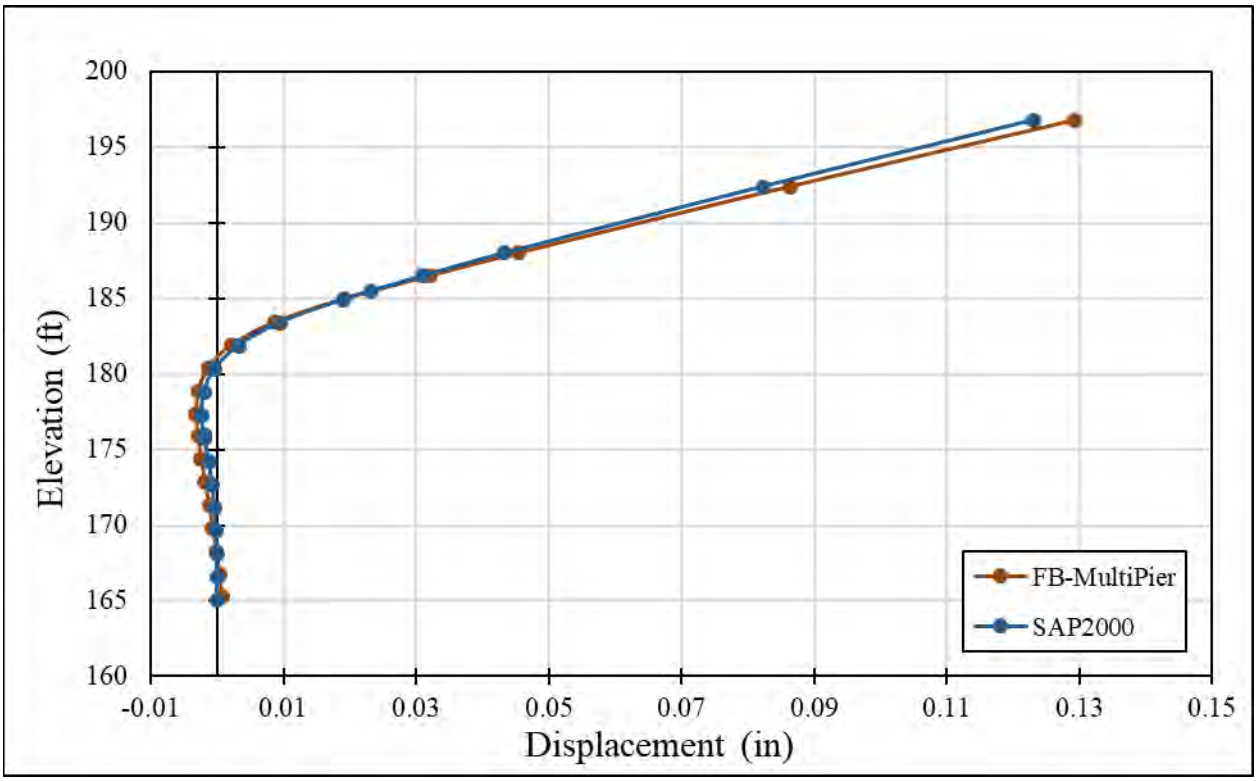

Figure A-5 – Displacement Comparisons for Pile 4 of Bent 2

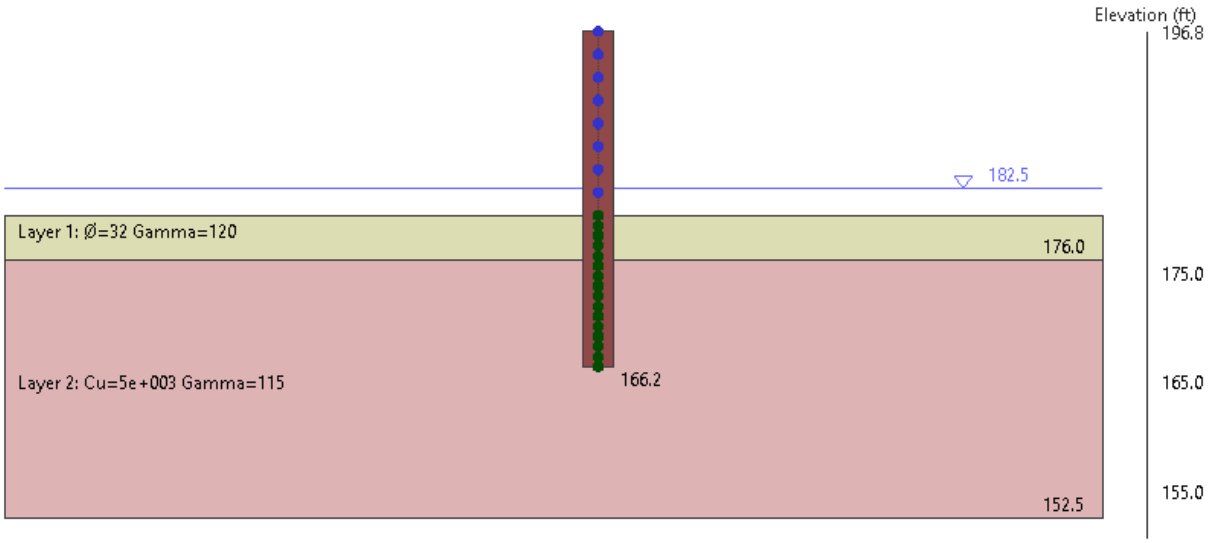

Figure A-6 – Bent 3 Elevation View in FBMP

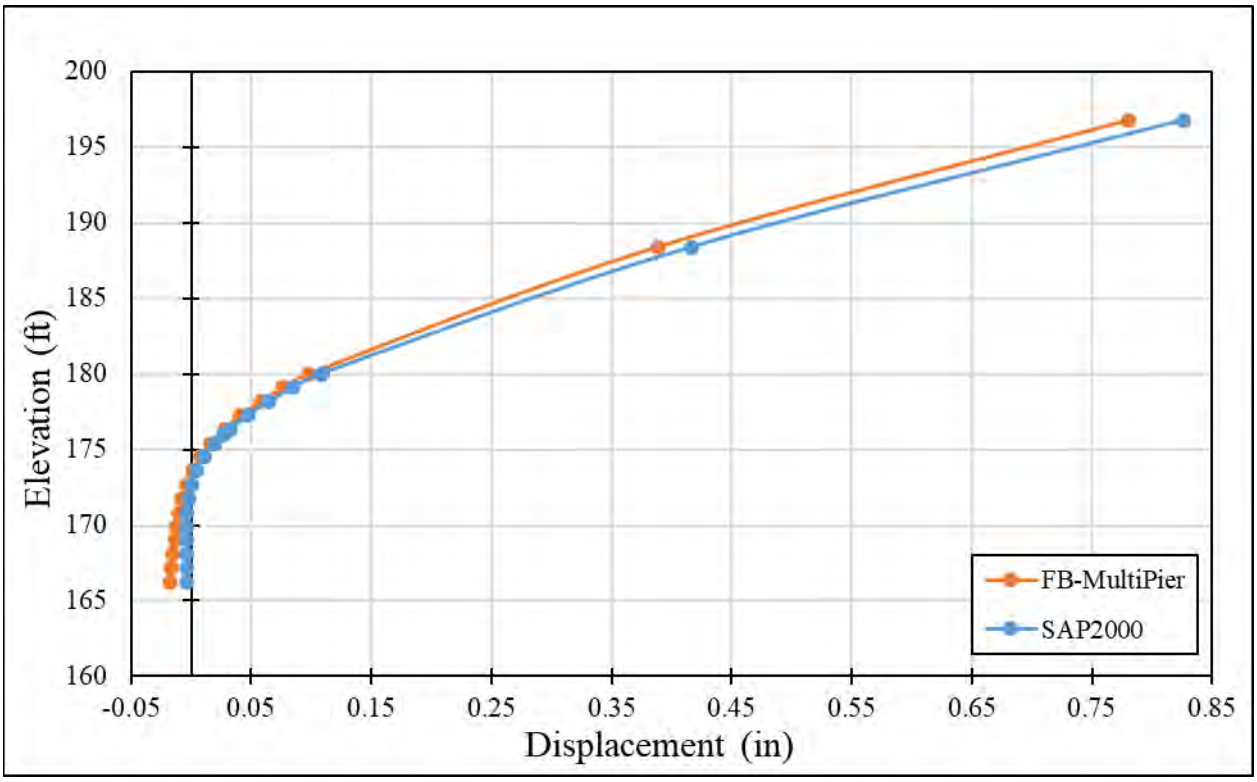

Figure A-7 – Displacement Comparisons for Pile 1 Bent 3

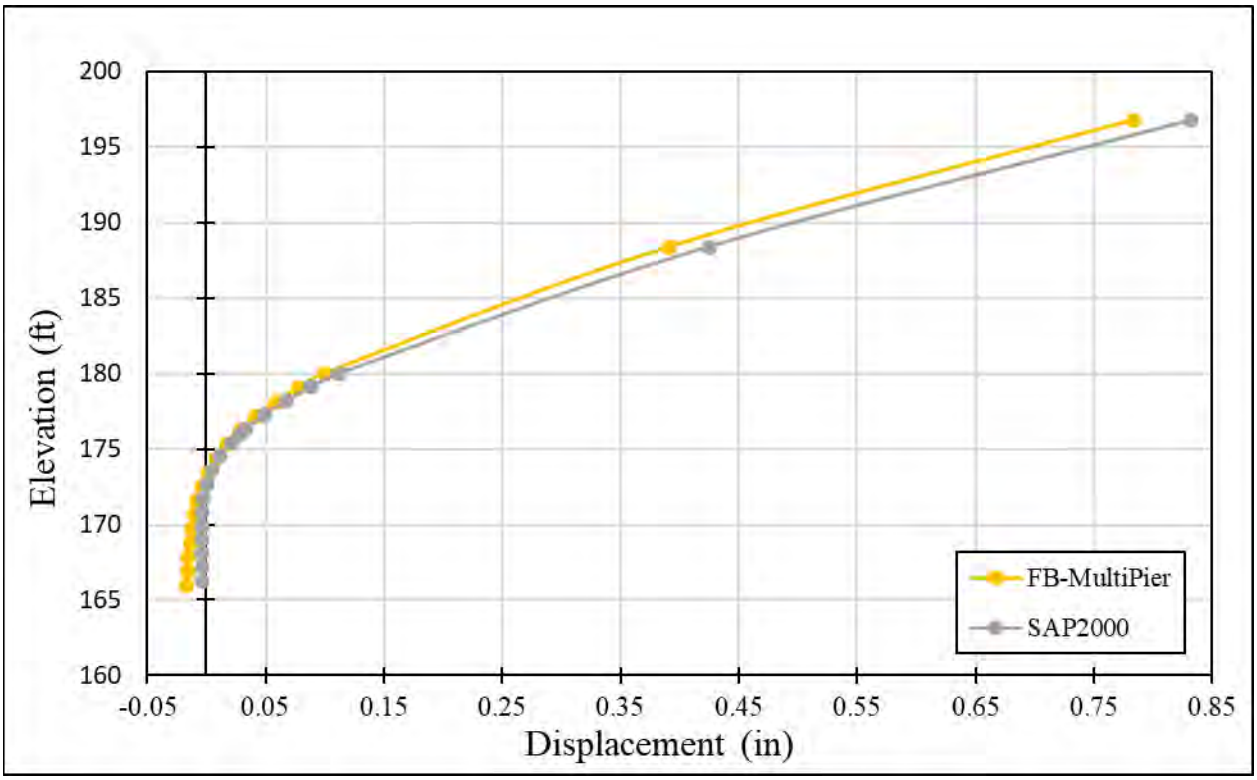

Figure A-8 – Displacement Comparisons for Pile 2 Bent 3

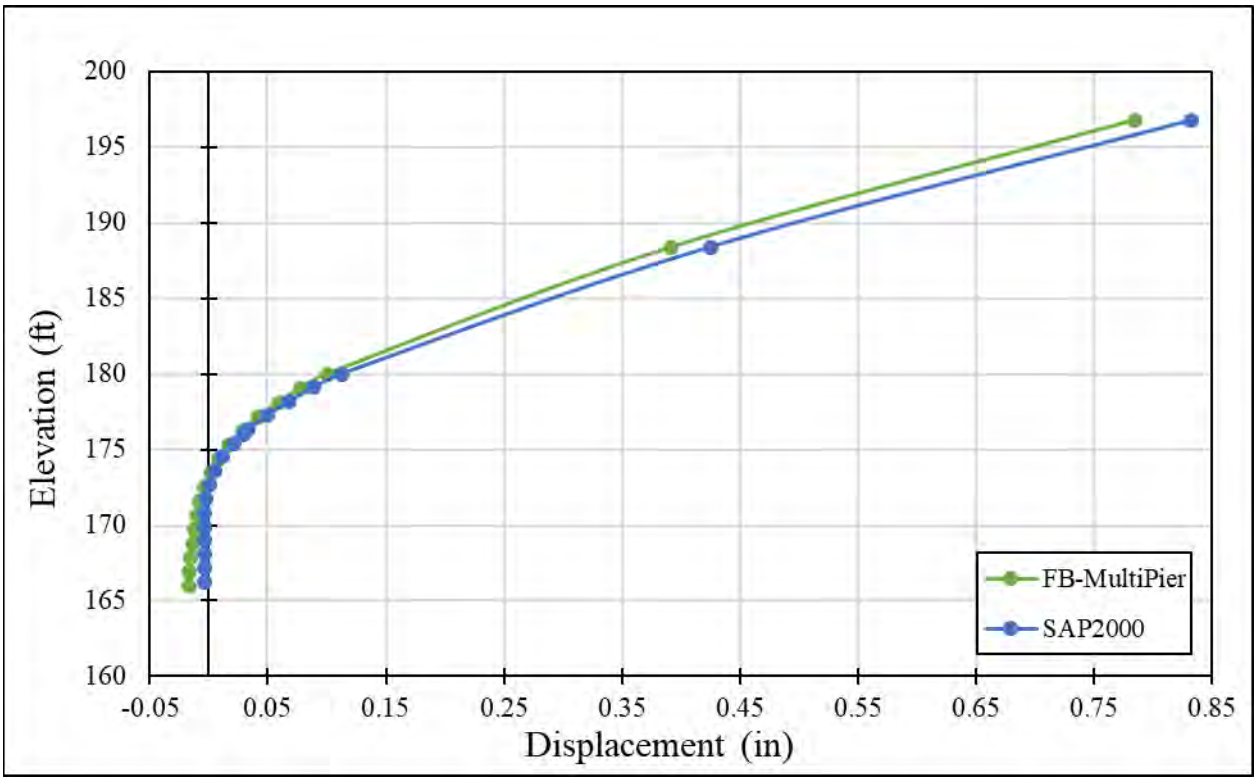

Figure A-9 – Displacement Comparisons for Pile 3 Bent 3

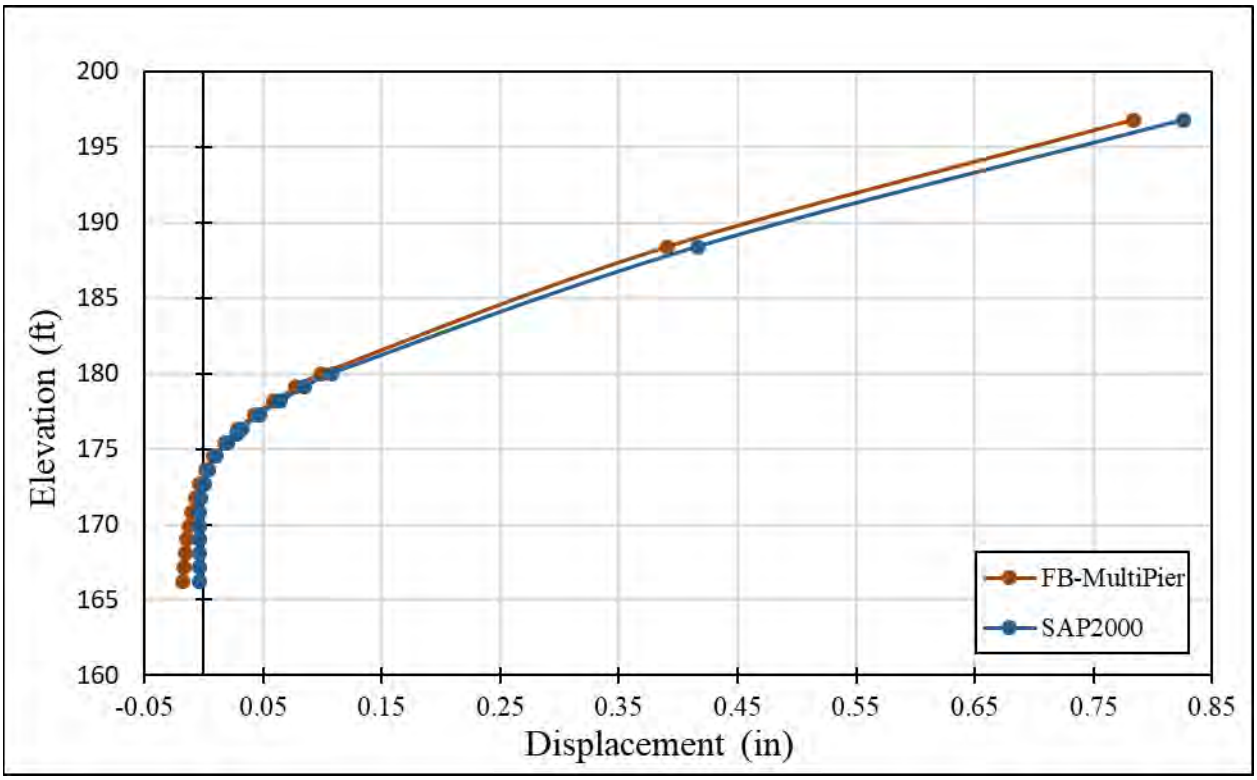

Figure A-10 – Displacement Comparisons for Pile 4 Bent 3

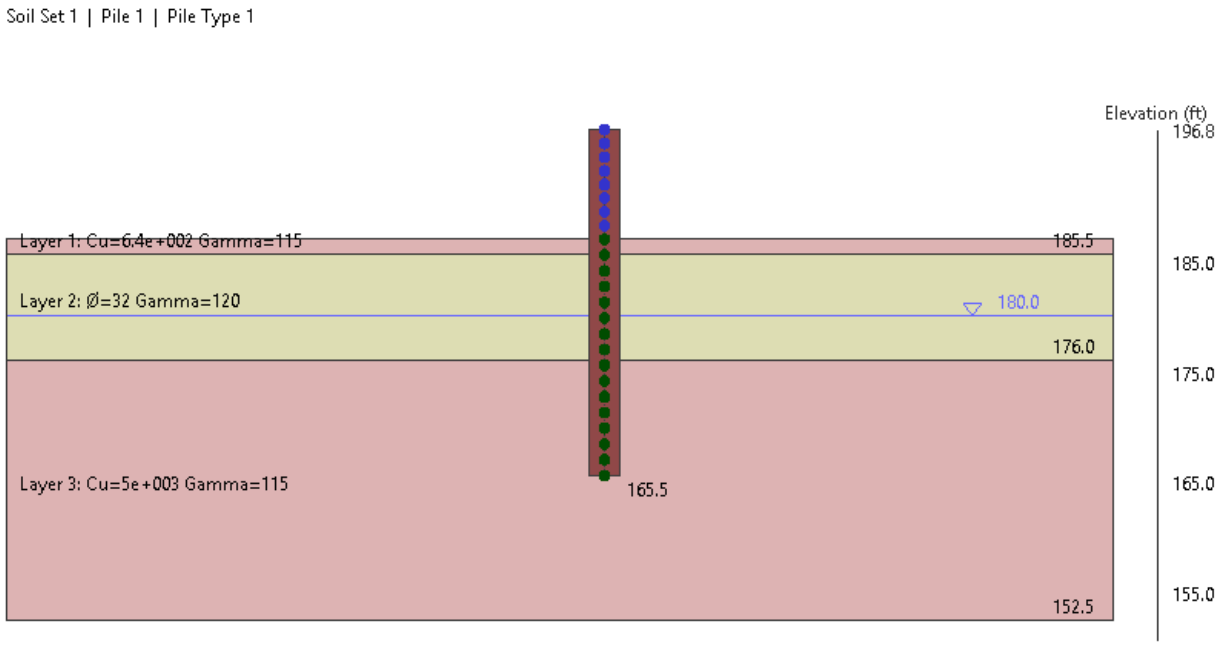

Figure A-11 – Bent 4 Elevation View in FBMP

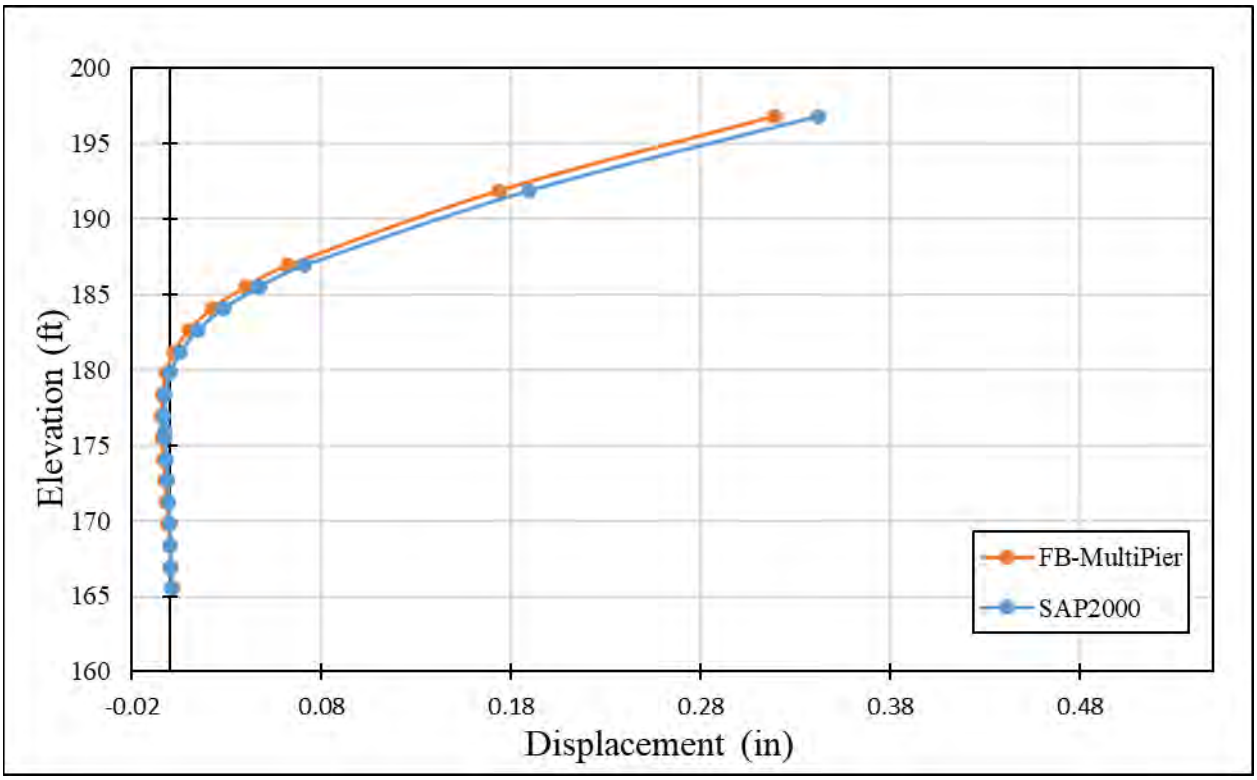

Figure A-12 – Displacement Comparisons for Pile 1 Bent 4

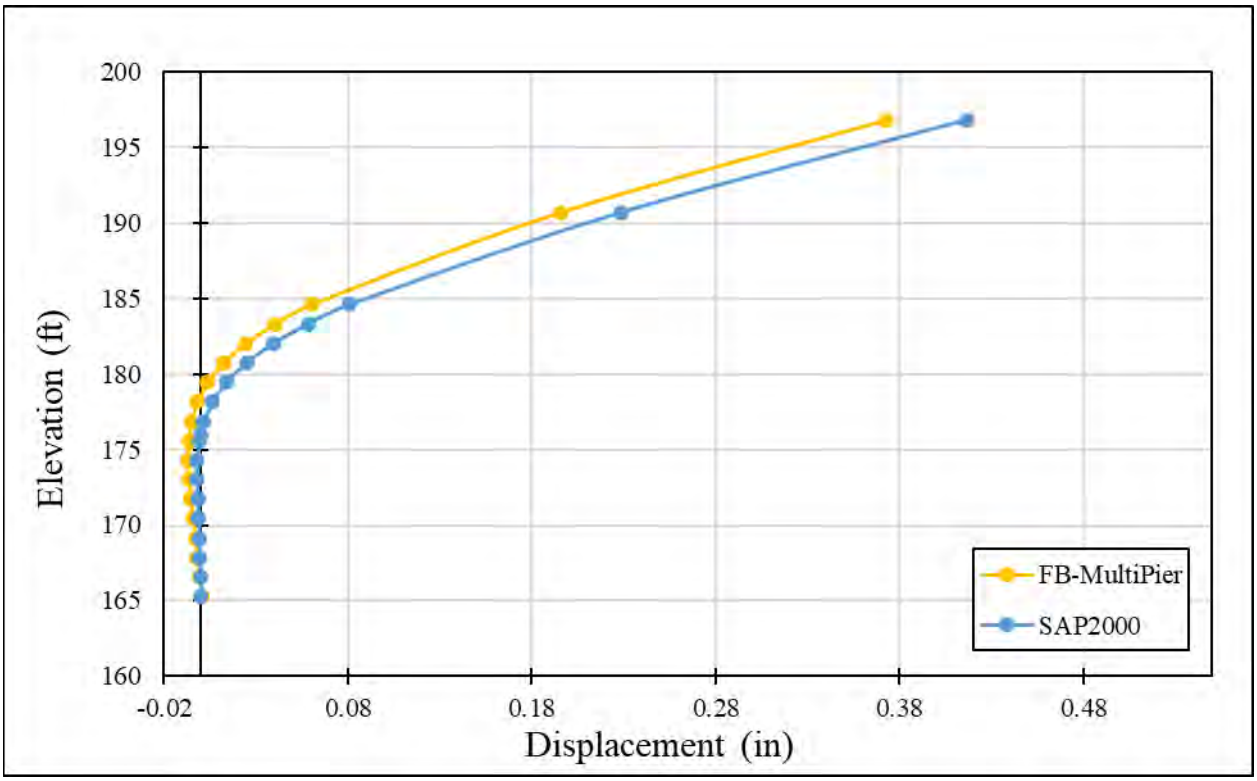

Figure A-13 – Displacement Comparisons for Pile 2 Bent 4

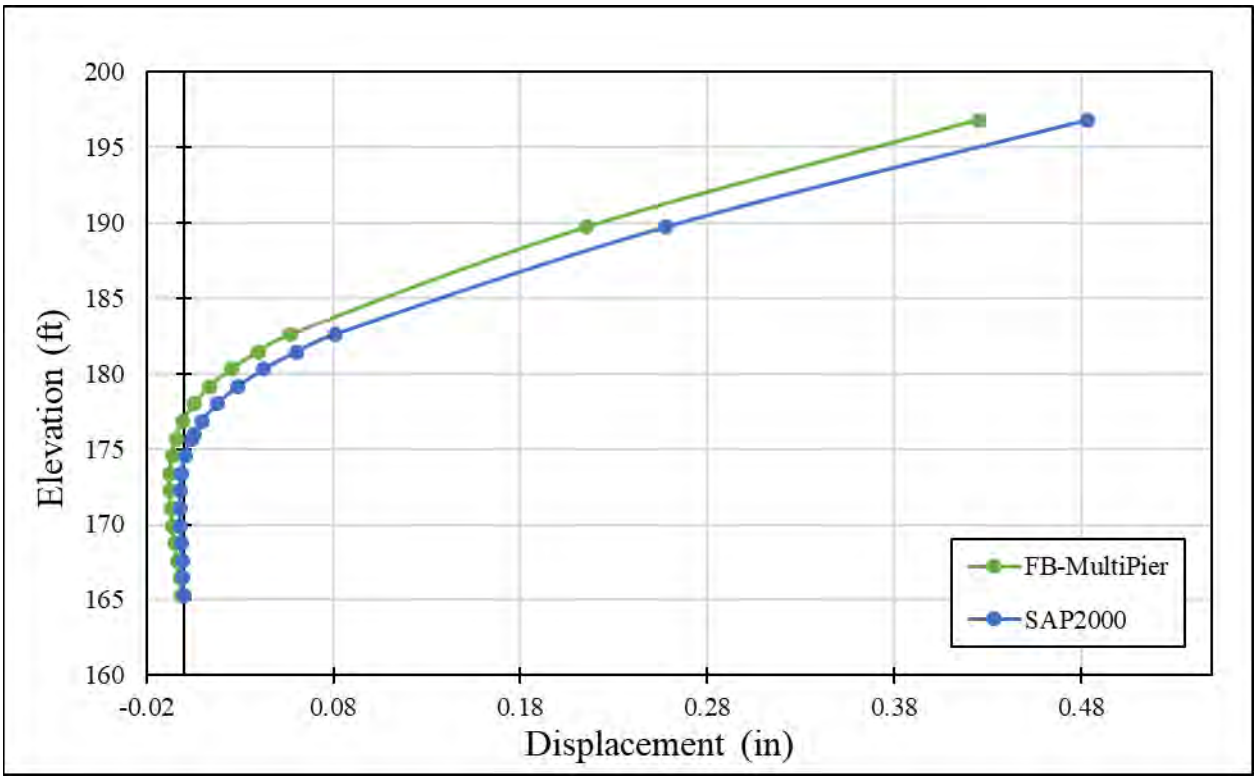

Figure A-14 – Displacement Comparisons for Pile 3 Bent 4

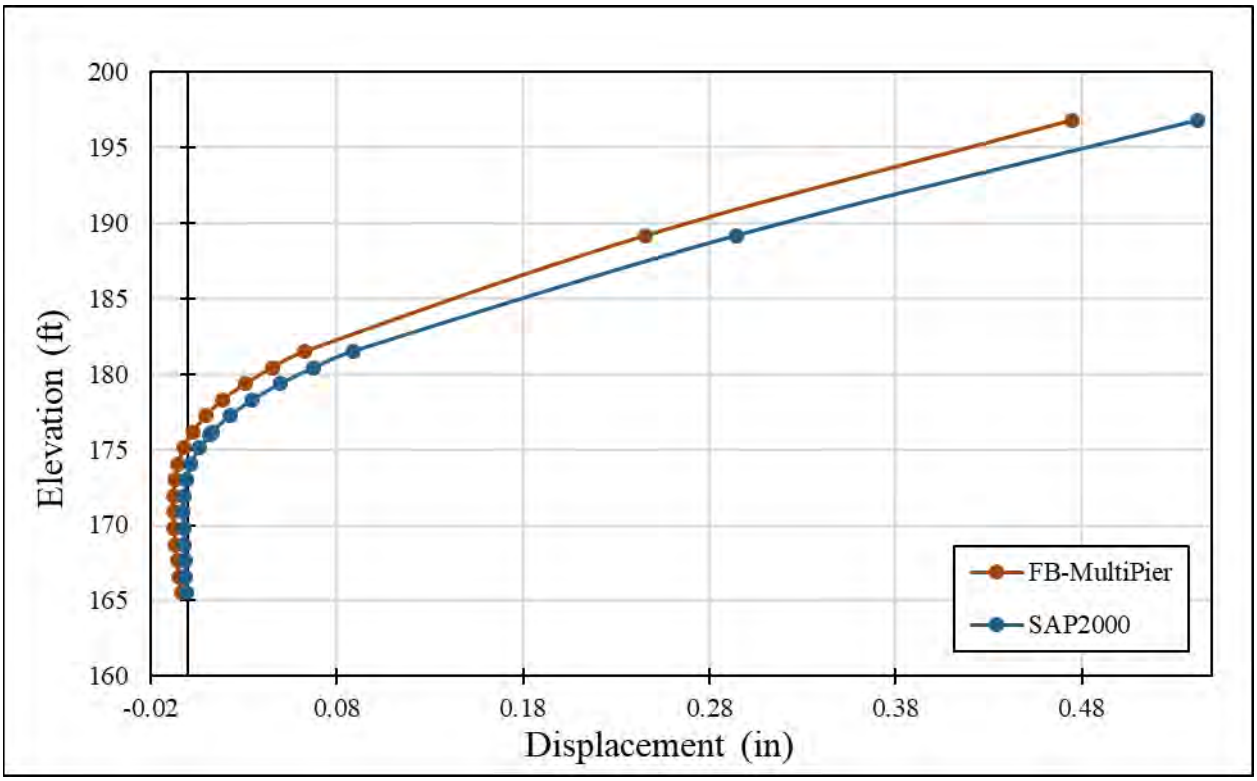

Figure A-15 – Displacement Comparisons for Pile 4 Bent 4

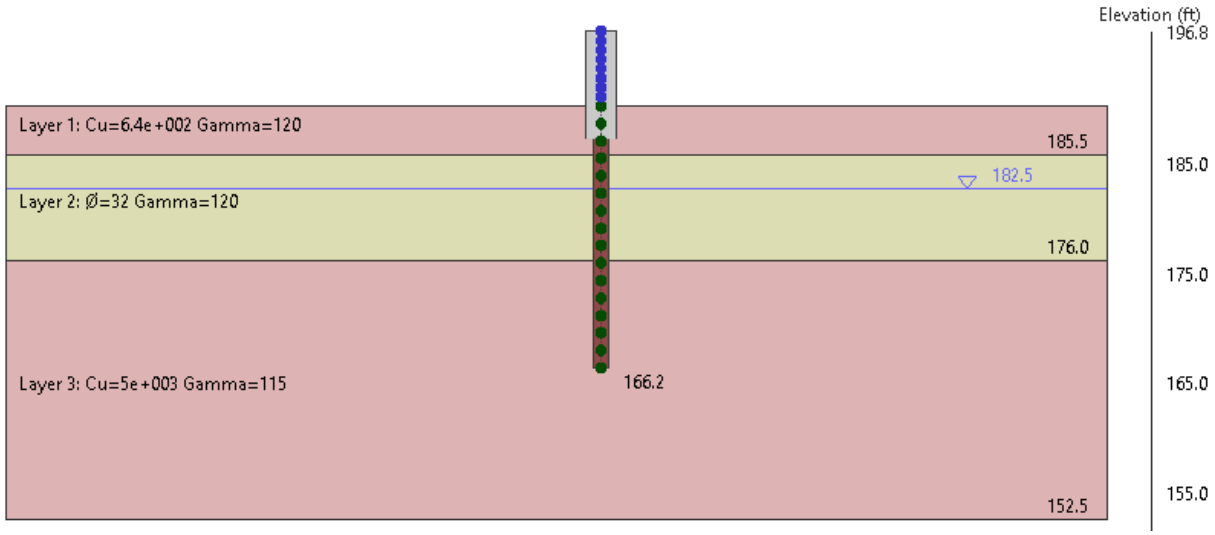

Figure A-16 – Bents 5 and 6 Elevation View in FBMP

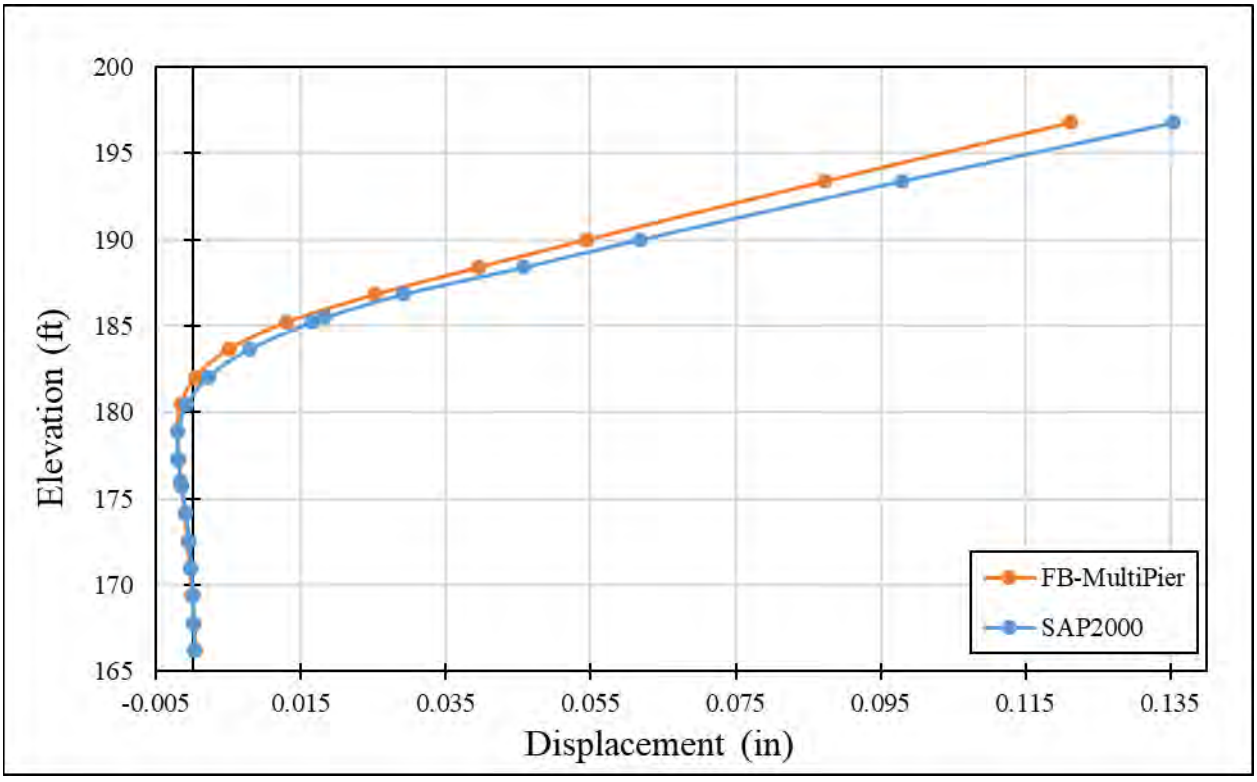

Figure A-17 – Displacement Comparisons for Pile 1 Bent 5&6

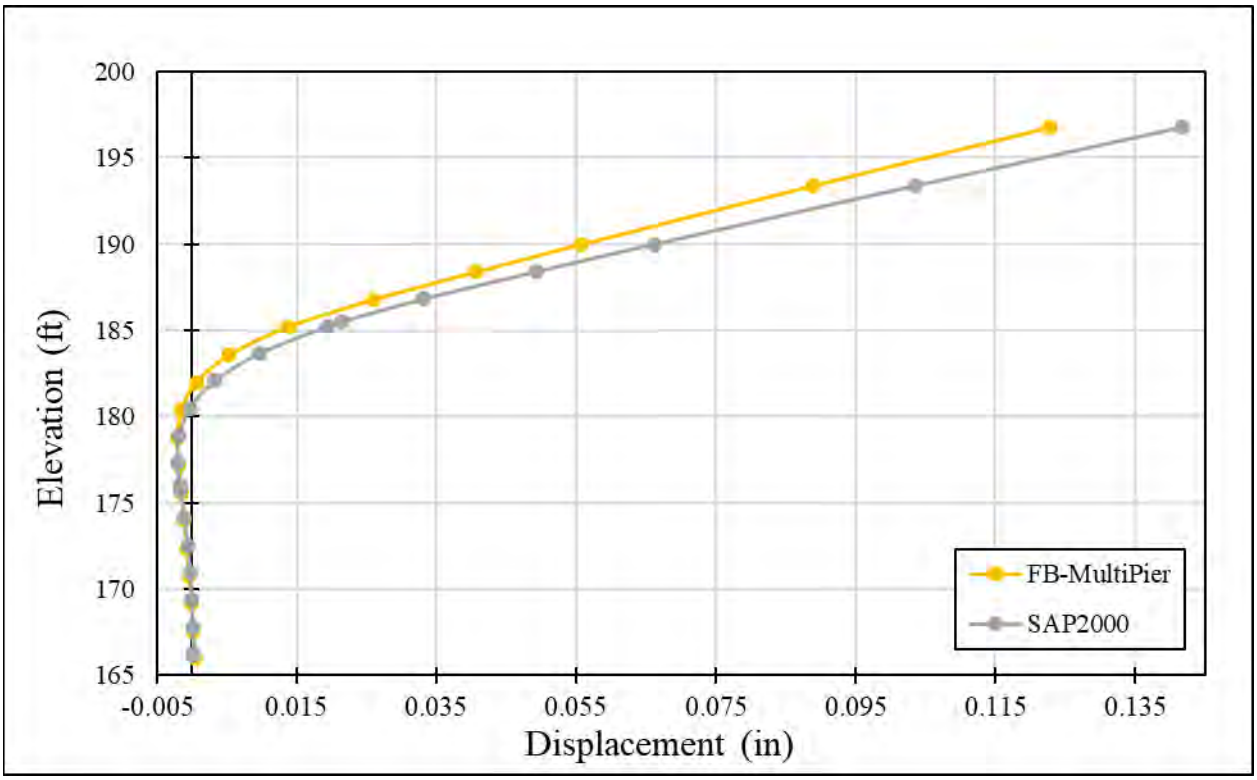

Figure A-18 – Displacement Comparisons for Pile 2 Bent 5&6

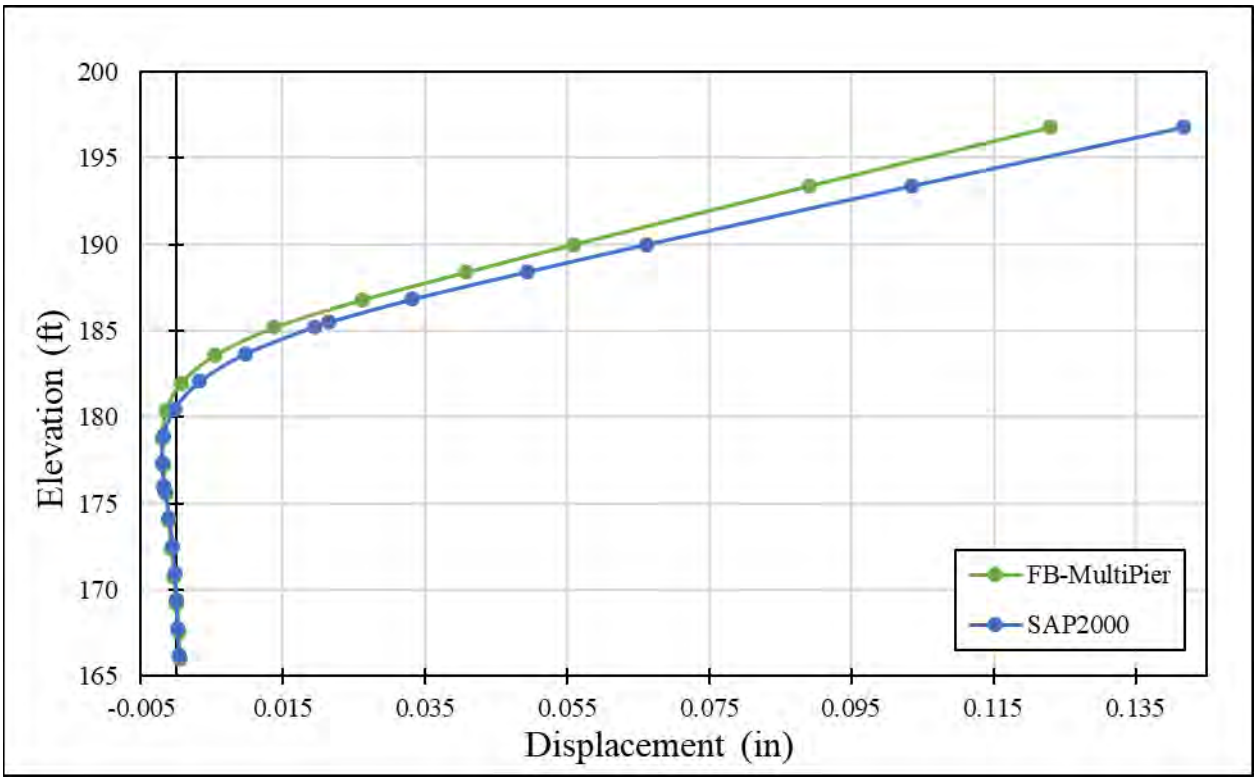

Figure A-19 – Displacement Comparisons for Pile 3 Bent 5&6

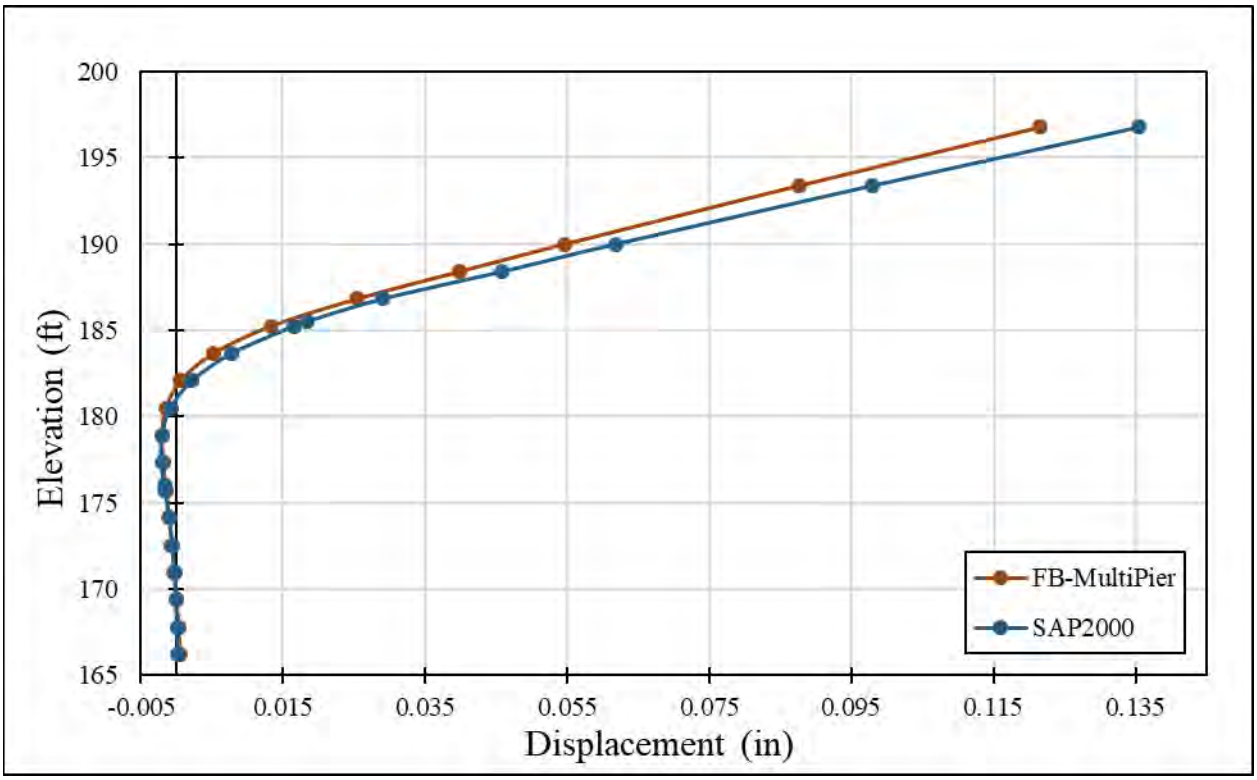

Figure A-20 – Displacement Comparisons for Pile 4 Bent 5&6

Appendix B. Static Tests Downsampled Data

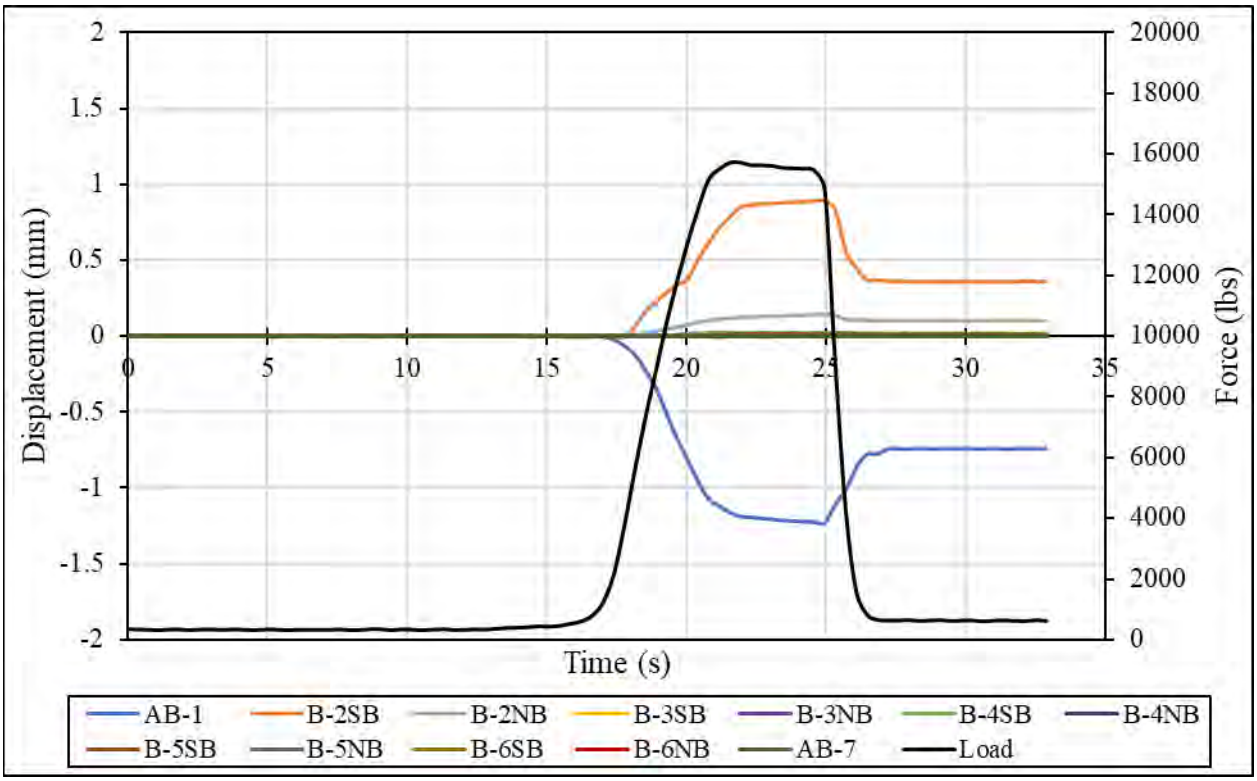

Figure B-1 – Load and Displacement over Time for Span 1 Static Pull Test

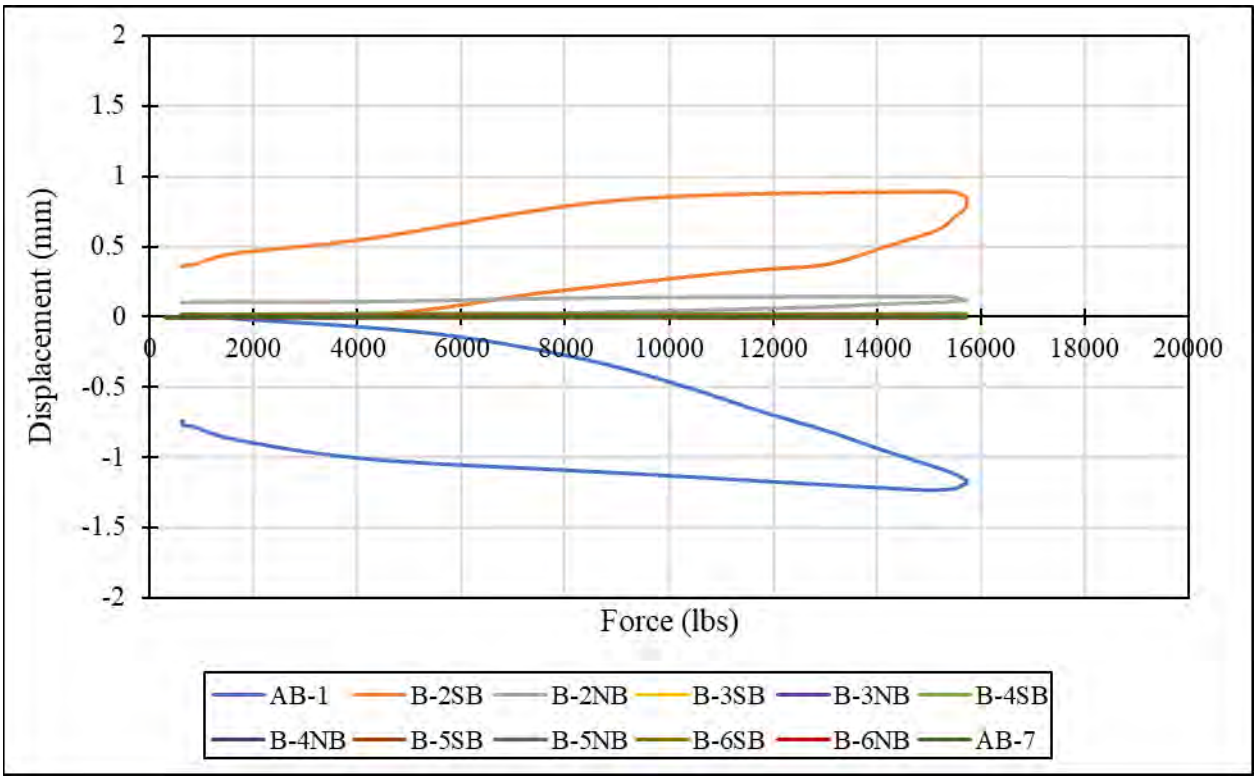

Figure B-2 – Displacement versus Applied Load for Span 1 Static Pull Test

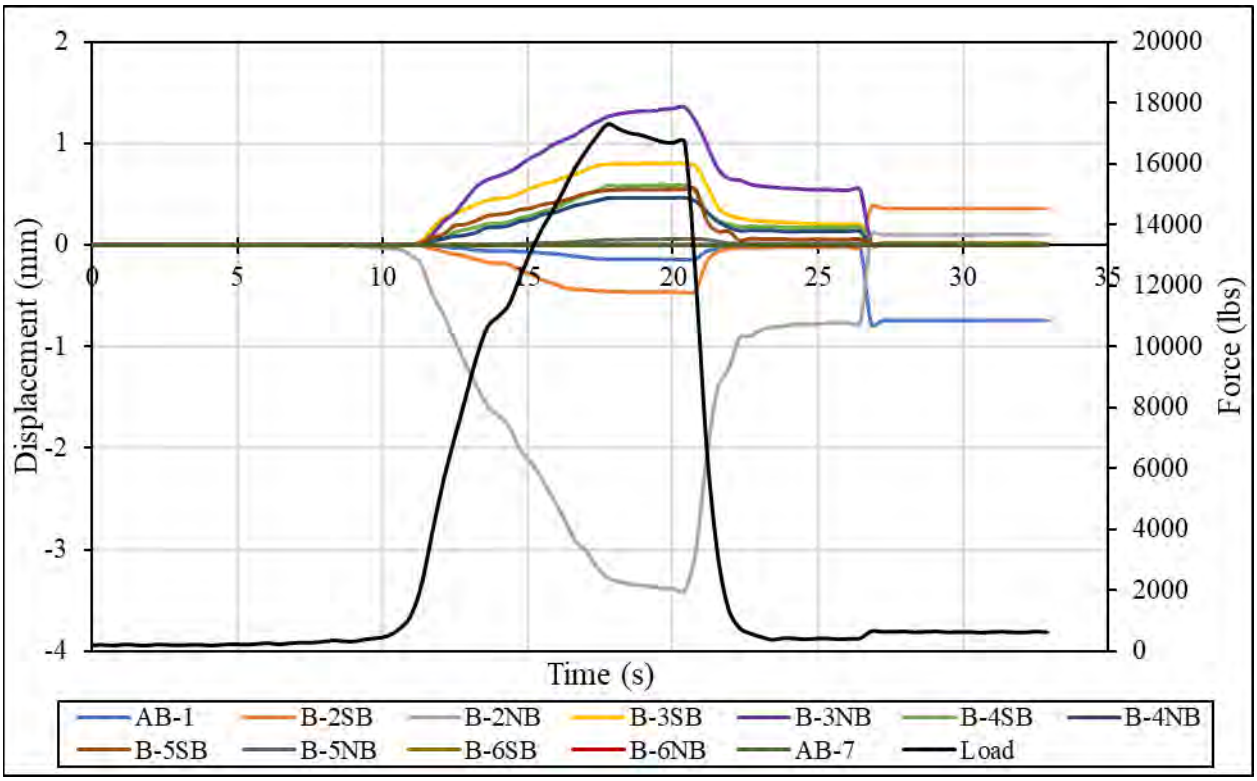

Figure B-3 – Load and Displacement over Time for Span 2 Static Pull Test

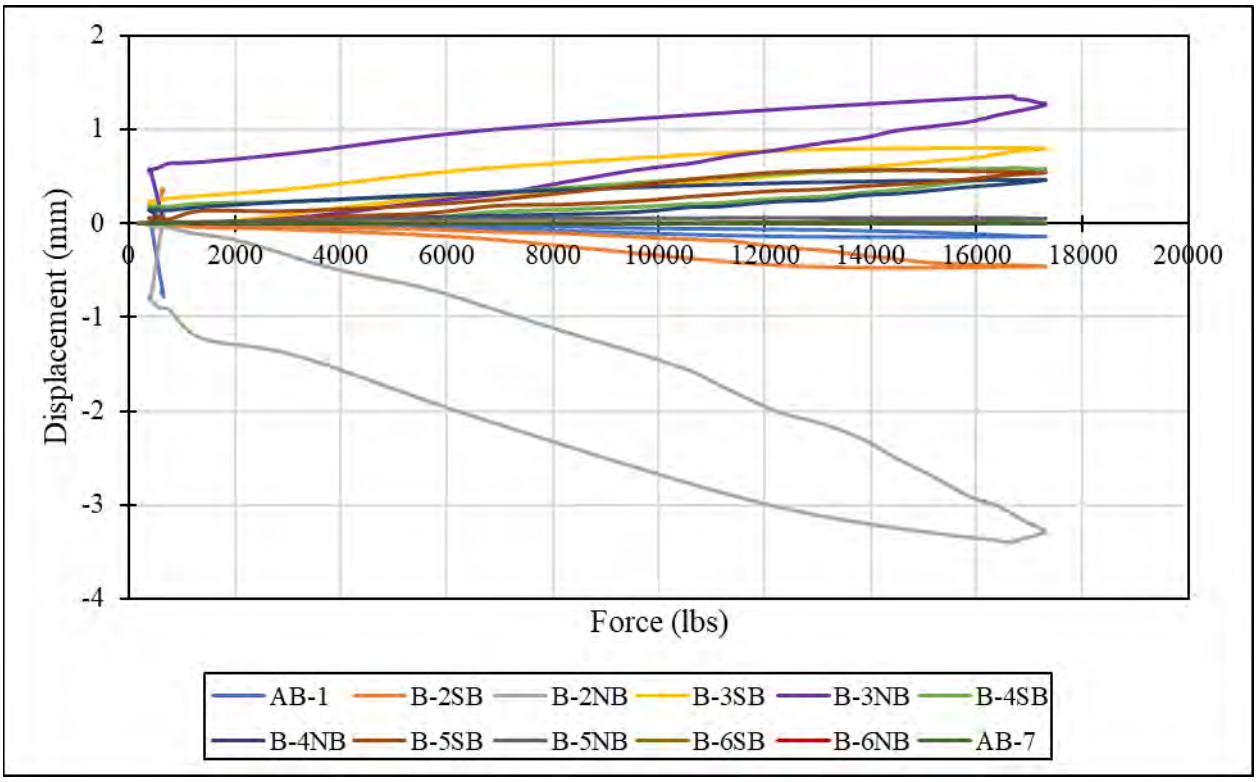

Figure B-4 – Displacement versus Applied Load for Span 2 Static Pull Test

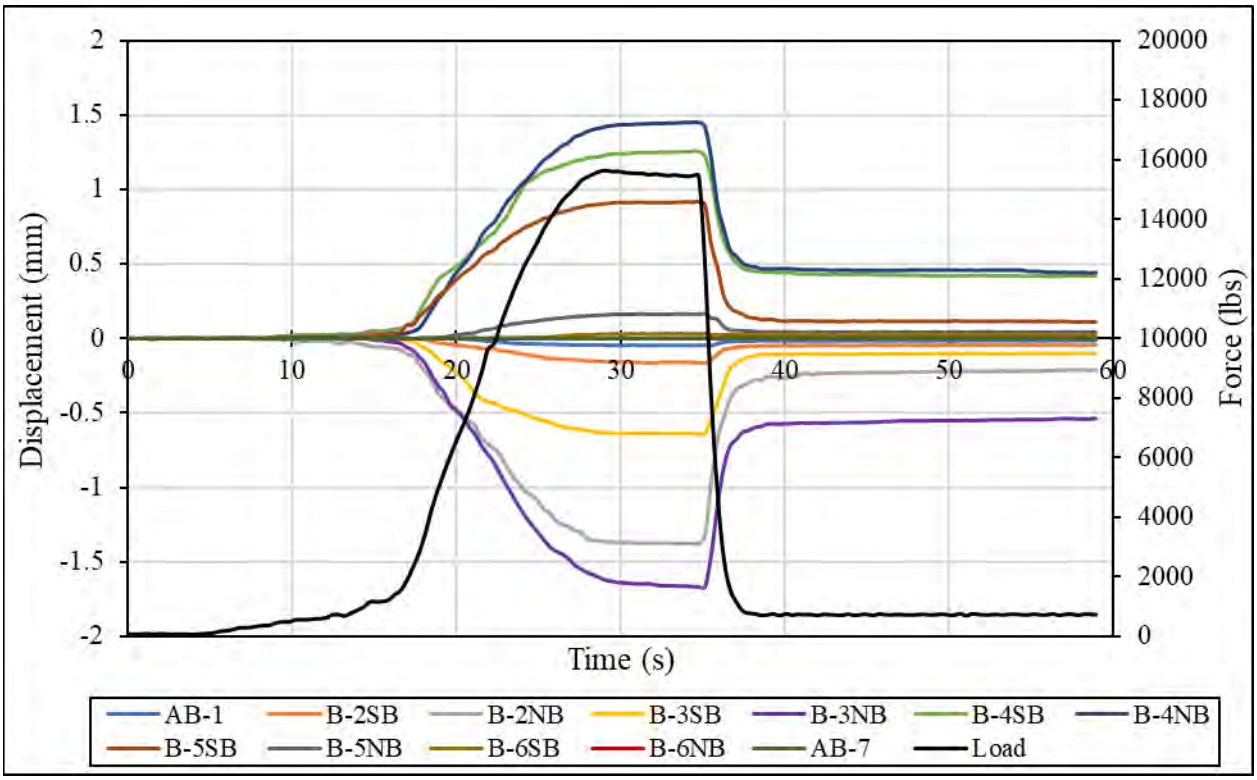

Figure B-5 – Load and Displacement over Time for Span 3 Static Pull Test

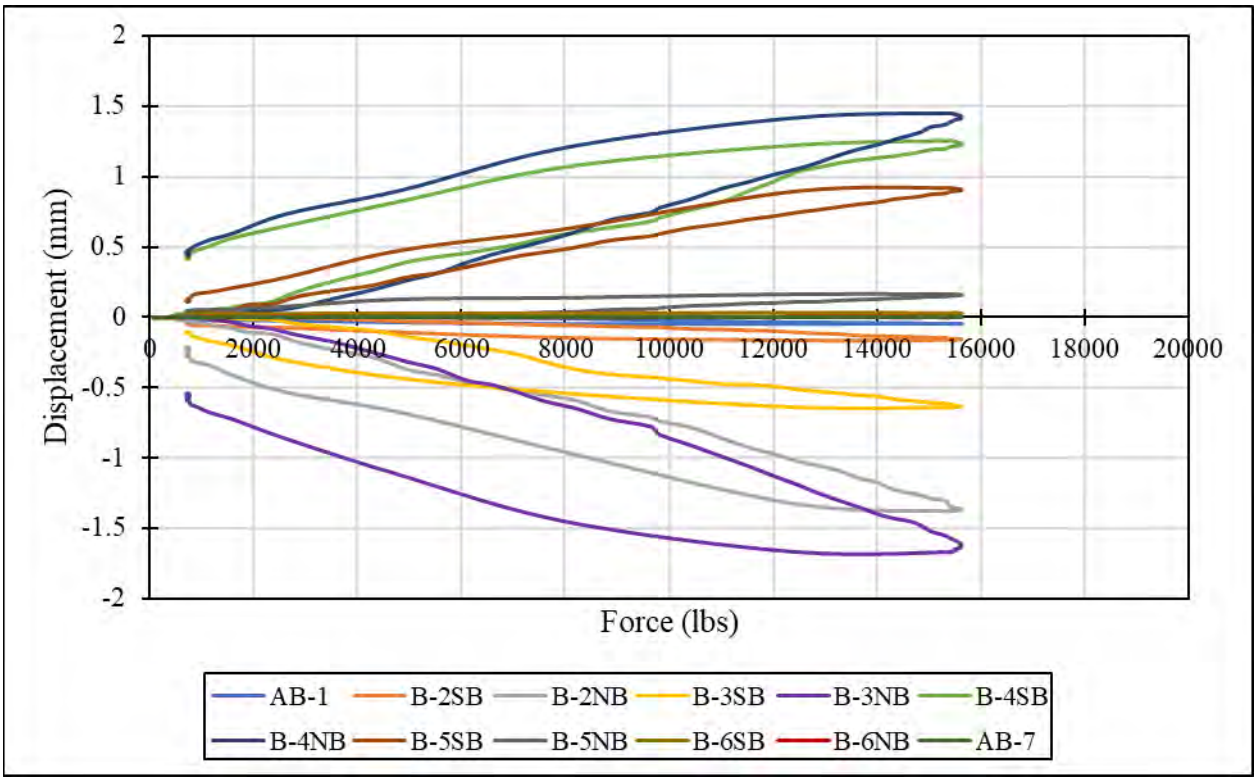

Figure B-6 – Displacement versus Applied Load for Span 3 Static Pull Test

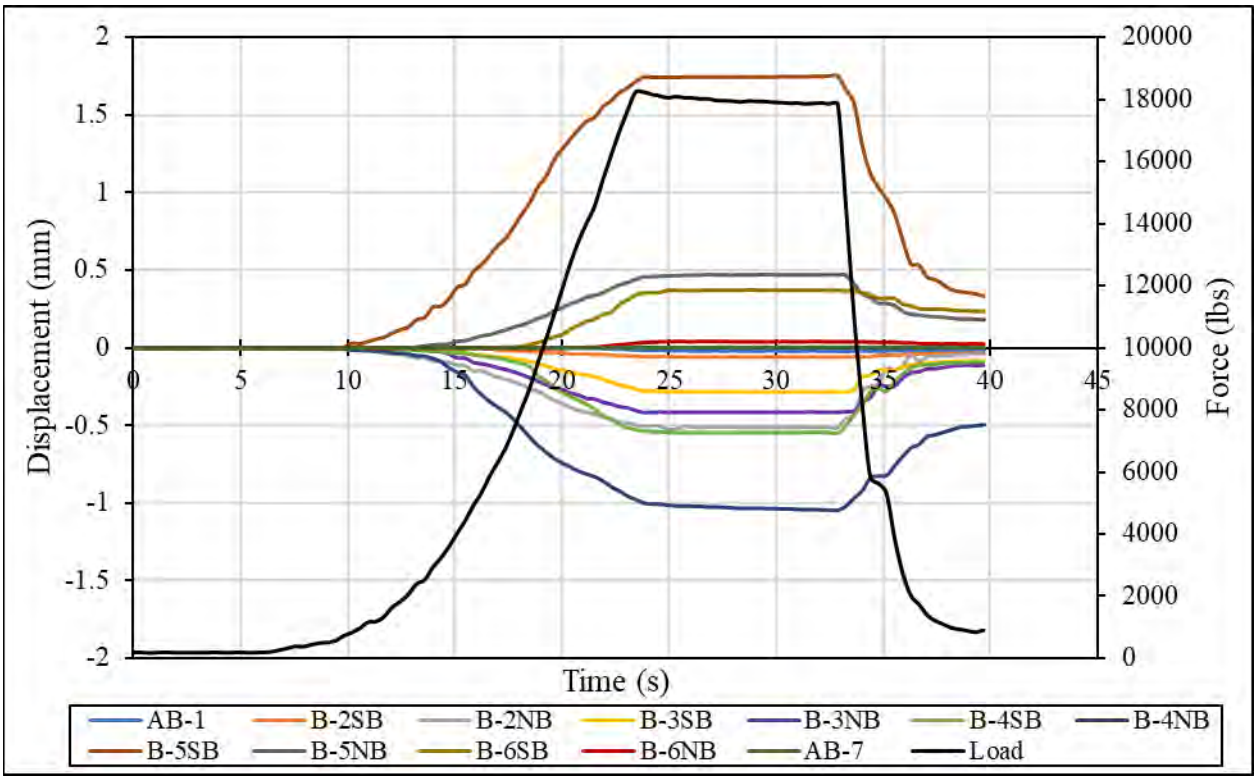

Figure B-7 – Load and Displacement over Time for Span 4 Static Pull Test

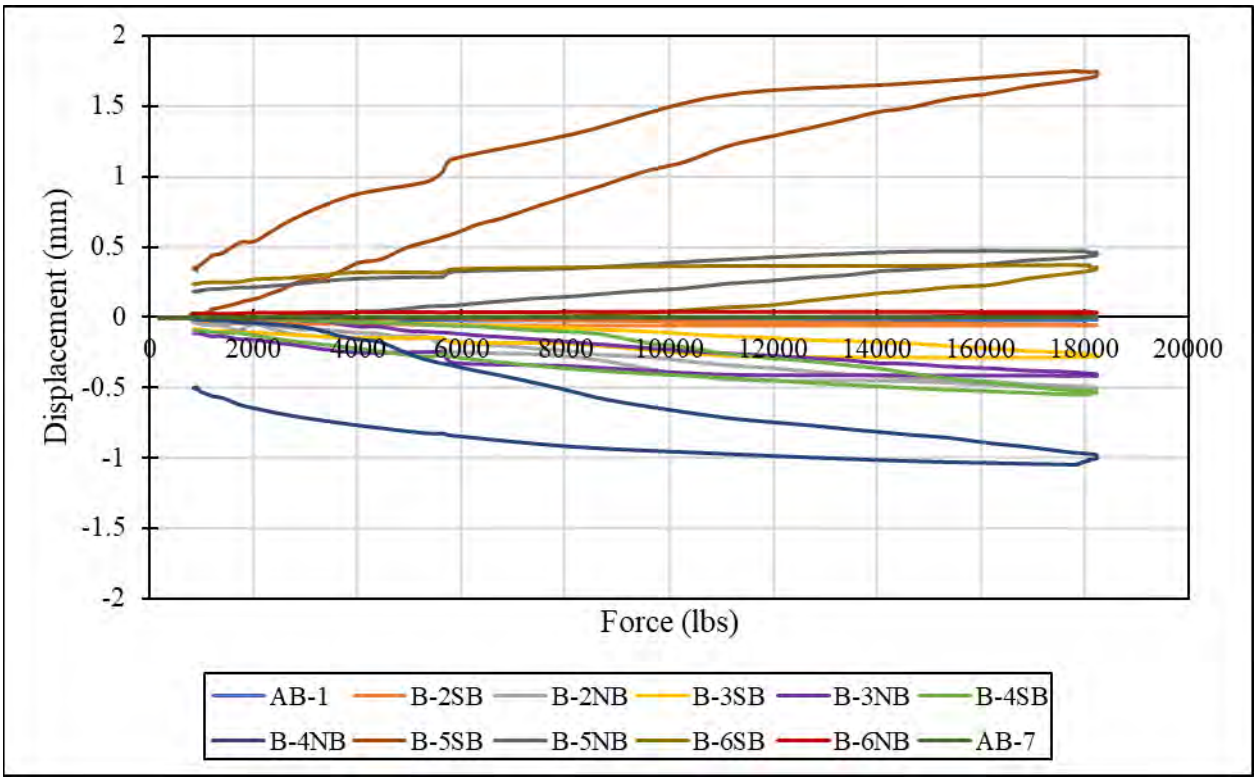

Figure B-8 – Displacement versus Applied Load for Span 4 Static Pull Test

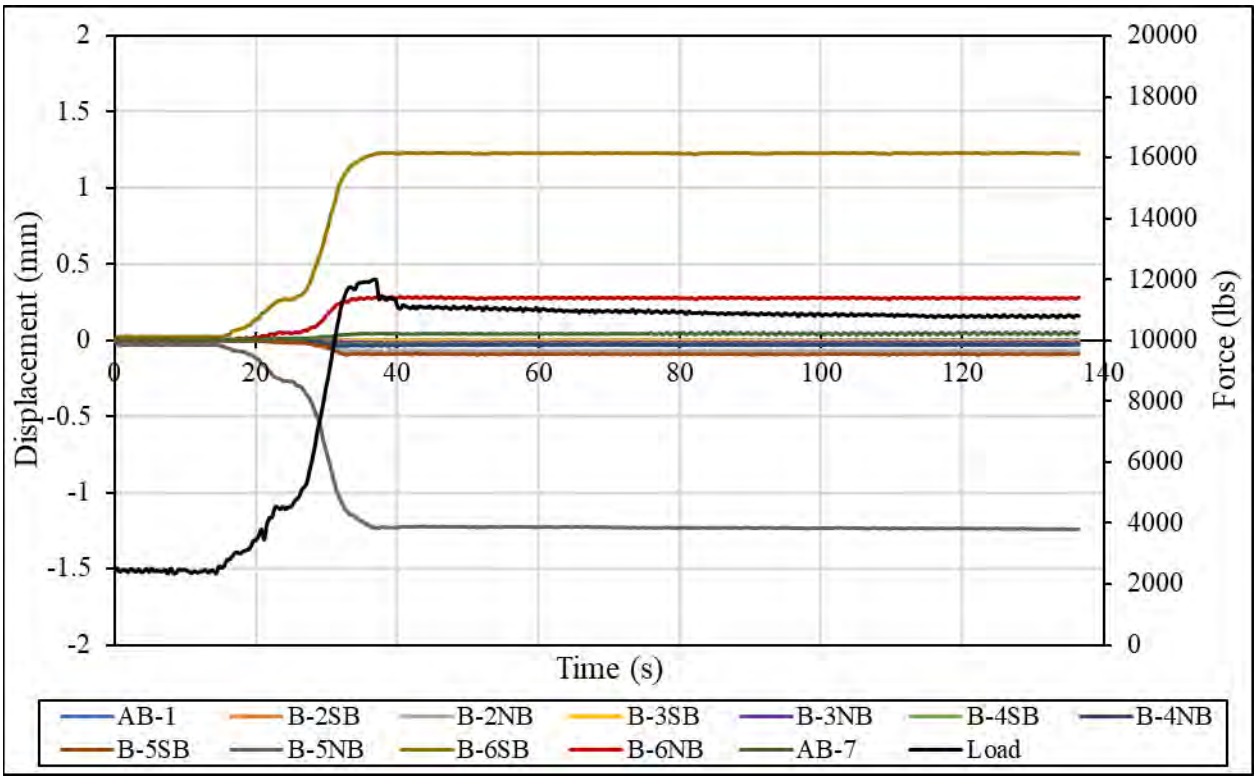

Figure B-9 – Load and Displacement over Time for Span 5 Static Pull Test

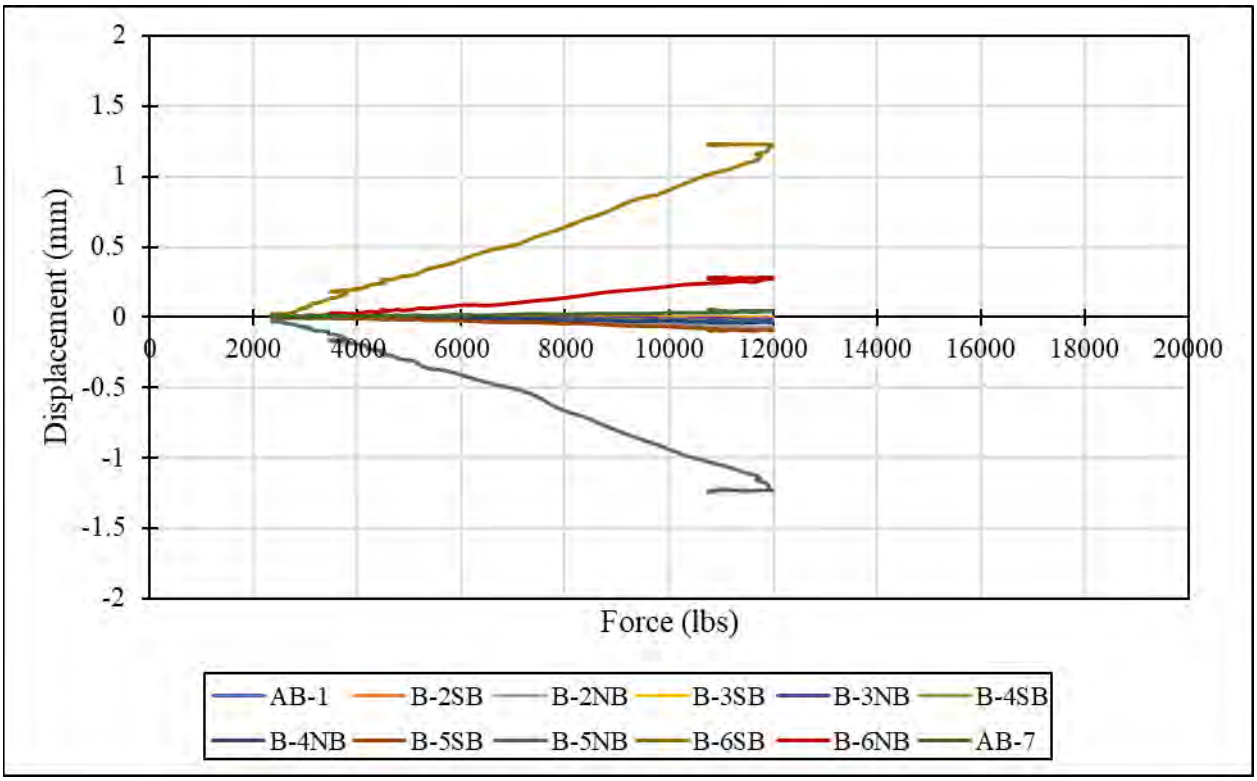

Figure B-10 – Displacement versus Applied Load for Span 5 Static Pull Test 1

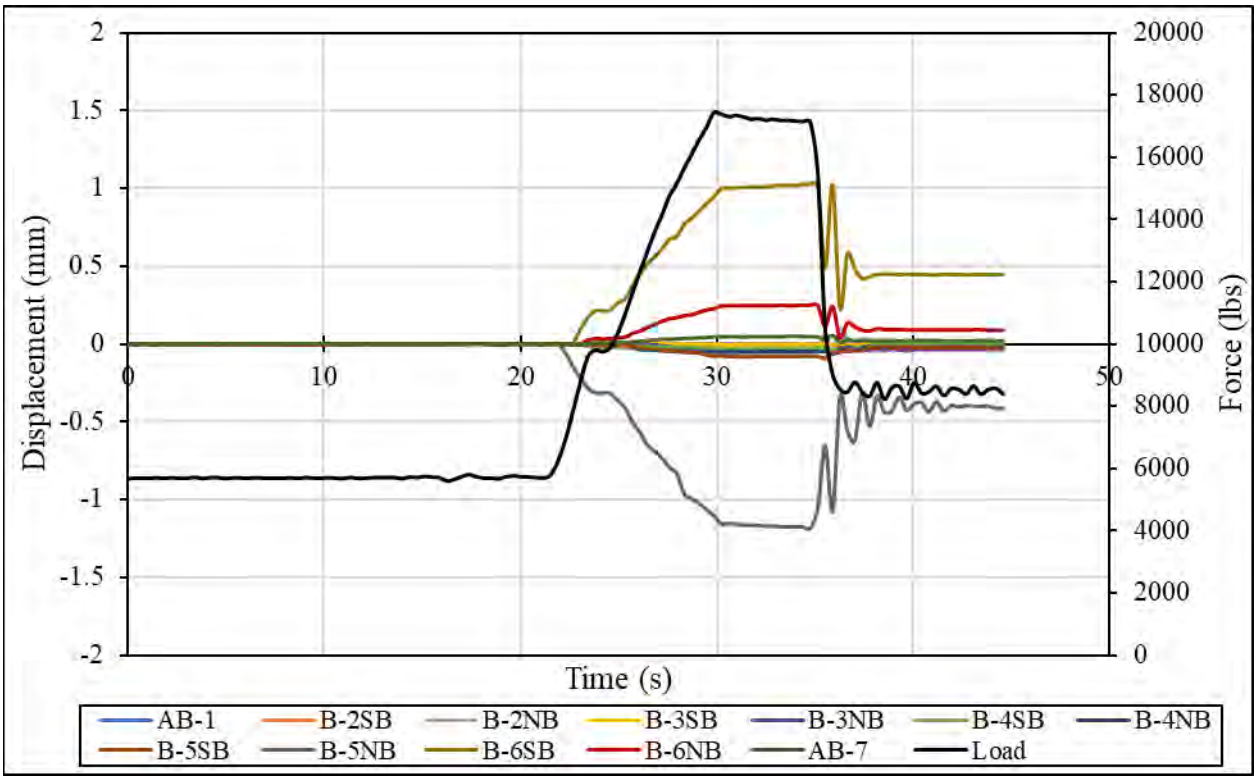

Figure B-11 – Load and Displacement over Time for Span 5 Static Pull Test 2

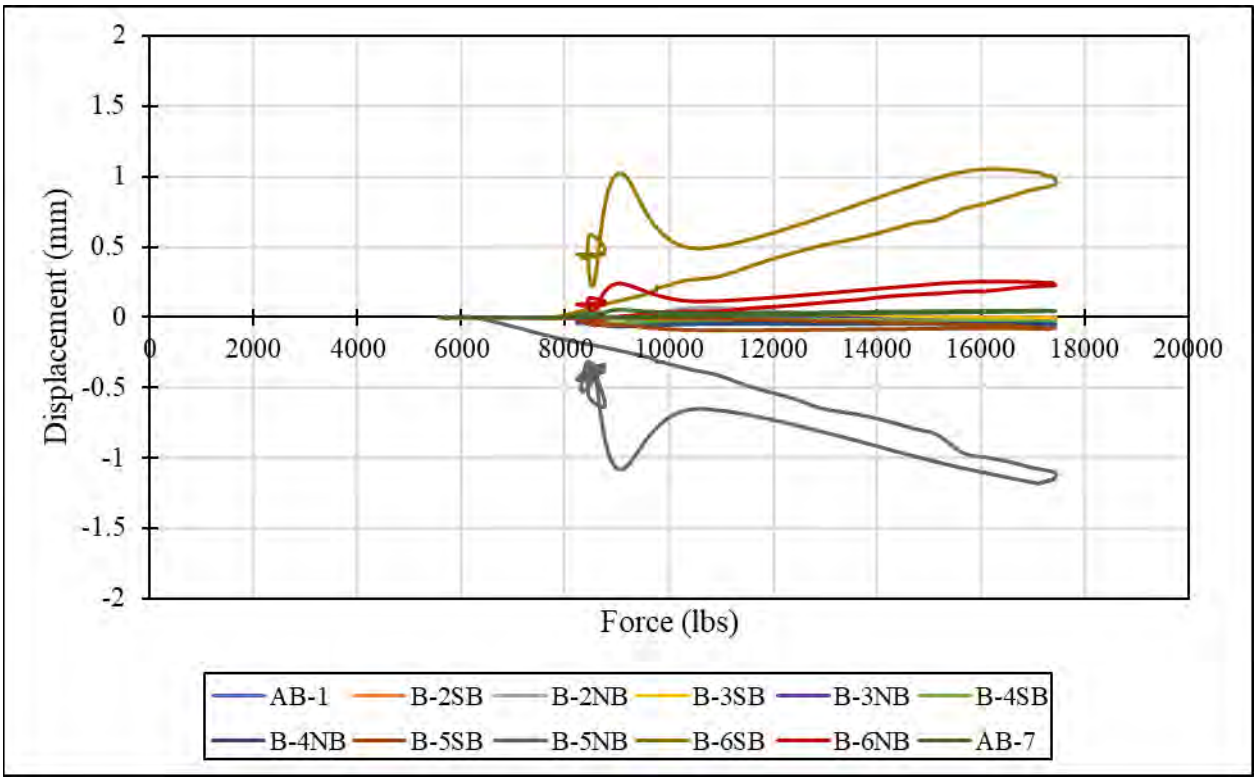

Figure B-12 – Displacement versus Applied Load for Span 5 Static Pull Test 2

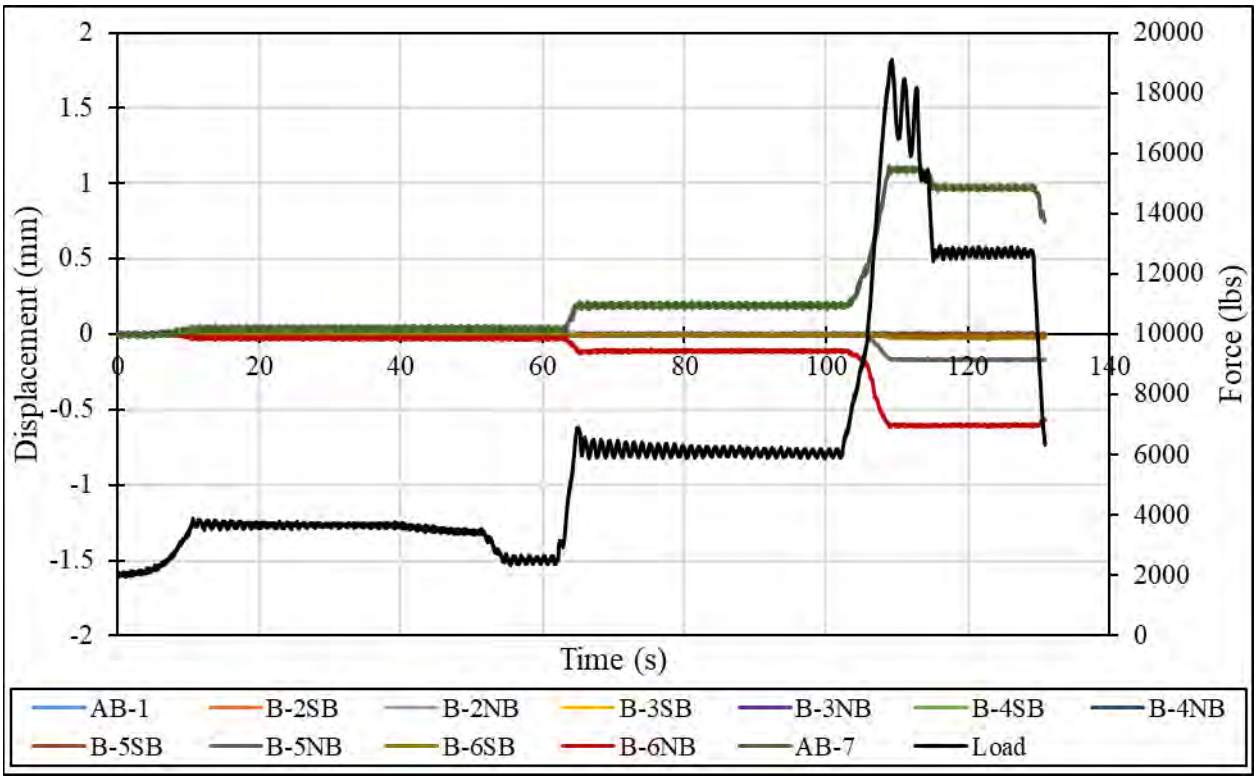

Figure B-13 – Load and Displacement over Time for Span 6 Static Pull Test

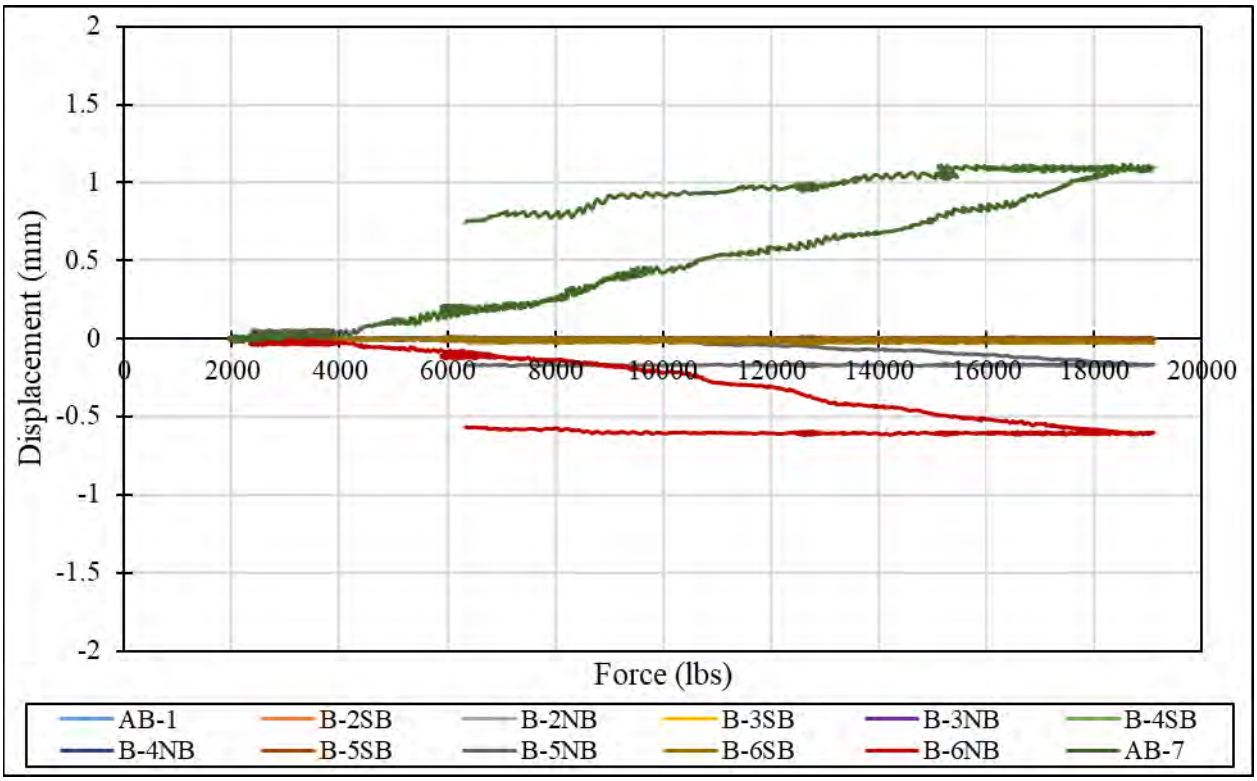

Figure B-14 – Displacement versus Applied Load for Span 6 Static Pull Test

Table B-1 – Field Test Displacement Data for Span 1

At 10400 lbs (ΔF = 10054 lbs) applied to Span 1			
Data From Field Tests			
	Displacement of Girder End Relative to Cap (in)	Displacement Relative to AB1 (in)	
A1	-0.0199	delta_S1	-0.0199
B2S1	0.0113	delta_B2	-0.0086
B2S2	0.0019	delta_S2	-0.0068
B3S2	0.0000	delta_B3	-0.0068
B3S3	0.0001	delta_S3	-0.0067
B4S3	0.0002	delta_B4	-0.0065
B4S4	0.0000	delta_S4	-0.0065
B5S4	0.0000	delta_B5	-0.0066
B5S5	0.0000	delta_S5	-0.0066
B6S5	0.0000	delta_B6	-0.0066
B6S6	0.0000	delta_S6	-0.0067
A7	0.0000	delta_AB7	-0.0067

Table B-2 – Field Test Displacement Data for Span 2

At 10613 lbs (ΔF = 10416 lbs) applied to Span 2			
Data From Field Tests			
	Displacement of Girder End Relative to Cap (in)	Displacement Relative to AB1 (in)	
A1	-0.0022	delta_S1	-0.0022
B2S1	-0.0066	delta_B2	-0.0088
B2S2	-0.0619	delta_S2	-0.0707
B3S2	0.0173	delta_B3	-0.0534
B3S3	0.0253	delta_S3	-0.0281
B4S3	0.0082	delta_B4	-0.0198
B4S4	0.0069	delta_S4	-0.0130
B5S4	0.0113	delta_B5	-0.0016
B5S5	0.0001	delta_S5	-0.0015
B6S5	0.0000	delta_B6	-0.0015
B6S6	0.0000	delta_S6	-0.0015
A7	0.0000	delta_AB7	-0.0015

Table B-3 – Field Test Displacement Data for Span 3

At 9823 lbs (ΔF = 9739 lbs) applied to Span 3			
Data From Field Tests			
	Displacement of Girder End Relative to Cap (in)	Displacement Relative to AB1 (in)	
A1	-0.0007	delta_S1	-0.0007
B2S1	-0.0028	delta_B2	-0.0035
B2S2	-0.0291	delta_S2	-0.0325
B3S2	-0.0170	delta_B3	-0.0496
B3S3	-0.0328	delta_S3	-0.0824
B4S3	0.0279	delta_B4	-0.0545
B4S4	0.0307	delta_S4	-0.0238
B5S4	0.0234	delta_B5	-0.0005
B5S5	0.0027	delta_S5	0.0022
B6S5	0.0001	delta_B6	0.0023
B6S6	0.0000	delta_S6	0.0023
A7	0.0000	delta_AB7	0.0023

Table B-4 – Field Test Displacement Data for Span 4

At 10307 lbs (ΔF = 10117 lbs) applied to Span 4			
Data From Field Tests			
	Displacement of Girder End Relative to Cap (in)	Displacement Relative to AB1 (in)	
A1	-0.0001	delta_S1	-0.0001
B2S1	-0.0012	delta_B2	-0.0013
B2S2	-0.0122	delta_S2	-0.0135
B3S2	-0.0046	delta_B3	-0.0181
B3S3	-0.0094	delta_S3	-0.0274
B4S3	-0.0083	delta_B4	-0.0358
B4S4	-0.0265	delta_S4	-0.0623
B5S4	0.0435	delta_B5	-0.0188
B5S5	0.0081	delta_S5	-0.0106
B6S5	0.0020	delta_B6	-0.0086
B6S6	-0.0001	delta_S6	-0.0087
A7	0.0000	delta_AB7	-0.0087

Table B-5 – Field Test Displacement Data for Span 5 Test 1

At 11998 lbs (ΔF = 9601 lbs) applied to Span 5			
Data From Field Tests			
	Displacement of Girder End Relative to Cap (in)	Displacement Relative to AB1 (in)	
A1	0.0000	delta_S1	0.0000
B2S1	0.0000	delta_B2	0.0000
B2S2	-0.0027	delta_S2	-0.0027
B3S2	-0.0001	delta_B3	-0.0028
B3S3	-0.0005	delta_S3	-0.0033
B4S3	-0.0010	delta_B4	-0.0043
B4S4	-0.0015	delta_S4	-0.0057
B5S4	-0.0036	delta_B5	-0.0093
B5S5	-0.0484	delta_S5	-0.0578
B6S5	0.0481	delta_B6	-0.0097
B6S6	0.0110	delta_S6	0.0013
A7	0.0017	delta_AB7	0.0030

Table B-6 – Field Test Displacement Data for Span 5 Test 2

At 15653 lbs (ΔF = 9977 lbs) applied to Span 5			
Data From Field Tests			
	Displacement of Girder End Relative to Cap (in)	Displacement Relative to AB1 (in)	
A1	0.0000	delta_S1	0.0000
B2S1	-0.0001	delta_B2	-0.0001
B2S2	-0.0022	delta_S2	-0.0023
B3S2	0.0000	delta_B3	-0.0023
B3S3	-0.0012	delta_S3	-0.0035
B4S3	-0.0010	delta_B4	-0.0045
B4S4	-0.0018	delta_S4	-0.0063
B5S4	-0.0020	delta_B5	-0.0083
B5S5	-0.0379	delta_S5	-0.0462
B6S5	0.0303	delta_B6	-0.0159
B6S6	0.0072	delta_S6	-0.0087
A7	0.0014	delta_AB7	-0.0073

Table B-7 – Field Test Displacement Data for Span 6

At 11954 lbs (ΔF = 9973 lbs) applied to Span 6			
Data From Field Tests			
	Displacement of Girder End Relative to Cap (in)	Displacement Relative to AB1 (in)	
A1	0.0000	delta_S1	0.0000
B2S1	-0.0002	delta_B2	-0.0002
B2S2	-0.0002	delta_S2	-0.0004
B3S2	0.0000	delta_B3	-0.0004
B3S3	-0.0003	delta_S3	-0.0007
B4S3	0.0000	delta_B4	-0.0007
B4S4	0.0000	delta_S4	-0.0007
B5S4	0.0001	delta_B5	-0.0007
B5S5	-0.0016	delta_S5	-0.0023
B6S5	-0.0001	delta_B6	-0.0024
B6S6	-0.0119	delta_S6	-0.0143
A7	0.0231	delta_AB7	0.0088

Appendix C. Dynamic Tests Downsampled Data

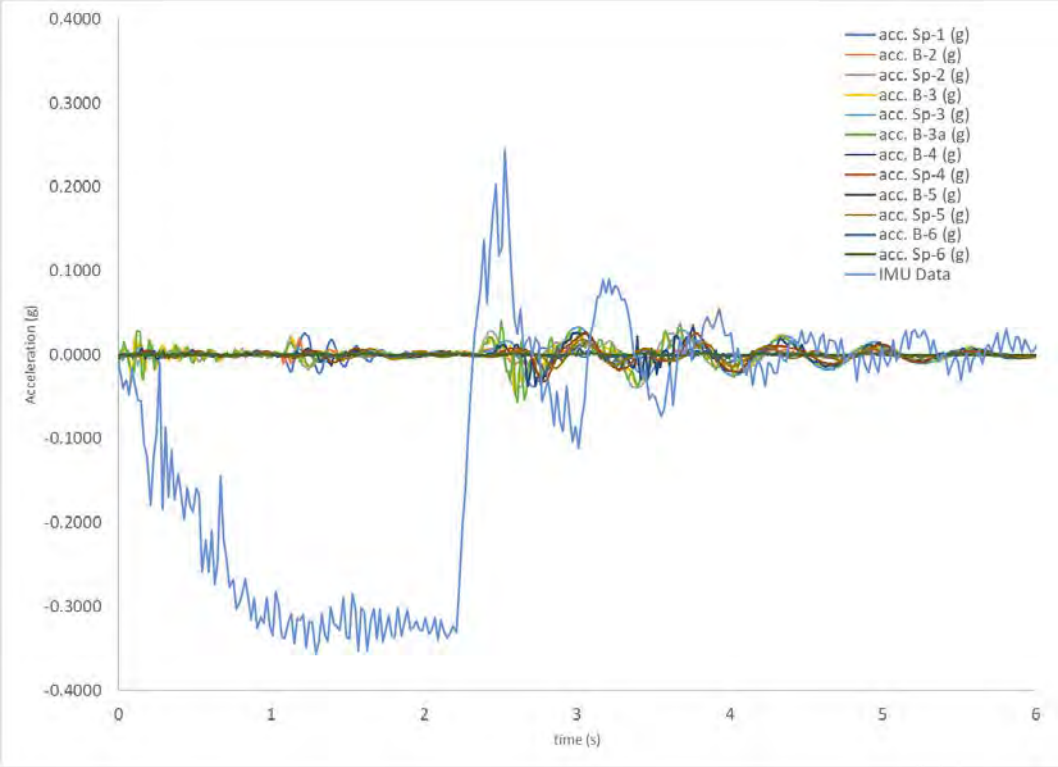

Figure C-1 – DAQ and IMU Data from Center of Span 2 Test 1

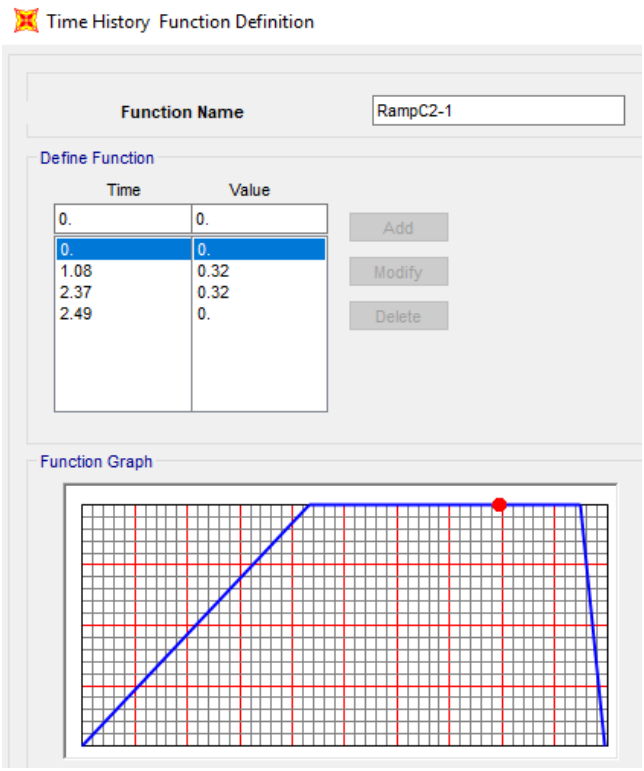

Figure C-2 – SAP2000 Time History Ramp Function from Braking Profile for C2-1

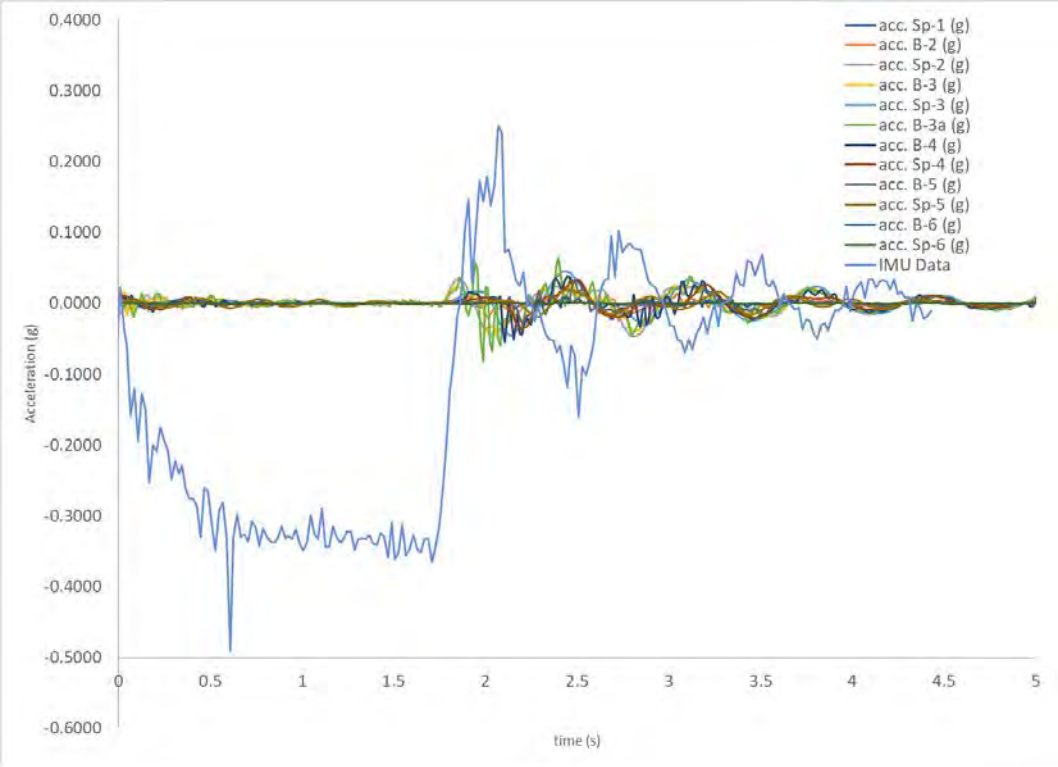

Figure C-3 – DAQ and IMU Data from Center of Span 2 Test 2

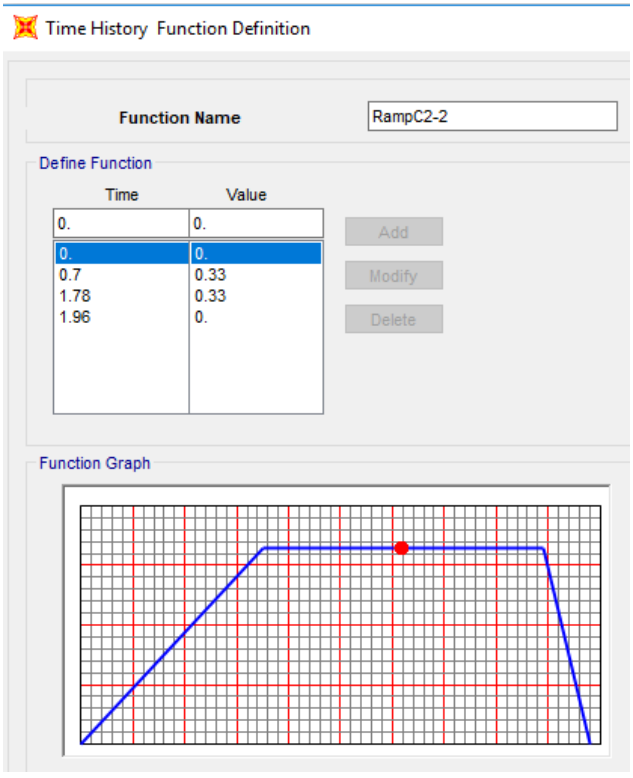

Figure C-4 – SAP2000 Time History Ramp Function from Braking Profile for C2-2

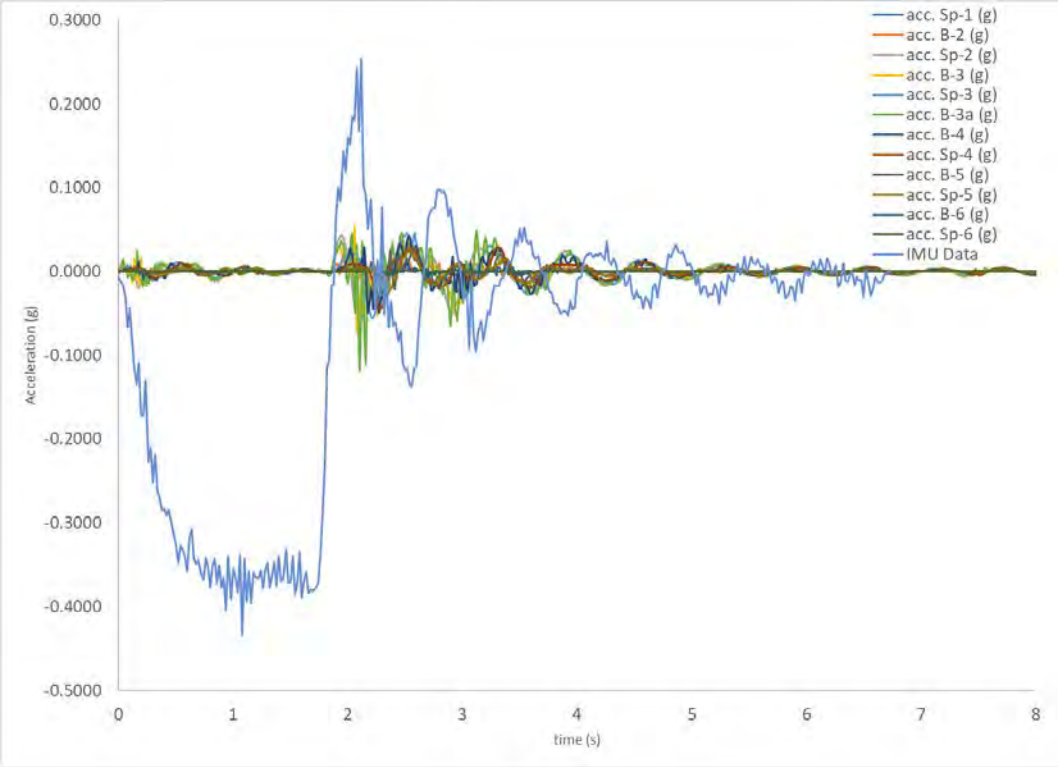

Figure C-5 – DAQ and IMU Data from Center of Span 2 Test 3

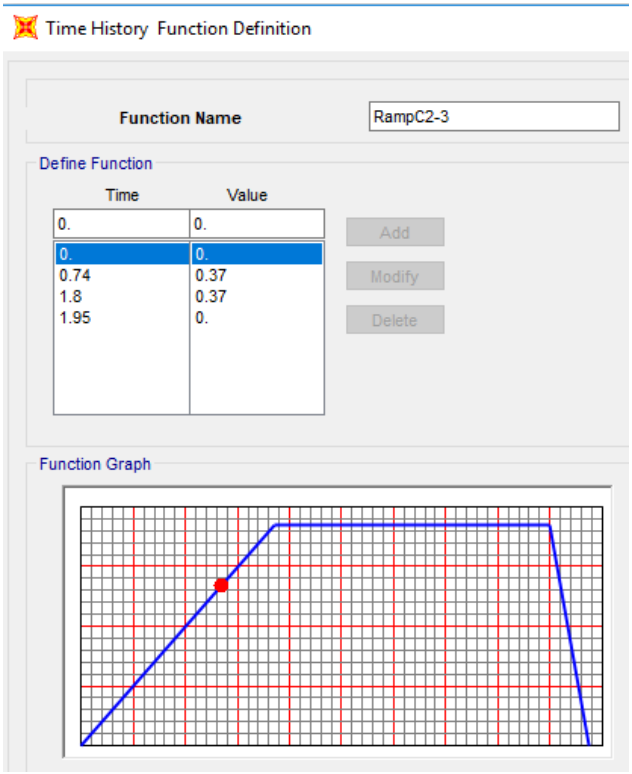

Figure C-6 – SAP2000 Time History Ramp Function from Braking Profile for C2-3

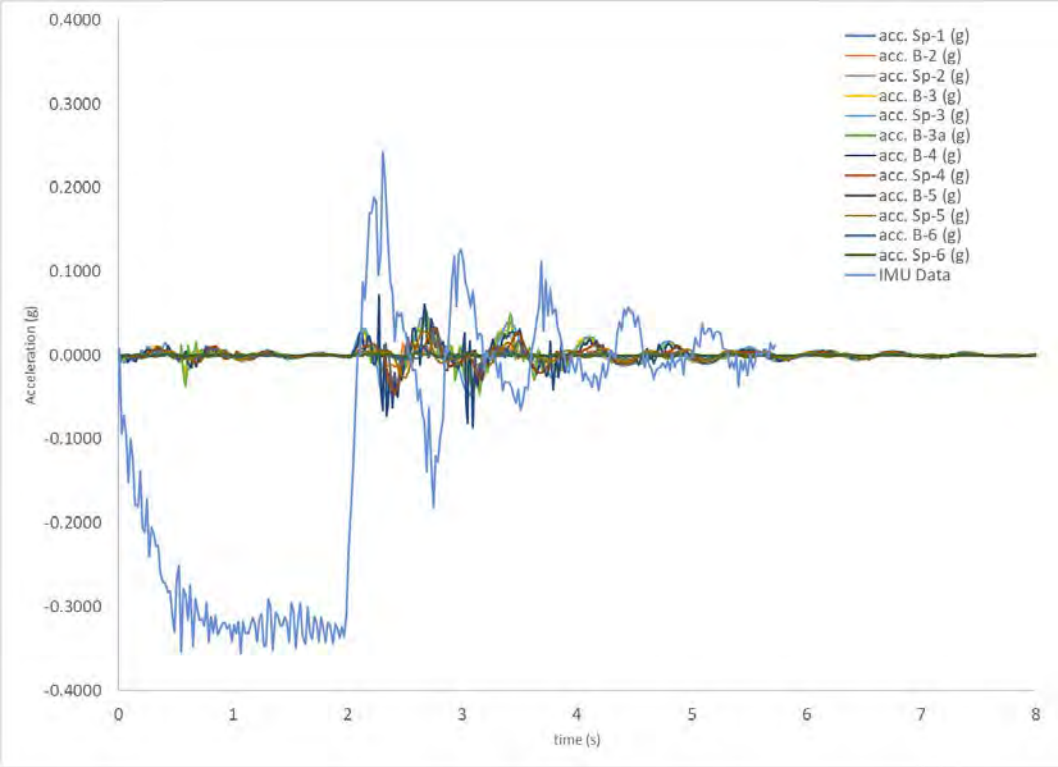

Figure C-7 – DAQ and IMU Data from Center of Span 3 Test 1

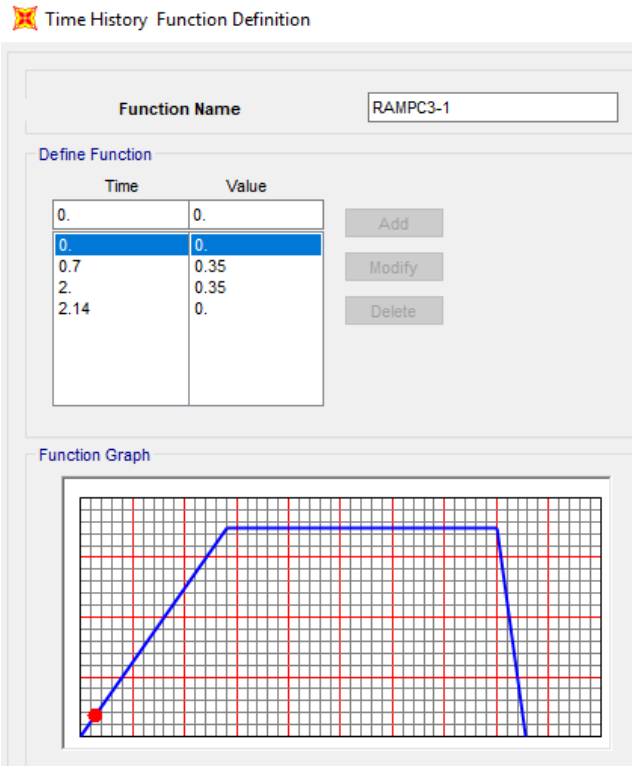

Figure C-8 – SAP2000 Time History Ramp Function from Braking Profile for C3-1

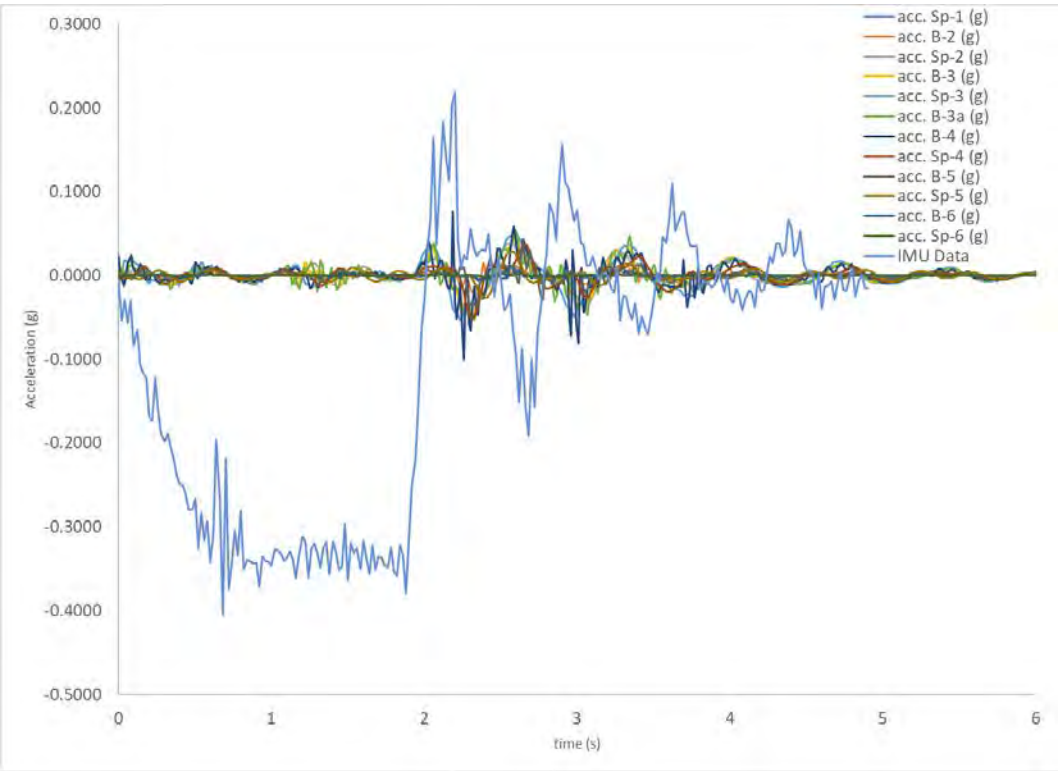

Figure C-9 – DAQ and IMU Data from Center of Span 3 Test 3

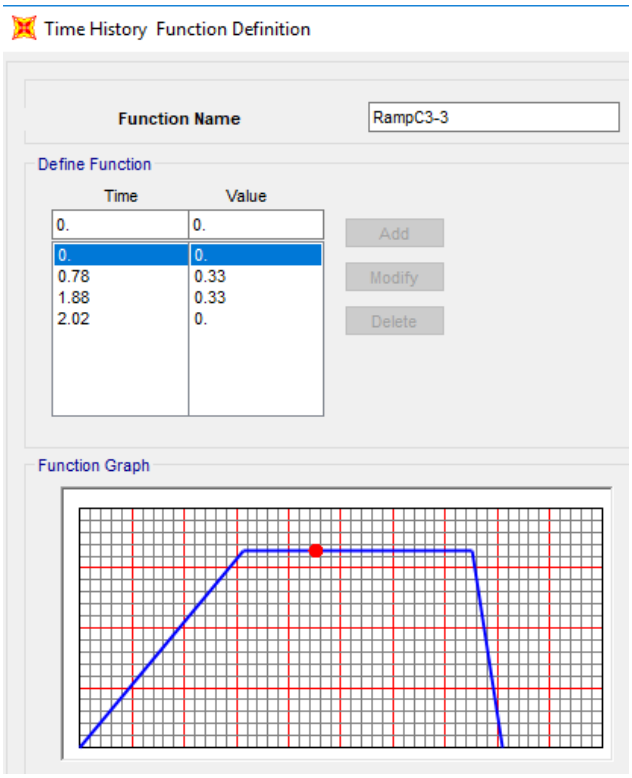

Figure C-10 – SAP2000 Time History Ramp Function from Braking Profile for C3-3

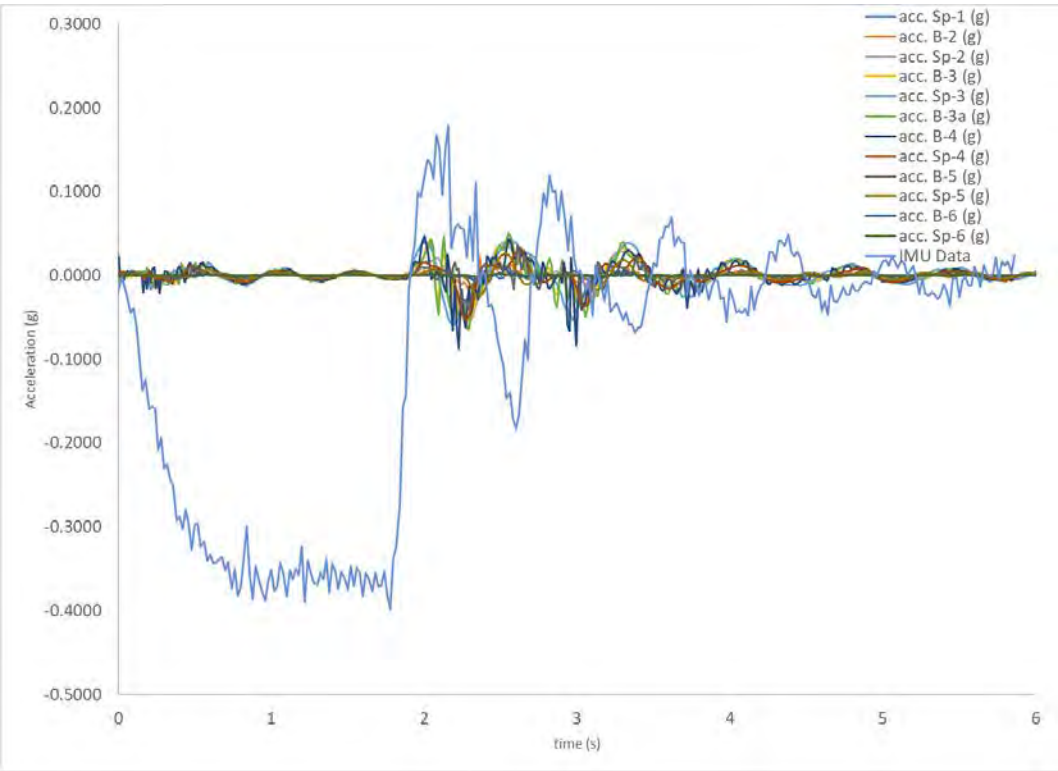

Figure C-11 – DAQ and IMU Data from Center of Span 3 Test 4

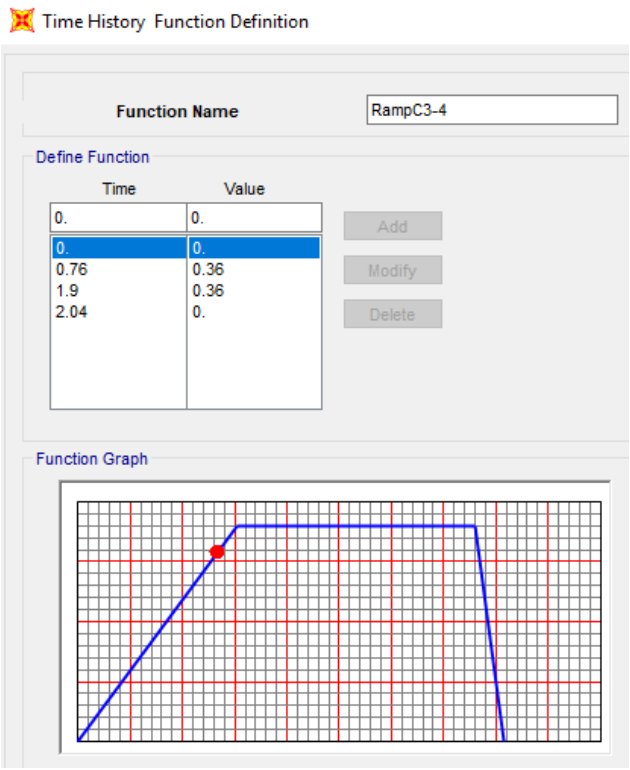

Figure C-12 – SAP2000 Time History Ramp Function from Braking Profile for C3-4

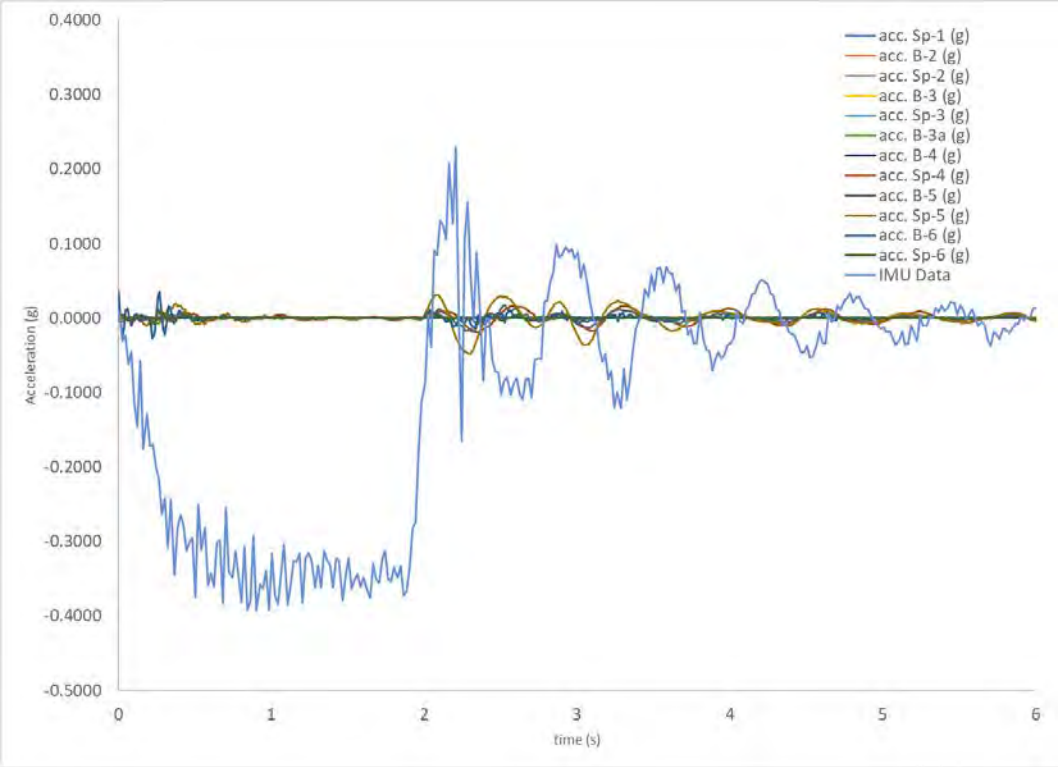

Figure C-13 – DAQ and IMU Data from Center of Span 5 Test 2

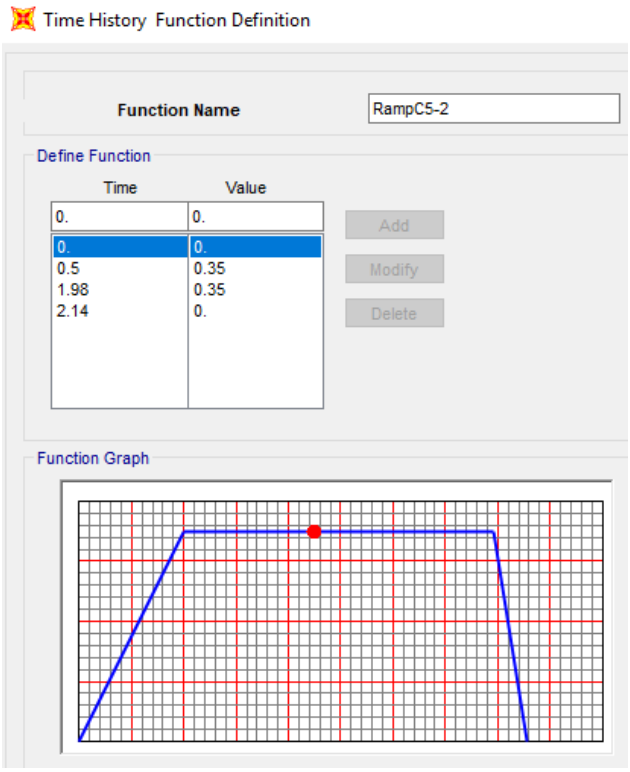

Figure C-14 – SAP2000 Time History Ramp Function from Braking Profile for C5-2

Appendix E.

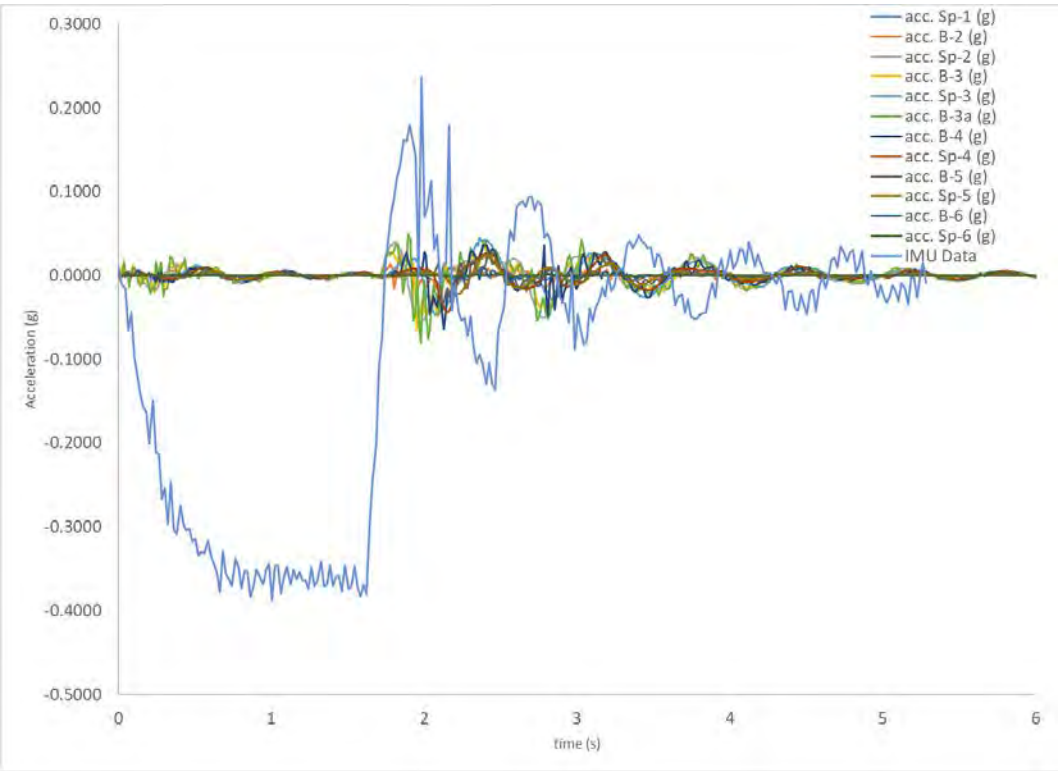

Figure C-15 – DAQ and IMU Data from the Right Side of Span 2 Test 2

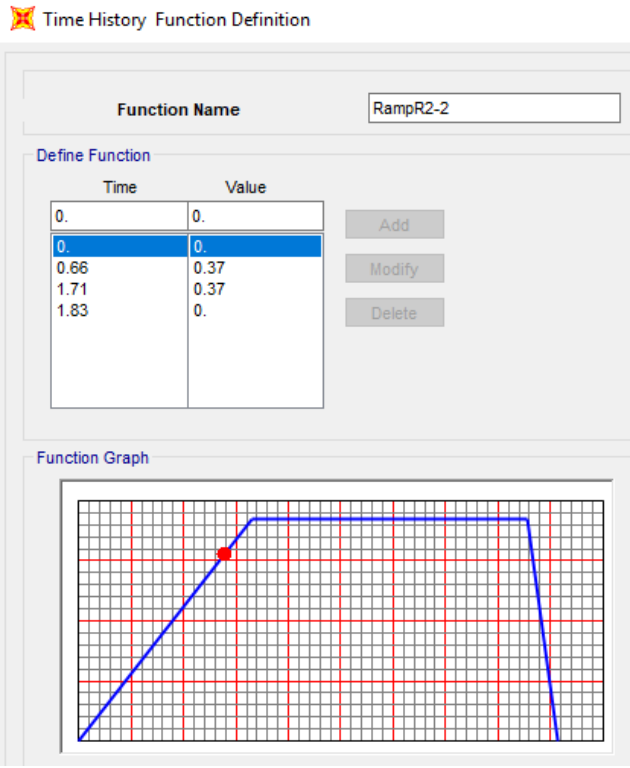

Figure C-16 – SAP2000 Time History Ramp Function from Braking Profile for R2-2

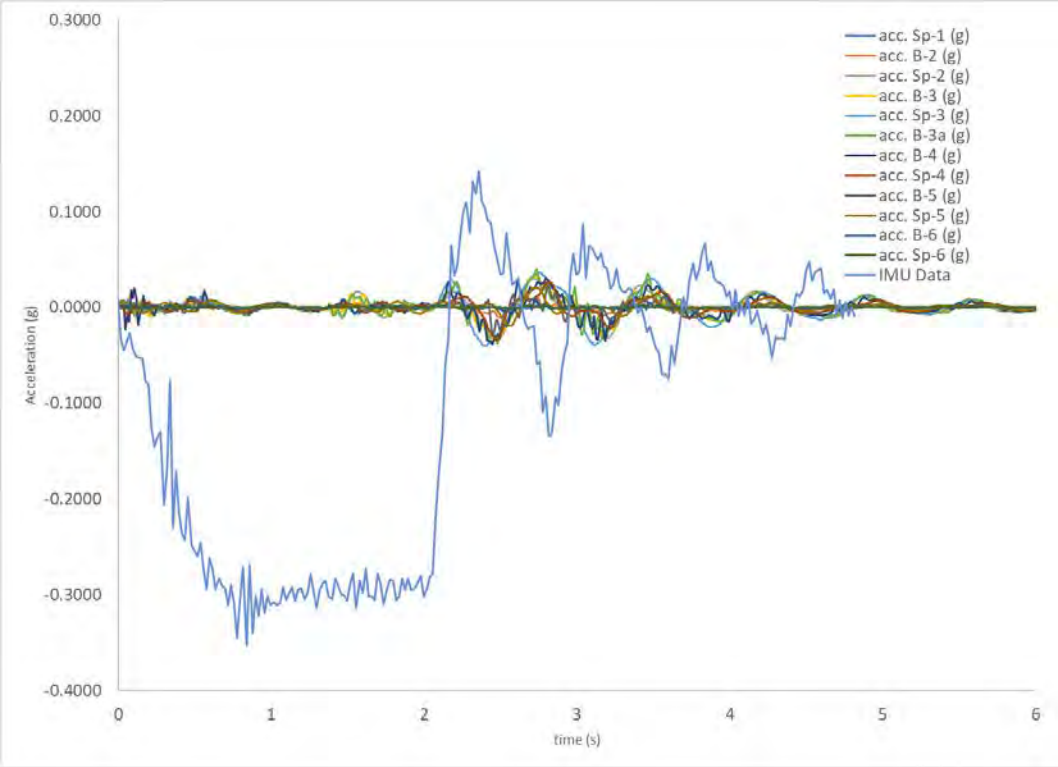

Figure C-17 – DAQ and IMU Data from the Right Side of Span 3 Test 3

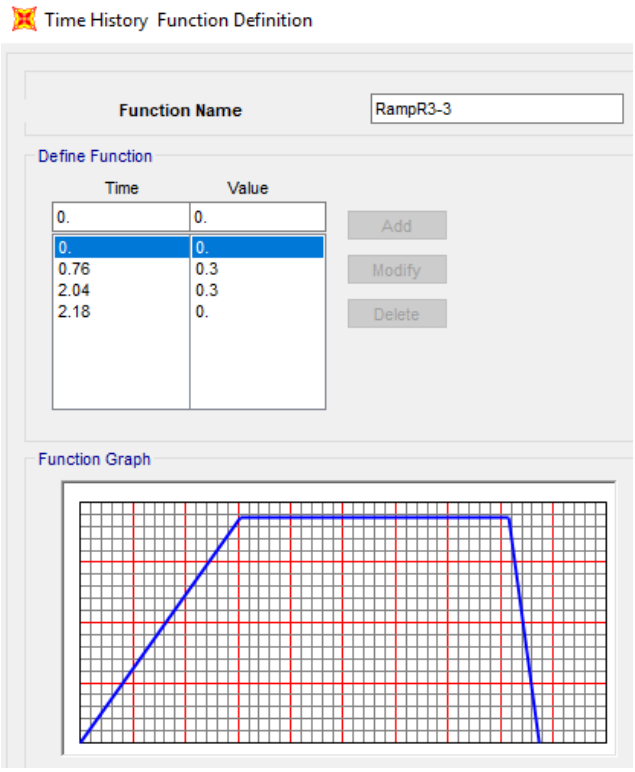

Figure C-18 – SAP2000 Time History Ramp Function from Braking Profile for R3-3

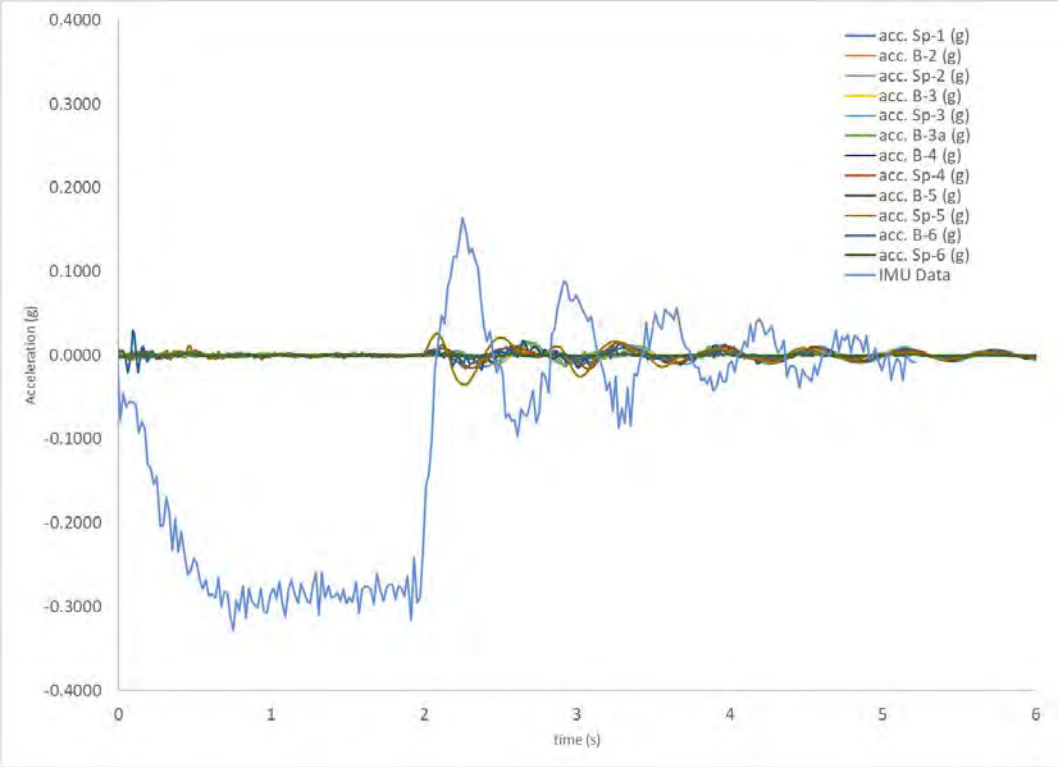

Figure C-19 – DAQ and IMU Data from the Right Side of Span 5 Test 1

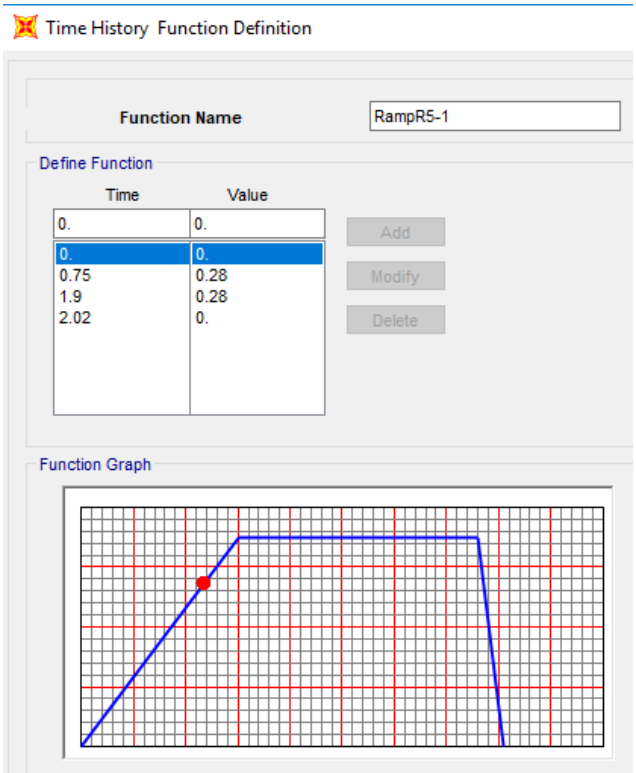

Figure C-20 – SAP2000 Time History Ramp Function from Braking Profile for R5-1

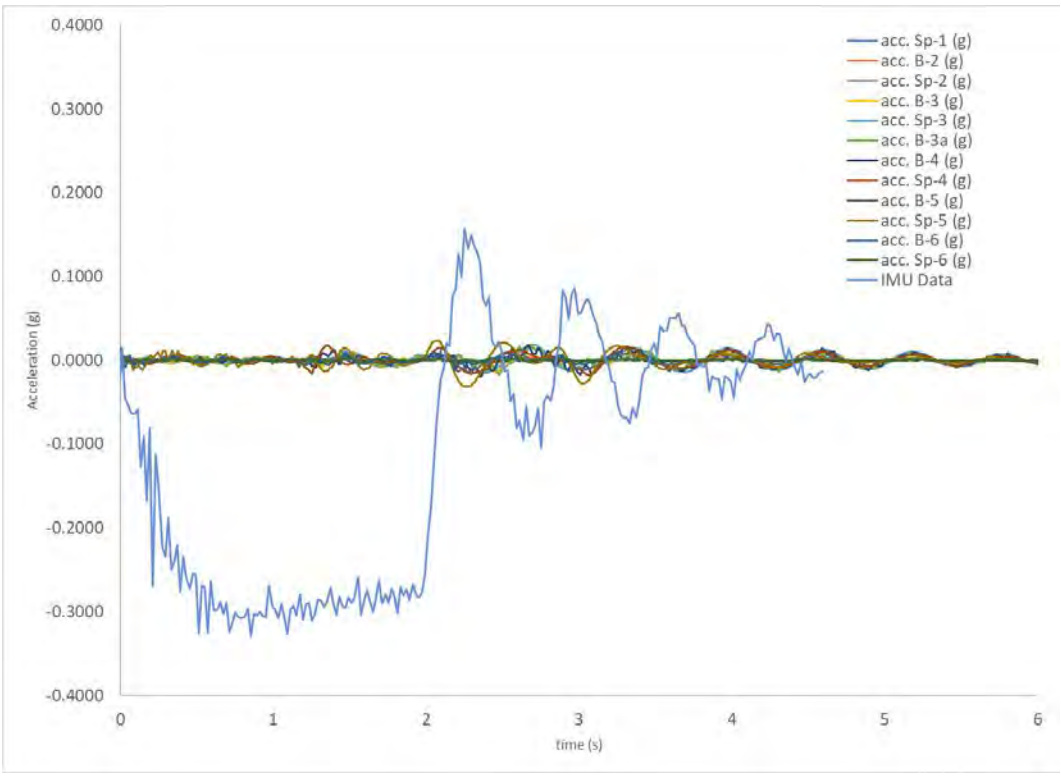

Figure C-21 – DAQ and IMU Data from the Right Side of Span 5 Test 3

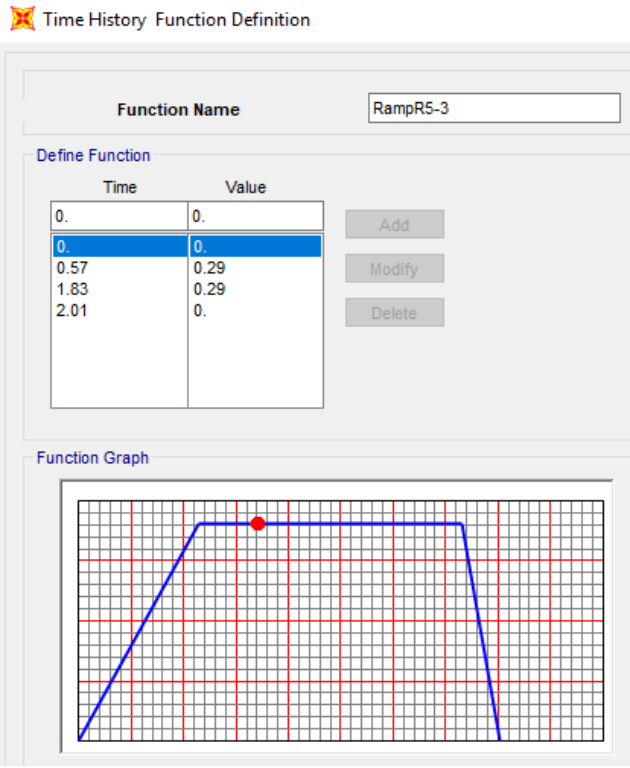

Figure C-22 – SAP2000 Time History Ramp Function from Braking Profile for R5-3